MANCHESTER METROPOLITAN UNIVERSITY

Quantifying the impacts of shipping NO_x emissions on tropospheric O_3, CH_4 and their radiative forcing

by

Jérôme D. J.-M. Hilaire

A thesis submitted in partial fulfillment for the degree of Doctor of Philosophy

in the

Faculty of Science and Engineering
School of Science and The Environment

April 2012

MANCHESTER METROPOLITAN UNIVERSITY

Abstract

Faculty of Science and Engineering

School of Science and The Environment

Doctor of Philosophy

by Jérôme D. J.-M. Hilaire

International shipping is a cornerstone of the global economy since it carries about 80% of the world trade by volume. It is also a growing sector that releases significant amounts of pollutants into the atmosphere. Shipping NO_x emissions could represent about 15% of the total anthropogenic NO_x emitted in 2000 and are particularly important since they perturb the concentrations of O_3 and CH_4, two greenhouse gases present in the atmosphere. Studies focusing on the impacts of shipping NO_x emissions on tropospheric chemistry and radiative forcing remain however quite recent and still bear significant uncertainties.

The aim of this study is to provide an extended view of the problem by making use of a state-of-art global chemistry-transport model (MOZART-4) in conjunction with a radiative transfer model (Edwards-Slingo). Since MOZART-4 has never been used before to analyse shipping NO_x impacts, a thorough comparison with the material reported in previous studies was carried out. The global model was further tested by performing a sensitivity analysis of shipping perturbations against various uncertainties in atmospheric processes and model changes. In addition, impacts from the implementation of a ship plume parameterisation based on the concept of effective reaction rates were assessed. The O_3 and CH_4 radiative forcings resulting from shipping NO_x emissions were then estimated with the help of Edwards-Slingo in 2000 and in the future by using the RCP scenarios. This last step laid the ground for a linearization of the global shipping NO_x-O_3-CH_4 system.

The assessment of MOZART-4 revealed that the model is suitable for the analysis of shipping NO_x impacts. Although it simulates larger O_3 perturbations in the free troposphere as well as a larger CH_4 lifetime perturbation, estimates remain within 1-σ standard deviation of the results reported in a previous multimodel study. Current uncertainties in shipping emissions and particularly their magnitude remain the largest contributor to the uncertainty in shipping O_3 and CH_4 perturbations ([-39%, 67%] and [-37%, 59%], respectively). The shipping emission parameterisation developed by Dr. Huszár was found to be unsuitable for usage in MOZART-4, partly because of the absence of NO_x sink processes. This was corrected by implementing the approach designed by Dr. Moldanová which

lead to NO_x and O_3 reductions larger than 20% at the surface of the oceans. A net radiative forcing from shipping NO_x emissions of -60 mW/m2 was computed with Edwards-Slingo in 2000. Under the RCP scenarios, the net radiative forcing range between -96 mW/m2 and -15 mW/m2. A linear relationship was finally derived between shipping NO_x emissions and the radiative forcing of shipping O_3 and CH_4. Estimates calculated with the linear model remain within 15% of the values computed with the global models.

Further work should focus on trying to reduce the uncertainties linked to the magnitude and spatial distribution of shipping emissions. The shipping emission parameterisation based on the concept of effective reaction rates still bear problems which should be addressed in the future. Finally, it would be interesting to estimate the future radiative forcings from shipping NO_x emissions under the SRES scenarios since these forecast values are larger shipping emissions. This would potentially increase the robustness of the linear model.

Acknowledgements

I would first like to thank the Department for Transport for providing the funding necessary to carry out this research as well as my supervisors for their encouragements and help. In particular, Prof. Dr. David Lee for his continuous support and helpful discussions. I am also deeply thankful to Prof. Dr. Veronika Eyring who helped me to join and collaborate with the group of scientists involved in the development and testing of the emission parameterisation based on the concept of effective reaction rate, and also to Dr. Steven Arnold for his time, motivating discussions and general help on global chemistry-transport models. I benefited extensively from verbal exchanges with Prof. Dr. David Raper and his knowledge regarding the MMU administration.

I am profoundly grateful to Dr. Ling Lim and Stacy Walters as well as the people from Streamline and CRAY who gave a lot of their time to test, configure and set up the CRAY-CX1 with which I was able to perform about 200 MOZART-4 simulations within a few months. Sandra Fletcher and the IT technicians at MMU were also of great help in this process. I also wish to thank the people at ECMWF for providing CATE with an account on super computers.

Special thanks go to Dr. Cristina Charlton-Perez, Dr. Jana Moldanová and Dr. Gabriela Sousa Santos. Firstly, Dr. Cristina Charlton-Perez kindly provided me with her high-resolution ship plume model's code that gave me the basis to develop the SPM-2D model. Secondly, I gained a better insight of the shipping emission parameterisation problem through useful discussions and collaboration with Dr. Jana Moldanová who hosted me for a week at IVL. Thirdly, Dr. Gabriela Sousa Santos allowed me to make use of the bromine chemical mechanism that she developed during her Ph.D. This, in turn, enabled me to analyse the impacts of bromine chemistry on shipping O_3 perturbations. Further thanks go to Dr. Beatriz Monge-Sanz who kindly introduced me to Dr. Steven Arnold and Dr. Matthew Evans and made possible my collaboration with Dr. Steven Arnold.

I am very grateful to the MOZART community and in particular to Dr. Jean-François Lamarque, Dr. Louisa Emmons, Stacy Walters, Dr. Doug Kinnison, Dr. Martin Schultz and Dr. Olaf Stein who were always considerate and helpful. The O_3 tagging scheme and the scripts to download ECMWF dynamical data from the MARS servers were particularly useful.

I would like to thank the various scientists that I had the privilege to meet during schools and conferences (some of which became friends). In particular, I am grateful to Dr. Roland von Glasow, Dr. David S. Stevenson, Dr. Alexander Archibald, Dr. Aoife Grant, Dr. Tom Breider, Dr. Matt Woodhouse, Dr. Nigel Richards and Sarah Monks for their interesting discussions.

A big thanks go to the people from CATE who were providing the required entertainment over these four years but also to those who were part of the reviewing process of this work.

I also wish to thank Prof. Dr. Andreas Petzold for interesting discussions on research and science that we shared around pints and curries in Manchester and Munich.

And last but surely not least, I am deeply grateful to my partner, M'elissa Truche as well as my family and friends for their support and understanding.

Contents

Abstract i

Acknowledgements iv

List of Figures xi

List of Tables xxi

Abbreviations xxiv

Website xxix

1 Introduction 1
- 1.1 The big picture . . . 1
- 1.2 Impacts of shipping NO_x emissions . . . 3
- 1.3 Research questions . . . 4
- 1.4 Thesis structure . . . 4

2 On the impacts of shipping emissions of nitrogen oxides on tropospheric ozone, methane and their radiative forcing 6
- 2.1 Shipping emissions . . . 8
  - 2.1.1 Fuel consumption . . . 10
  - 2.1.2 Emission factors . . . 11
  - 2.1.3 Spatial distribution . . . 12
  - 2.1.4 Future emission estimates . . . 13
- 2.2 Shipping emissions of nitrogen oxides in the context of tropospheric chemistry and transport . . . 14
  - 2.2.1 From the small scale... . . . 15
  - 2.2.2 ...to the global scale . . . 19
    - 2.2.2.1 The NO_x-O_3-HO_x photochemical system . . . 19
    - 2.2.2.2 NO_x . . . 19
    - 2.2.2.3 O_3 . . . 20

2.2.2.4 OH . . . 22
2.2.2.5 CH_4 . . . 22
2.2.3 Future impacts . . . 23
2.3 Radiative forcing impacts . . . 23
2.3.1 Earth's energy budget and radiative forcing . . . 23
2.3.2 Radiative forcing of shipping NO_x . . . 26

3 Description of the models 29
3.1 Introduction . . . 29
3.2 SPM-2D . . . 29
3.2.1 Chemical mechanism . . . 30
3.2.2 Ship plume dynamics . . . 32
3.2.3 Description of calculations . . . 33
3.3 MOZART-4 . . . 34
3.4 Edwards-Slingo . . . 38

4 MOZART-4's ability to represent the Marine Boundary Layer and the free troposphere 40
4.1 Introduction . . . 41
4.2 Methodology . . . 42
4.2.1 MOZART-4 set-up . . . 42
4.2.2 World Data Center for Greenhouse Gases . . . 43
4.2.3 WOUDC . . . 45
4.2.4 Aircraft data composites . . . 45
4.2.5 TES . . . 48
4.3 Results . . . 50
4.3.1 Comparison with WDCGG ozone data . . . 50
4.3.2 Comparison with WOUDC data . . . 63
4.3.3 Comparison with aircraft data composites . . . 65
4.3.3.1 TOPSE campaign in 2000 . . . 65
4.3.3.2 Gridded climatologies . . . 72
4.3.4 Comparison with TES data . . . 75
4.4 Discussion . . . 79

5 MOZART-4's ability to represent shipping perturbations 82
5.1 Introduction . . . 83
5.2 Methodology . . . 84
5.3 Results . . . 86
5.3.1 Nitrogen oxides . . . 86
5.3.1.1 Comparison with E2007 . . . 86
5.3.1.2 Comparisons between the three methodologies . . . 87
5.3.2 Ozone . . . 92
5.3.2.1 Comparison with E2007 . . . 92
5.3.2.2 Comparisons between the three methodologies . . . 93
5.3.3 Hydroxyl radical . . . 101

5.3.4 Methane . . . 103
5.4 Discussion . . . 104

6 Sensitivity of shipping perturbations to current uncertainties from various atmospheric processes 106
6.1 Introduction . . . 107
6.2 Methodology . . . 110
6.2.1 Dynamical data . . . 111
6.2.2 Shipping emissions . . . 113
6.2.3 Background anthropogenic emissions . . . 114
6.2.4 Photolysis and chemical activity . . . 115
6.2.5 Lightning . . . 119
6.2.6 Horizontal resolution . . . 119
6.2.7 Summary of the simulations . . . 121
6.3 Results . . . 124
6.3.1 Changes in shipping perturbations of NO_x and O_3 near the surface . . . 124
6.3.1.1 Shipping emission magnitude . . . 129
6.3.1.2 Shipping emission spatial distribution . . . 129
6.3.1.3 Horizontal resolution . . . 132
6.3.1.4 Dynamical data . . . 133
6.3.1.5 Offline photolysis scheme . . . 137
6.3.1.6 Other photochemistry . . . 137
6.3.1.7 Lightning activity . . . 139
6.3.1.8 Background anthropogenic emissions . . . 140
6.3.2 Vertical structure of the changes of shipping perturbations of O_3 and OH . . . 145
6.3.2.1 Shipping emission magnitude . . . 145
6.3.2.2 Offline photolysis scheme . . . 151
6.3.2.3 Shipping emission spatial distribution . . . 151
6.3.2.4 Lightning activity . . . 152
6.3.2.5 Other photochemistry . . . 153
6.3.2.6 Dynamical data . . . 156
6.3.2.7 Horizontal resolution . . . 158
6.3.2.8 Background anthropogenic emissions . . . 158
6.3.3 Changes in tropospheric O_3 columns of shipping perturbations 159
6.3.3.1 Shipping emission magnitude . . . 161
6.3.3.2 Offline photolysis scheme . . . 161
6.3.3.3 Horizontal resolution . . . 163
6.3.3.4 Lightning activity . . . 164
6.3.3.5 Shipping emission spatial distribution . . . 165
6.3.3.6 Background anthropogenic emissions . . . 166
6.3.3.7 Other photochemistry . . . 166
6.3.3.8 Dynamical data . . . 167

6.3.4 Changes in global O_3 burden, global OH concentrations and global CH_4 lifetime . . . 167
6.3.4.1 Shipping emission magnitude . . . 168
6.3.4.2 Offline photolysis scheme . . . 169
6.3.4.3 Shipping emission spatial distribution . . . 170
6.3.4.4 Lightning activity . . . 170
6.3.4.5 Other photochemistry . . . 170
6.3.4.6 Horizontal resolution . . . 170
6.3.4.7 Background anthropogenic emissions . . . 171
6.3.4.8 Dynamical data . . . 171
6.4 Discussion . . . 171

7 Effects of including a ship plume parameterisation 174
7.1 Introduction . . . 175
7.2 Extension of Huszár's work . . . 177
7.2.1 Methodology . . . 177
7.2.2 Results . . . 178
7.2.3 Discussion . . . 191
7.3 Implementing Moldanová's approach . . . 193
7.3.1 Methodology . . . 193
7.3.2 Results . . . 193
7.3.3 Discussion . . . 198

8 Radiative forcing of ozone and methane in 2000 and in the future 200
8.1 Introduction . . . 201
8.2 Methodology . . . 204
8.2.1 MOZART-4: Calculating ozone and methane concentration perturbations . . . 205
8.2.2 Edwards-Slingo: Calculating ozone and methane radiative forcing . . . 207
8.3 Results . . . 208
8.3.1 RF estimates of O_3 and CH_4 in 2000 and in the future . . . 208
8.3.2 Linear relationships between global metrics of shipping perturbations and parameterisation of the O_3 and CH_4 RF responses to shipping NO_x emissions . . . 211
8.4 Discussion . . . 220

9 Summary of the results 222

10 Conclusions and recommendations for further work 226

A Description of the dynamical data used in MOZART-4 229
A.1 NCEP Reanalysis . . . 229
A.2 ECMWF INTERIM . . . 230

B ACCMIP and RCP emission inventories **231**
B.1 Comparison of the ACCMIP emission inventory with the POET emission inventory . . . 232
B.2 Historical inventory representative of the year 2000 (ACCMIP) . . . 234
B.3 RCP emission inventories . . . 235

C Supporting data to chapter 4 **244**
C.1 WDCGG . . . 244
C.2 Aircraft data composites . . . 246

D Supporting data to chapter 6 **247**
D.1 Surface concentrations of nitrogen oxides . . . 247
D.2 Surface concentrations of ozone . . . 251
D.3 Zonal means of ozone . . . 255
D.4 Zonal means of hydroxyl radicals . . . 259
D.5 Tropospheric ozone columns . . . 263

E Supporting data to chapter 7 **267**

F Publications **270**

Bibliography **282**

List of Figures

2.1 Diagram showing the increase of uncertainty and policy relevance with the advance of a climate impact study. The area highlighted in light blue contains the steps treated in this study. Figure adapted from Fuglestvedt et al. [2003] 7
2.2 Earth radiative budget. Figure taken from Trenberth et al. [2009] . 24
2.3 Radiative forcing resulting from anthropogenic activities in 2000. That resulting from shipping is displayed in cyan. Figure adapted from Solomon et al. [2007]. 25
2.4 Zonal mean RF of O_3 and CH_4 in 2007 [Hilaire et al., 2009] 28

3.1 Main framework employed in this study to quantify the impacts of shipping NO_x emissions 30
3.2 Example of simulation with the SPM-2D model in the case of a tropical neutral atmosphere (D) with a MBL height of 500 meters, a temperature of 296 K, a pressure of 975 hPa and a ship speed of 5 m/s. Blue lines indicate background concentrations. Red lines show inner plume concentrations while grey dashed lines show plume concentrations for each ring. 34
3.3 The MOZART-4 framework is split into two main sections. During the **setup**, one defines and compiles the model while during **execution**, the model performs the defined simulation. 35

4.1 Location of the CO (square) and O_3 (circle) WDCGG daily-monitoring stationary stations used in this section. The altitude of these stations is indicated by a white to red color scale. The shipping emission magnitude is only provided as an indication to help the reader locate the stations which are close to ship lanes. 44
4.2 Location of the 27 WOUDC stations selected in 2000. The shipping emission magnitude is only provided as an indication to help the reader locate the stations which are close to ship lanes. 46
4.3 Geographical regions covered by the aircraft campaigns contained in the aircraft data composites. Circle and square sizes are proportional to the number of O_3 and CO observations respectively. The shipping emission magnitude is only provided as an indication to help the reader locate the stations which are close to ship lanes. . . 47
4.4 Mask generated with the shipping NO_x emission file read in by MOZART-4. Threshold: 5.0×10^9 molecules.cm^{-2}.s^{-1}. 49

4.5 Close-up displaying the conditions surrounding the location of the Angra do Heroismo station over the months of July to September in 2000. The plot in the upper left corner shows the shipping and background NO_x emissions and the seasonal mean wind directions. The plot in the bottom left corner shows the O_3 VMR calculated by MOZART-4. Box plots presenting the minimum, maximum and mean values as well as the median and the first and the third quartile are displayed in the upper right corner. Mean and standard deviations are also provided in the bottom right corner. 54
4.6 Same as figure 4.5 but for Mace Head in 2005. 55
4.7 Taylor diagrams showing the differences in standard deviations and correlations between MOZART-4 results and WDCGG measurements of CO and O_3 concentrations in 2000 and 2005. The red color indicates the MOZART-4 simulations including all emissions whereas the blue color correspond to the simulations where shipping emissions have been removed. The symbols define the geographic location of the points: 90°N-60°N ($*$), 60°N−30°N ($+$), 30°N−EQ ($\square$), EQ−30°S ($\triangle$), 30°S−60°S ($\bigcirc$), 60°S−90°S ($\times$). Station identification labels are placed next to the simulation with all emissions (red) when possible. 56
4.8 Time series of CO concentrations in 2000 from 12 WDCGG ground stations (green line) and the corresponding time series extracted from two simulations with MOZART-4: all emissions (red line) and shipping emissions removed (blue line). Climatological means and standard deviations of WDCGG data are also plotted (black line and shaded areas) and the time range is indicated in the upper right corner. The symbol used on the Taylor diagrams is displayed in the upper left corner. For each time series including, the annual mean and standard deviation are shown in the right band of each plot. . . 57
4.9 Same as figure 4.8 but in 2005. 58
4.10 Same as figure 4.8 but for O_3. 59
4.10 Figure 4.10 continuing. 60
4.11 Same as figure 4.8 but for O_3 in 2005. 61
4.11 Figure 4.11 continuing. 62
4.12 Comparison of O_3 volume mixing ratios for different clusters of altitude and latitude ranges between ozonesonde measurements and MOZART-4 in 2000. Averages of the WOUDC data are plotted in black whereas results from the MOZART-4 simulation with all emissions are displayed in red. The grey areas represent the 1-σ standard deviation of the measurements and the red bars represent those of the simulation results. WOUDC and MOZART-4 annual means are provided together with their standard deviations (in brackets) for each cluster. Correlation coefficients between the two signals are also given. 64

4.13 Comparison of O_3, OH, NO_x, NO_y, HNO_3, PAN concentrations between measurements taken during the TOPSE campaign and MOZART-4. For each of the 4 altitudes presented on plots, the 4 monthly averaged concentrations and standard deviations from the TOPSE campaign (grey scale) and MOZART-4 (yellow-to-red color scale) are displayed. Symbols and lines at the bottom of an altitude band correspond to the month of February while upper ones correspond to the month of May. Those in between correspond to the months of March and April and are placed in chronological order. 68
4.14 Figure 4.13 continuing. 69
4.15 Comparison of CO, CH_4, H_2O, H_2O_2 concentrations as well as JNO_2 and $JO(^1D)$ photolysis rates between measurements taken during the TOPSE campaign and MOZART-4. (Same as figure 4.13) . . . 70
4.16 Figure 4.15 continuing. 71
4.17 Comparison of NO_x volume mixing ratios between two MOZART-4 simulations (with and without shipping emissions) and observations from compiled flight campaigns [Emmons et al., 2000]. The black lines correspond to the mean value of observational data whereas the shaded areas display their standard deviations. The blue triangle and red rhombus symbols and the bars show mean values and standard deviations of the simulations with MOZART-4 respectively. The green colour is used to plot the concentrations resulting from the simulation without shipping emissions whereas the red colour is used for the simulation with shipping emissions. 73
4.18 Same as figure 4.17 but for O_3 volume mixing ratios. 74
4.19 Maps showing the number of mask-filtered TES profiles in the 4 seasons. The 4 bottom right insets display the total number of profiles per oceanic region for a given season. 76
4.20 Means and standard deviations of O_3 volume mixing ratios monitored by TES and resulting from the two MOZART-4 simulations run in 2005 in the 4 pre-defined oceanic regions. Data have been grouped by pressure bands (light grey areas). TES data are shown in black while MOZART-4 data are displayed in red and blue for the WS and NS simulations respectively. The dashed grey lines departing from the TES means indicate the mean of the averaging kernel peaks for a given pressure band. 77
4.21 Means and standard deviations of O_3 volume mixing ratios monitored by TES and resulting from the two MOZART-4 simulations run in 2005 in the 4 pre-defined oceanic regions. Data have been grouped by pressure bands (light grey areas). TES data are shown in black while MOZART-4 data are displayed in red and blue for the WS and NS simulations respectively. The dashed grey lines departing from the TES means indicate the mean of the averaging kernel peaks for a given pressure band. 78

5.1 Annual mean of shipping NO_x emissions in the EDGAR v3.2 and ACCMIP emission inventories in 2000 on a T42LR horizontal grid. . 86

5.2 Comparison of near-surface shipping-induced NO_2 volume mixing ratios and ratios with respect to background NO_2 volume mixing ratios in January and July between E2007 and the present study. Note that arrows were collated to the original colour bar when values computed by MOZART-4 were found larger or smaller than the minimum and maximum levels of the colour bar. 89
5.3 Near-surface shipping-induced NO_2 volume mixing ratios and ratios with respect to background NO_2 volume mixing ratios in January and July in the three cases using ACCMIP emissions. Note that the background concentrations used for the 5% removal case is the same as in the 100% removal case. 90
5.4 Correlations between NO_x concentrations and HNO_3 concentrations, O_3 concentrations and PBLH in summer and winter in the Atlantic and Pacific regions. 91
5.5 Comparison of near-surface shipping-induced O_3 volume mixing ratios and ratios with respect to background O_3 volume mixing ratios in January and July between E2007 and the present study. Note that arrows were collated to the original colour bar when values computed by MOZART-4 were found larger or smaller than the minimum and maximum levels of the colour bar. 94
5.6 Comparison of annual zonal mean shipping-induced O_3 volume mixing ratios between E2007 and the present study. 95
5.7 Comparison of annual shipping-induced tropospheric O_3 column between E2007 and the present study. 96
5.8 Near-surface shipping-induced O_3 volume mixing ratios and ratios with respect to background O_3 volume mixing ratios in January and July in the three cases using ACCMIP emissions. Note that the background concentrations used for the 5% removal case is the same as in the 100% removal case. 98
5.9 Annual zonal mean shipping-induced O_3 volume mixing ratios and ratios with respect to background O_3 volume mixing ratios in January and July in the three cases using ACCMIP emissions. 99
5.10 Annual tropospheric column shipping-induced O_3 volume mixing ratios and ratios with respect to background O_3 volume mixing ratios in January and July in the three cases using ACCMIP emissions. 100
5.11 Near-surface shipping-induced OH volume mixing ratios and ratios with respect to background OH volume mixing ratios in January and July in the three cases using ACCMIP emissions. 102
5.12 Annual zonal mean shipping-induced OH volume mixing ratios and ratios with respect to background OH volume mixing ratios in January and July in the three cases using ACCMIP emissions. 103

6.1 Flowchart representing the modelling framework employed in this chapter. The input data and model processes altered for the purpose of this study are highlighted in yellow. 112

6.2 Zonal plot of shipping NO_x emissions from 3 different emissions inventories. The shaded areas represent the 1-σ standard deviation of the monthly temporal variability. 114
6.3 Regions defined in the background emission cases. (1.Asia (AS), 2.Europe (EU), 3.North America (NA)) 115
6.4 Proportions of anthropogenic NO_x emissions excluding aviation and shipping compared to 2000 emissions taken from IIASA RCP database. The grey dotted lines show the values chosen in this study. 116
6.5 Uncertainty in $O(^1D)$ quantum yield as a function of wavelength [Sander et al., 2006]. The three coloured lines indicate the best estimate values (red) and the uncertainty of the quantum yield function at 298K (blue and green) whereas the grey lines present these estimates for a temperature of 263K. The green dotted line corresponds to the uncertainty applied in this study. 118
6.6 Uncertainties in the $NO+HO_2$ and NO_2+OH reactions as a function of temperature [Sander et al., 2006]. As in figure 6.5, the plain lines give the best estimates whereas the dotted lines provide the 1-σ uncertainty. The green dotted lines correspond to the uncertainties applied in this study. 118
6.7 Statistical summary of annually averaged near-surface NO_x shipping perturbations and relative differences between cases. The blue-and-red coloured filled circles display mean values while the small black dots present the minimum and maximum values. The box-and-whisker plots show further statistics: bars display medians, box extents show the lower and upper quartiles and the ends of the whiskers present the 5^{th} and 95^{th} percentiles. Statistical information about shipping perturbations in the reference case (**RF1**) is provided at the top of the table in the shaded row. Statistical information about relative differences between shipping perturbations in the perturbation and reference cases (**RF1** & **RF2**) are listed below. N is the number of values used to performed the statistical calculations. The coloured symbols identify the zonal mean curves on figures 6.9 and 6.10. 125
6.8 Same as figure 6.7 for O_3 126
6.9 Annually averaged NO_x zonal means at the model lowest level. The left plots show cases with global means or standard deviations larger than 10% while the right plots display the remaining cases. The symbol and colour codes are also given on figures 6.7 and 6.8. . . . 127
6.10 Annually averaged O_3 zonal means at the model lowest level. The left plots show cases with global means or standard deviations larger than 10% while the right plots display the remaining cases. The symbol and colour codes are also given on figures 6.7 and 6.8. . . . 128
6.11 NO_x (a) and O_3 (b) relative differences between the SEM-[x2] and RF1 cases in July. 130
6.12 Annually averaged NO_x (a,b) and O_3 (c,d) relative differences between the SESD-[AM], SESD-[IC/AM] and RF1 cases. 131

6.13 NO_x relative differences between the R-[T21], R-[T106] and RF2 cases in January and July. . . . 133
6.14 O_3 relative differences between the R-[T21] and RF2 cases in January (a) and July (b). . . . 134
6.15 Annually averaged NO_x relative differences between the D-[2001], D-[2002] and RF1 cases. . . . 135
6.16 O_3 relative differences between the D-[2001], D-[2002] and RF1 cases in January and July. . . . 136
6.17 Annually averaged NO_x and O_3 relative differences between the PC-[OffPhot] and RF1 cases. . . . 138
6.18 NO_x and O_3 relative differences between the PC-[O3+hv] and RF1 cases in January and July. . . . 139
6.19 NO_x relative differences between the PC-[NO2+OH] and RF1 cases. 140
6.20 O_3 relative differences between the PC-[NoAero] and RF1 cases. . . 141
6.21 O_3 relative differences between the LGT-[8], LGT-[3] and RF1 cases. 142
6.22 Annually averaged NO_x and O_3 relative differences between the BAE-[ASx2], BAE-[EUx2], BAE-[NAx2] and RF1 cases. . . . 143
6.23 and O_3 relative differences between the BAE-[ASx2], BAE-[AS/2], BAE-[EUx2], BAE-[EU/2], BAE-[NAx2], BAE-[NA/2] and RF1 cases in January. . . . 144
6.24 Statistical summary of annually averaged zonal mean O_3. Statistical information about shipping perturbations in the reference case (**RF1**) is provided at the top of the table in the shaded row. Statistical information about relative differences between shipping perturbations in the perturbation and reference cases (**RF1** & **RF2**) are listed below. N is the number of values used to performed the statistical calculations. The coloured symbols identify the zonal mean curves on figures 6.26 and 6.27. . . . 146
6.25 Same as figure 6.24 for OH . . . 147
6.26 Annually and spatially averaged O_3 vertical profiles. The left plots show cases with global means or standard deviations larger than 10% while the right plots display the remaining cases. The symbol and colour codes are also given on figures 6.24 and 6.25. . . . 148
6.27 Annually and spatially averaged OH vertical profiles. The left plots show cases with global means or standard deviations larger than 10% while the right plots display the remaining cases. The symbol and colour codes are also given on figures 6.24 and 6.25. . . . 149
6.28 O_3 relative differences between the SEM-[/2], SEM-[x2] and RF1 cases in January and July. . . . 150
6.29 O_3 relative differences between the PC-[OffPhot] and RF1 cases in January and July. . . . 152
6.30 O_3 relative differences between the SESD-[AM], SESD-[IC/AM] and RF1 cases in January and July. . . . 153
6.31 O_3 relative differences between the LGT-[8], LGT-[3] and RF1 cases in January and July. . . . 154

6.32 OH relative differences between the PC-[NO2+OH] and RF1 cases in July. . . . 155
6.33 O_3 and OH relative differences between the PC-[NoAero] and RF1 cases in January and July. . . . 155
6.34 Annually averaged O_3 and OH relative differences between the D-[2001], D-[2002] and RF1 cases. . . . 156
6.35 Annually averaged O_3 relative differences between the R-[T21], R-[T31], R-[T63], R-[T106] and RF2 cases. . . . 159
6.36 and O_3 relative differences between the BAE-[ASx2], BAE-[AS/2], BAE-[EUx2], BAE-[EU/2], BAE-[NAx2], BAE-[NA/2] and RF1 cases in January. . . . 160
6.37 Zonal average of O_3 columns for the different perturbation cases in January, July and on an annual average. The cases are gathered by type: α for the dynamical data, β for shipping emissions, γ for background emissions, δ for photochemistry, ϵ for lightning and ζ for resolution. . . . 162
6.38 O_3 relative differences between the SEM-[x2], SEM-[/2] and RF1 cases in January and July. . . . 163
6.39 O_3 relative differences between the PC-[OffPhot] and RF1 cases in January and July. . . . 164
6.40 O_3 relative differences between the LGT-[8], LGT-[3] and RF1 cases in January and July. . . . 165
6.41 O_3 relative differences between the SESD-[AM] and RF1 cases in July. . . . 166
6.42 O_3 relative differences between the PC-[NoAreo] and RF1 cases in January. . . . 167
6.43 O_3 relative differences between the D-[2001], D-[2002] and RF1 cases in January and July. . . . 168

7.1 Comparison between the EMEP and ACCMIP shipping emission inventories in 2000. EMEP data was downloaded from `www.ceip.at` 180
7.2 Comparison between seasonal background NO_x absolute differences in H2010 and this study. . . . 181
7.3 Comparison between seasonal background NO_x relative differences in H2010 and this study. . . . 182
7.4 Meridonal cross-sections at 45.2°N showing absolute and relative NO_x differences between the SNP and NS simulations performed with MOZART-4. . . . 183
7.5 Comparison between annually averaged SHIPTR volume mixing ratios in H2010 and this study. . . . 183
7.6 Comparison between seasonal NO_x absolute differences in H2010 and this study. . . . 184
7.7 Comparison between seasonal NO_x relative differences in H2010 and this study. . . . 185
7.8 Comparison between seasonal O_3 absolute differences in H2010 and this study. . . . 186

7.9 Comparison between seasonal O_3 relative differences in H2010 and this study. . . . 187
7.10 Meridional cross-sections at 45.2°N showing the absolute and relative NO_x differences between the SPP and SNP simulations performed with MOZART-4 . . . 188
7.11 Same as figure 7.10 but for O_3 . . . 188
7.12 Sensitivity of the parameterised O_3 removal to the K_{eff} parameter. . 189
7.13 Sensitivity of NO_x and O_3 concentrations to the τ parameter at the bottom level. ΔNO_x and ΔO_3 represent concentration differences between the simulation with and without the shipping emission parameterisation. Filled symbols display grid cells found above oceans and influenced by shipping emissions whereas empty ones display the remaining grid cells. Tropical regions are shown with circles, mid-latitudes are displayed with a square symbol and polar regions are represented by triangles. . . . 190
7.14 Flowchart displaying the functioning of the ship emission parameterisation proposed by Dr. Jana Moldanová. Processes are displayed with hexagon symbols while gas species are shown with circles. 194
7.15 Absolute and relative differences of shipping NO_x concentrations between simulations SPPM and SNP at the bottom level. . . . 196
7.16 Absolute and relative differences of shipping O_3 concentrations between simulations SPPM and SNP at the bottom level. . . . 196
7.17 Absolute and relative differences of shipping NO_x zonal averages between simulations SPPM and SNP. . . . 197
7.18 Absolute and relative differences of shipping O_3 zonal averages between simulations SPPM and SNP. . . . 197
7.19 Sensitivity of shipping NO_x and O_3 concentrations to K_{eff}. Filled symbols display grid cells found above oceans and influenced by shipping emissions whereas empty ones display the remaining grid cells. Tropical regions are shown with circles, mid-latitudes are displayed with a square symbol and polar regions are represented by triangles. . . . 198

8.1 SRES families against the two main dimensions. Figure adapted from figure 1.4 of section 1.7.2 in Nakicenovic et al. [2000]. . . . 202
8.2 Similarities between the SRES (grey) and RCP (black) scenarios. The names of the IAMs are provided in brackets below RCP scenarios names. Figure adapted from figures 5 and 7 in van Vuuren et al. [2010]. . . . 203
8.3 Past and future shipping NO_x emissions as calculated in the AC-CMIP project. The filled circles indicate those used in this chapter. Source: IIASA RCP Database `http://www.iiasa.ac.at/web-apps/tnt/RcpDb/` . . . 207

8.4 Bar plots showing radiative forcing from shipping NO_x emissions in 2000, 2010, 2020, 2050 and 2100 following the RCP scenarios. The contribution from O_3 RF, CH_4 RF, CH_4-induced O_3 RF and stratospheric H_2O are plotted in independent rectangles. The 2 black vertical bars behind the rectangles indicate 2 net radiative forcings. Those on the right are the result of combining O_3 RF and CH_4 RF while those on the left correspond to the sum of all contributions. 211
8.5 Zonal average of annually-averaged O_3 (red) and CH_4 (blue) RF in 2000 (thick lines) and in the RCP scenarios (thin lines). The net forcing is displayed in black while the spread is hatched. 212
8.6 Plots showing the correlations between different global figures such as total shipping NO_x emissions, global shipping O_3 column, global shipping CH_4 lifetime, global shipping O_3 radiative forcing and global shipping CH_4 radiative forcing. 214
8.7 Plots showing the correlations between different global figures such as total shipping NO_x emissions, global shipping O_3 column, global shipping CH_4 lifetime, global shipping O_3 radiative forcing and global shipping CH_4 radiative forcing. 215
8.8 Results from the two multi-linear regression models using 4 variables: Total shipping NO_x emissions, background CH_4 concentrations, background NO_x emissions and background CO emissions. . . 217

D.1 Near-surface maps of NO_x relative differences between the 24 perturbations cases and the reference case. The cutting-value threshold was taken at 10% of relative shipping NO_x perturbations. The corresponding filtered-out regions are displayed with a 135°-angle hatched pattern for the reference case and with a 45°-angle hatched pattern for the perturbation cases. 250
D.2 Same as figure D.1 but for O_3. The cutting-value threshold was taken at 5% of relative shipping O_3 perturbations. 254
D.3 Zonal mean plots of O_3 relative differences between the 24 perturbations cases and the reference case. The cutting-value threshold was taken at 1% of relative shipping O_3 perturbations. The corresponding filtered-out regions are displayed with a 135°-angle hatched pattern for the reference case and with a 45°-angle hatched pattern for the perturbation cases. 258
D.4 Same as figure D.3 but for OH. 262
D.5 Maps of tropospheric O_3 column relative differences between the 24 perturbations cases and the reference case. The cutting-value threshold was taken at 0.03% of relative shipping O_3 perturbations. The corresponding filtered-out regions are displayed with a 135°-angle hatched pattern for the reference case and with a 45°-angle hatched pattern for the perturbation cases. 266

E.1 Proposition of parameterisation using various characteristic times (decaying times) and several effective reaction rates to control the production of O_3 and the loss of NO_x. 269

List of Tables

2.1 Best estimates of various compounds emitted by the commercial world fleet and other anthropogenic and natural sectors in 2000 taken from the ACCMIP and POET emission inventories (see appendix B). Shipping NO_x emissions are in bold. 8

2.2 Maximum NO_x concentrations during the month of July found across the literature. In remote regions of the Atlantic and the Pacific NO_x concentrations are usually found to equal a few tens of parts per trillion in volume. 21

2.3 Annual global average of O_3 and CH_4 radiative forcing estimates in 2000 reported across the literature. 27

3.1 6 photolysis reactions represented by the small-scale model and drawn from the MCM mechanism. For the O_3 photolysis reaction, a steady-state approximation is assumed that allows the omission of the $O(^1D)$ species. 31

3.2 18 chemical reactions represented by the small-scale model and drawn from the MCM mechanism. Reactions without right hand-side term indicate that the products are lost outside of the system, as in Charlton-Perez et al. [2009]. 31

3.3 Definition of the coefficients defined in Song et al. [2003a] and Kim et al. [2009]. 32

4.1 Availability of the data depending on the year (A cross means that the data is available whereas a dash means otherwise). 42

5.1 MOZART-4 simulations performed in this chapter. 85

5.2 Shipping perturbation cases calculated from the simulations in table 5.1. 85

5.3 Changes in global tropospheric O_3 burden owing to shipping emissions. 97

5.4 Changes in global CH_4 lifetime owing to shipping emissions. 104

6.1 Scaling factors used in the study and associated global lightning NO_x productions (default value in bold). 119

6.2 Horizontal resolutions used in this study (default value and reference case in bold). 120

6.3 Summary of the simulation cases run in this study (continue on the next page). 122

2.1 Shipping emissions

Owing to the burning of fossil fuels in diesel engines, ships emit several gaseous species and particulate matter such as CO_2, CO, NO_x, SO_x, VOC, BC and POM into the troposphere. In particular, shipping NO_x emissions result mainly from the combustion of fuel at very high temperatures (typically above 2000 K in large marine engines: two-stroke and four-stroke engines, which constitute about 95% of the world fleet) [Goldsworthy, 2002, Kowalski and Tarelko, 2009]. This is known as the Zeldovich mechanism which results in the production of NO when molecular nitrogen (N_2) and oxygen (O_2) present in the air are subject to great temperatures. In addition, the smaller the engine load, the longer the time period spent by the fuel spray in the combustion chamber and the higher NO_x emissions. A fraction of about 6% ±3 of NO is converted to NO_2 during combustion [EPA, 2000]. Current best estimates of global shipping emissions in 2000 are given in table 2.1 along with global emissions from other sources. These data have been compiled to support the calculations of the IPCC Assessment Report 5 and are currently used within the Atmospheric Chemistry and Climate Intercomparison Project (ACCMIP) [Lamarque et al., 2010]. In this emission inventory, shipping NO_x emissions represent a proportion of about 18% of the total anthropogenic NO_x emissions (including fossil fuel combustion and biomass burning) and 12% of the global NO_x emissions (including lightning and soils). More details on the emission inventory may be found in appendix B.

TABLE 2.1: Best estimates of various compounds emitted by the commercial world fleet and other anthropogenic and natural sectors in 2000 taken from the ACCMIP and POET emission inventories (see appendix B). Shipping NO_x emissions are in bold.

	CO_2	CO	**NO_x**	SO_x	VOC	BC	POM
	Tg(CO_2)/a	Tg(CO)/a	**Tg(N)/a**	Tg(S)/a	Tg(VOC)/a	Tg(C)/a	Tg(POM)/a
shipping	780	1.18	**5.43**	5.54	1.28	0.13	0.14
anthropogenic	5776	608	26.5	46.4	65.19	5.02	2.82
biomass burning	5663	459	4.52	1.92	11.76	12.57	23.27
biogenic	-	160	-	-	-	-	-
soil	-	-	5.21	-	-	-	-
lightning	-	-	5.00	-	-	-	-

Shipping emission inventories such as the one included in ACCMIP are computed using various methodologies which may be divided into four categories. These four categories result from combinations of top-down and bottom-up approaches to estimate both the magnitude and the spatial distribution of ship emissions which are often calculated separately.

A top-down approach generally consists in breaking down a system into several categories and is usually employed in problems where detailed data may be difficult to acquire. In the case of shipping emissions for instance, the magnitude is usually estimated by multiplying fuel consumption statistics of the whole fleet (IEA, UN) with emission factors; while the spatial distribution is determined by way of using global spatial proxies.

Conversely, a bottom-up approach relies on detailed information about a system. The data can then be summarised by aggregation. In the case of shipping emissions for example, the magnitude can be calculated by defining in great detail emissions released by each vessel or vessel category and summing them up to obtain global shipping emissions; while the spatial distribution is calculated from detailed information about ship traffic. A summary of the various methodologies employed in the literature is given in the study of Miola and Ciuffo [2011].

If the spatial distribution of shipping emissions is relatively directly obtained by either a top-down or a bottom-up approach, the magnitude of shipping emissions further relies on the calculation of fuel consumption and emission factors. Fuel consumption, emission factors and spatial distribution are central to the construction of emission inventories. It is important to note that previous studies focusing on this problem have made different assumptions regarding the definition of the world ship fleet as emphasized by Wang et al. [2008]. Some inventories include military and fishing vessels while others are limited to commercial vessels only. A common aspect to these inventories is the vessel mass threshold that defines the limit below which vessels are not taken into account. This threshold has been set

to 100 Gross Tonnes (GT) [2]. Recently, a group of experts appointed by the International Maritime Organization (IMO) have reviewed the various methodologies employed and defined a set of standard definitions for the world ship fleet [Buhaug et al., 2009].

It is also important to bear in mind that both top-down and bottom-up approaches depend upon a plethora of shipping activity measurements. These measurements generally focus on fuel consumption, emission factors and spatial distribution. Indeed, the combination of emission factors with fuel consumption allows to derive estimates of the magnitude of shipping emissions. Additional information on the routes followed by ships help to distribute shipping emissions spatially. In summary, shipping emissions may be defined by the following formula:

$$E_s(x,y,t) = \sum_{k=0}^{N} FC(k) * EF_s(k) * FT(x,y,t)$$

Where k is a category regrouping ships of similar types, E_s represents the gridded shipping emissions of species S, FC is the fuel consumption, EF_s is the emission factor of species S and FT is a spatial proxy such as the density of ship traffic at a particular location and moment. This formula may be divided into further categories such as the number of days at sea in order to refine the results.

The next three subsections will focus on these three important parameters.

2.1.1 Fuel consumption

The fuel consumption of the world fleet is currently subject to large uncertainties and still constitutes a major scientific debate. Two methodologies are predominantly employed to estimate it. On the one hand, fuel consumption is calculated by using fuel sale statistics which generally leads to values around 200 Mt/yr [Buhaug

[2]Gross Tonnes are expressed in metric unit and are used for tonnage measurements as defined by the International Convention on Tonnage Measurement of Ships, 1969 (London-Rules) adopted by the IMO. This convention applies to all vessels constructed after July 1982.

et al., 2009, Endresen et al., 2003, 2007]. On the other hand, activity-based modelling including installed-engine power, engine load profiles, engine running hours and power-based specific fuel-oil consumption is also used to compute it. However, the latter method currently yields higher values of about 300 Mt/yr [Buhaug et al., 2009, Corbett, 2003, Eyring et al., 2005b]. This discrepancy has been originally attributed to the underreporting of fuel sales which sometimes occurs in developing countries or outside ports, but Endresen et al. [2007] recently claimed that the main responsible factor is the number of days at sea which has effectively decreased over the last decades. It is still not clear what the exact answer is however a consensus seems to be emerging as estimates are converging towards a value between 200 and 300 Mt/yr.

2.1.2 Emission factors

Emission factors are ratios that relate the mass of an emitted species to the mass of the fuel consumed by the engine. Many methodologies exist to calculate emission factors. For a single ship, it can be done theoretically in test-bed rigs as encouraged by the IMO [IMO, 2008] or on-board ships by monitoring exhaust in the stack [Agrawal et al., 2008b,a, 2009, Moldanová et al., 2009]. Futhermore, in-plume observations from instruments on board aircraft are used to estimate NO_x emission factors from a single ship [Hobbs et al., 2000, Chen et al., 2005, Schlager et al., 2006]. Satellite measurements have also proven to be reliable instruments to provide good estimates of the magnitude of ship NO_x emissions from which emission factors can be derived assuming typical NO_x lifetime of the marine environment [Beirle et al., 2004, Richter et al., 2004]. These measurements are then used to estimate emission factors for the whole commercial fleet. Compared with aircraft or road vehicles, large ships equipped with slow-speed and medium-speed diesel engines have a larger NO_x emission factor which ranges between 69 and 73 g(NO)/kg(fuel) at typical cruise engine loading depending on the method used to measure emissions (A. Petzold, personal communication 2010). This shows that NO_x emission factors present nowadays a relatively small degree of uncertainty.

2.1.3 Spatial distribution

As mentioned earlier, the spatial distribution of the world fleet is generally calculated independently in a top-down approach. This is performed by way of using spatial proxies of the ship traffic. Early inventories by Endresen et al. [2003] and Eyring et al. [2005b] have made use of three datasets, namely Comprehensive Ocean-Atmosphere Data Set (COADS), Automated Mutual-Assistance Vessel Rescue System (AMVER) and Purple Finder (PF). However the PF has been rapidly abandoned in favour of the AMVER and COADS datasets because of the small proportion of ships that it represents (about 4%) [Eyring et al., 2005b]. The AMVER and the International Comprehensive Ocean-Atmosphere Data Set (ICOADS) - formerly COADS - datasets represent respectively 9.5% and 4.5% of the world ship fleet in 2000 [Wang et al., 2008]. In addition, the distribution of ship types in the AMVER and ICOADS datasets are different from that of the ship fleet. In particular, ICOADS gives more weight to non-cargo vessels whereas AMVER approximates better the real distribution of the fleet [Endresen et al., 2003]. Recently, Wang et al. [2008] have improved these spatial proxies by removing redundant data and have created an additional proxy by combining the first two. They concluded that none of the three datasets provide a realistic spatial distribution of the ship fleet and therefore studies looking at the impacts on the tropospheric composition and the radiative forcing from ship emissions should consider using all of them. However, only the ICOADS spatial proxy was employed in the ACCMIP emission inventories to distribute shipping emissions. More recently, Eyring et al. [2009] have used data from Automatic Identification System[3] (AIS) to produce a spatial proxy. It is interesting to note that shipping emissions in ports have been estimated to contribute to only 5% of the total emissions [Dalsøren et al., 2009]. They will therefore be assumed to be insignificant in the rest of this study.

[3]System created to avoid collisions between ships.

2.1.4 Future emission estimates

Estimates of shipping future emissions require also to determine fuel consumption, emission factors and spatial distribution. Based on the four storylines[4] of the Special Report on Emission Scenarios (SRES) of the IPCC [Nakicenovic et al., 2000], Eyring et al. [2005a] built four demand scenarios which they combined with four technological scenarios to obtain a total of sixteen scenario cases. The key factors affecting these estimates are economic growth, technological improvement and alternative fuel changes. Future shipping NO_x emissions were found to range between 2.7 Tg(N)/yr and 7.6 Tg(N)/yr in 2020 and between 0.9 Tg(N)/yr and 11.8 Tg(N)/yr in 2050. Later on, a similar approach was followed by the IMO expert group working on the Second IMO GHG study [Buhaug et al., 2009]. However, this new study employed an open Delphi process gathering experts from around the world to determine the assumptions lying under technological improvement and fuel changes and usage. A total of 324 scenarios were developed. In addition, the IMO study was compared to that carried by the OPRF (Ocean Policy Research Foundation) that accounted for further anticipated changes in the world such as the enlarging of the Panama Canal, the construction of pipelines in Asia or the opening of shipping Arctic routes [Miyashita et al., 2008]. The final estimates resulted from the average of the two studies. They lie between 6.5 Tg(N)/yr and 7.6 Tg(N)/yr in 2020 and between 10.1 Tg(N)/yr and 15.5 Tg(N)/yr in 2050. Recently, the SRES scenarios were criticised for providing inaccurate visions of the future [Höök et al., 2010, Patzek and Croft, 2010]. Consequently, the Representative Concentration Pathways (RCP) were built to respond to this problem [Moss et al., 2010]. Four RCP scenarios based on published results from four integrated assessment modelling studies were retained [Van Vuuren et al., 2007, 2010, Clarke et al., 2007, Thomson et al., 2010, Masui et al., 2010, Riahi et al., 2007, 2010]. Under these scenarios, future estimates range between 4.4 Tg(N)/yr and 6.2 Tg(N)/yr in 2020, between 3.1 Tg(N)/yr and 6.7 Tg(N)/yr in 2050 and between 0.5 Tg(N)/yr and 5.6 Tg(N)/yr in 2100. The large discrepancies between

[4]The four storylines are called A1, A2, B1 and B2. They correspond to narrative descriptions of plausible futures that depend upon two development axis: Economic versus Environmental and Global versus Regional. See Chapter 8 for more details.

these estimates testify of the difficulty to estimate future emissions. The spatial distribution of future shipping emissions has been hardly discussed in the literature. Paxian et al. [2010] remain the only team to have developed an optimisation algorithm to calculate the shortest shipping routes under a set of constraints (wave height, canal passages, sea ice and land). The resulting emission inventory is the first global bottom-up shipping emission inventory that takes the opening of the Arctic routes into account. Other Arctic emission inventories were developed by Granier et al. [2006], Corbett et al. [2010] and Peters et al. [2011]. Peters et al. [2011] calculated that their emission estimates were between those of Paxian et al. [2010] and Corbett et al. [2010] whereas Corbett et al. [2010] found good agreement with Granier et al. [2006].

2.2 Shipping emissions of nitrogen oxides in the context of tropospheric chemistry and transport

In the troposphere, various chemical and physical processes such as gas-phase and heterogeneous chemistry, photolysis, advection, convection, diffusion and dry and wet deposition processes determine the fate of shipping NO_x molecules. Besides, these processes occur at different spatial and temporal scales spanning several order of magnitudes. It is therefore crucial to understand the whole chain of processes ranging from the small scale to the large scale in order to comprehend the impacts of shipping NO_x emissions.

2.2.1 From the small scale...

At the small scale[5], shipping NO_x emissions are contained in the ship plume which expands and disperse into the atmosphere. This dispersion associated to a dilution process is the result of atmospheric diffusion which is itself controlled by wind speed, atmospheric stability and boundary layer height. Based on findings by Hanna et al. [1982, 1985], Song et al. [2003b] described mathematically the dilution of ship plumes for different atmospheric stability. Recently, these have been extended to all atmospheric stability classes [Kim et al., 2009]. Other mathematical formulas have been provided by von Glasow et al. [2003] and Chosson et al. [2008]. Generally, once the plume has reached the top of the Marine Boundary Layer (MBL), the plume does not expand further vertically because of the temperature inversion and so, the dilution slows down and occurs in the horizontal direction only. It is worthwhile to note that a few studies have reported that the initial buoyancy flux from ship stack has little influence on the plume dilution [Hobbs et al., 2000, Chosson et al., 2008].

In addition, the dilution which results from the entrainment of background air, modifies the concentrations of gas species and particulate matter in the ship plume and therefore, the chemistry occurring in the plume. In-plume chemical transformations pertaining to the NO_x-HO_x-O_3 chemical system have been first described by Song et al. [2003b] and von Glasow et al. [2003]. With the help of comprehensive photochemical box models, they found a mechanism describing the chemical evolution of in-plume NO_x during day-time and night-time conditions under various meteorological conditions. The principles of this mechanism were brought to light by early studies on tropospheric NO_x [Crutzen, 1970, Isaksen et al., 1978, Liu et al., 1987].

During day time, this mechanism may be split into three stages. The first stage lasts a few minutes and corresponds to a titration of background O_3 by NO

[5]In this work, the small scale is bounded on the upper end by the size of a ship plume from which the plume has been sufficiently diluted in the background so that non-linearities have become insignificant. This corresponds to a few tens of kilometres horizontally and a few hundred meters vertically, typically the height of the marine boundary layer.

molecules emitted by ships (reactions 2.1). During this short period of time, most of the O_3 inside the plume is converted into NO_2 which prevents the production of OH. Recent studies have revealed that O_3 may also be created during this stage near the plume interface with background air where NO levels are too low to titrate O_3 [Kim et al., 2009, Charlton-Perez et al., 2009].

Then, NO_x molecules are sufficiently diluted to allow a recovery of O_3 as well as OH concentrations which defines the second stage of ship plumes lifetime. The production of O_3 inside the plume is made possible by the presence of peroxy radicals (HO_2) and organic peroxy radicals (RO_2) which come from the oxidation of carbon monoxide (CO) and volatile organic compounds[6] (VOC) by OH (reactions 2.2 and 2.3). Chemical reactions of NO with peroxy radicals yield to the formation of NO_2 (reaction 2.4 and 2.5) and subsequently O_3 via NO_2 photolysis (reactions 2.6 and 2.7). This chemical mechanism constitutes the main path to O_3 production which in turn creates OH via reactions (reactions 2.8 and 2.9). Moreover, this process is effective above the remote regions of the oceans as these regions are NO_x-limited [Eyring et al., 2007].

$$NO + O_3 \longrightarrow NO_2 + O_2 \tag{2.1}$$

$$CO + OH \longrightarrow HO_2 + CO_2 \tag{2.2}$$

$$VOC + OH \longrightarrow RO_2 + H_2O \tag{2.3}$$

$$NO + HO_2 \longrightarrow NO_2 + OH \tag{2.4}$$

$$NO + RO_2 \longrightarrow NO_2 + RO \tag{2.5}$$

$$NO_2 + h\nu \longrightarrow NO + O(^3P) \tag{2.6}$$

$$O(^3P) + O_2 + M \longrightarrow O_3 + M \tag{2.7}$$

$$O_3 + h\nu \longrightarrow O(^1D) \tag{2.8}$$

$$O(^1D) + H_2O \longrightarrow 2OH \tag{2.9}$$

Finally, the third stage is characterized by further dilution and therefore lower in-plume NO_x concentrations. This leads to further O_3 production and as a result

[6] VOC include hydrocarbons such as methane (CH_4), alkanes and alkenes.

raises O_3 concentrations above background levels. Overall, shipping NO_x emissions enhance O_3 levels in the MBL. The ship plume chemistry mechanism has been confirmed by observations during the Intercontinental Transport and Chemical Transformation 2002 (ITCT2K2) in May 2002 over the Pacific Ocean [Chen et al., 2005] as well as during a ICARTT-ITOP campaign off the coast of Brittany and over the English Channel [Schlager et al., 2006].

In addition to these reactions, NO_x molecules react with hydroxyl and peroxy radicals which leads to the production of oxyacids of nitrogen, namely: nitrous acid (HONO) (reaction 2.10), nitric acid (HNO_3) (reaction 2.11) and peroxynitric acid (HO_2NO_2) (reaction 2.12).

$$NO + OH + M \longrightarrow HONO + M \tag{2.10}$$

$$NO_2 + OH + M \longrightarrow HNO_3 + M \tag{2.11}$$

$$NO_2 + HO_2 + M \longrightarrow HO_2NO_2 + M \tag{2.12}$$

The reaction between NO_2 and OH represents the main sink of NO_x because HNO_3 is efficiently removed by dry[7] and wet[8] deposition processes (reaction 2.11).

Oxidation reactions between NO_x and peroxy radicals as well as NO_x and organic peroxy radicals are the source of organic nitrates and organic peroxy nitrates. The most common form of these nitrate species is peroxy acetyl nitrate (PAN) which has a long lifetime outside the planetary boundary layer and acts, as a result, as a NO_x reservoir which may be transported over great distances. Indeed, the main removal processes for PAN are by thermal and photolysis loss. Contrary to photolysis loss, thermal loss is a function of altitude with largest values near the surface. In the upper troposphere, photolysis loss prevails over thermal loss which allows for long-range transport. Chen et al. [2005] calculated that 80% of NO_x is lost by reaction with OH and 20% by reaction forming PAN under the specific thermodynamic conditions used in their study.

[7] HNO_3 has a typical dry deposition velocity of 1 $cm.^{-1}$ over oceans which is more than 14, 50 and 300 times those of O_3, NO_2 and NO [Seinfeld and Pandis, 2006].

[8] HNO_3 is a very soluble species as attested by its large Henry's law coefficient of 2.1×10^5 [Seinfeld and Pandis, 2006].

Overnight, the chemistry is different since photolysis, and in particular the photolysis of NO_2 and O_3, is no longer active. However, the first step remains similar to that during day time. Indeed, when the nocturnal chemical mechanism takes place O_3 is transformed into NO_3 and N_2O_5 species, which act as temporary reservoirs and are produced by reactions 2.13, 2.14, 2.15 and 2.16.

$$NO + O_3 \longrightarrow NO_2 + O_2 \tag{2.13}$$

$$NO_2 + O_3 \longrightarrow NO_3 + O_2 \tag{2.14}$$

$$NO_2 + NO_3 \rightleftarrows N_2O_5 \tag{2.15}$$

$$N_2O_5 + H_2O \rightleftarrows 2HNO_3 \tag{2.16}$$

It is also important to mention that halogen species and aerosols constitute a significant part of the composition of the marine boundary layer. Recently, Read et al. [2008] have proven the importance of halogen chemistry in the MBL as a removal path for O_3. Indeed, the release of halogen species such as bromine (Br) and chloride (Cl) by sea salt aerosols may contribute to an extra 50% loss of O_3 in the tropical regions. von Glasow et al. [2003] studied the impacts of halogen chemistry on the ship plume chemistry and found little effect from the bromine chemistry on the O_x family. As for heterogeneous reactions, the same study shows that the most important ones are those converting HNO_3 and N_2O_5 into nitrates.

Overall, depending on the magnitude of NO_x emissions, the background concentrations of NO_x and O_3 and the composition of the MBL, the time of the day, the season and the region considered, the effects of shipping NO_x emissions on O_3 are different. For instance, larger effects are simulated during summer in the tropical regions [Song et al., 2003b, von Glasow et al., 2003]. However, in order to understand the response from these different parameters and the extent of their influence, it is necessary to consider larger scales and take a global view of the problem.

2.2.2 ...to the global scale

As mentioned in the previous section of this chapter, satellites are not yet suitable for the retrieval of shipping emissions at the global scale[9]. Instead, scientists resort to global models in order to understand and quantify the impacts of shipping NO_x emissions on O_3 and CH_4.

2.2.2.1 The NO_x-O_3-HO_x photochemical system

Over the past decade, a few studies have examined the global impacts of shipping NO_x emissions. In an attempt to reduce uncertainties and address the non-linearity problem arising from the NO_x-HO_x-O_3 chemical system [Lin et al., 1988], these studies have made use of different global models with different emission data (especially, shipping emission data) and have also followed different methodologies. These methodologies may be divided into two categories. The first category gathers the studies where shipping perturbations are calculated as differences between a simulation with all emissions and a simulation removing shipping emissions [Lawrence and Crutzen, 1999, Davis et al., 2001, Endresen et al., 2003, Eyring et al., 2007, Dalsøren et al., 2009] whereas in the second category, shipping perturbations result from differences between a simulation with all emissions and a simulation where a small fraction of shipping emissions was removed [Hoor et al., 2009, Koffi et al., 2010].

2.2.2.2 NO_x

Although uncertainties in the magnitude and spatial distribution of the shipping perturbations remain, previous studies agree on the general aspects of these perturbations. For instance, because NO_x is known to have a short lifetime of hours to days in the Planetary Boundary Layer (PBL) [Seinfeld and Pandis, 2006], concentrations of this species have a limited vertical reach and tend to stay close to ship lanes and ports. Scientists have generally reported that NO_x concentrations

[9] In this study, the global scale corresponds to the entire troposphere.

reach several hundreds of parts per trillion in volume (pptv) near the main ship lanes over remote regions of the Atlantic and the Pacific (table 2.2). Lawrence and Crutzen [1999] have initially reported that NO_x levels observed in some regions of the North Atlantic MBL were lower than those predicted by their global model whilst including shipping emissions. A couple of years later, two studies presenting a comparison between observations (Azores Island station, NARE 1997 campaign and PEM campaigns) and model-calculated values in the North Atlantic MBL and in the North Pacific MBL have shown that NO_x and NO_y levels were overestimated when shipping NO_x emissions were taken into account [Kasibhatla et al., 2000, Davis et al., 2001]. For instance, they found that NO_x was generally overestimated by a factor of 10 in the North Atlantic MBL and by a factor of 3 in the North Pacific MBL. However Davis et al. [2001] also pointed that the global model was already showing a positive bias without shipping emissions. More recently, Eyring et al. [2007] used compiled data from aircraft observation campaigns [Emmons et al., 2000] in order to assess the results from several global models running with shipping emissions. They found that the majority of models were giving a good representation of NO_x concentrations in the free troposphere and were, depending on the season, either overestimating or underestimating NO_x levels in the MBL. They also managed to reproduce results from Kasibhatla et al. [2000] and Davis et al. [2001]. This was also confirmed by Dalsøren et al. [2007] who compared modelled values to measurements from various ground stations. Therefore, these comparisons seem to indicate that global models tend to overestimate NO_x and NO_y concentrations in the MBL, but this effect is significantly reduced in the free troposphere.

2.2.2.3 O_3

Regarding O_3, its longer lifetime of days to months allows it to be transported further up in the troposphere and also, away from the ship lanes. Since most shipping emissions occur in the northern hemisphere between 30°N and 60°N, large scale motion, including convection, transports O_3 produced by shipping NO_x emissions as well as O_3 precursors to the top of the troposphere. This particular

TABLE 2.2: Maximum NO_x concentrations during the month of July found across the literature. In remote regions of the Atlantic and the Pacific NO_x concentrations are usually found to equal a few tens of parts per trillion in volume.

Study	Global NO_x emissions [Tg(N)/yr]	Spatial distribution	Maximum NO_x concentrations (location) [pptv]
Lawrence and Crutzen [1999]	3.0	EDGAR v2.0	> 1000 (Atlantic and European coasts)
Kasibhatla et al. [2000]	3.0	Corbett and Köhler [2003]	> 1000 (European coasts)
Endresen et al. [2003]	3.5	Endresen et al. [2003]	> 200 (North Atlantic) > 400 (European coasts) > 200 (North Atlantic and Pacific)
Eyring et al. [2007]	3.1	EDGAR v2.0	2300 (Baltic sea) > 200 (North Atlantic)
Dalsøren et al. [2007]	3.5	Endresen et al. [2003]	> 500 (European coasts) > 150 (North Atlantic)

location means that O_3 production is also subject to a strong seasonality with highest production in summer. Generally, the largest shipping O_3 concentrations are found in the remote Atlantic and Pacific regions where they may reach more than 10 ppbv in summer [Endresen et al., 2003, Dalsøren et al., 2007, Eyring et al., 2007]. The shape of the tropospheric zonal mean perturbation is also generally in good agreement across studies. O_3 concentrations decrease relatively quickly with altitude and present a north slant that reaches the Arctic tropopause [Eyring et al., 2007, Hoor et al., 2009]. In the upper troposphere, they have been found to be slightly lower than 1 ppbv [Eyring et al., 2007]. It is worthwhile to note that, in Europe, a titration effect may happen as a result of large NO_x background concentrations [Eyring et al., 2007]. In terms of tropospheric burden, Fuglestvedt et al. [2008] found shipping NO_x emissions responsible for an increase of 13 Tg/yr while Eyring et al. [2007] reported a mean value of 4 Tg/yr.

In addition, NO_x and O_3 have a shorter lifetime over land compared with water because of faster deposition velocities and oxidation processes. Including VOC in shipping inventories has been shown to have a small effect on O_3 production because oceans are NO_x-limited regions [Endresen et al., 2003, Eyring et al., 2007].

2.2.2.4 OH

OH is the main tropospheric oxidant and is often called tropospheric cleanser [Logan et al., 1981]. The main OH production route being the photolysis of O_3 followed by reaction with water vapour, it is expected to find that the largest shipping OH perturbations are located in the tropical regions. These regions are characterised by deep convection which result in effective transport of this species in the upper troposphere. According to studies from Endresen et al. [2003] and Dalsøren et al. [2009], the global yearly average OH difference is about 3%. In a previous study, Dalsøren et al. [2007] found somewhat a lower value which they attributed to model resolution. However, recent simulation at the same resolution did not show such results.

2.2.2.5 CH_4

CH_4 has a lifetime of about 10 years. However, this figure is highly dependent upon the global model used to calculate it. Shindell et al. [2006] performed a multimodel study involving 25 state-of-the-art global chemistry transport models and global circulation models and reported CH_4 lifetimes ranging between 4 and 15 years. One-year simulations do not represent the complete impact of the OH increase on CH_4. Instead, researchers apply a feedback factor of 1.4 which provides the equilibrium value that the system would reach after several CH_4 lifetimes, in the case of constant emissions. Over the past decade, studies have usually agreed on the global CH_4 lifetime perturbation and have found values between -4.17% to -7.5% [Lawrence and Crutzen, 1999, Endresen et al., 2003, Dalsøren et al., 2009]. However, two studies in 2007 reported values around -1.5% which are in agreement with the global OH perturbations but are somewhat much lower [Dalsøren et al., 2007, Eyring et al., 2007].

2.2.3 Future impacts

In the future, potential increases in shipping NO_x emissions will increase O_3 levels. Indeed, although O_3 chemistry is non-linear and O_3 production decreases when air masses are saturated in NO_x molecules, no saturation effect has been detected by global models even when shipping emissions totalled up to about 6 Tg(N)/yr [Eyring et al., 2007]. However, previous forecast values of shipping NO_x emissions in 2030 now correspond to current best estimates of the year 2007. Recently, Koffi et al. [2010] employed the small-perturbation method introduced by Hoor et al. [2009] to quantify the contribution of shipping NO_x emissions on O_3 in the future. They expect shipping to become the main contributor to O_3 concentrations in the marine regions of the lower Northern Hemisphere and the Southern Hemisphere. In addition, the opening of the Northern Arctic routes which could potentially halve travel time could also enhance O_3 concentrations to levels typically found in many industrialized regions of the Northern Hemisphere, contributing then to the warming of the north polar region [Granier et al., 2006, Ødemark et al., 2011].

2.3 Radiative forcing impacts

2.3.1 Earth's energy budget and radiative forcing

The climate system is a physical subsystem of the Earth system. A convenient way of characterising a physical system is through its energy budget. Sources of energy in the Earth system are manifold and of different nature. However, with a proportion of 99.97%, the largest contribution comes from the sun in the form of radiation. Figure 2.2 shows the various radiative energy flows within the Earth system.

As short-wave solar radiation travels through the atmosphere, they encounter various gas species and particles by which they may get absorbed (20%), scattered or reflected (20%). About half of this radiation eventually reaches the surface of the

Earth which reflects the remaining part back into space. This absorption results in heating of the surface of the Earth which in turn radiates long-wave radiation towards outer-space. In the same fashion, the terrestrial radiation interacts also with the elements present in the composition of the atmosphere. In particular, certain gas species, the so-called greenhouse gases absorb these long-wave radiations before re-emitting them in all directions, some of them being directed back towards the surface of the Earth. Greenhouse gases include water vapour, CO_2, CH_4, N_2O and O_3. This phenomenon leads to the rising of temperatures in the troposphere.

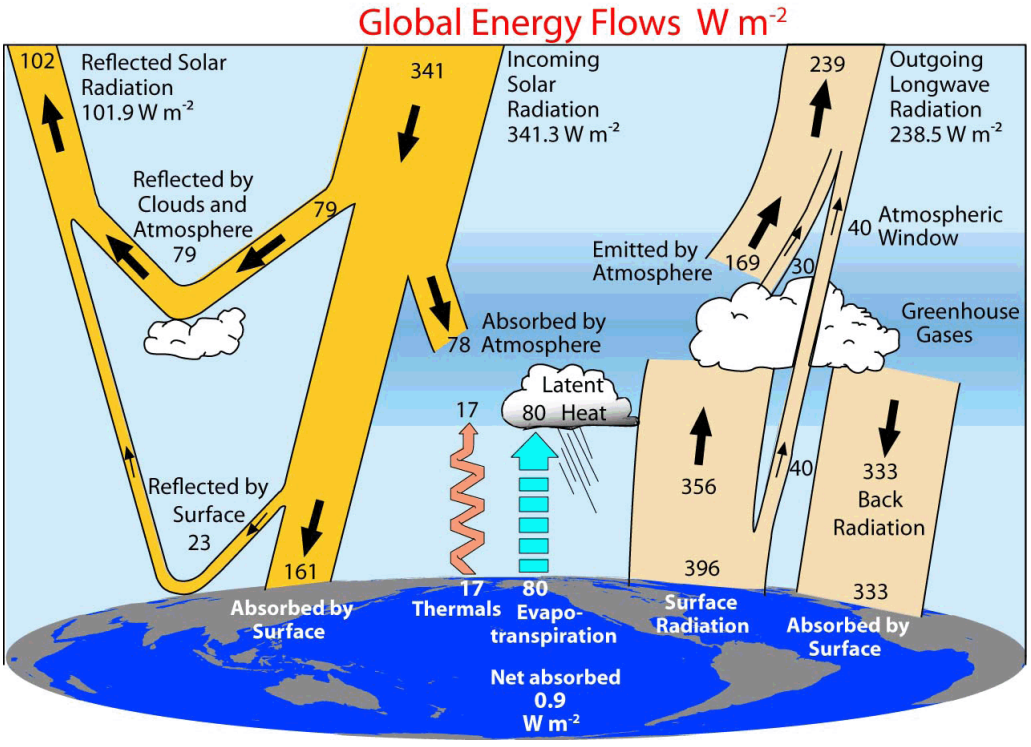

FIGURE 2.2: Earth radiative budget. Figure taken from Trenberth et al. [2009]

Anthropogenic activities such as energy production, industrial processes and transport lead to the production of greenhouse gases and greenhouse gas precursors which perturbs the natural composition of the atmosphere and as a result modifies the energy budget of the Earth. A metric called radiative forcing (RF) has been introduced by the IPCC in order to measure the magnitude of the effects from these anthropogenic activities. Indeed, RF is defined in the Third Assessment Report

(TAR) to the IPCC as follows: "The radiative forcing of the surface-troposphere system due to the perturbation in or the introduction of an agent (say, a change in greenhouse gas concentrations) is the change in net (down minus up) irradiance (solar plus long-wave; in $W.m^{-2}$) at the tropopause AFTER allowing for stratospheric temperatures to readjust to radiative equilibrium, but with surface and tropospheric temperatures and state held fixed at the unperturbed values". The reference case defined to calculate the perturbation generally corresponds to the composition of the atmosphere in 1750 (before the industrial revolution). The RF from each greenhouse gas as well as other components affecting the climate system may be seen on figure 2.3. The RF from the shipping sector is also displayed on the same figure to allow comparison.

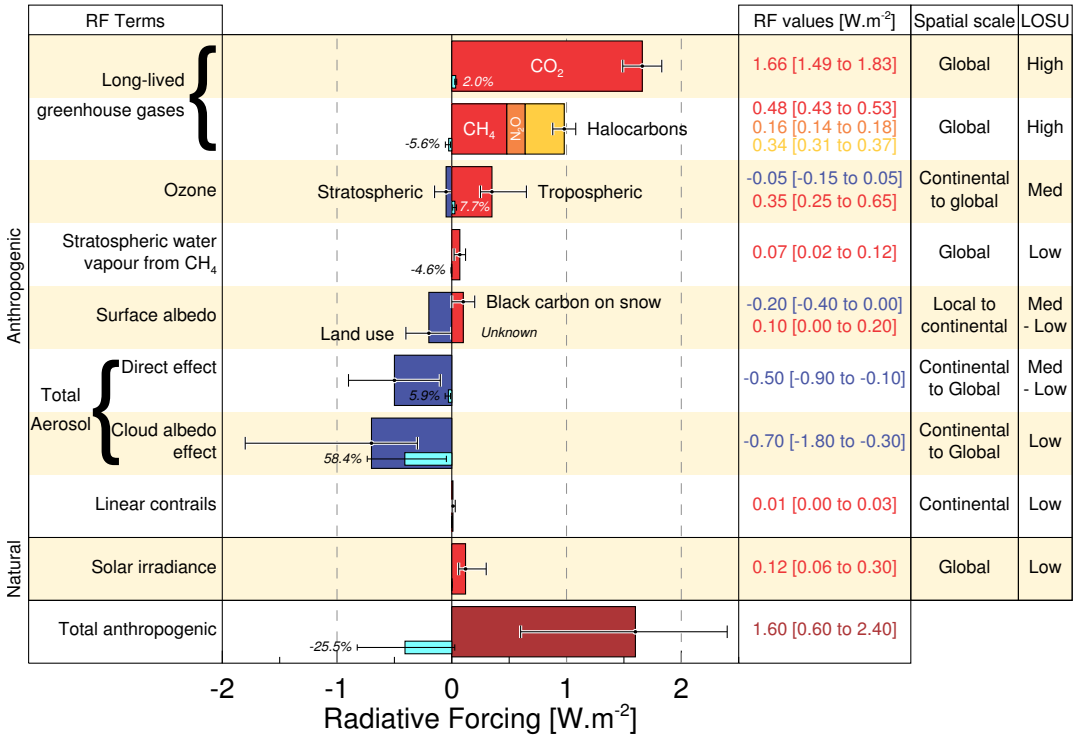

FIGURE 2.3: Radiative forcing resulting from anthropogenic activities in 2000. That resulting from shipping is displayed in cyan. Figure adapted from Solomon et al. [2007].

2.3.2 Radiative forcing of shipping NO_x

The previous section on photochemistry described how NO_x emissions perturb the concentrations of O_3 and CH_4 in the atmosphere. Since O_3 and CH_4 are both greenhouse gases, they will induce a radiative forcing. In addition, a decrease in CH_4 lifetime leads to a decrease in O_3 levels as well as a decrease in stratospheric H_2O [Myhre et al., 2009]. O_3 may also alter the carbon cycle by damaging vegetation [Stich et al., 2007] and the formation of nitrate aerosols [Forster et al., 2007] whereas CH_4 could potentially modify the sulphate burden by enhancing OH levels [Unger et al., 2006, Shindell et al., 2009].

Impacts of anthropogenic NO_x emissions on RF through perturbations of O_3 and CH_4 concentrations started to gather momentum over the last decades of the 20^{th} century [Wang and Sze, 1980, Ramanathan et al., 1987, Lacis et al., 1990, Derwent, 1990]. However, studies regarding the impacts from shipping NO_x emissions are quite recent. Endresen et al. [2003] were the first to estimate the O_3 and CH_4 RF arising from shipping NO_x emissions. Since then, five more studies were dedicated to this task. The O_3 and CH_4 RF encountered across the literature are given in table 2.3. These different studies estimated a O_3 RF ranging between 8 $mW.m^{-2}$ and 41 $mW.m^{-2}$ and a CH_4 RF ranging between -56 $mW.m^{-2}$ and -11 $mW.m^{-2}$ in 2000. Compared with the global anthropogenic O_3 and CH_4 RF, the mean shipping O_3 and CH_4 perturbation account for about 4.7% and -5.6% of the totals respectively [Solomon et al., 2007].

The large range of O_3 and CH_4 RF stems from differences in emission inventories, models and methodologies. For instance, Endresen et al. [2003] calculated the O_3 and CH_4 lifetime perturbations with a CTM and then made use of formulas taken from the TAR to estimate these RF whereas Lee et al. [2006] utilized a simple climate model. The remaining studies have all applied O_3 and CH_4 lifetime perturbations to an offline RTM to estimate O_3 and CH_4 RF. It is interesting to note that the magnitude of the ratio between O_3 RF and CH_4 RF varies greatly. In particular, O_3 RF had originally been estimated to be larger in magnitude than CH_4 RF [Endresen et al., 2003, Lee et al., 2006], but lately the opposite was

TABLE 2.3: Annual global average of O_3 and CH_4 radiative forcing estimates in 2000 reported across the literature.

Study	Global NO_x emissions [Tg(N)/yr]	O_3 RF [mW.m^{-2}]	CH_4 RF [mW.m^{-2}]
Endresen et al. [2003]	3.5	**29**	-28
Lee et al. [2006]	6.5	**21**	-11
Eyring et al. [2007]	3.1	9.8 ±2.0	**-14.0**
Fuglestvedt et al. [2008]	3.5	32 ±9	**-43** ±13
Hoor et al. [2009]	4.1	27.3 ±2.2	**-37.2** ±9.3
Unger et al. [2010]	2.9	3.0	**-18.0**
Myhre et al. [2011]	4.1	24.0	**-27.0**

reported [Eyring et al., 2007, Fuglestvedt et al., 2008, Hoor et al., 2009, Myhre et al., 2011].

Furthermore, the use of simple scaling factors by Endresen et al. [2003] taken from the TAR have originally brought scientists to conclude that these two components nearly cancel out [Endresen et al., 2003]. However, more recent comprehensive studies employing a combination of global chemistry models with radiative transfer models and global circulation models have highlighted the temporal and spatial differences in O_3 and CH_4 RF [Hilaire et al., 2009]. Indeed, because of its relatively short lifetime compared with CH_4, O_3 RF exhibits strong seasonal and spatial variabilities whereas CH_4 RF presents a more homogeneous picture (figure 2.4). Therefore, globally averaged RF values may not provide an adequate metric to study the impacts of shipping NO_x emissions unless presented with maps or zonal mean plots showing the spatial variability[10]. This simple metric remains nevertheless largely employed across the literature and gives a good first order approximation of the impacts of shipping NO_x emissions. Although early studies using scaling factors and simple climate models revealed a stronger magnitude in O_3 RF than CH_4 RF in absolute terms, recent studies making use of complex global models show an opposite tendency. The ratio between the O_3 RF and the CH_4 RF is also different from one model to another, owing to the various ways employed to solve the transport and chemical equations. Myhre et al. [2011] found that the largest uncertainty was associated with O_3 and that the overall uncertainty equals

[10]See TAR, http://www.grida.no/publications/other/ipcc_tar/?src=/climate/ipcc_tar/wg1/216.htm

10 mW.m^{-2} which represents more than 50% of the net RF. A summary of the values found across the literature is displayed in table 2.3. It is important to note that O_3 changes in the upper troposphere have a greater impact on RF because of colder temperatures in this region [Lacis et al., 1990, Hansen et al., 1997].

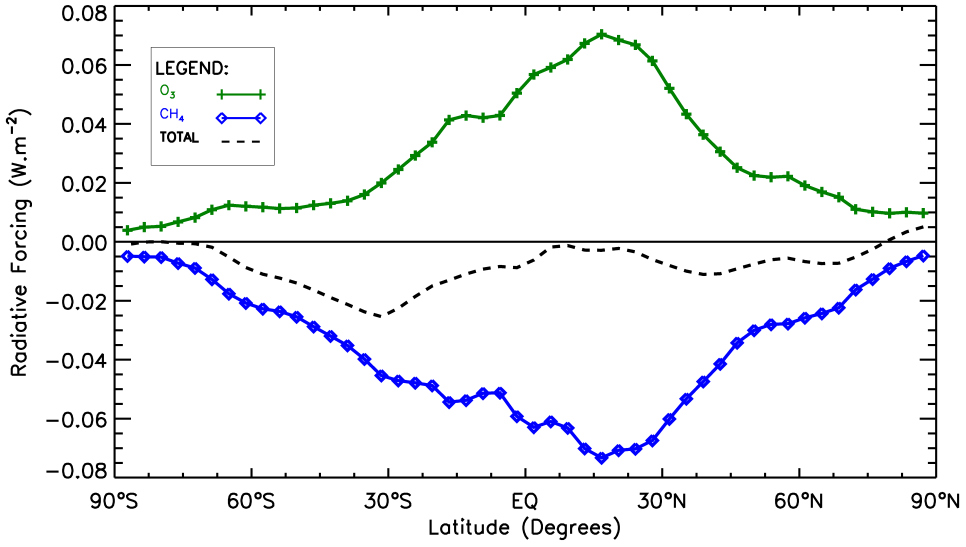

FIGURE 2.4: Zonal mean RF of O_3 and CH_4 in 2007 [Hilaire et al., 2009]

Only two studies have looked at future impacts of shipping NO_x emissions on radiative forcings. Eyring et al. [2007] reported a 3.8 mW.m^{-2} increase of the O_3 RF and a -7 mW.m^{-2} decrease of the CH_4 RF between 2000 and 2030. Fuglestvedt et al. [2008] integrated RF for different species emitted by four transport sectors over several time horizons (20, 100 and 500 years). After 100 years, the O_3 and CH_4 perturbations from shipping NO_x emissions are still present. Nonetheless, the overall contribution from shipping compared with road transport is small in magnitude and of opposite sign. However, at a shorter time horizon of 20 years, shipping will become quite significant, representing nearly 60% of the magnitude of the road RF. Hodnebrog et al. [2011a] used the B1 emission scenario in 2025 and 2050 and reported -28.0±5.1 mW.m^{-2} and -30.8±4.8 mW.m^{-2} respectively. These two estimates are close to that from Myhre et al. [2011] since shipping emissions under the B1 scenario do not grow much between 2000 and 2050 but also because the MOCAGE model was included in Hodnebrog et al. [2011a].

Chapter 3

Description of the models

3.1 Introduction

Studying the impacts of shipping NO_x emissions on O_3 and CH_4 is challenging because of the multiplicity of spatial and time scales of the physical and chemical processes that they cover. The purpose of this work being to quantify these impacts, it is necessary to use different modelling tools in order to capture and understand the various processes occurring at different scales. For instance, a 2-dimensional Gaussian plume model (GPM) was developed and employed with a view to represent the small-scale chemical and physical phenomena occurring in ship plumes whereas the use of a global chemistry transport model (GCTM) provides a wider picture of the problem. Finally, an offline radiative transfer model (RTM) was utilised to estimate the radiative forcings from the resulting O_3 and CH_4. The general framework followed in this study is displayed on figure 3.1. A detailed description of the three models is given in the next sections.

3.2 SPM-2D

For the purpose of this study, a 2D model of ship plume physics and chemistry has been developed (SPM-2D). This model derives from that including the simple

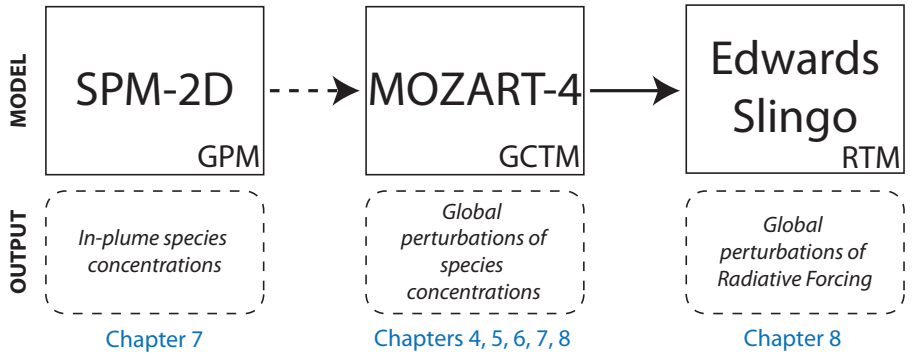

FIGURE 3.1: Main framework employed in this study to quantify the impacts of shipping NO_x emissions

NO_x-O_3 photochemical chemical mechanism [Charlton-Perez et al., 2009]. It is further combined with the Gaussian plume approach for the modelling of ship plume dynamics introduced by Song et al. [2003a], Kim et al. [2009] and Vinken et al. [2011]. The model was originally coded in FORTRAN-77 and has been updated for the purpose of this study to a mixture of FORTRAN-77/95 which allows the reading of a namelist containing various input parameters such as emission time, emission rate, boundary layer height, temperature, pressure, meteorological stability case and initial species concentrations. It runs very efficiently on a laptop under the CYGWIN environment.

3.2.1 Chemical mechanism

The chemical mechanism accounts for a total of 12 tracers (O_3, NO, NO_2, OH, HO_2, NO_3, N_2O_5, HNO_3, CH_3O_2, CH_2O, CH_3COOH and H_2O_2) and 4 fixed species (H_2O, CO, CH_4, PAN). 6 Photolysis rates and 18 constant reaction rates are extracted from the Master Chemical Mechanism v3.1[1] (see tables 3.1 and 3.2). The obtained ordinary differential equation system describing the chemical mechanism is solved via a GEAR solver [Gear, 1971] pertaining to the VODE library [Brown et al., 1989].

where ζ is the solar zenith angle.

[1] http://mcm.leeds.ac.uk/MCM/

TABLE 3.1: 6 photolysis reactions represented by the small-scale model and drawn from the MCM mechanism. For the O_3 photolysis reaction, a steady-state approximation is assumed that allows the omission of the $O(^1D)$ species.

#	Photolysis reaction	Rate
J1	$O_3 + h\nu \rightarrow 2OH$	$J1 = 6.073 \times 10^{-5} cos(\zeta^{1.743}) exp(-0.474/cos\zeta)$
J2	$NO_2 + h\nu \rightarrow NO + O$	$J2 = 1.165 \times 10^{-2} cos(\zeta^{0.244}) exp(-0.267/cos\zeta)$
J3	$CH_2O + h\nu \rightarrow CO$	$J3 = 6.853 \times 10^{-5} cos(\zeta^{0.477}) exp(-0.353/cos\zeta)$
J4	$CH_2O + h\nu \rightarrow CO + 2HO_2$	$J4 = 4.642 \times 10^{-5} cos(\zeta^{0.762}) exp(-0.353/cos\zeta)$
J5	$NO_3 + h\nu \rightarrow NO$	$J5 = 2.485 \times 10^{-2} cos(\zeta^{0.168}) exp(-0.108/cos\zeta)$
J6	$NO_3 + h\nu \rightarrow NO_2 + O3$	$J6 = 1.747 \times 10^{-1} cos(\zeta^{0.155}) exp(-0.125/cos\zeta)$

TABLE 3.2: 18 chemical reactions represented by the small-scale model and drawn from the MCM mechanism. Reactions without right hand-side term indicate that the products are lost outside of the system, as in Charlton-Perez et al. [2009].

#	Chemical reaction	Reaction rate constant
R1	$NO + O_3 \rightarrow NO_2$	$k1 = 1.4 \times 10^{-12} exp(-1310/T)$
R2	$OH + CO \rightarrow HO_2$	$k2 = 1.30 \times 10^{-13}$
R3	$OH + CH_4 \rightarrow CH_3O_2$	$k3 = 9.65 \times 10^{-20} (T^{2.58}) exp(-1082/T)$
R4	$HO_2 + NO \rightarrow NO_2 + OH$	$k4 = 3.6 \times 10^{-12} exp(270/T)$
R5	$HO_2 + O_3 \rightarrow OH$	$k5 = 2.03 \times 10^{-16} (T/300)^{4.57} exp(693/T)$
R6	$CH_3O_2 + NO \rightarrow CH_3O + NO_2$	$k6 = 1.82 \times 10^{-13} exp(416/T)$
R7	$CH_3O_2 + HO_2 \rightarrow$	$k7 = 3.80 \times 10^{-13} exp(780/T)$
R8	$HO_2 + HO_2 \rightarrow H_2O_2$	$k8 = 2.20 \times 10^{-13} exp(600/T) + M1.90 \times 10^{-33} exp(980/T)$
R9	$OH + NO_2 \rightarrow HNO_3$	$k9 = k_0 k_i f/(k_0 + k_i)[k_0 = M3.3 \times 10^{-30} (T/300)^{-3}$, $k_i = 4.1 \times 10^{-11}$, $f = 10^{(log_{10} 0.4/(1+(log_{10}(k_0/k_i))^2))}]$
R10	$OH + HO_2 \rightarrow$	$k10 = 4.80 \times 10^{-11} exp(250/T)$
R11	$CH_3O_2 + CH_3O_2 \rightarrow$	$k11 = 1.82 \times 10^{-13} exp(416/T)$
R12	$NO_2 + O_3 \rightarrow NO_3$	$k12 = 1.40 \times 10^{-13} exp(-2470/T)$
R13	$NO + NO_3 \rightarrow 2NO_2$	$k13 = 1.80 \times 10^{-11} exp(110/T)$
R14	$NO_2 + NO_3 \rightarrow N_2O_5$	$k14 = k_0 k_i f/(k_0 + k_i)[k_0 = M3.60 \times 10^{-30} (T/300)^{-4.1}$, $k_i = 1.90 \times 10^{-12} (T/300)^{0.2}$, $f = 10^{(log_{10} 0.35/(1+(log_{10}(k_0/k_i))^2))}]$
R15	$N_2O_5 \rightarrow NO_2 + NO_3$	$k15 = k_0 k_i f/(k_0 + k_i)[k_0 = M1.00 \times 10^{-3} (T/300)^{-3.5} exp(-11000/T)$, $k_i = 9.7 \times 10^{14} (T/300)^{0.1} exp(-11080/T)$, $f = 10^{(log_{10} 0.35/(1+(log_{10}(k_0/k_i))^2))}]$
R16	$PAN \rightarrow NO_2$	$k16 = 9.25 \times 10^3$
R17	$N_2O_5 \rightarrow 2HNO_3$	$k17 = 4.0 \times 10^{-4}$
R18	$NO_2 + NO_3 \rightarrow NO + NO_2$	$k18 = 4.50 \times 10^{-14} exp(-1260/T)$

where T is the temperature in Kelvins, p is the atmospheric pressure in hectoPascals and M is the number density of air in molecules.cm$^-$3. $R10$ reaction product is H_2O, $R18$ is a substitute for PAN decomposition and $R17$ represents the heterogeneous uptake of N_2O_5.

TABLE 3.3: Definition of the σ coefficients defined in Song et al. [2003a] and Kim et al. [2009].

S	$\sigma_y(y < 10km)$	$\sigma_y(y > 10km)$	σ_z
A	$0.11x(u/u_r)(1+0.0001x(u/u_r))^{(}-0.5)$	$0.11x(u/u_r)(1+u/u_r)^{(}-0.5)$	$0.10x(u/u_r)$
B	$0.08x(u/u_r)(1+0.0001x(u/u_r))^{(}-0.5)$	$0.08x(u/u_r)(1+u/u_r)^{(}-0.5)$	$0.06x(u/u_r)$
C	$0.055x(u/u_r)(1+0.0001x(u/u_r))^{(}-0.5)$	$0.055x(u/u_r)(1+u/u_r)^{(}-0.5)$	$0.04x(u/u_r)(1+0.0002x(u/u_r))^{(}-0.5)$
D	$0.04x(u/u_r)(1+0.0001x(u/u_r))^{(}-0.5)$	$0.04x(u/u_r)(1+u/u_r)^{(}-0.5)$	$0.03x(u/u_r)(1+0.0015x(u/u_r))^{(}-0.5)$
E	$0.03x(u/u_r)(1+0.0001x(u/u_r)^{(}-0.5)$	$0.03x(u/u_r)(1+u/u_r)^{(}-0.5)$	$0.015x(u/u_r)(1+0.0003x(u/u_r))^{(}-1.0)$
F	$0.02x(u/u_r)(1+0.0001x(u/u_r))^{(}-0.5)$	$0.02x(u/u_r)(1+u/u_r)^{(}-0.5)$	$0.008x(u/u_r)(1+0.0003x(u/u_r))^{(}-1.0)$

3.2.2 Ship plume dynamics

In order to represent the plume expansion and its dilution into background air, a Gaussian approach similar to the one developed by Song et al. [2003a] is taken which rests upon two parameters: the lateral and vertical dispersion coefficients. In his study, Song et al. [2003a] followed the work of Briggs [1972] and that of Hanna et al. [1982, 1985] on the Ocean and Coastal Dispersion model and adapted the dispersion coefficients to the marine boundary layer conditions, taking into account sea surface roughness and meteorological stability. A few years later, Kim et al. [2009] expanded these coefficients to other stability classes: A, C and F (see table 3.3). The lateral and vertical dispersion coefficients are given in table 3.3.

In addition, Kim et al. [2009] increased the spatial dimensionality of the original Lagrangian photochemical box model from Song et al. [2003a] by assuming a Gaussian dispersion of the primary pollutants such as NO_x and SO_2 and taking fractions of the standard deviation. A similar has also been adopted by Vinken et al. [2011] who followed the work of Freiberg [1976] and Melo et al. [1978]. These works from the late seventies describe a method that makes use of concentric rings. Each ring contains the same amount of a primary species assuming that it follows a Gaussian distribution (e.g. NO_x). Dilution between rings and entrainment of background air are both taken into account. This method is implemented in the 2D photochemical model described here. It is worthwhile to note that deposition processes are not resolved by this model.

3.2.3 Description of calculations

At each time step, the concentrations of NO_x at the centre of the plume are calculated assuming a Gaussian plume approach as described in the previous section and they read the following formula:

$$C^{CL}_{NO_x}(t) = \frac{Q_{NO_x}}{\pi u_r \sigma_y(t)\sigma_z(t)}$$

This formula allows to derive the concentrations along the y and z axis:

$$C^{y}_{NO_x}(t) = C^{CL}_{NO_x}(t) \exp \frac{-y^2}{2\sigma_y(t)^2}$$

$$C^{z}_{NO_x}(t) = C^{CL}_{NO_x}(t) \exp \frac{-z^2}{2\sigma_z(t)^2}$$

Then, the GEAR solver calculates the changes of species concentrations due to photochemical activity. Finally, entrainment of background air in the plume is ensured by a dilution term derived from the expansion of the plume:

$$D(t) = \frac{\sigma_y(t)\sigma_z(t)}{\sigma_y(t+\Delta t)\sigma_z(t+\Delta t)}$$

$$C^{4\sigma_y(t)}_{NO_x}(t) = D(t) C^{4\sigma_y(t)}_{NO_x}(t) + (1 - D(t)) C_{bg}$$

$$C^{4\sigma_z(t)}_{NO_x}(t) = D(t) C^{4\sigma_z(t)}_{NO_x}(t) + (1 - D(t)) C_{bg}$$

$$D(t) = \frac{\sigma_y(t)}{\sigma_y(t)\sigma_z(t+\Delta t)}$$

$$C^{4\sigma_y(t)}_{NO_x}(t) = D(t) C^{4\sigma_y(t)}_{NO_x}(t) + (1 - D(t)) C_{bg}$$

This model was found to provide results in good agreement with previous studies [Song et al., 2003b, von Glasow et al., 2003, Chen et al., 2005, Vinken et al., 2011]

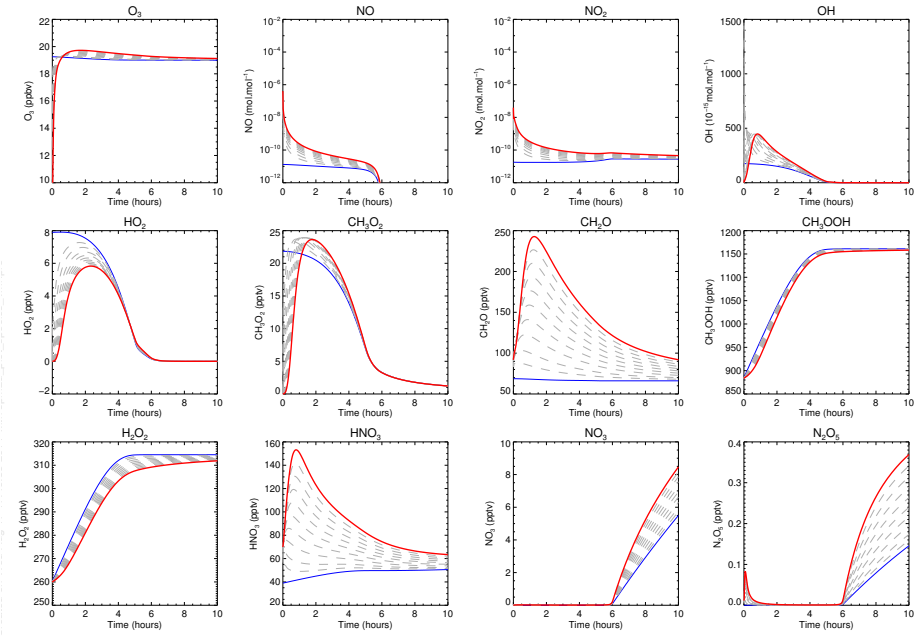

FIGURE 3.2: Example of simulation with the SPM-2D model in the case of a tropical neutral atmosphere (D) with a MBL height of 500 meters, a temperature of 296 K, a pressure of 975 hPa and a ship speed of 5 m/s. Blue lines indicate background concentrations. Red lines show inner plume concentrations while grey dashed lines show plume concentrations for each ring.

(see figure 3.2) and it was used in chapter 7 to develop and tune a ship plume parameterisation implemented in MOZART-4.

3.3 MOZART-4

MOZART (Modelling OZone And Relative Tracers) is a Global Chemistry Transport Model (GCTM) that has originally been developed by the National Center for Atmospheric Research (NCAR), the National Oceanic and Atmospheric Administration (NOAA), the Max-Planck Institute of Meteorology (MPI-Hamburg), the Geophysical Fluid Dynamics Laboratory (GFDL) and Princeton University. However, recent versions such as version 3 and version 4 have been updated and released by the NCAR group. The model is built upon the framework of Model of Atmospheric Transport and Chemistry (MATCH) proposed by Rasch et al. [1997]. One advantage of this framework is the pre-processing tool which builds

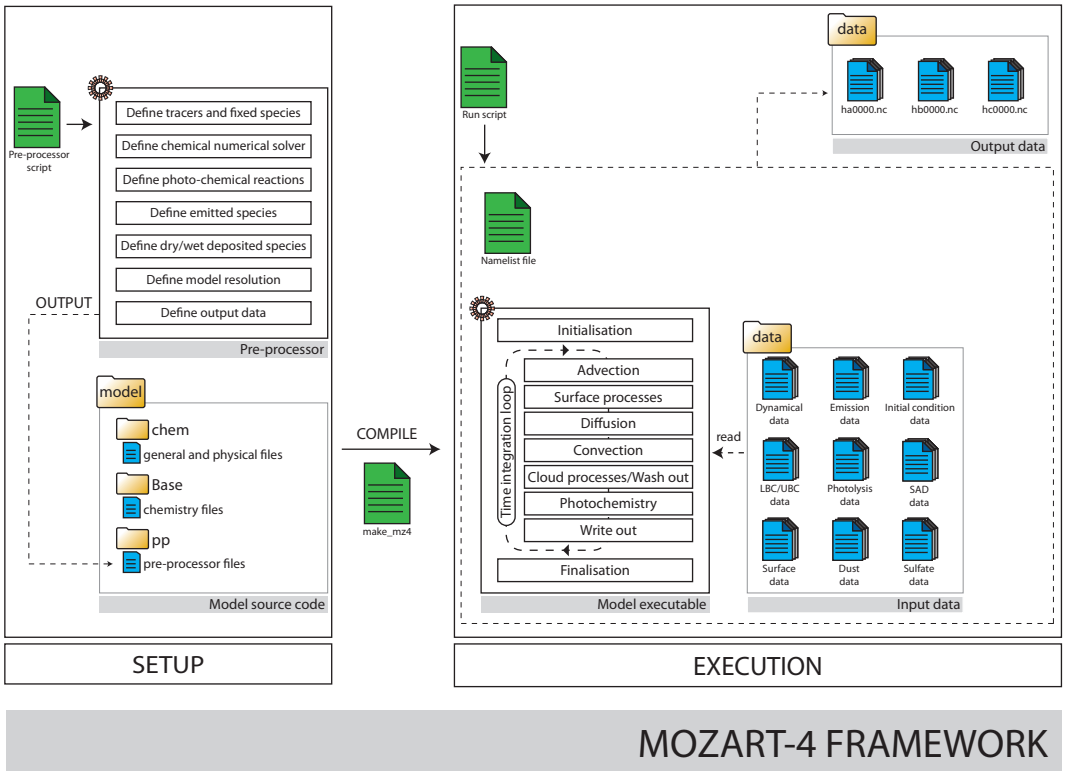

FIGURE 3.3: The MOZART-4 framework is split into two main sections. During the **setup**, one defines and compiles the model while during **execution**, the model performs the defined simulation.

a tailor-made photochemical numerical solver based on the sparse-matrix reduction algorithm developed by Markowitz [1957]. Another important aspect of the model is the use of hybrid sigma-pressure vertical coordinates which have been introduced in the model to allow the wind components to follow the orography of the Earth's surface [Simmons and Strüfing, 1981].

In this study, the model was driven by NCEP Reanalysis and ECMWF-INTERIM offline dynamical data which consists of temperature, pressure, specific humidity, wind speed, wind surface stress, surface fluxes of heat and momentum and downward solar radiation flux data (see Appendix A). This input data, which is provided every 6 hours to the model, is principally used in the transport sections of the model. Besides, transport is ensured by three main components:

Firstly, the advection is performed by the Flux-Form Semi-Lagrangian scheme (FFSL) developed by Lin and Rood which ensures mass conservation and preserves tracer correlations [Lin and Rood, 1996]. A pressure-fixer developed by P.

Cameron-Smith was added to the FFSL by Horowitz et al. [2003] and ensures mass conservation by modifying the meridional and zonal components of the wind in order to make the surface pressure consistent with the meteorological data [Horowitz et al., 2003].

Secondly, the convection is resolved by two schemes, one for shallow and mid altitude convection [Hack, 1994] and another one for deep convection [Zhang and McFarlane, 1995].

Thirdly, diffusion within the planetary boundary layer is parameterised by a prognostic equation that calculates vertical eddy fluxes and is described in Hosltag and Boville [1993]. The cloud water content and the precipitation flux rates are calculated by way of using the parameterisation developed by Rasch and Kristjansson [1998].

Furthermore, the photochemical mechanism contains 97 tracer species including 12 bulk aerosols compounds, 39 photolysis reactions and 157 chemical reactions [Emmons et al., 2010b]. Hydrocarbons with a large number of carbon atoms are lumped into 3 species depending on their type (Alkenes with 4 or more carbon atoms are lumped in the BIGENE species. Alkanes with 5 or more carbon atoms are lumped in the BIGALK species. Aromatic species with 7 or more carbon atoms are lumped in the TOLUENE species). Photolysis rates are calculated online using the Fast Tropospheric Ultraviolet-Visible (FTUV) radiation model developed by Tie et al. [2003]. Depending on the species lifetime, the photochemical system is numerically solved by either an explicit or an implicit scheme. The implicit scheme is ensured by a fully implicit Euler backward with Newton-Raphson iteration. In addition, 2 species have fixed concentrations N_2, O_2. The concentrations of water vapour are calculated online using specific humidity data from the meteorology advected by the model.

A number of tropospheric aerosols such as dust, sulphates, black and organic carbons, secondary organic aerosols, ammonium nitrates and sea salts have been added to MOZART-4. Online-calculated emissions of isoprene and monoterpenes are based on the Model of Emissions of Gases and Aerosols from Nature (MEGAN)

developed by Guenther et al. [2006]. This parameterisation requires global maps of emission factors as well as plant function type and leaf area index. In addition, anthropogenic and biogenic soil NO_x emissions are taken into account using a bucket-style parameterisation [Bouwman et al., 2002, Yienger and Levy, 1995]. Dry deposition processes are calculated online using the 3-resistance parameterisation developed by Wesely [1989] and the vegetation distribution from Bonan et al. [2003]. Wet deposition is solved by a first-order loss equation which depends on the Henry Laws constant of the gas considered for in-cloud scavenging [Giorgi and Chameides, 1985] and on the concentration of dissolved gas in cloud droplets for below-cloud scavenging [Brasseur et al., 1998]. This scheme does not take into account the evaporation of rain drops. The lightning parameterisation is based on the work of Price et al. [1997] which defines the production of lightning NO_x as a function of convective cloud top heights. The vertical distribution is further defined by a C-shape parameterisation which reduces emissions close to the surface [Pickering et al., 1998, DeCaria et al., 2005]. Moreover, the magnitude of cloud-to-cloud lightning strikes equals that of cloud-to-ground strikes [Ridley et al., 2005]. Prescribed concentrations of long lived species such as N_2O and CH_4 are applied at the surface and at the top of the model. In addition, O_3 and NO_x species rely on upper boundary conditions which are relaxed towards the tropopause within 10 days. For most of the simulations of this study, the model was run on a T42LR horizontal grid (128 x 64 grid boxes) with 28 vertical levels and required a 20-minute global timestep for all processes to converge. The input data consisted of NCEP Reanalysis data and IPCC-AR5 historic data both representative of the year 2000.

This model was configured as in Emmons et al. [2010b] and was employed in chapters 4, 5, 6, 7 and 8 for a variety of studies.

3.4 Edwards-Slingo

Edwards-Slingo is an offline radiative transfer model (RTM) that calculates radiative fluxes and heating rates across the atmosphere using the δ-Eddington form of the two-stream equations [Edwards and Slingo, 1996]. The model has the ability to run either for a solar or a thermal source in order to study radiations in the short-wave (SW) and long-wave (LW) regions of the light spectrum. The model version used in this study has been set up and maintained by Dr. Ruben Rodriguez-de-León[2] which obtained the code from Prof. Dr. Piers Forster[3]. In its current version, there are 9 bands in the long-waves ranging from 3 μm to 1 cm and 6 bands in the short-waves ranging from 200 nm to 10 μm. The two-stream equation is solved for five different zenith angles in the short-waves. The horizontal grid is subdivided into 144 boxes in the longitudinal dimension and 72 in the latitudinal dimension whereas vertical levels are defined on 23 pressure levels ranging from 1 hPa to 995 hPa. The ISCCP[4] climatology is used to estimate the position and amount of water and ice clouds in the atmosphere. Their vertical distribution is ensured by a random overlap method. Regarding gas species, 5 of them are defined in the long-waves (H_2O, CO_2, N_2O, O_3, CH_4) while 4 of them are defined in the short-waves (H_2O, CO_2, O_3, O_2). Concentrations of aerosols, halocarbons and chlorofluorocarbons are all set to 0. Edwards and Slingo has been tested over a significant number of studies [Edwards and Slingo, 1996, Stevenson et al., 1998, 2006, Eyring et al., 2007, Myhre et al., 2009].

O_3 volume mixing ratios calculated by MOZART-4 are converted into mass mixing ratios and linearly interpolated onto the Edwards-Slingo horizontal grid and pressure levels. In addition, since MOZART-4 is a tropospheric model which does not resolve physical and chemical processes occurring in the stratosphere, stratospheric concentrations of gas species such as H_2O, CO_2, O_3, N_2O and CH_4 are prescribed in Edwards-Slingo by a climatology derived from ECMWF data (Dr.

[2]Dalton Research Institute, Manchester metropolitan University, Manchester, UK
[3]School of Earth and Environment, University of Leeds, Leeds, UK
[4]International Satellite Cloud Climatology Project, http://isccp.giss.nasa.gov

R. Rodriguez-de-León, personal communication 2009). The tropopause is defined as the maximum height where O_3 volume mixing ratios are lower than 150 ppbv.

This model was used in chapter 8 to analyse the impacts of future scenarios of shipping emissions.

Chapter 4

MOZART-4's ability to represent the Marine Boundary Layer and the free troposphere

In this chapter, MOZART-4 was assessed to verify how it represents the composition of Marine Boundary Layer (MBL) and the free troposphere by comparing its output to various observational datasets. The following results were found:

- At the global scale, MOZART-4 provides a good representation of NO_x, O_3 and CO in the MBL and the free troposphere.
- As expected, MOZART-4 cannot capture some of the details occurring in the vicinity of some monitoring instruments.
- MOZART-4 does not always simulate accurately O_3 concentrations and their temporal variations in the UT/LS, but modelled values generally remain within 1-σ standard deviation of the measurements.
- The absence of halogen chemistry mechanism in MOZART-4 leads to overestimations of modelled O_3 in the polar regions in spring.

4.1 Introduction

Global chemistry-transport models are designed to provide a representation of the gas and aerosol composition of the atmosphere. In order to achieve this goal, they rely on a complex set of numerical schemes and parameterisations of atmospheric processes as well as on input data. Since input data carry various degrees of uncertainty and numerical schemes and parameterisations introduce errors into the results, modellers resort to observational data to test their models and validate them. A number of studies have proved that MOZART-4 has skills in simulating the composition of the atmosphere [Pfister et al., 2006, 2008b,a, Park et al., 2009, Sousa Santos, 2008, Emmons et al., 2010a]. In particular, Emmons et al. [2010b] published a reference paper describing and assessing it. In this publication, they notably pointed out the ability of MOZART-4 to reproduce the seasonal variability of O_3 but noticed that the model overestimates somehow its concentrations in the upper troposphere. As for hydroxyl radical levels, they were found to be lower than the climatology calculated by Spivakovsky et al. [2000], but in good agreement with results from previous simulations performed with MATCH, a model related to MOZART-4. Other publications from the ACCENT project showed that results from MOZART-4 stay within the 1-σ standard deviation of multi-model analysis [Stevenson et al., 2006, van Noije et al., 2006]. Although these studies showed that MOZART-4 has capabilities to reproduce the atmospheric composition with a relatively good accuracy, they did not specifically focus on the marine environment. Hence, this chapter aims at providing a detailed analysis of the abilities that MOZART-4 has in reproducing the environment in which shipping perturbations take place. This chapter presents a comparison of two MOZART-4 simulations to observational data from several sources: the World Data Center for Greenhouse Gases (WDCGG), the World Ozone and Ultraviolet radiation Data Center (WOUDC), Aircraft data composites and the Tropospheric Emission Spectrometer (TES). Each observational dataset possesses its own uncertainty as well as spatial and temporal domains. Several types of them were therefore employed in hope to obtain a clearer picture of MOZART-4's ability to

TABLE 4.1: Availability of the data depending on the year (A cross means that the data is available whereas a dash means otherwise).

	2000	2005
MOZART-4	X	X
WDCGG	X	X
WOUDC	X	X
Emmons	X	-
TES	-	X

simulate shipping perturbations of tropospheric composition at different scales. A methodology section provides a description of these sources as well as the way they were processed. Results for each of these sources are then presented and lead the way to a discussion on MOZART-4's ability to represent the MBL and the free troposphere.

4.2 Methodology

The model set-up is first presented. Then, a description of each dataset used in this study is given. Since these datasets have different temporal availabilities, comparisons were performed for two different years, in 2000 and in 2005 as shown in table 4.1.

4.2.1 MOZART-4 set-up

In this chapter, MOZART-4 was driven by NCEP-Reanalysis data representative of the year 2000. Nonetheless, the more recent ACCMIP historical emission inventory representative of the year 2000 was employed in this study instead of the POET emission inventory Emmons et al. [2010b]. A comparison of these two datasets are provided in table B.1 in appendix B. Furthermore, modelled data were output every hour as well as on daily averages to allow comparisons with observational data.

4.2.2 World Data Center for Greenhouse Gases

The World Data Center for Greenhouse Gases (WDCGG) is one of the six World Data Centers developed under the Global Atmospheric Watch (GAW) program of the World Meteorological Office that pursue the acquisition of gas species concentrations by using a variety of methods, instruments and platforms across the globe. It is lead by the Japanese Meteorological Agency (JMA). The quality of the data is insured by third-party organisations such as Central Calibration Laboratories, World Calibration Centers and Quality Assurance Science Activity Centres. All these organisations provide scientific and technical guidance to the groups in charge of the monitoring network. In addition, data provided by each monitoring site are further checked and validated by the WDCGG. For detailed information about the GAW program the reader may consider visiting the following website: http://www.wmo.int/gaw.

As mentioned earlier, the monitoring network comprises different types of measurement platforms including stationary stations and mobile stations such as aircraft and ship. Gas concentration measurements from ice cores are also available. This study focused on stationary stations only. These stations generally host several instruments which may sometimes be owned by different groups. Gas species concentrations recorded by these instruments include CO_2, CO, CH_4, O_3, NO_x, VOCs ... Depending on the instrument or the method used to measure a particular gas species, data may be available hourly, daily and/or monthly and also in different units. The whole dataset was spread across thousands of ASCII text files which are sorted by species, data frequency, station and provider. The dataset was downloaded on the 25^{th} of June 2011 from the WDCGG FTP server: ftp://gaw.kishou.go.jp/pub/data.

In this study, daily averaged CO and O_3 values monitored by coastal stationary stations were employed. Coastal stations were defined as being less than 50 km away from the coastline except for stations located in the polar regions where the anthropogenic influence is not as significant and the radius was extended to 100 km. This operation resulted in a selection of 35% of all CO stations and 32% of

all O_3 stations. The selection is displayed on figure 4.1 and a table in appendix C provides their geographical locations (see table C.1). Three units were found in this selection of stations: ppb, $\mu g/m^3$-20C and $\mu g/m^3$-25C. All data were converted to volume mixing ratios to allow comparison with MOZART-4 data. Given the size of the dataset, a file index was generated to optimise the time required to search for the files matching a specific set of criteria (e.g. time, location ...). It is important to bear in mind that daily averages are calculated from different number of observations per day in the WDCGG dataset whereas daily averages from MOZART-4 always have the same number of data. When validating flags were indicated in WDCGG, data were kept accordingly.

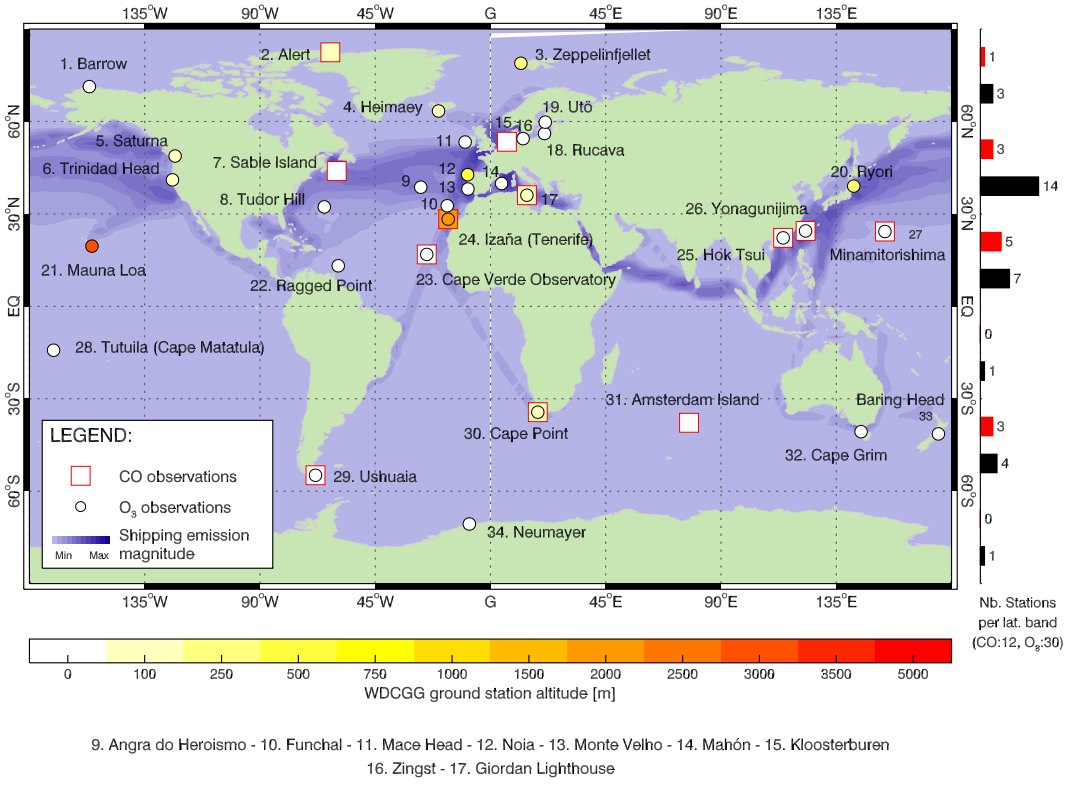

FIGURE 4.1: Location of the CO (square) and O_3 (circle) WDCGG daily-monitoring stationary stations used in this section. The altitude of these stations is indicated by a white to red color scale. The shipping emission magnitude is only provided as an indication to help the reader locate the stations which are close to ship lanes.

4.2.3 WOUDC

The World Ozone and Ultraviolet radiation Data Center (WOUDC), another GAW's World Data Center, is lead by the Meteorological Service of Canada which aims at providing O_3 and ultraviolet radiation observations by using a network of more than 400 stations. These stations have been reporting data over nearly 50 years. Regarding O_3, different measurement platforms and categories of observations exist, as in the WDCGG dataset. Indeed, surface measurements from ground stations, profiles from LIDAR, Ozonesondes and total O_3 columns are available in the WOUDC dataset. For the purpose of this study, Ozonesonde data were employed. For more information, please refer to the WOUDC website: http://www.woudc.org/.

The structure of the Ozonesonde dataset is organised in directories spreading over three levels which break data down into stations, instruments and year. Each year directory comprises CSV text files that are sorted by launch date. These files contain metadata including platform, instrument, location and time information, a flight summary as well as O_3 profile measurements and pump correction factors at certain pressure levels. The dataset was downloaded off the WOUDC FTP server: ftp://woudc:woudc*@ftp.tor.ec.gc.ca/ on the 6th of September 2010.

Stations retained in Emmons et al. [2010b] were used and further filtered to select those close to oceanic regions. O_3 profiles in 2000 were extracted. Pump correction factors were then applied to the selected profiles. Instantaneous hourly data from MOZART-4 were extracted at times corresponding to Ozonesonde launch times. Both WOUDC and MOZART-4 O_3 profiles were interpolated on a common pressure scale. Data were then gathered into latitudinal and pressure regions prior to statistical calculations.

4.2.4 Aircraft data composites

The aircraft data composites compiled by Emmons et al. [2000] were also utilised in this chapter. Since its publication in 2000, this dataset has been updated

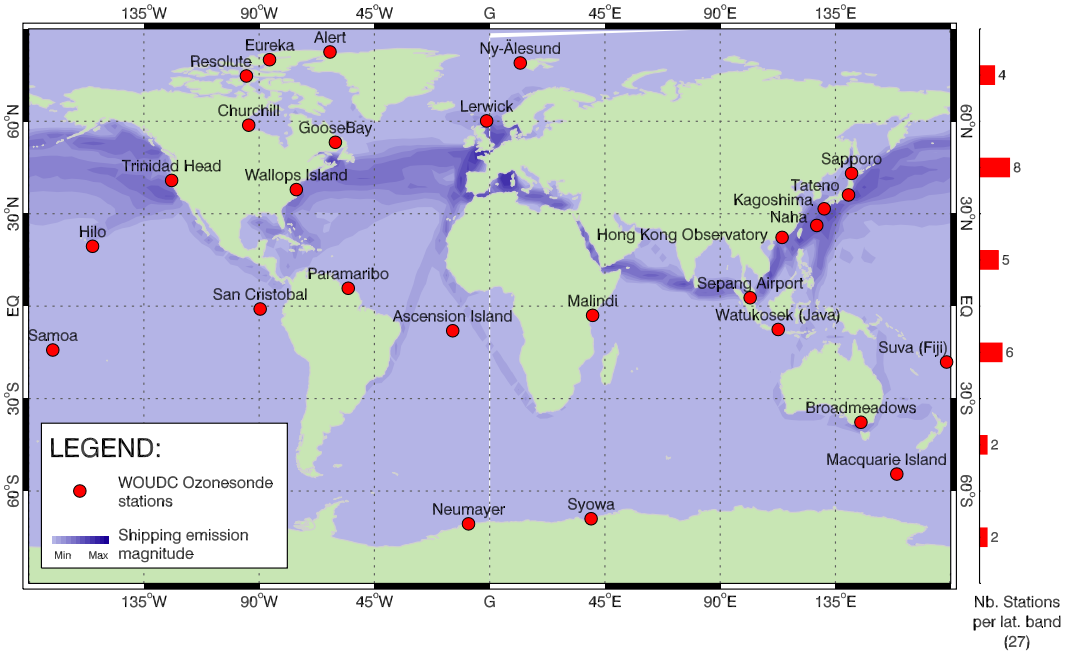

FIGURE 4.2: Location of the 27 WOUDC stations selected in 2000. The shipping emission magnitude is only provided as an indication to help the reader locate the stations which are close to ship lanes.

with a few recent campaigns while some others have been removed. It now comprises 30 aircraft campaigns that provide tropospheric measurements of O_3 and its precursors over the period 1984-2001 (see map on figure 4.3 and table C.2 in appendix C). These measurements were taken by different instruments on-board different aircraft. O_3 measurements were made using C_2H_4-chemiluminescence and NO-chemiluminescence techniques whereas NO and NO_2 were retrieved by laser-induced fluorescence methods. Uncertainties in O_3 measurements are smaller than 5% or 3 ppbv (whichever is the largest). Regarding NO_x, accuracy and precision depend on their measurement frequency. For measurements made every seconds, the accuracy is usually smaller than 20% while the precision can be as large as 15 pptv. For measurements made every 100 seconds, the accuracy is generally smaller than 10% but the precision remains as large as 15 pptv. For more details about these aircraft campaigns the reader is invited to visit the following websites: http://www-gte.larc.nasa.gov/, http://www.espo.nasa.gov/success/, http://www.pa.op.dlr.de/polinat/, http://www.espo.nasa.gov/sonex/ and http://topse.acd.ucar.edu. The data are

provided as regional profiles and gridded climatologies. They were downloaded on 26th of October 2010 from the website of the Atmospheric Chemistry Division at NCAR http://www.acd.ucar.edu/gctm/data/.

Two comparisons were made with this dataset: one with the aggregated regional profiles of the TOPSE campaigns (Tropospheric Ozone Production about the Spring Equinox) that were undertaken in spring 2000 and one with the gridded NO_x and O_3 climatologies. The former is crucial to understand how well the model simulates O_3 in the Northern hemisphere above 30°N during spring, although measurements have been done above land and in the Arctic region. The latter provides a robust dataset of marine and coastal environment measurements to test MOZART-4 against. The approach followed by Eyring et al. [2007] was taken in this study. All 5°x5° grid boxes outside oceanic regions and the 30°N-60°N latitudinal band were filtered out.

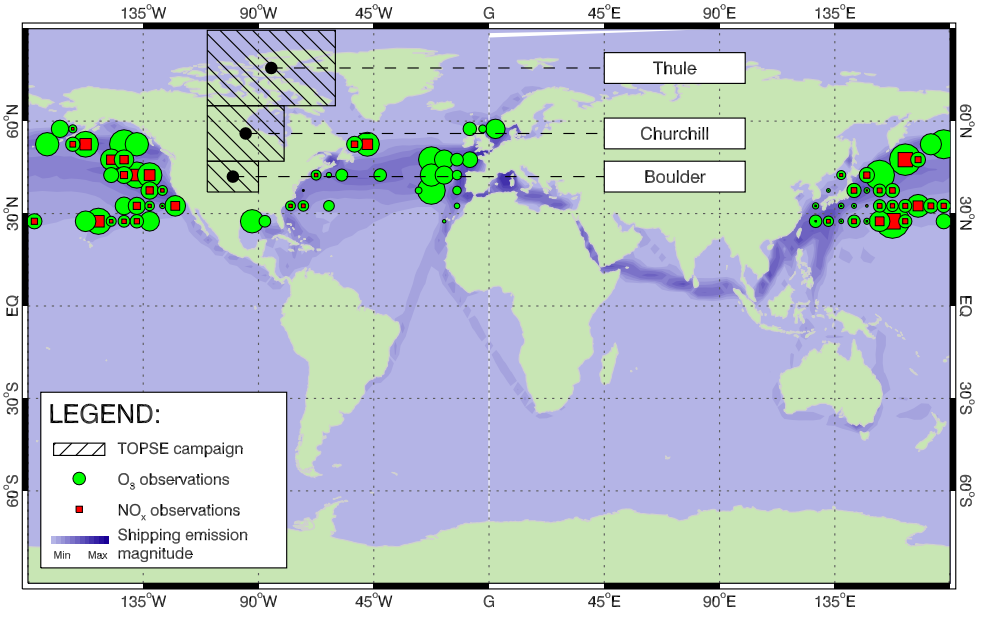

FIGURE 4.3: Geographical regions covered by the aircraft campaigns contained in the aircraft data composites. Circle and square sizes are proportional to the number of O_3 and CO observations respectively. The shipping emission magnitude is only provided as an indication to help the reader locate the stations which are close to ship lanes.

4.2.5 TES

TES (Tropospheric Emission Spectrometer) is an infrared Fourier-transform spectrometer instrument (FTIR) that runs onboard the NASAs Aura satellite and measures infrared radiations emitted by the Earth and some gas species in the atmosphere. This instrument captures high-resolution images of infrared spectra interferences which are later processed by a Fourier-transform algorithm in order to retrieve the whole light spectrum. Nadir and limb view modes are both available to acquire various type of gas species. In this chapter, version 4 of the O_3 level 2 product[1] was used. The frequency of the measurements is 16 orbits in a 50% duty-cycle which roughly correspond to measurements every other day. A number of studies have compared this data product to a variety of observations and noticed a 5% to 15% bias in the troposphere which translates into a 3.7 ppbv to 9.2 ppbv bias in the lower troposphere [Richards et al., 2008, Osterman et al., 2008, Nassar et al., 2008]. The data and documentation are available on the NASA Langley Research Center (LRC) website. The whole dataset consists of HDF-EOS5 files and was downloaded from the LRC Atmospheric Science Data Center FTP server `ftp://l4ftl01.larc.nasa.gov/TES/` on the 16th of September 2010.

For the purpose of this study, TES data from 2005 were used (note that the month of June is not available in 2005). A mask created by filtering out all shipping NO_x emissions smaller than 5.0 x 10^9 molecules.cm^{-2}.s^{-1} was used to select TES profiles close to the main ship lanes (see figure 4.4). In addition, this mask was further divided into four oceanic regions: Atlantic ocean, Pacific ocean, Indian ocean and Mediterranean sea. For the valid TES profiles, corresponding MOZART-4 profiles were extracted and interpolated on the 67 TES vertical levels before applying the TES averaging kernels. Averaging kernels are 2-dimensional square matrices which size equals the number of retrieved vertical levels. For data at a given pressure level, they provide information about the relative contribution of the whole range of pressure levels to this particular level. TES and MOZART-4 profiles were further averaged over the 4 oceanic regions, 4 pressure bands and 4 seasons. The

[1] Available at `http://eosweb.larc.nasa.gov/PRODOCS/tes/table_tes.html` Last access in 2011

4 pressure bands were taken between 1000 and 800, 800 and 500, 500 and 300 and 300 and 100 (in hPa).

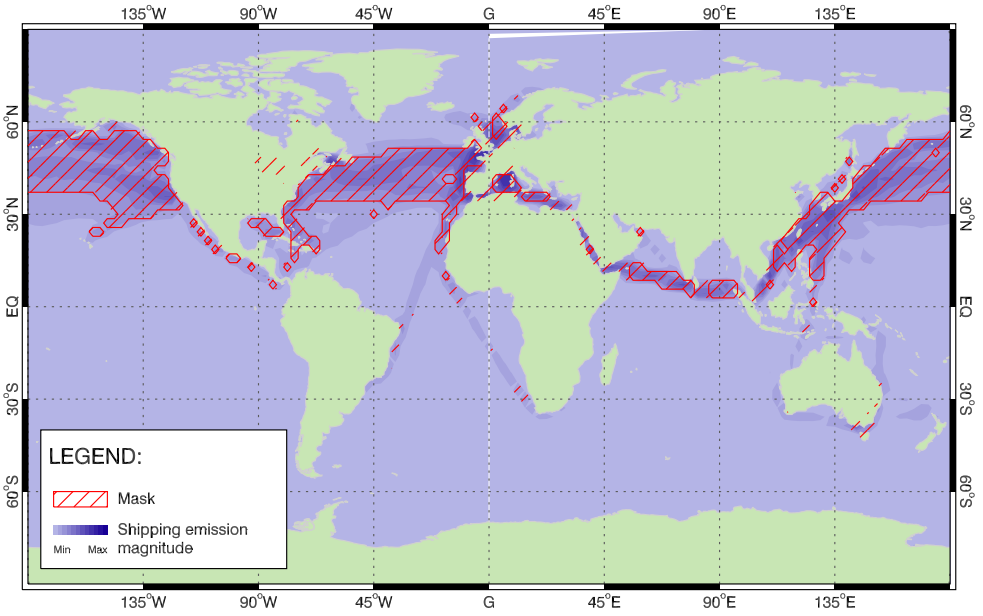

FIGURE 4.4: Mask generated with the shipping NO_x emission file read in by MOZART-4. Threshold: 5.0×10^9 molecules.cm^{-2}.s^{-1}.

4.3 Results

4.3.1 Comparison with WDCGG ozone data

Before comparing MOZART-4 data to the WDCGG dataset, it is worth noting that the distribution of the 34 CO and O_3 stationary stations displayed on figure 4.1 is quite sparse. 74% of the stations are located in the northern hemisphere and particularly in the European region which hosts 26% of them. About half of these stations are located close to the main ship lanes.

Simulated time series of CO and O_3 daily means were processed at station's locations in 2000 and 2005 and are displayed on figures 4.8, 4.9, 4.10 and 4.11. For each WDCGG station, multi-annual means and standard deviations were further calculated and then added to these plots to help the reader better understand the temporal variability of the different time series. The mean and standard deviation of each time series (WDCGG climatological, WDCGG specific year, MOZART-4 simulation with shipping, MOZART-4 simulation without shipping) have also been provided on the right side of each plot. Moreover, four Taylor diagrams have been plotted with a view to provide a clearer picture of MOZART-4 skills in reproducing the CO and O_3 concentrations in the troposphere. Taylor diagrams are effective graphical tools to summarise and compare observed and modelled data. For each WDCGG stationary station available in 2000 and 2005 and providing measurements of CO and O_3, standard deviations and correlations of daily mean values were calculated and used in conjunction with MOZART-4 computed daily mean values to plot Taylor diagrams (see figure 4.7). Root-mean square error (RMSE) thresholds are also plotted in light grey to attribute score to the data points.

Regarding CO, 12 stations reported data to the WDCGG between 1986 and 2011 but only 7 of them provided data in 2000 and 2005. Their distribution is sparse: 1 station is located in the North Polar region, 3 in the northern mid-latitudes, 5 in the northern tropics and another 3 in the southern mid-latitudes.

The 2000 and 2005 CO Taylor diagrams displayed on figure 4.7 indicate that there are strong relationships between measured and modelled CO VMR. Indeed, amidst the 7 stations providing data in 2000 and 2005, only Sable Island (7) has a correlation coefficient below 0.50. The variability of CO concentrations simulated by the model at this location is somehow much larger than that retrieved by the station's instrument. Moreover, 67% and 50% of the data points have a normalised standard deviation smaller than the reference, suggesting that modelled CO time series are generally smoother as expected since the model is climatological in essence. Another point reflected by the Taylor diagrams is that the model is in better agreement with stations located in the southern hemisphere than those located in the northern hemisphere in terms of correlation. This suggests that temporal variations in the Southern midlatitudes are well reproduced by the model. One may also notice the impacts of shipping which are barely perceptible, except at Alert and Sable Island. In the case of Alert which is distant by a couple of thousand kilometres from shipping emissions, it indicates that transport of shipping pollution may affect the Arctic region.

The 2000 and 2005 time series of CO VMR are shown on figures 4.8 and 4.9 and provide further information on the skills of the global model. In general, the magnitude and temporal variations of CO are well reproduced by the model but a few discrepancies may be noticed. For instance, the model fails to represent accurately the temporal variation of CO at Alert. This failure is likely to arise from the omission of tropospheric halogens in the model (see next paragraph on O_3). At Sable Island station in 2005, the modelled CO mixing ratios present a larger variability compared with measurements, which results in the poor correlation seen on the Taylor diagram. Since this station is situated off the eastern coast of North America, the peaks are likely to originate from anthropogenic pollution from the United States of America. The Ushuaïa and Cape Point stations both located in the southern mid-latitudes captured smaller values in comparison with MOZART-4 results. Indeed, there is a bias ranging between 10 ppbv and 21 ppbv on average that translates into a significant relative difference ranging between 22% and 40%. Conversely, the model underestimates CO concentrations in the northern tropics

at most station's locations except at Izaña station. This is especially the case in winter at Hok Tsui, Yonagunijima and Minatorishima where differences can be as large as 300 ppbv. It is interesting to note that both the Izaña and Cape Verde Observatory stations present a similar pattern of underestimation in spring. As for the northern mid-latitudes, modelled CO concentrations are also smaller in summer than those measured at Giordan Lighthouse in 2000 but larger than the climatological data spanning over 9 years. The large concentration peaks simulated by MOZART-4 at Sable Island and Cape Point may be attributed to the meteorology.

As for O_3, 30 stations monitored it from 1971 to 2011. However, only 18 of them provided data in 2000 whereas there were 19 in 2005. Their distribution is also sparse: 3 stations in the North Polar region, 14 stations in the northern mid-latitudes, 7 stations in the northern tropics, 1 station in the southern tropics, 4 stations in the southern mid-latitudes and 1 station in the south polar region.

44% and 26% of data points have a correlation coefficient smaller than 0.5 in 2000 and 2005 respectively as shown on the Taylor diagrams. Interestingly, the data points form a cluster between 0.5 and 1.5 standard deviation and between 0.5 and 0.9 correlation in 2005 while they are more scattered in 2000. These results emphasize the impact of meteorological data upon simulation results. It is worth mentioning that there is also a negative correlation at Barrow (1) which will be explained in the next paragraph. Contrary to CO, shipping O_3 perturbations are clearly visible, especially at Angra do Heroismo (9) and Yonagunijima (26) in 2000 and Trinidad Head (6), Mace Head (11) and Yonagunijima (26) in 2005. Apart from the stations of Minatorishima (27) and Tutuila (28) in 2000 and 2005 and those of Saturna (5) and Giordan Lighthouse (17) in 2005, the inclusion of shipping emissions does not improve model accuracy in terms of RMSE.

On the O_3 time series plots, one may notice that the data point with a negative correlation corresponds to Barrow's station located in the North Polar region. MOZART-4 clearly fails to represent the drop in O_3 concentrations in spring. This

drop is a well-know phenomenon which is linked to a bromine concentration explosion that catalytically destroys O_3 molecules [Wennberg, 1999]. This phenomenon is also revealed by the Zeppelinfjellet plots. Another problem in the Northern polar region is that the model underestimates O_3 concentrations which range between 20 ppbv and 50 ppbv whereas instruments at the station measured values ranging between 40 ppbv and 90 ppbv. These large discrepancies could be attributed to a misrepresentation of the transport of O_3 precursors from the North American and European regions. Interestingly, modelled data including shipping emissions clearly show an overestimation of O_3 concentrations at Angra do Heroismo and to a lesser extent at Cape Verde Observatory and Mace Head whereas simulations without shipping emissions better agree with measurements. The special location of the Angra do Heroismo station reveals a weakness in the model which under certain conditions may overestimate the impacts from shipping emissions. Figure 4.5 shows the anticyclonic conditions which stay close to the island during summer and favours the production of O_3. Even more importantly, the shipping O_3 perturbation of nearly 12 ppbv is consistent with those previously reported in the literature [Eyring et al., 2007, Endresen et al., 2003, Dalsøren et al., 2007]. The station of Mace Head is located on the west coast of Ireland. It has been shown to be representative of background air in Europe and is periodically influenced by Atlantic marine air masses [Grant et al., 2010]. However, the comparison presented here shows a very different picture from the large differences plotted at Angra do Heroismo in 2000. Dalsøren et al. [2010] performed a transient simulation from 2000 until 2007 to study the impact of shipping emissions on tropospheric O_3 and found similar results. In fact, the maximum shipping O_3 perturbation appears to be located at a lower latitude and does not influence much of the air captured at Mace Head (see figure 4.6).

In the southern hemisphere, the model underestimates O_3 concentrations at locations far away from intensive anthropogenic activity. In summertime, large O_3 peaks are simulated by MOZART-4 at several locations including Ryori, Yonagunijima, Saturna, Trinidad Head, Cape Grim and Baring Head. At Cape Grim, it appears that the peaks are correlated with low boundary layer height.

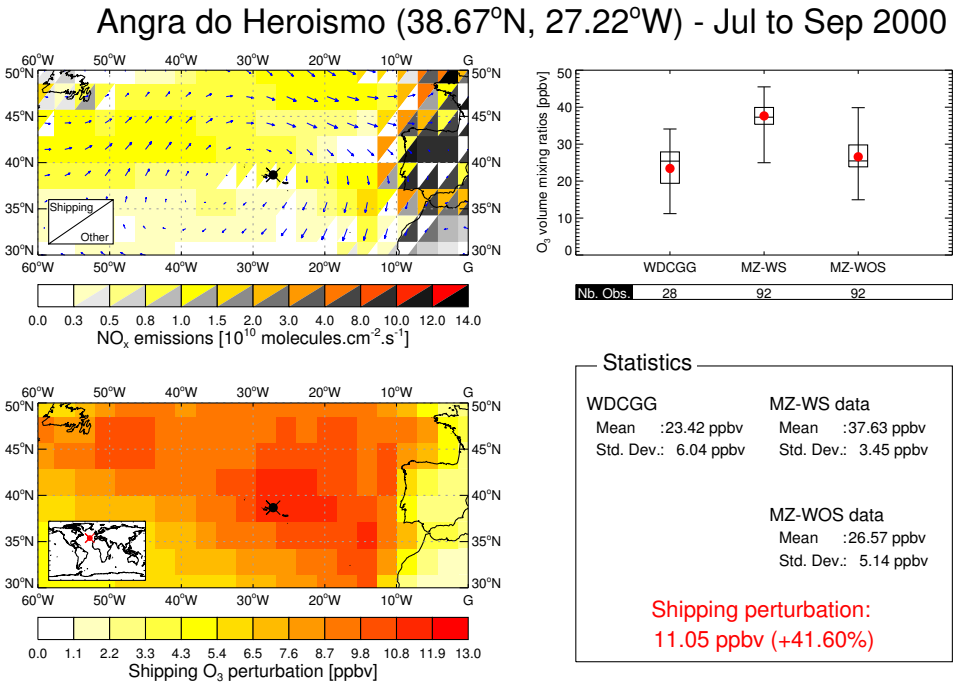

FIGURE 4.5: Close-up displaying the conditions surrounding the location of the Angra do Heroismo station over the months of July to September in 2000. The plot in the upper left corner shows the shipping and background NO_x emissions and the seasonal mean wind directions. The plot in the bottom left corner shows the O_3 VMR calculated by MOZART-4. Box plots presenting the minimum, maximum and mean values as well as the median and the first and the third quartile are displayed in the upper right corner. Mean and standard deviations are also provided in the bottom right corner.

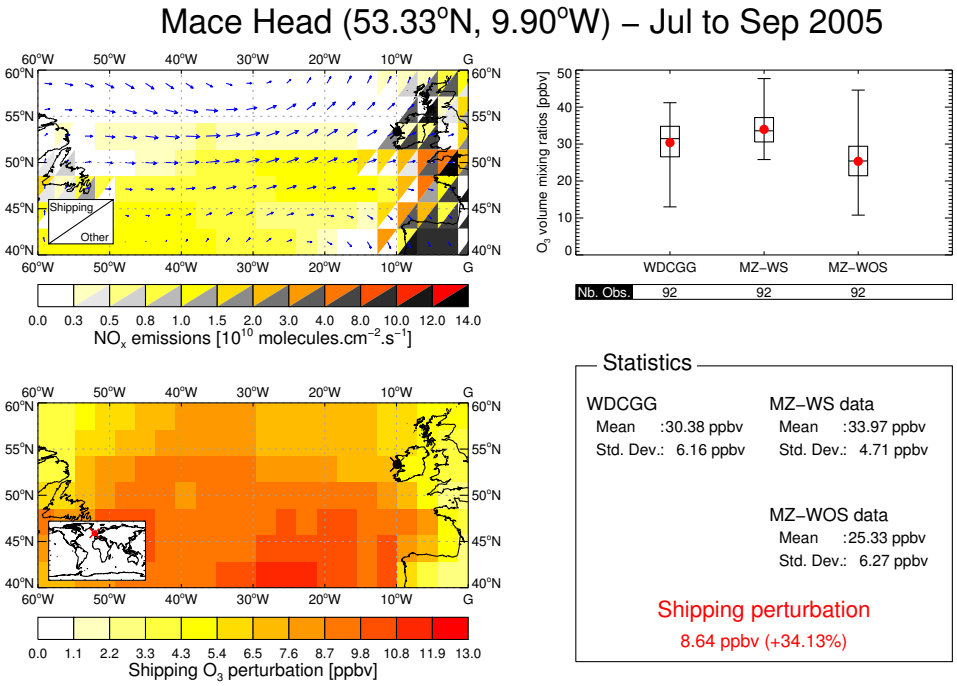

FIGURE 4.6: Same as figure 4.5 but for Mace Head in 2005.

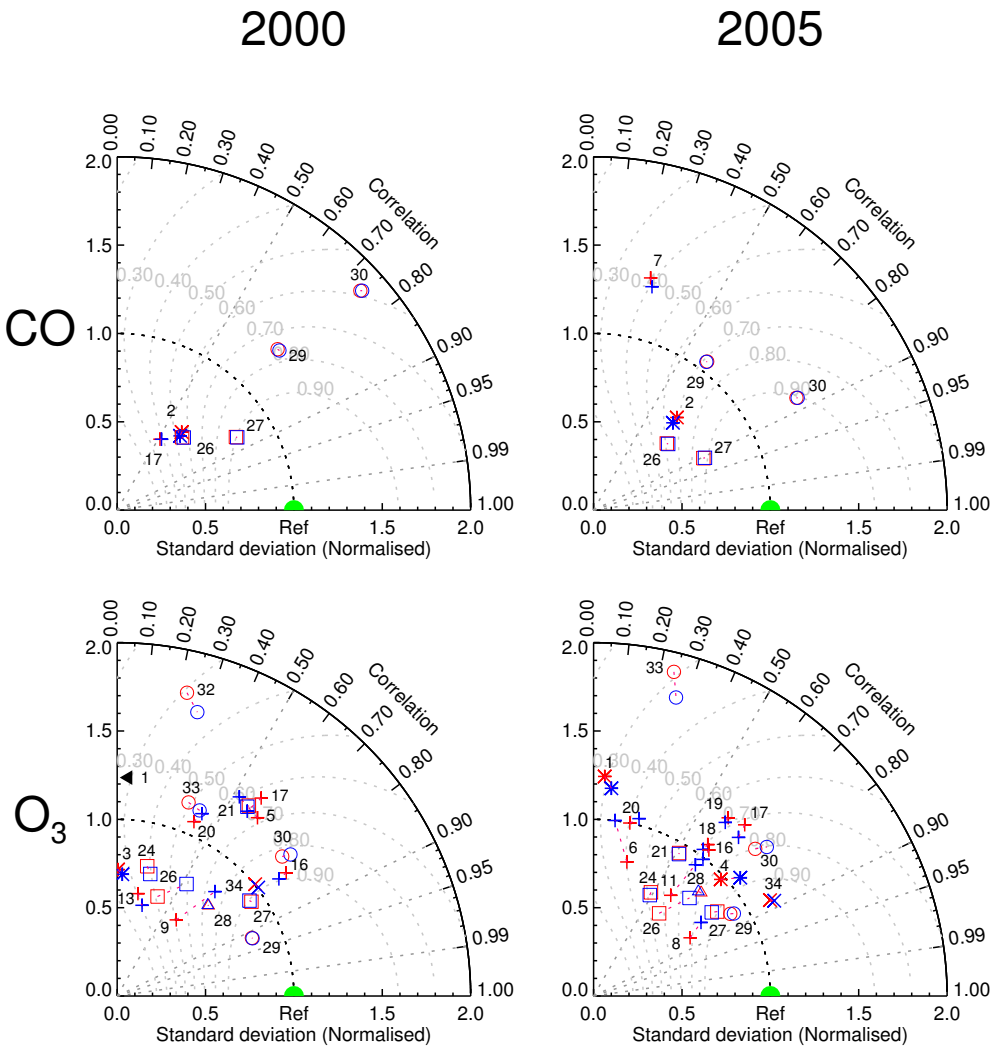

FIGURE 4.7: Taylor diagrams showing the differences in standard deviations and correlations between MOZART-4 results and WDCGG measurements of CO and O_3 concentrations in 2000 and 2005. The red color indicates the MOZART-4 simulations including all emissions whereas the blue color correspond to the simulations where shipping emissions have been removed. The symbols define the geographic location of the points: 90°N-60°N (∗), 60°N−30°N (+), 30°N−EQ (□), EQ−30°S (△), 30°S−60°S (○), 60°S−90°S (×). Station identification labels are placed next to the simulation with all emissions (red) when possible.

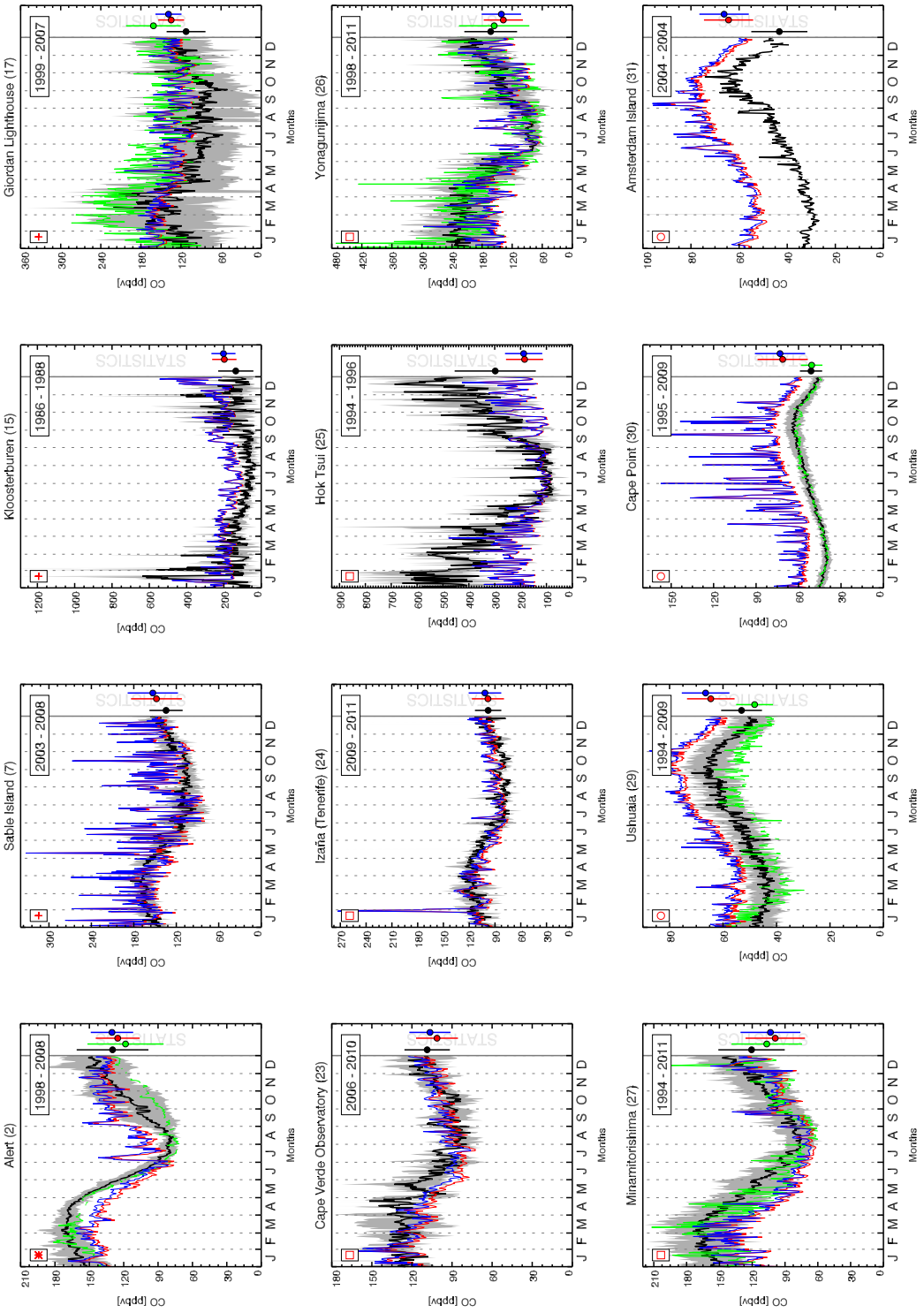

FIGURE 4.8: Time series of CO concentrations in 2000 from 12 WDCGG ground stations (green line) and the corresponding time series extracted from two simulations with MOZART-4: all emissions (red line) and shipping emissions removed (blue line). Climatological means and standard deviations of WDCGG data are also plotted (black line and shaded areas) and the time range is indicated in the upper right corner. The symbol used on the Taylor diagrams is displayed in the upper left corner. For each time series including, the annual mean and standard deviation are shown in the right band of each plot.

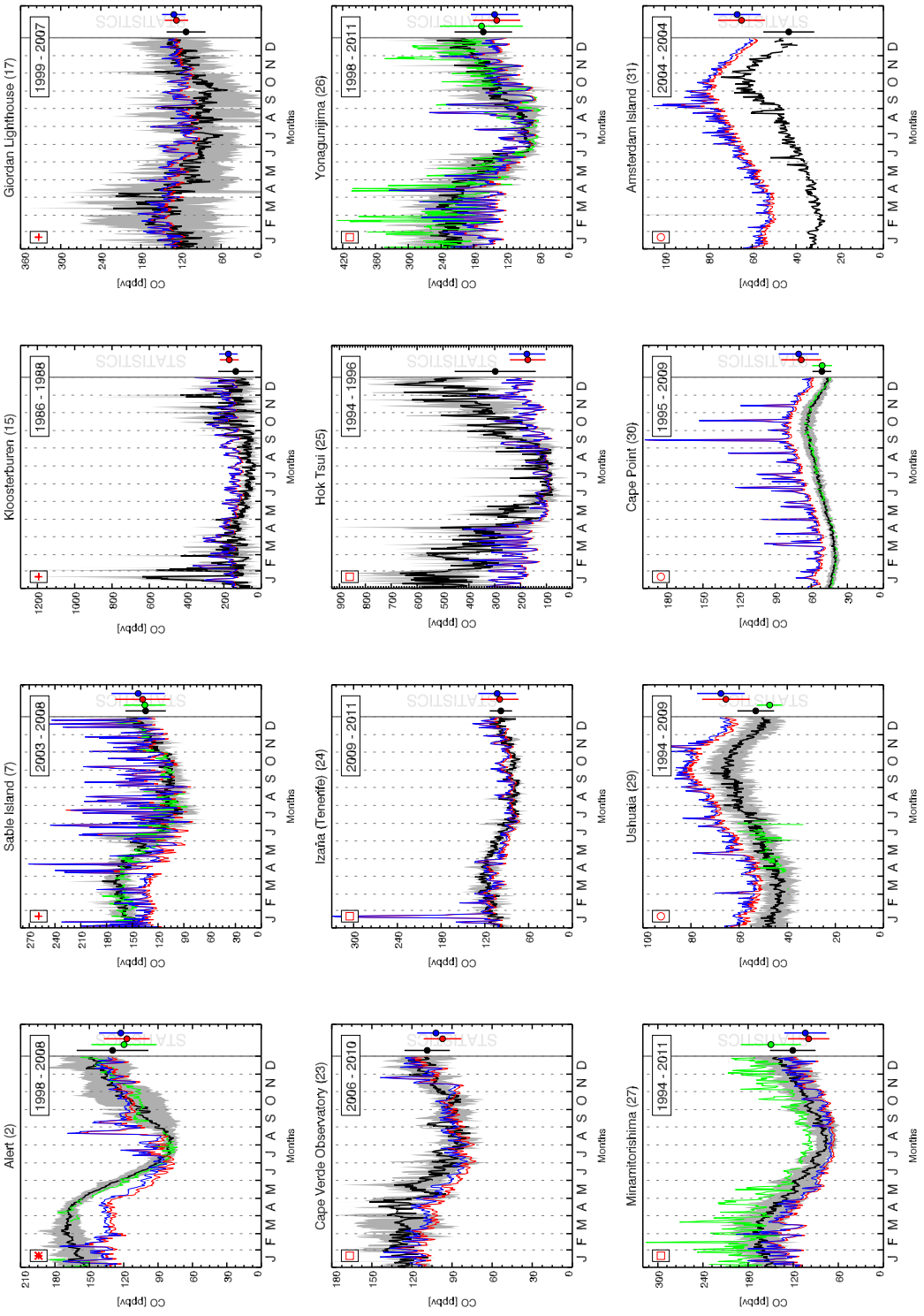

FIGURE 4.9: Same as figure 4.8 but in 2005.

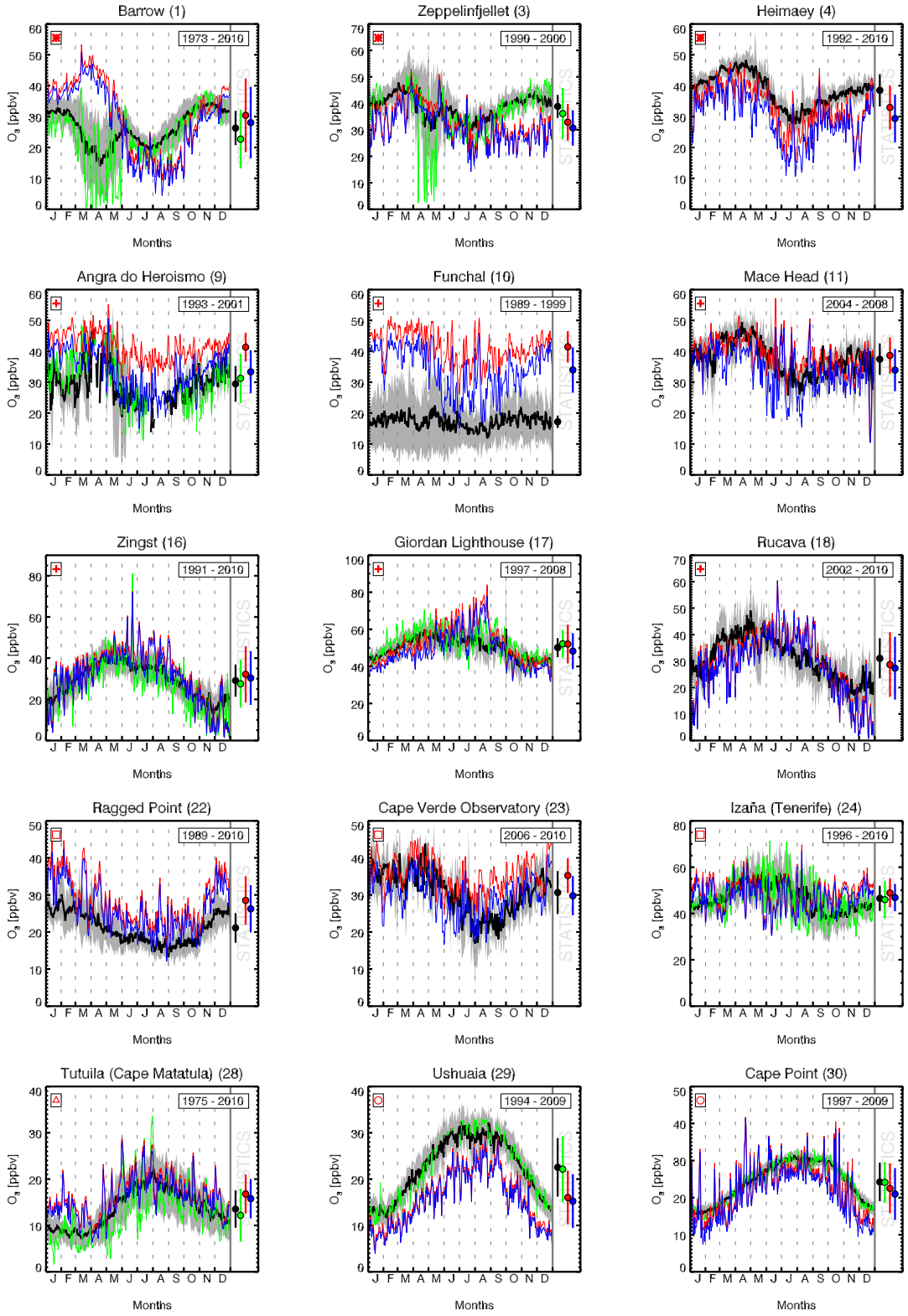

FIGURE 4.10: Same as figure 4.8 but for O_3.

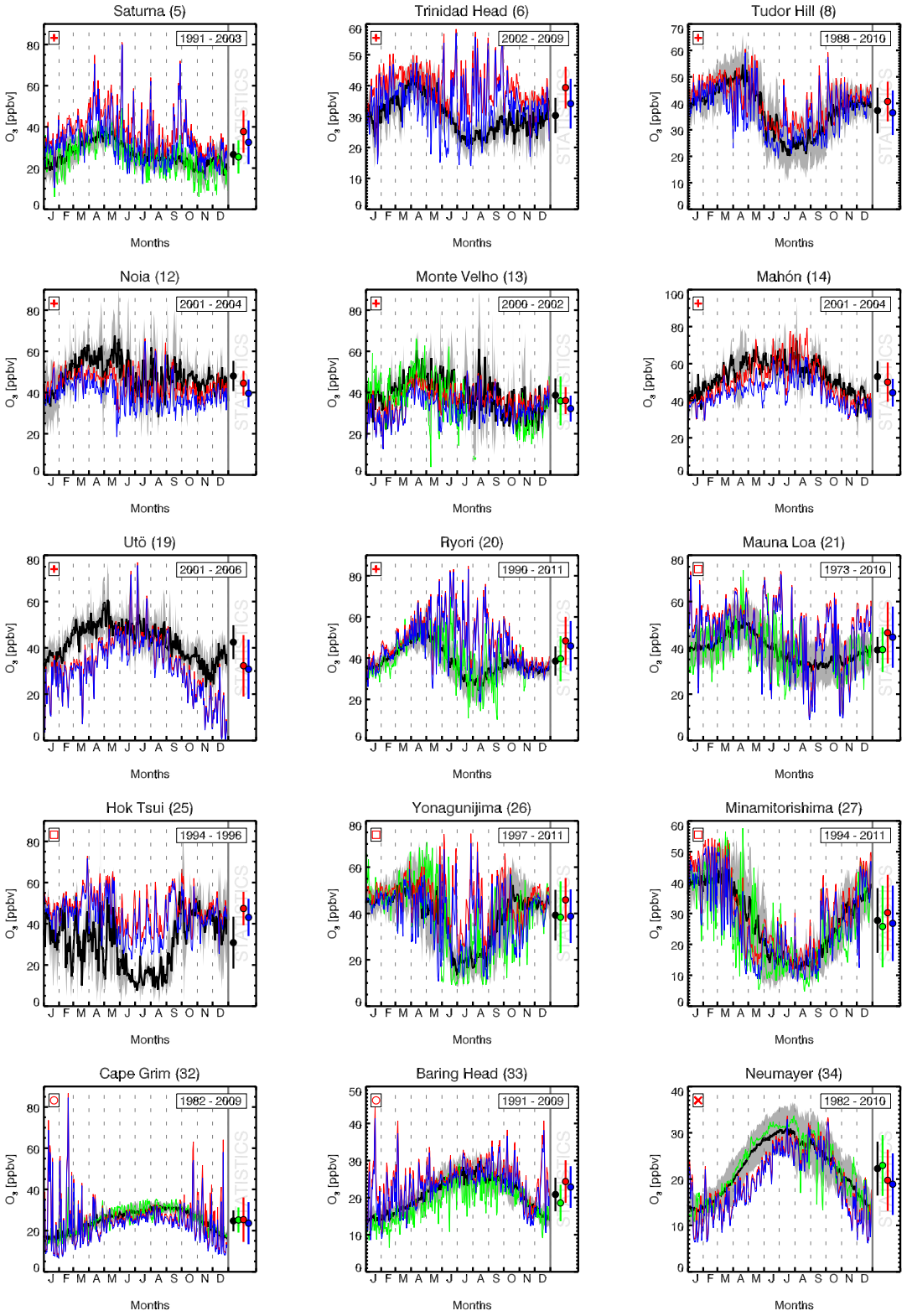

FIGURE 4.10: Figure 4.10 continuing.

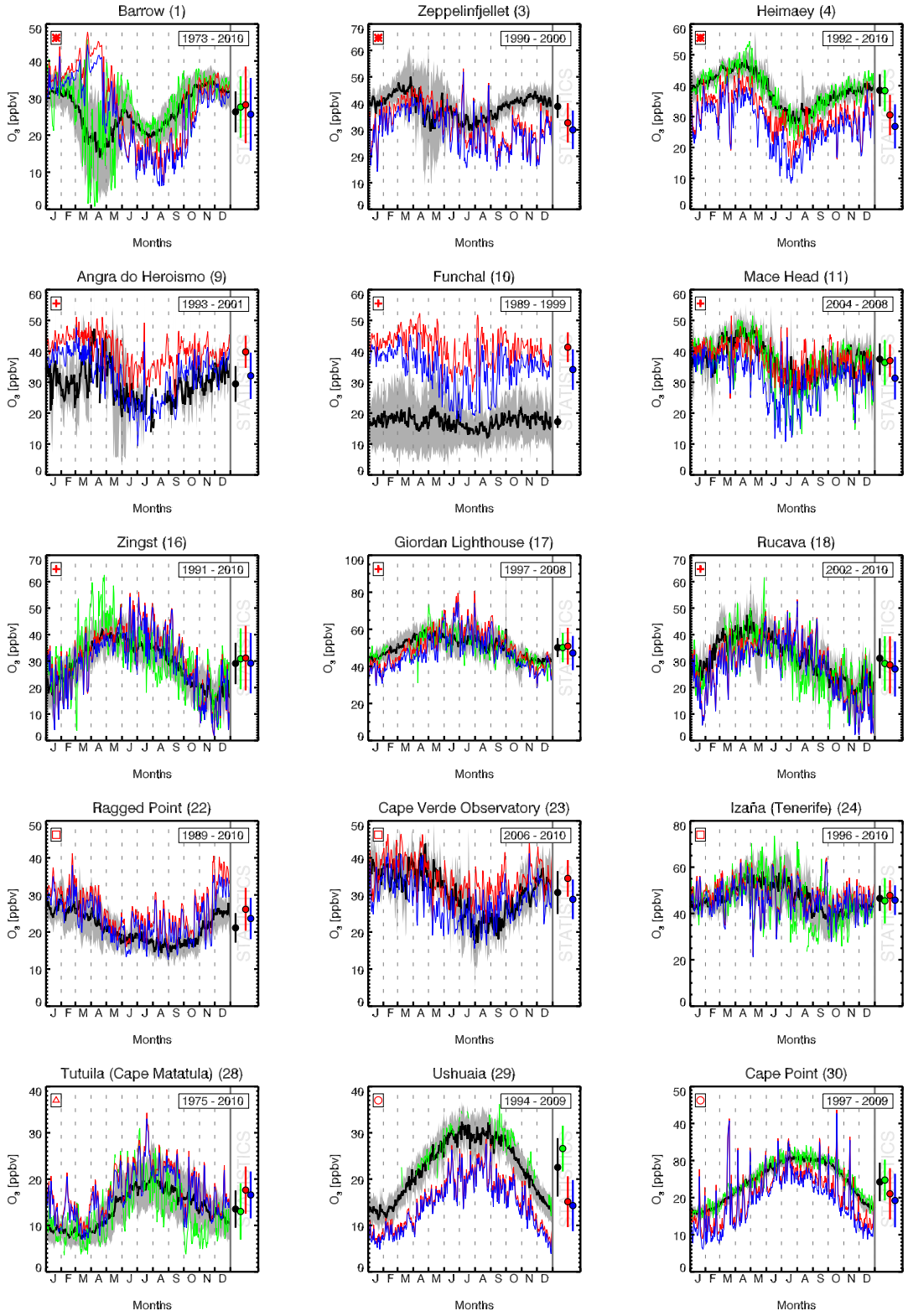

FIGURE 4.11: Same as figure 4.8 but for O_3 in 2005.

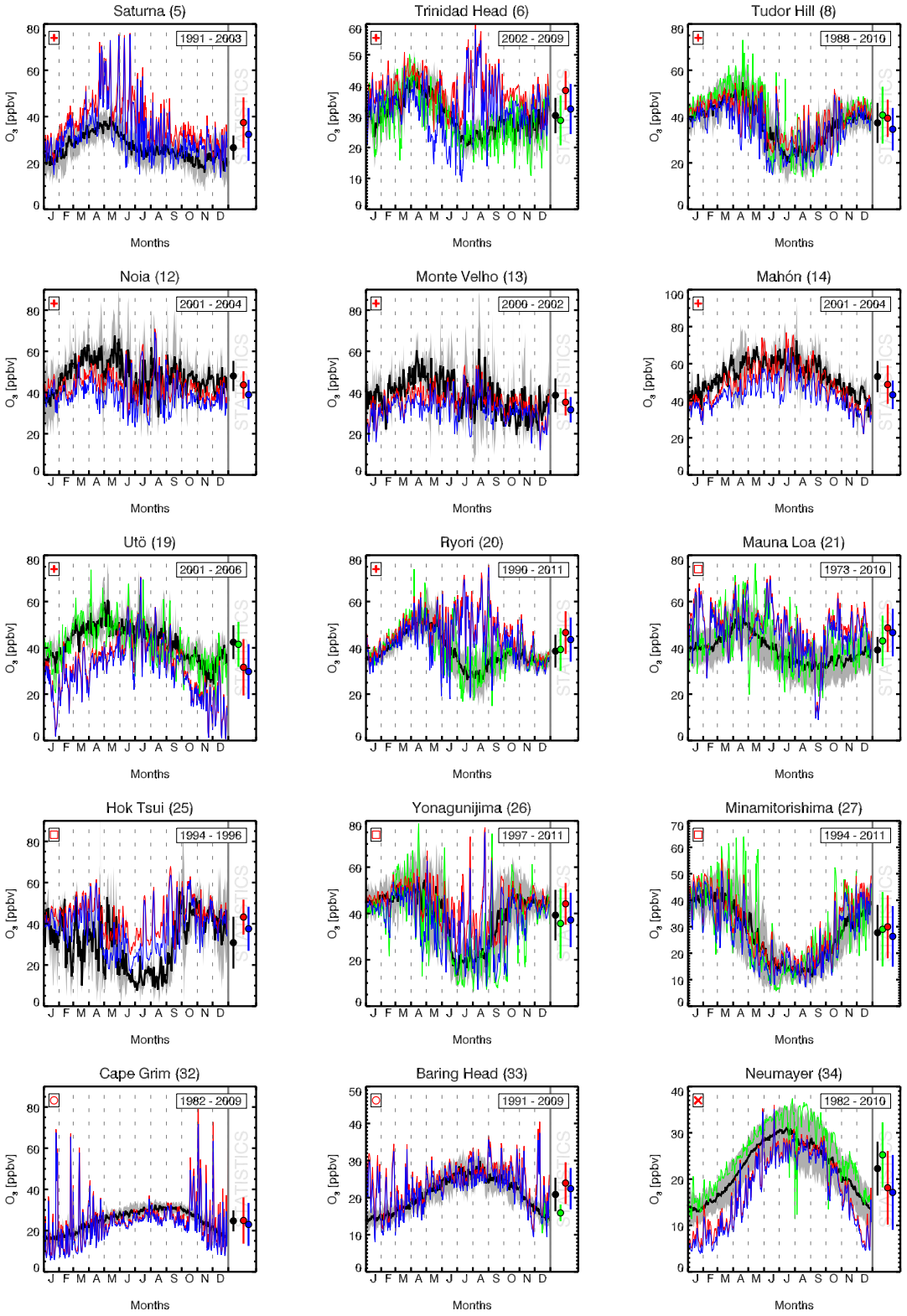

FIGURE 4.11: Figure 4.11 continuing.

4.3.2 Comparison with WOUDC data

Monthly comparisons between MOZART-4 output and data from the selected WOUDC stations in 2000 are shown on figure 4.12. MOZART-4 performs well at the surface (1000 hPa to 800 hPa) where correlation coefficients are all above 0.83 for the 6 latitudinal regions (the minimum value being in the Northern Tropics). Absolute differences between the model and WOUDC mean values range between -3.0 ppbv and 7.7 ppbv which translate into a [-12.7%, 25.4%] relative difference range. The minimum and maximum values are found in the Antarctic region and in the Northern Tropics respectively. In addition, comparisons at the surface also show that the model underestimates O_3 concentrations in the Northern and Southern polar regions as well as in the Southern mid-latitudes while it overestimates them in the other regions. In the 750 hPa to 500 hPa pressure band, most latitudinal regions see their correlation coefficients drop by a few points except in the Northern tropics where it increases by 1.2%. However, these correlation coefficients remain larger than 0.70, emphasizing the model's skills. Moreover, mean differences decrease in most regions apart from the Arctic where it gains 2.1 ppbv and in the 60°S-30°S region where it increases by 4.2 ppbv. Since O_3 concentrations increase with altitude, one may wonder if this result holds in terms of relative differences. It only does in the 60°S-30°S region where values change from -6.5% to -16.3%. This change results from discrepancies in winter during which the WOUDC data exhibits peaks whereas MOZART-4 displays a smoother signal. In the 500-300 hPa pressure band, the picture looks quite different. Firstly, standard deviations are clearly much larger in the upper troposphere. This results from the proximity with the tropopause where O_3 gradients are large and might not be well represented by the model [Horowitz et al., 2003]. Secondly, the correlation coefficient is only 0.2 in the Antarctic, owing to large discrepancies in summer. However, correlation coefficients are all above 0.6 in the rest of the latitudinal regions. Absolute differences in mean values lay between -5.6 ppbv and 2.6 ppbv while relative differences remain between -11.1% and 4.8%. It is interesting to note that observations in the Northern mid-latitudes suggest that the model fails to capture the O_3 spring maximum above 750 hPa.

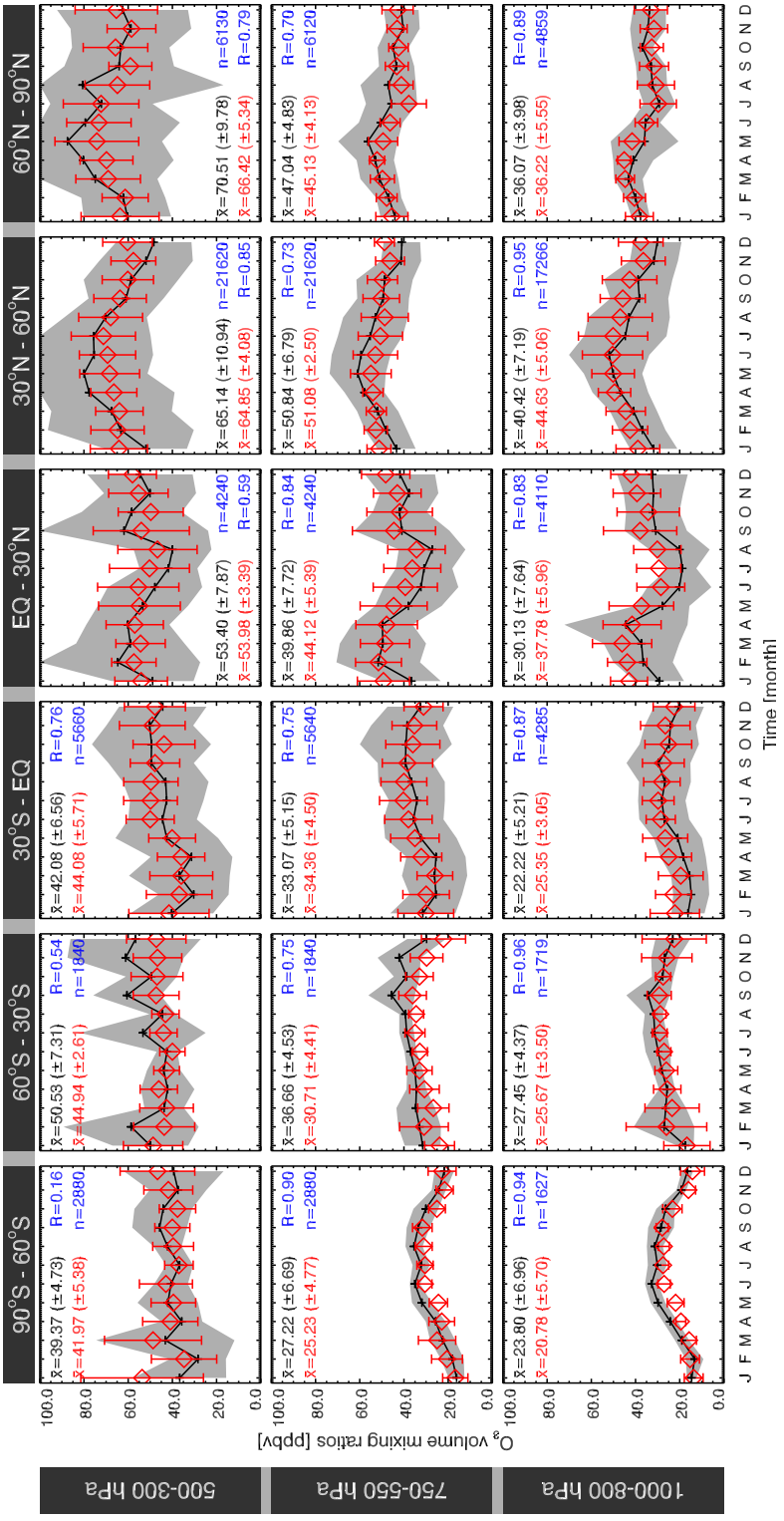

FIGURE 4.12: Comparison of O_3 volume mixing ratios for different clusters of altitude and latitude ranges between ozonesonde measurements and MOZART-4 in 2000. Averages of the WOUDC data are plotted in black whereas results from the MOZART-4 simulation with all emissions are displayed in red. The grey areas represent the 1-σ standard deviation of the measurements and the red bars represent those of the simulation results. WOUDC and MOZART-4 annual means are provided together with their standard deviations (in brackets) for each cluster. Correlation coefficients between the two signals are also given.

4.3.3 Comparison with aircraft data composites

4.3.3.1 TOPSE campaign in 2000

With measurements taken in spring in the Northern midlatitudes and the polar region over several altitude levels, the TOPSE campaign is extremely useful to assess the model's ability to simulate O_3 and its precursors (see figure 4.3). Comparisons between measurements from this campaign and MOZART-4 data are shown on figures 4.13 and 4.15.

Starting to look at oxidised nitrogen species (NO_x, NO_y, HNO_3 and PAN), the seasonal and vertical variabilities are quite well reproduced by MOZART-4. Nevertheless, one may notice a clear recurrent pattern: at the surface of the model and regardless of the month, these species are evidently overestimated in the Boulder area but get closer to measurements with increasing altitude and distance from anthropogenic influence. For instance, modelled mean NO_x concentrations can be 6.3 times larger than those measured in March. A damper to this result is however the number of observations which is relatively small and ranges between 8 and 16. The rest of the concentrations simulated by the model lies generally within 1-σ of the observations except for PAN which is overestimated by up to a factor of 5 everywhere in February and March.

Regarding CO and CH_4, the model reproduces relatively well the seasonal and vertical variabilities of these two species. Modelled mean CO concentrations are overestimated at the surface of regions influenced by anthropogenic activity. For example, MOZART-4 simulated 28.6% more CO in March at the surface of the Boulder area. Everywhere else the plots suggest that the model underestimates CO concentrations but these underestimations remain relatively small (<24.0%). It is interesting to notice that standard deviations are larger at the surface of the model and decrease with increasing altitude whereas an opposite trend is exhibited in the measurements. As for CH_4 concentrations, standard deviations from MOZART-4 and observational data match well. Mean values however display an interesting

trend: the model overestimates concentrations by up to a factor of 1.2 in February whereas it underestimates them by up to a factor of 1.9 in April and May.

Simulated O_3 concentrations are overestimated by 76.7% and 88.3% in April at the surface of the Churchill and Thule regions, respectively. This discrepancy is very likely to arise from the omission of halogen mechanism in the model as explained in section 4.3.1. Apart from these overestimations, the modelled O_3 concentrations are below the measurements with maximum decrease of -42.8% found in May in the Churchill region at 6.5 km. This result, in turn, suggests that the UT/LS may not be very well represented in the model. Standard deviations are smaller in the model which is expected given its climatological nature. In addition, seasonal and vertical variations are well reproduced by MOZART-4.

The rapid decrease of H_2O with height and its increase as the spring season unfolds is moderately well simulated by MOZART-4. At 0.5 km, the model calculates water vapour concentrations up to 2.3 times larger and 23% smaller. The largest difference is found in May in the region of Boulder. The region above is in better agreement with measurements since relative differences lie between -28.2% and 26.6%. However, at 4.5 km and 6.5 km, modelled values move away from the measurements again. The largest difference occurs in May in the Churchill region at 6.5 km where a factor of 4.9 separates modelled values and measurements.

H_2O_2 is another gas species clearly influenced by anthropogenic activity. However, this influence is much more pronounced in MOZART-4 results than in the measurements. In fact, MOZART-4 overestimates concentrations of this species everywhere except at the surface of the Thule region in February where the mean difference equals -56%. The seasonal variability is not very well reproduced by the model either. For instance, H_2O_2 concentrations increase by more than a factor of 4 between February and May at the surface of the Boulder region whereas only a factor of 1.8 is seen in measurements. Consequently, relative mean differences increase as spring develops and can be as large as 1291% (in May in Churchill at 6.5 km).

The photolysis rates of NO_2 and O_3 calculated by the model are generally smaller than those measured during the TOPSE campaign. Indeed, for both photolysis rates 40 values out of 48 are smaller over the 3 areas, 4 altitudes and 4 months. The largest differences are found in both cases at 6.5 km in the Arctic region. However, results show that O_3 photolysis rates can be 2.6 times larger in MOZART-4 than in measurements at the surface of the boulder area in March. Interestingly, differences in NO_2 photolysis rates between model data and measurements are increasing with increasing latitude whereas the model simulates an opposite trend for O_3 photolysis rates.

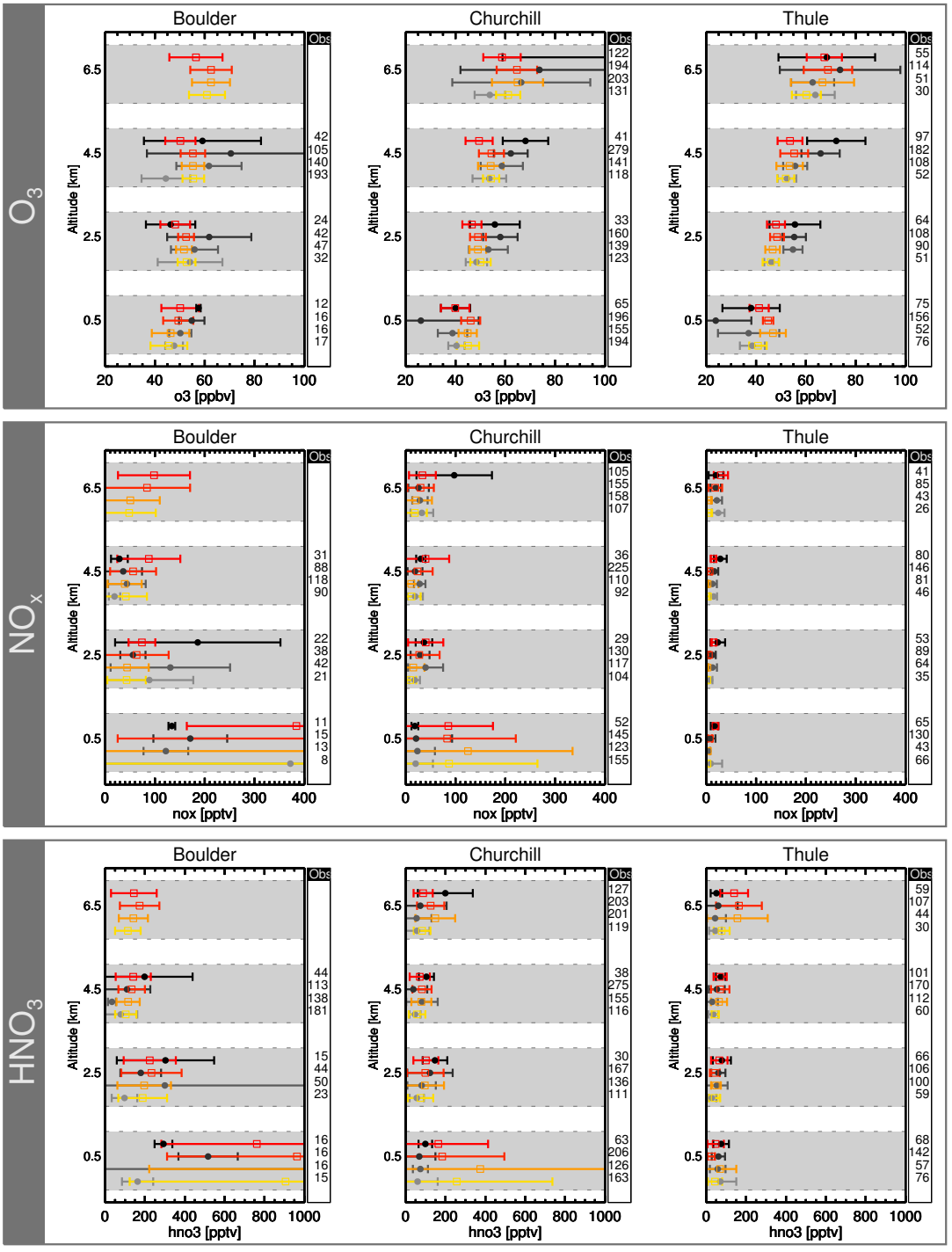

FIGURE 4.13: Comparison of O_3, OH, NO_x, NO_y, HNO_3, PAN concentrations between measurements taken during the TOPSE campaign and MOZART-4. For each of the 4 altitudes presented on plots, the 4 monthly averaged concentrations and standard deviations from the TOPSE campaign (grey scale) and MOZART-4 (yellow-to-red color scale) are displayed. Symbols and lines at the bottom of an altitude band correspond to the month of February while upper ones correspond to the month of May. Those in between correspond to the months of March and April and are placed in chronological order.

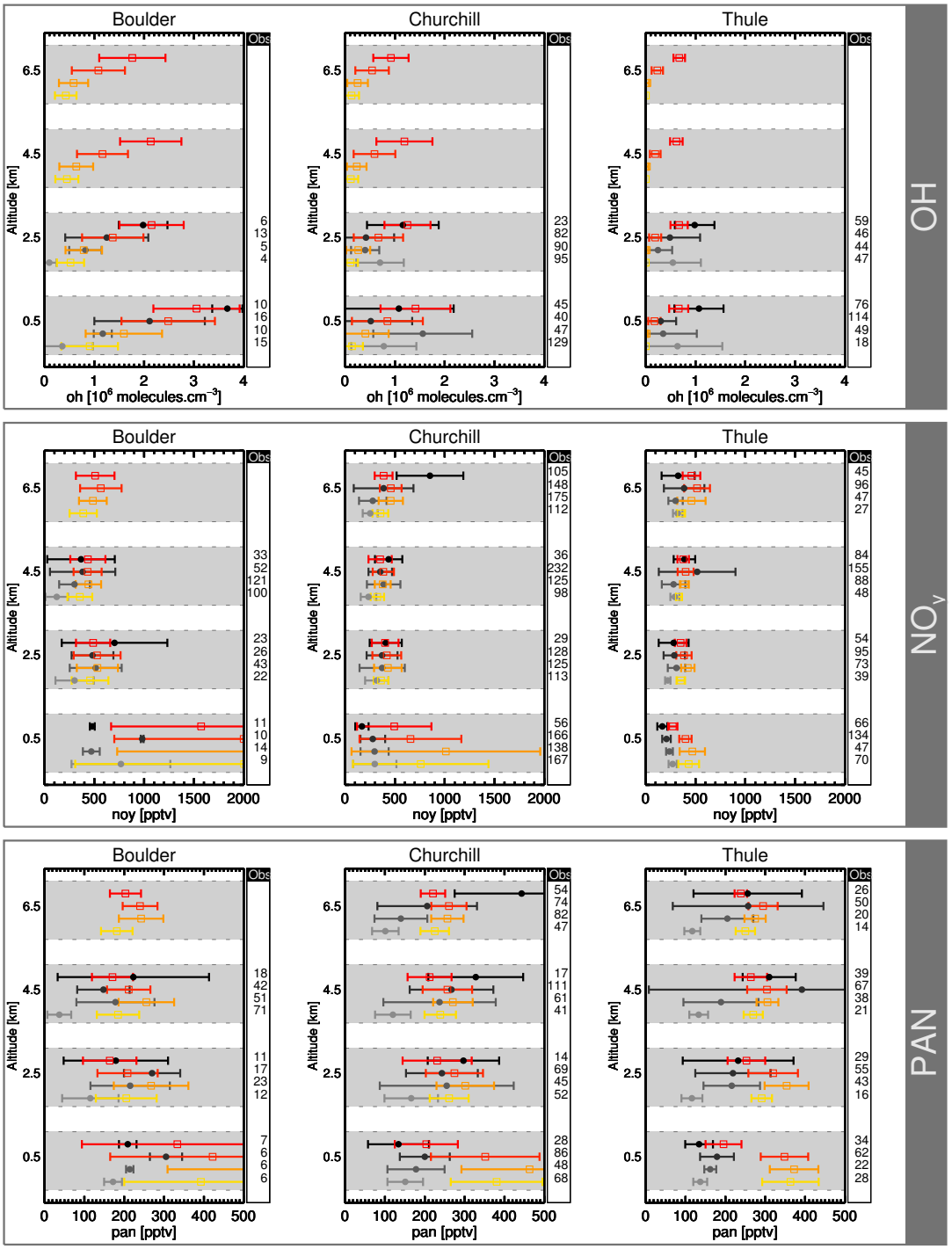

FIGURE 4.14: Figure 4.13 continuing.

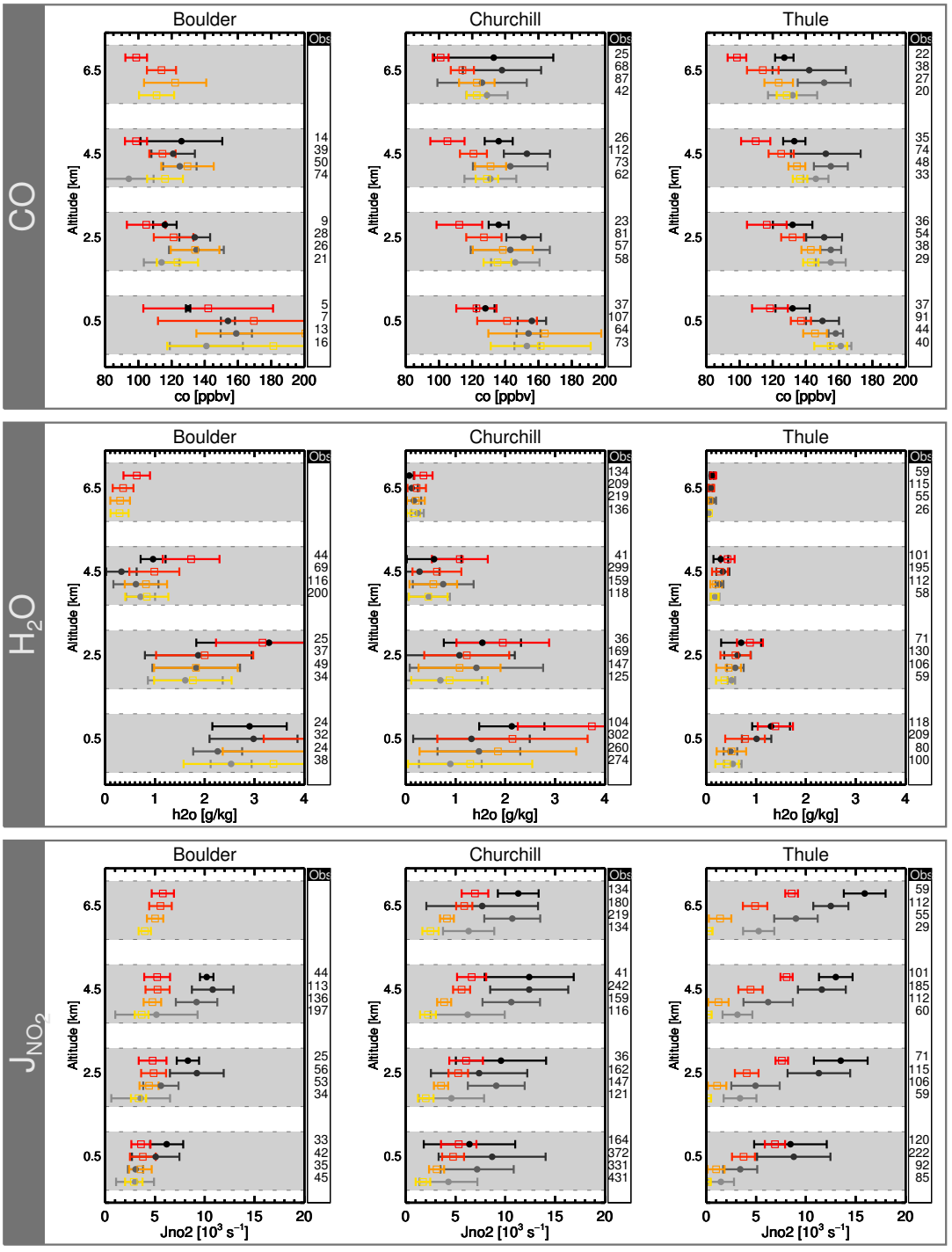

FIGURE 4.15: Comparison of CO, CH_4, H_2O, H_2O_2 concentrations as well as JNO_2 and $JO(^1D)$ photolysis rates between measurements taken during the TOPSE campaign and MOZART-4. (Same as figure 4.13)

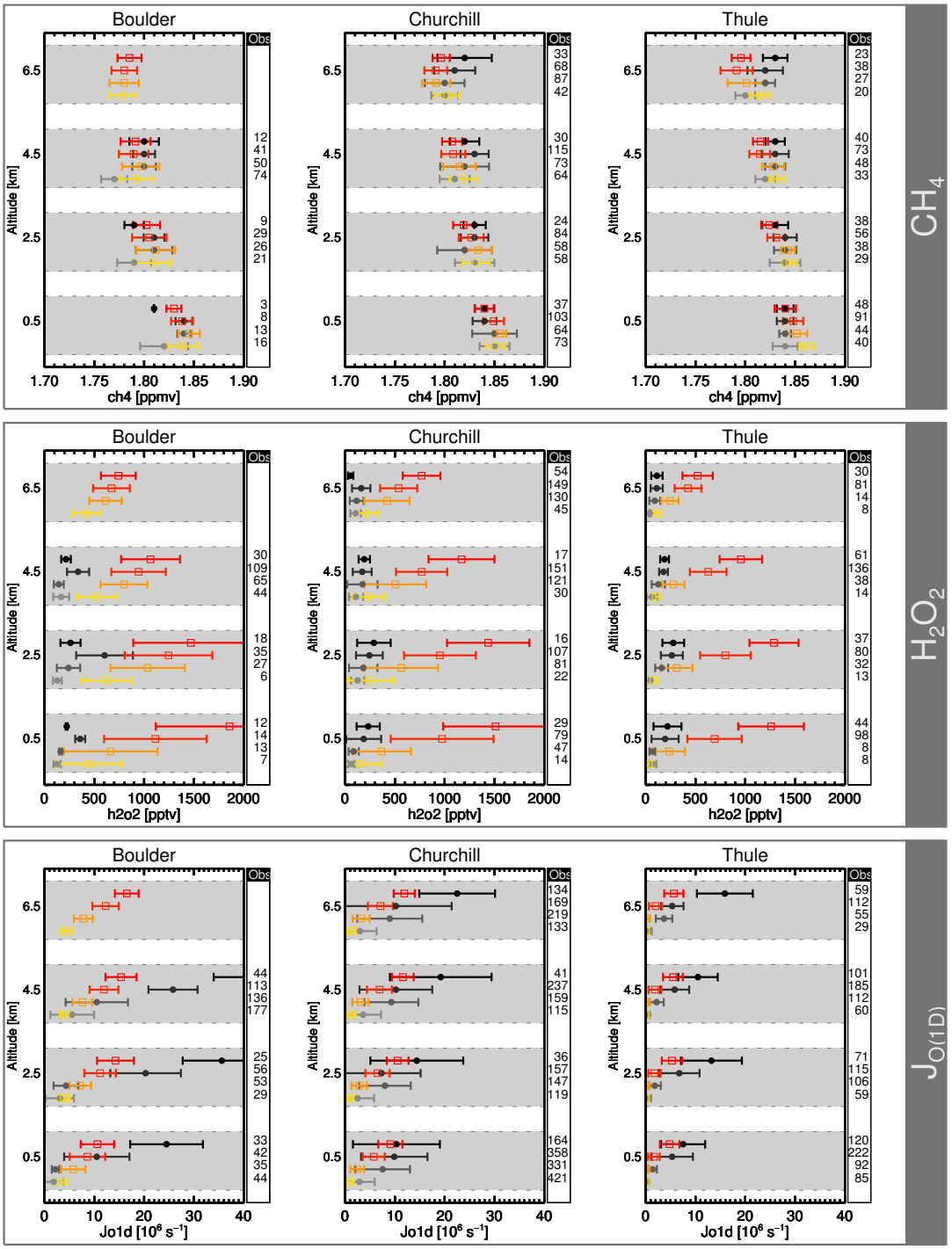

FIGURE 4.16: Figure 4.15 continuing.

4.3.3.2 Gridded climatologies

The two MOZART-4 simulations with and without shipping emissions are also compared to the gridded NO_x and O_3 climatological data produced by Emmons et al. [2000]. NO_x concentrations are shown on figure 4.17. Near the surface, NO_x levels are large with mean values ranging between 40 and 350 pptv and highly variable, especially during the winter and spring seasons, both in the MOZART-4 simulations and in the observational data. Depending on the season, NO_x levels from the simulation with shipping emissions can be closer to measurements than those from the simulation without shipping emissions. The figure shows three examples of this: in spring in the midlatitudes and in winter and summer in the tropics. In general, results from the modelling activity have a larger variability near the surface than measurements. However in the observational case corresponding to winter conditions in the tropical region, the standard deviation is as large as that predicted by MOZART-4. From 2 to 8 kilometres, NO_x concentrations and the variability linked to them are reduced both in the modelled and observed data which show a good degree of agreement between each other. Above 8 kilometres, differences become larger. In the midlatitudes, one can notice a "C-shape" which is present all year long. This could stem from lightning production or stratospheric transport. In winter, spring and autumn, MOZART-4 overestimates the concentrations of NO_x by up to about a 100 pptv in this region of the atmosphere whereas the model underestimated them by a similar magnitude in summer.

As for O_3 concentrations, they are displayed on figure 4.18. Clearly, MOZART-4 has skills in reproducing the concentrations of O_3 situated in the lower part of the atmosphere and above oceanic regions. The largest contribution from shipping NO_x emissions is found in midlatitudes in summer and has a magnitude of about 12 ppbv as reported by Eyring et al. [2007], Dalsøren et al. [2009]. MOZART-4 simulates this peak as well which in that case is much closer to the mean value of the observations. On the one hand, the UT region is subject to overestimations from the model in the midlatitudes in summer and generally in the tropics. On

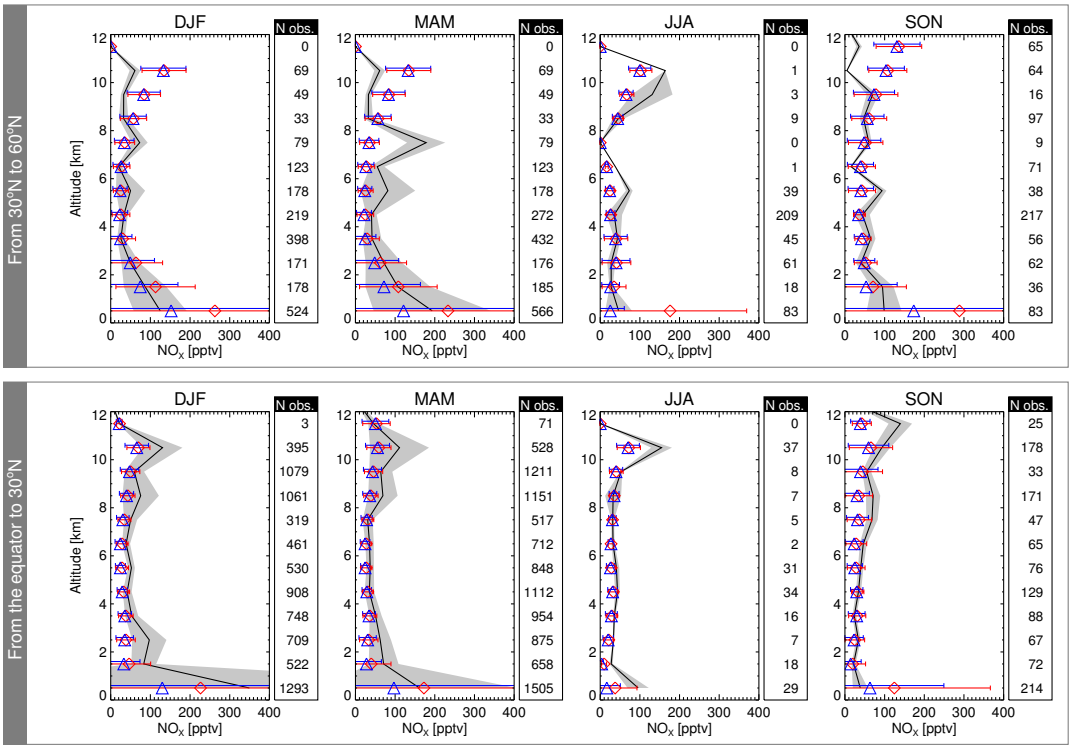

FIGURE 4.17: Comparison of NO_x volume mixing ratios between two MOZART-4 simulations (with and without shipping emissions) and observations from compiled flight campaigns [Emmons et al., 2000]. The black lines correspond to the mean value of observational data whereas the shaded areas display their standard deviations. The blue triangle and red rhombus symbols and the bars show mean values and standard deviations of the simulations with MOZART-4 respectively. The green colour is used to plot the concentrations resulting from the simulation without shipping emissions whereas the red colour is used for the simulation with shipping emissions.

the other hand, the model underestimates O_3 concentrations in the midlatitudes in winter and spring.

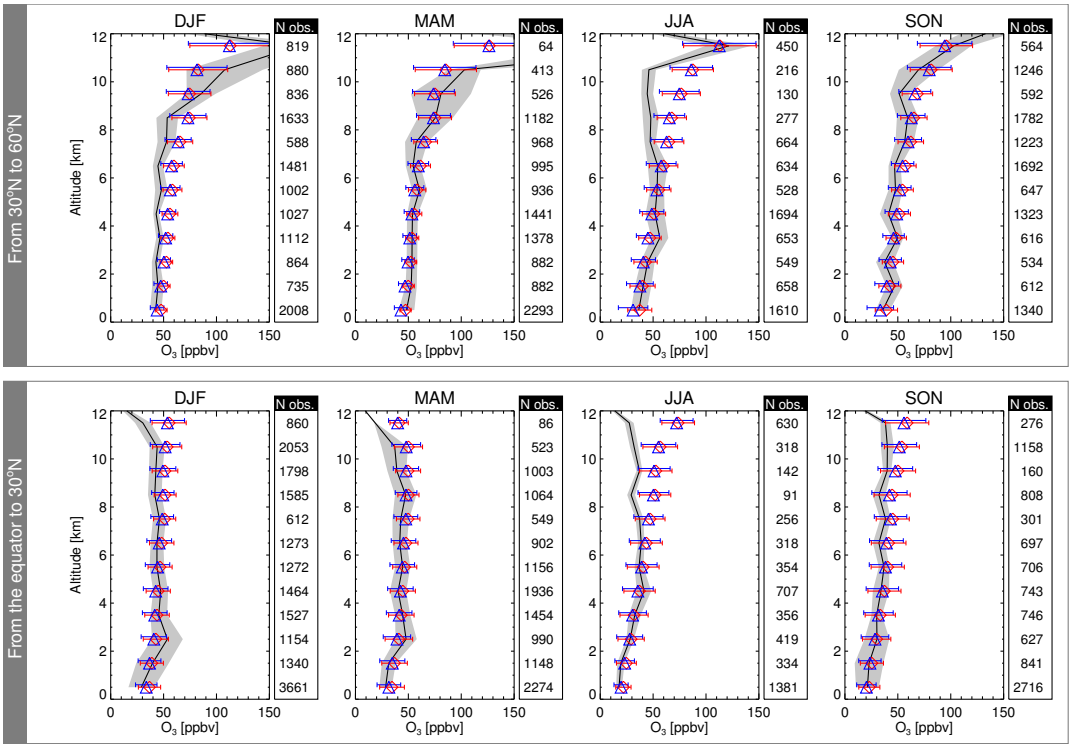

FIGURE 4.18: Same as figure 4.17 but for O_3 volume mixing ratios.

4.3.4 Comparison with TES data

The series of operations applied to the TES data and described in the methodology results in the distribution of profiles shown on figure 4.19. The regions with large areas (e.g. Atlantic and Pacific) obviously contain the greatest amounts of profiles. In 2005, the total number of profiles equal 5016, 10036, 920 and 341 for the Atlantic, Pacific, Indian and Mediterranean regions respectively. Figure 4.19 also reveals seasonal differences between the number of profiles. For instance, there are less than half the number of winter profiles in spring, but this number increases by factors of 1.3 and 1.6 in summer and autumn respectively.

Figures 4.20 and 4.21 display the mean values of TES and MOZART-4 data as well as their associated standard deviation per oceanic region, season and pressure band. Additional information is provided at the right side of each plot where the number of observations and the distribution of the averaging kernel peaks is given for each pressure band. MOZART-4 mean values and standard deviations are in good agreement with those from TES in the lower pressure bands, especially in the Atlantic, Pacific and Indian regions where relative differences remain smaller than 10% (except in the Indian region in summer between 500 and 800 hPa). Differences are somewhat much larger in the Mediterranean region. Apart from the 5.1% difference in the 800-1000 hPa pressure band in autumn, the rest of them are all above 10%. In any cases, MOZART-4 means lie within the 1-σ standard deviation of the measurements. It is interesting to notice that averaging kernels in the bottom pressure band peaks more than 50% of the time above 800 hPa. This indicates that the values of the lower pressure band are not entirely representative of this layer but of higher vertical levels.

In the 300-500 hPa pressure band, differences increase substantially in the Atlantic, Indian and Mediterranean regions for all seasons. In the Atlantic, mean values from MOZART-4 are overestimated by 12% and 19% compared to TES values in winter and summer respectively. In the Indian and Mediterranean regions, the change is even larger. Mean values calculated by MOZART-4 in the Indian ocean are underestimated by a minimum of -26% and up to -37% whereas

relative differences range between 14% and 31% in the Mediterranean which sees a significant overestimation.

Interestingly, all mean values calculated from MOZART-4 data are underestimated in the 100-300 hPa pressure range. The largest differences are found in the Indian regions with values smaller than -73% while the smallest differences are located in the Mediterranean region, the smallest being equal to -35%. In the Atlantic and the Pacific, these differences range between -50% and -40%. This effect can be again explained by the large O_3 gradients located in the UT/LS which may not be accurately represented in the model.

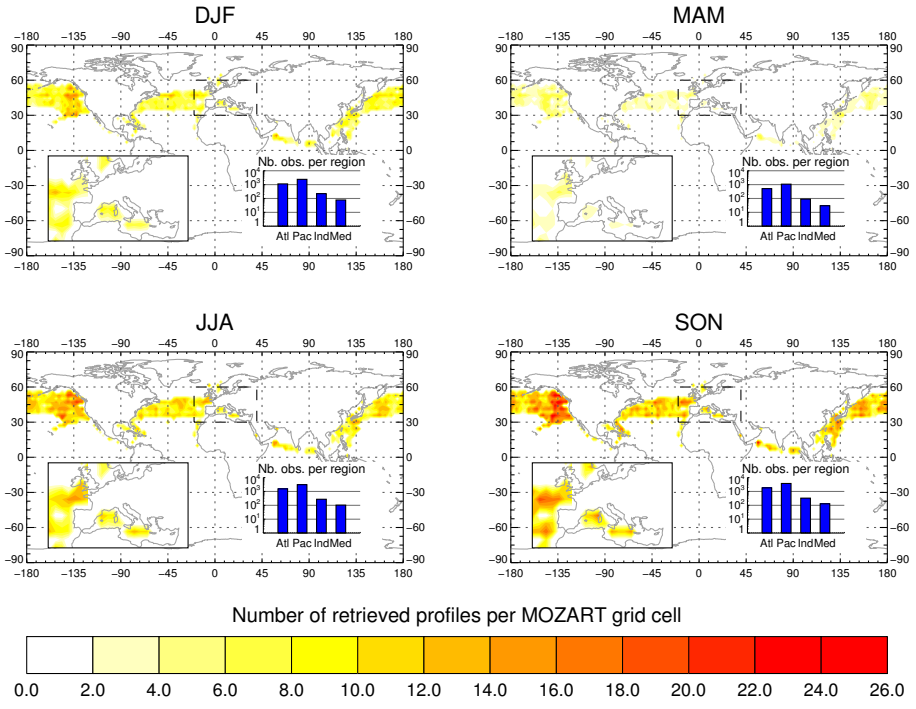

FIGURE 4.19: Maps showing the number of mask-filtered TES profiles in the 4 seasons. The 4 bottom right insets display the total number of profiles per oceanic region for a given season.

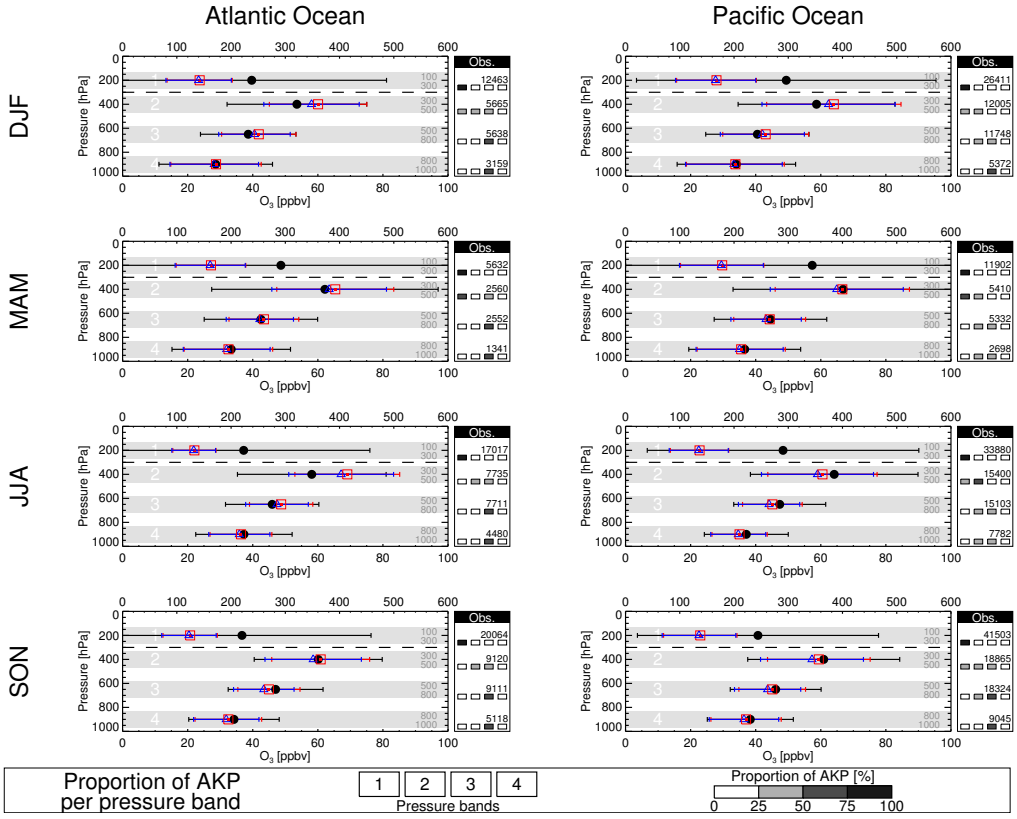

FIGURE 4.20: Means and standard deviations of O_3 volume mixing ratios monitored by TES and resulting from the two MOZART-4 simulations run in 2005 in the 4 pre-defined oceanic regions. Data have been grouped by pressure bands (light grey areas). TES data are shown in black while MOZART-4 data are displayed in red and blue for the WS and NS simulations respectively. The dashed grey lines departing from the TES means indicate the mean of the averaging kernel peaks for a given pressure band.

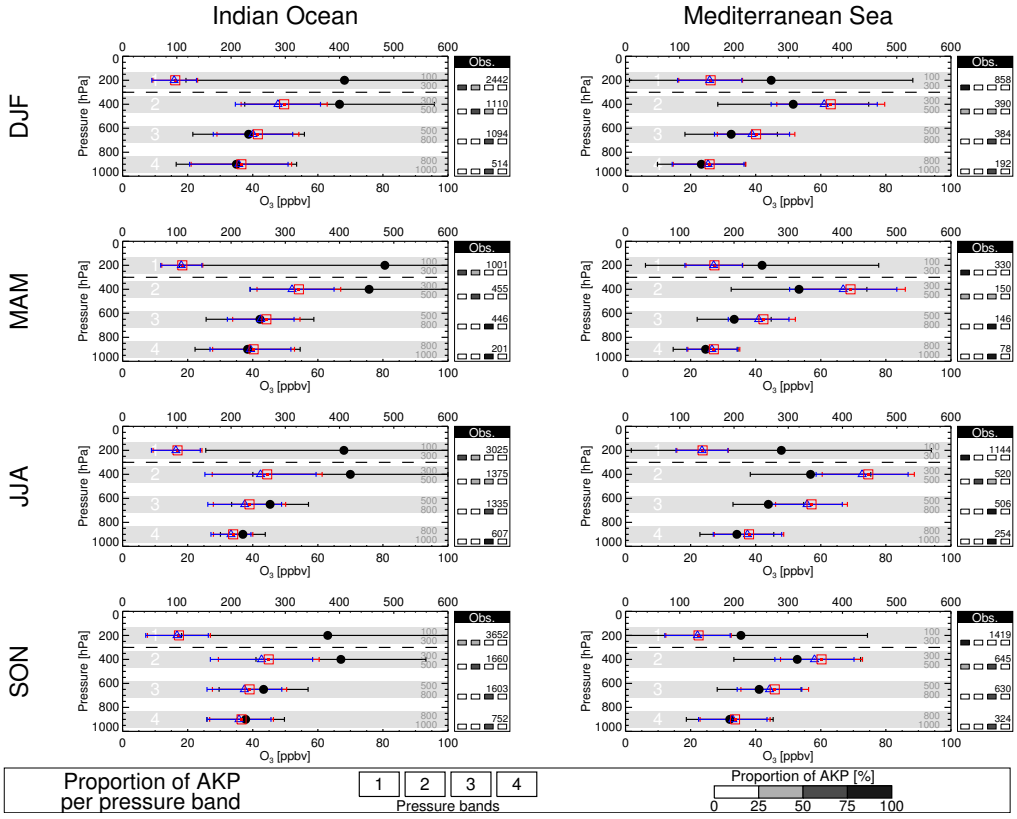

FIGURE 4.21: Means and standard deviations of O_3 volume mixing ratios monitored by TES and resulting from the two MOZART-4 simulations run in 2005 in the 4 pre-defined oceanic regions. Data have been grouped by pressure bands (light grey areas). TES data are shown in black while MOZART-4 data are displayed in red and blue for the WS and NS simulations respectively. The dashed grey lines departing from the TES means indicate the mean of the averaging kernel peaks for a given pressure band.

4.4 Discussion

In this chapter, MOZART-4 performance was assessed with respect to the NO_x-O_3-HO_x chemical system, at different temporal and spatial scales through the use of different types of measurements. Findings are here discussed by gas species, starting with NO_x, then CO and CH_4 and finally O_3.

The aircraft data composites reveal that NO_x and the other nitrogenous species are generally overestimated by up to one order of magnitude at the surface of the model when shipping emissions are included, especially in regions influenced by strong anthropogenic activity (Northern midlatitudes). However, modelled values lie within 1-σ standard deviation of the measurements in most cases. In the Northern tropics, simulations including shipping emissions have a surface NO_x mean in better agreement with observations. In the free and upper troposphere, NO_x differences between simulations with and without shipping emissions are small. The larger NO_x concentrations near the surface are likely to stem from the PBL mixing scheme that tends to trap atmospheric compounds in the PBL [Horowitz et al., 2003]. Interestingly, results from Eyring et al. [2007] were in disagreement with previous findings from Kasibhatla et al. [2000] and Davis et al. [2001]. Eyring et al. [2007] commented that the dataset they used contained more observations and was therefore more robust which is true. However, it should be reminded that most of the aircraft data composites are located in the Pacific region where concentrations of NO_x computed in the multi-model study were small.

Model comparison with WDCGG data suggests that there is a 10 ppbv to 21 ppbv bias in the simulated CO concentrations in Southern hemisphere. Similar biases of 14 ppbv and 26 ppbv were previously simulated with MOZART-4 at the South Pole and Cape Grim stations respectively [Emmons et al., 2010b, see figure 5]. These biases were assumed to be attributed to either large biomass burning emissions included in the GFED-v2 fire emission inventory or simulated OH concentrations. An interesting aspect of the CO concentrations simulated in this study is their great daily variability which can sometimes exhibit peaks of more than 200 ppbv. These large peaks were found to be associated with

low PBL height which leads to concentration build-up. Emmons et al. [2010b] did not reported such behaviour but they were using monthly means instead. In the northern hemisphere, the WDCGG and TOPSE datasets provide some evidence that the global model overestimates CO concentrations over the surface of the midlatitudes. This effect was not specifically simulated in Emmons et al. [2010b] where biases ranged between -5 ppbv and 4 ppbv across 8 years. In the free troposphere, the comparisons with TOPSE data suggest however that CO concentrations are underestimated. This underestimation remains consistent not only with the MOZART-4 versus MOPITT comparison performed by Emmons et al. [2010b, see figure 6] but also with the multimodel study carried out by Shindell et al. [2006] that revealed all 26 models were largely underestimating CO concentrations in that region. Regarding CH_4 concentrations, both MOZART-4 and TOPSE data are in good agreement with each other which is expected since CH_4 is prescribed at the surface of the model and has a longer lifetime compared with the duration of model simulations.

Apart from O_3 concentrations in the Arctic region, the model performs relatively well everywhere else. Both the WDCGG and the WOUDC datasets highlight that the values calculated by the model in the Southern hemisphere (away from anthropogenic activity) are underestimated by more than 10%. An interesting result is that the model does not necessarily perform less well when shipping emissions are included. For instance, O_3 concentrations calculated in the simulation with shipping emissions are about 10 ppbv closer to observations in summer in the Northern midlatitudes. In contrast, results at the WDCGG station of Angra do Heroismo suggests that the model does overestimate O_3 concentration at this location during summer. Modelled values at the location of the Mace Head station which are are however in good agreement which can be explained by the longer distance from the main shipping lanes. In the free and upper troposphere, the WOUDC dataset and TOPSE campaigns emphasize the fact that the model underestimates concentrations in spring in the Northern midlatitudes. Nonetheless, the positive difference between the model and the WOUDC dataset in this region in winter and autumn is in disagreement with comparisons between MOZART-4 and TES

data. It is possible that the tropospheric model simulates the tropopause location and the stratospheric-tropospheric O_3 exchange in a different way compared with what the satellite captures. Furthermore, TES measurements in the troposphere have been found to be biased by 5% to 15% [Richards et al., 2008] and stratospheric column have been reported to be biased by 4 DU [Osterman et al., 2008]. The juxtaposition of MOZART-4 and TES data revealed that the model performs however well in the free troposphere above the main oceanic regions affected by intense shipping activity. It is also important to bear in mind that O_3 concentrations are not accurately represented in the Arctic region since no halogen chemical mechanism has been taken into account in the model as revealed by comparisons with WDCGG data and aircraft data composites.

In addition, the TOPSE campaign suggests that OH, H_2O and H_2O_2 are overestimated in the midlatitudes over North America by MOZART-4.

Depending on the dataset used for comparison and the location considered, the global model provides a more or less reliable picture. This is, however, expected since some of the grid boxes of a large-scale model such as MOZART-4 may contain several types of lands and orography and may therefore be representative of a mixing of different conditions. Conversely, monitoring instruments based at ground stations may capture more local characteristics and therefore, are unable to provide background. In addition, most seasonal and vertical variabilities were well reproduced by the model. More MBL observations with various instruments would be required to perform a more robust comparison of model against measurements. Overall, MOZART-4 performs well at the global scale which is what is expected from a global model and what is required for the analysis of shipping perturbations.

Chapter 5

MOZART-4's ability to represent shipping perturbations

In this chapter, MOZART-4 was further assessed by testing its ability to represent shipping perturbations. The following results were found:

- MOZART-4 simulates shipping perturbations of NO_x, O_3, OH and CH_4 in good agreement with previous studies.
- The simulated shipping O_3 perturbation is larger in the free and upper troposphere (1.0 ppbv (+25%) compared with [Eyring et al., 2007]).
- The modelled shipping CH_4 lifetime perturbation is at the upper end of the range of values published in the literature (-0.29 year which is more than a factor of 2 compared with [Eyring et al., 2007]).
- Low PBL height in the North Pacific ocean leads to large NO_x concentrations in summer.
- The O_3-tagging method is currently not suitable for the analysis of shipping perturbations since its use leads to unrealistic O_3 volume mixing ratios in the atmosphere. The simulated shipping O_3 maximum is about

650 ppbv at the surface in summer against approximatively 20 ppbv in the 100%-removal case.

5.1 Introduction

As mentioned in chapter 2, a few studies have already looked at the global shipping perturbations of the chemical NO_x-O_3-HO_x system by making use of global atmospheric models. The first one to highlight the importance of impacts of shipping NO_x emissions on O_3, OH and CH_4 was carried out by Lawrence and Crutzen [1999] with the help of the MATCH-MPIC model in conjunction with the EDGAR v2 emission inventory [Olivier, 1996]. This study was followed by two others that focused exclusively on the performance of the GFDL model to simulate NO_x concentrations resulting from shipping emissions [Kasibhatla et al., 2000, Davis et al., 2001]. The authors noticed large NO_x overestimations and attributed them to the misrepresentation of in-plume chemistry, although background NO_x levels were also overestimated in their model as revealed in Davis et al. [2001]. Later on four more studies analysed shipping perturbations of NO_x, OH, O_3 and CH_4 in more detail [Endresen et al., 2003, Dalsøren et al., 2007, Eyring et al., 2007, Dalsøren et al., 2009]. Even though different analysis of shipping impacts on tropospheric composition are crucial, the use of different models, meteorological data and emission inventories makes it difficult to compare them between each other. This difficulty is sometimes enhanced by the use of different metrics to analyse results. In order to palliate this problem, Eyring et al. [2007] (E2007 hereafter) performed a multi model analysis with 10 models using the same emission inventory for anthropogenic and biomass burning emissions (EDGAR v3.2 [Olivier and Berdowski, 2001]) which has the merit of providing robust statistics on shipping perturbations. More recently, Hoor et al. [2009] developed the concept of small perturbation as part of a multimodel study to avoid the non-linear effects of chemistry that may become significant when a total removal of shipping emissions is applied. This approach was employed to allow for a direct comparison

of perturbations from other transport modes (road and aviation) and its authors claim that it leads to more realistic emission changes. They showed that absolute differences arising from the use of the small-perturbation concept lead to decreases in the tropics and Southern hemisphere (up to -0.4 ppbv) and to increases in the Northern mid-latitudes and polar region (up to 0.3 ppbv). The shape of shipping perturbations remain however similar to those reported in studies applying a total removal of shipping emissions [Endresen et al., 2003, Dalsøren et al., 2007, Eyring et al., 2007, Dalsøren et al., 2009]. Koffi et al. [2010] and Hodnebrog et al. [2011a] made use of this approach to simulate future scenarios of emissions from different transport sectors. Interestingly, the concept of O_3 tagging which consists in duplicating the NO_x-O_3-HO_x chemical system to analyse impacts of a particular NO_x emission sector on atmosphere composition has never been used to study impacts of shipping NO_x emissions [Lamarque et al., 2005, Pfister et al., 2006, Hess and Lamarque, 2007]. In this chapter, MOZART-4's ability to simulate shipping perturbations of tropospheric composition is assessed by using the different methodologies listed above and comparing the results with previous findings from the literature.

5.2 Methodology

MOZART-4 was set-up as in chapter 4 with the same meteorological and emission data (NCEP-Reanalysis 2000 and ACCMIP emission inventory) in order to analyse shipping perturbations of NO_x, O_3, OH and CH_4. However, for the purpose of offering a better view of the global model's ability, three more cases were computed. In one case, shipping emissions in ACCMIP were replaced by those of EDGAR v3.2 in order to compare model results with the multimodel assessment carried out by Eyring et al. [2007]. Shipping emission data from EDGAR v3.2 in 1995 were thus extrapolated to 2000 using a 1.5% growth as in the multimodel study. This calculation yields a total annual shipping NO_x emissions of 3.14 Tg(N)/yr against 5.43 Tg(N)/yr in ACCMIP. Shipping emissions from these two inventories are plotted on figure 5.1. Results from this case were interpolated on a 5°x5°

TABLE 5.1: MOZART-4 simulations performed in this chapter.

#	Simulation	Comment
1	Sref	default all emissions (ACCMIP)
2	Sns	no shipping emissions (ACCMIP)
3	Sspa	5% shipping emission reduction (ACCMIP)
4	Stag	O_3 tagging technique (ACCMIP)
5	Sedg	ACCMIP + EDGAR v3.2 shipping emissions

TABLE 5.2: Shipping perturbation cases calculated from the simulations in table 5.1.

#	Cases	Operation
1	100%R-EDGAR	Sedg - Sns
2	100%R-ACCMIP	Sref - Sns
3	5%R-ACCMIP	20x(Sref - Sspa)
4	O_3 tagging ACCMIP	Stag

horizontal grid and 19 vertical levels as in E2007. In another case, shipping emissions were reduced by 5% and results were then multiplied by 20 to allow comparison with studies following the small-perturbation concept of Hoor et al. [2009]. Finally, the O_3 tagging technique was configured to track shipping NO_x emissions and their resulting perturbations. The duplicated photochemical system has a total of 11 photolysis reactions and 87 chemical reactions. Heterogeneous reaction as well as dry and wet depositions are also taken into account. Lamarque et al. [2005] estimated that this method can reproduce O_3 production with an accuracy better than 95% on a monthly basis. The O_3 tagging code was provided by Dr. J.-F. Lamarque on the 6^{th} of October 2010.

The list of simulations performed in this chapter are provided in table 5.1. A total of four shipping perturbations stem from these simulations (table 5.2).

In the next section, results are presented by gas species, starting with NO_x, continuing with O_3 and OH and finishing with CH_4. For each species, shipping perturbations resulting from simulations with and without the EDGAR emission inventory are first compared with E2007. Results from the cases following the three different methodologies (total shipping emission removal, 5% shipping emission removal and O_3 tagging) are then presented and compared with each other as well as with results from the literature.

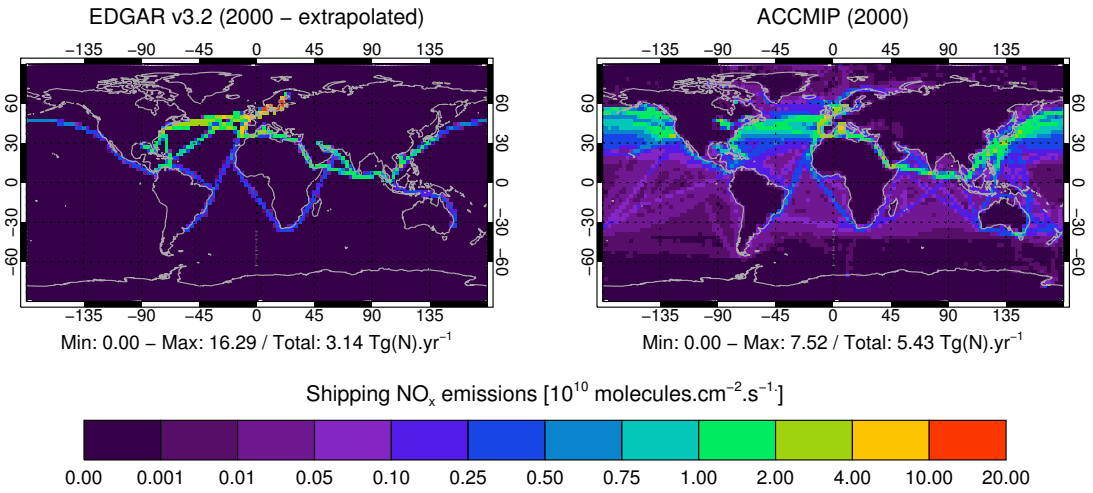

FIGURE 5.1: Annual mean of shipping NO_x emissions in the EDGAR v3.2 and ACCMIP emission inventories in 2000 on a T42LR horizontal grid.

5.3 Results

5.3.1 Nitrogen oxides

Since NO_x has a short lifetime of 1 to 2 days in the MBL [Kasibhatla et al., 2000], NO_x perturbations induced by shipping emissions are large near the ship lanes and rapidly fade out with distance. It is therefore legitimate to focus on the surface level of the model to make comparisons. A comparison of the case with EDGAR v3.2 emissions with E2007 is first presented. Then, the three other methodologies employing ACCMIP shipping emissions are analysed.

5.3.1.1 Comparison with E2007

NO_2 shipping perturbations calculated by MOZART-4 with EDGAR v3.2 emissions in January and July are plotted against data from the multimodel study on figure 5.2. On the one hand, the model reproduces well near-surface NO_2 concentrations resulting from shipping emissions even though comparisons from the plots suggest that these concentrations are larger by a factor of 2 in the Atlantic and

Pacific oceans and smaller by more than a factor of 4 in the Baltic sea. On the other hand, relative differences depict a different story. Since NO_2 differences are larger than 106% in the main ship lanes and over much of the Northern oceanic regions, the plots indicate that MOZART-4 has very low background NO_2 levels in oceanic regions compared with the multimodel study.

5.3.1.2 Comparisons between the three methodologies

Shipping perturbations resulting from the 100% and 5% removals of shipping emissions as well as those resulting from the O_3 tagging technique are displayed on figure 5.3. In the rest of this chapter, results from these three cases will be presented in the same order. Absolute differences are in very good agreement between the three cases. For instance, the largest NO_2 concentrations peak at 2.53 ppbv, 2.62 ppbv and 1.91 ppbv in January in the three cases and are located in the Mediterranean sea near the port of Marseilles. In all cases, ratios between the two simulations are very small in this region and indicates that this area is already saturated in NO_x. In July, shipping NO_x emissions are largest in the North Pacific where the model does not appear to remove NO_x as efficiently as everywhere else. This results in very large concentrations of NO_x in this region which reach 2.53 ppbv, 2.91 ppbv and 3.22 ppbv off the Northern coast of Japan. The largest ratio is found in the middle of the North Pacific at latitude 44°N and equals 598, 537 and 1309. These large values are consistent with those reported by Lawrence and Crutzen [1999] who found that NO_x concentrations are enhanced by more than a factor of 200 in the main ship lanes but do not agree with more recent studies [Dalsøren et al., 2007, Eyring et al., 2007, Dalsøren et al., 2009]. This could indicate that the MBL parameterisation in MOZART-4 tends to trap molecules at the surface, since the model used by Lawrence and Crutzen [1999] is related to MOZART-4. In the rest of the oceans, including the Atlantic and the Indian Oceans, increases are similar to those recent studies. The dry deposition of NO_x is about one order of magnitude larger over land (except for deserts) then over

the oceans. This sharp gradient prevents shipping NO_x concentrations from penetrating further in land and thus, effects remain above the oceans and at coastal locations.

NO_x concentrations in the Pacific region are further investigated by plotting them against those in the Atlantic region (see figure 5.4). In the Pacific region during summertime, shipping NO_x concentrations clearly reach higher levels peaking at more than 70×10^9 molecules.cm^{-3} (corresponding to about 2.8 ppbv). One may notice from the plot at the bottom left that the MBL height in that region is often below 200 metres. This results in concentrations building-up which entails a saturation of the NO_x-O_3-HO_x chemical system and prevents as a result NO_x to be efficiently removed (see upper figures with O_3 and HNO_3).

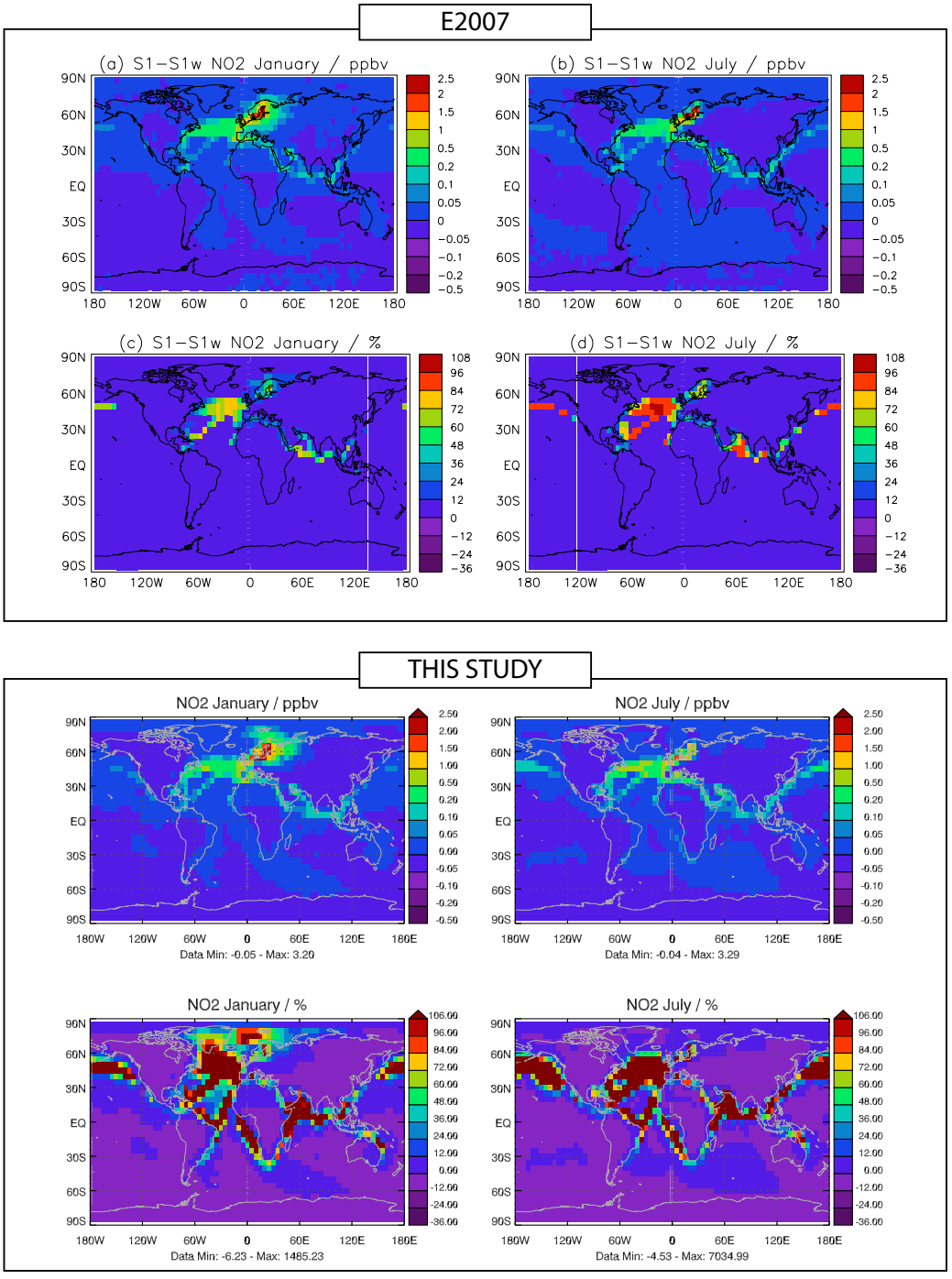

FIGURE 5.2: Comparison of near-surface shipping-induced NO_2 volume mixing ratios and ratios with respect to background NO_2 volume mixing ratios in January and July between E2007 and the present study. Note that arrows were collated to the original colour bar when values computed by MOZART-4 were found larger or smaller than the minimum and maximum levels of the colour bar.

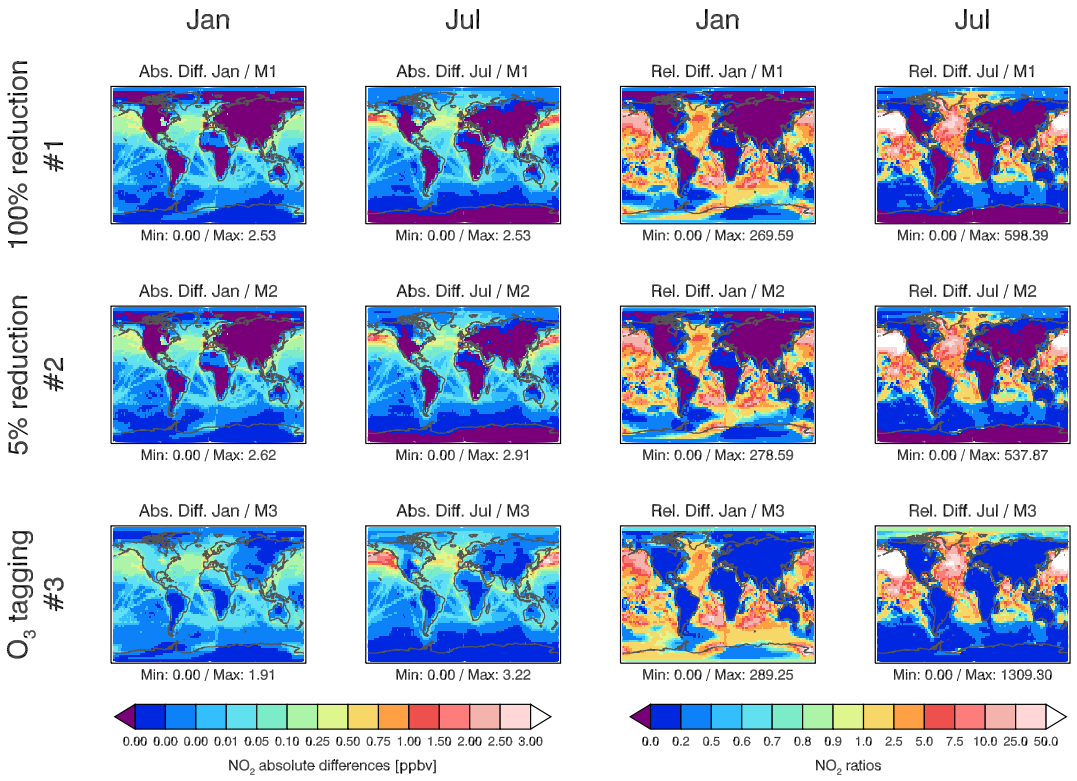

FIGURE 5.3: Near-surface shipping-induced NO_2 volume mixing ratios and ratios with respect to background NO_2 volume mixing ratios in January and July in the three cases using ACCMIP emissions. Note that the background concentrations used for the 5% removal case is the same as in the 100% removal case.

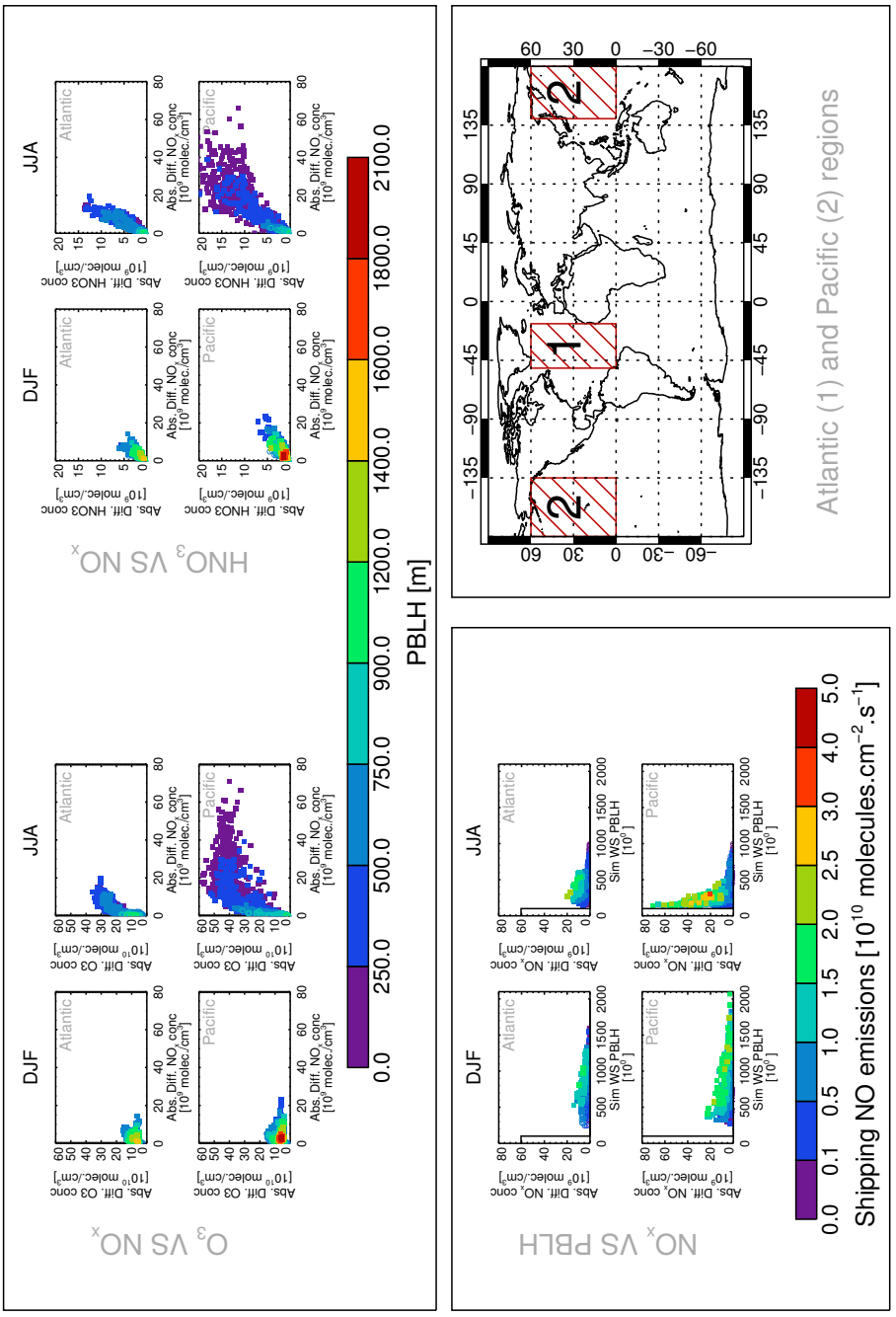

FIGURE 5.4: Correlations between NO_x concentrations and HNO_3 concentrations, O_3 concentrations and PBLH in summer and winter in the Atlantic and Pacific regions.

5.3.2 Ozone

Unlike NO_x, O_3 has a longer lifetime of several days to one month and reach therefore higher altitudes in the troposphere. This is why the following analysis will look at shipping impacts at the surface as well as across the whole troposphere.

5.3.2.1 Comparison with E2007

Near-surface O_3 volume mixing ratios resulting from EDGAR v3.2 shipping emissions are plotted on figures 5.5 and 5.6. Results from MOZART-4 in January and July are in good agreement with the multimodel study. The decrease of O_3 noticed by Eyring et al. [2007] in winter is also reproduced by the model employed in the present study and with a similar magnitude of -4.0 ppbv (-20.2%). Moreover, the summer peak in the Atlantic is well simulated by MOZART-4 although it spreads more across the ocean in the latitudinal direction. In terms of relative differences, results in January are in good agreement but background O_3 levels are too low in MOZART-4 in summer which is likely to be a consequence of the low NO_2 levels (see section 5.3.1.1).

Annual O_3 zonal means presented on figure 5.6 highlight MOZART-4's ability to simulate a shipping O_3 perturbation similar to those produced by the 10 models included in the multimodel study. In particular, the shape of the perturbation is very similar to that from the MATCH-MPIC model which comprises the same convection and boundary mixing schemes and a similar advection scheme. The magnitude of the perturbation is however larger by a few tenth of ppbv in MOZART-4. Compared with the ensemble mean, MOZART-4 performs well at the surface but simulates larger O_3 volume mixing ratios by a less than 0.10 ppbv in the lower troposphere between 30°N and 90°N and by less than 0.40 ppbv in the upper troposphere between 0.0 and 30.0°N. O_3 volume mixing ratios reach also lower hybrid-sigma pressure levels in the Arctic region in MOZART-4 (0.4, similar to that in the OSLO CTM2) compared with the ensemble mean.

O_3 tropospheric column perturbations are larger in MOZART-4 in the Atlantic and Indian oceans as indicated on figure 5.7. In the Atlantic ocean, values calculated by MOZART-4 peak at 1.27 DU resulting in a relative difference of 41%. In the Indian ocean, values calculated by MOZART-4 peak at 1.58 DU and result from the larger O_3 concentrations present in the free and upper troposphere, as shown on figure 5.6. In this region, O_3 tropospheric column perturbations do not exceed 1.35 DU in E2007 corresponding to a maximum of 32% difference. O_3 tropospheric columns are also denser in the Arctic region in MOZART-4 compared with the ensemble mean of the multimodel study.

The global tropospheric O_3 burden induced by shipping emissions equals 4.10 $Tg.yr^{-1}$ in MOZART-4 while it lies between 2.0 and 3.5 $Tg.yr^{-1}$ in the multimodel study (see table 5.3). This larger burden arises from the larger O_3 concentrations in the free troposphere. This result shows again the capacity of MOZART-4 to simulate comparable shipping perturbations with respect to E2007.

5.3.2.2 Comparisons between the three methodologies

The three cases with different methodologies are presented on figures 5.8, 5.9 and 5.10. One remarkable point is that while the O_3 tagging method simulates well NO_x concentrations, it clearly overestimates O_3 concentrations everywhere in the troposphere in January and July. Since O_3 production is very sensitive to NO_x concentrations and is larger where background NO_x concentrations are low [Lawrence and Crutzen, 1999], the absence of background NO_x resulting from the use of the O_3 tagging scheme could well lead to a larger and unrealistic O_3 production.

Near-surface O_3 volume mixing ratios are displayed on figure 5.8. In January, O_3 volume mixing ratios reach up to 9.93 ppbv, 7.41 ppbv and 58.28 ppbv mainly in the Indian ocean in the three cases. In July, they peak at 22.62 ppbv, 8.04 ppbv and 654.66 ppbv in the North Pacific region. In the North Atlantic region, the maximum value is 12.2 ppbv which is in good agreement with studies from Endresen et al. [2003], Eyring et al. [2007] and Dalsøren et al. [2007]. It is worth

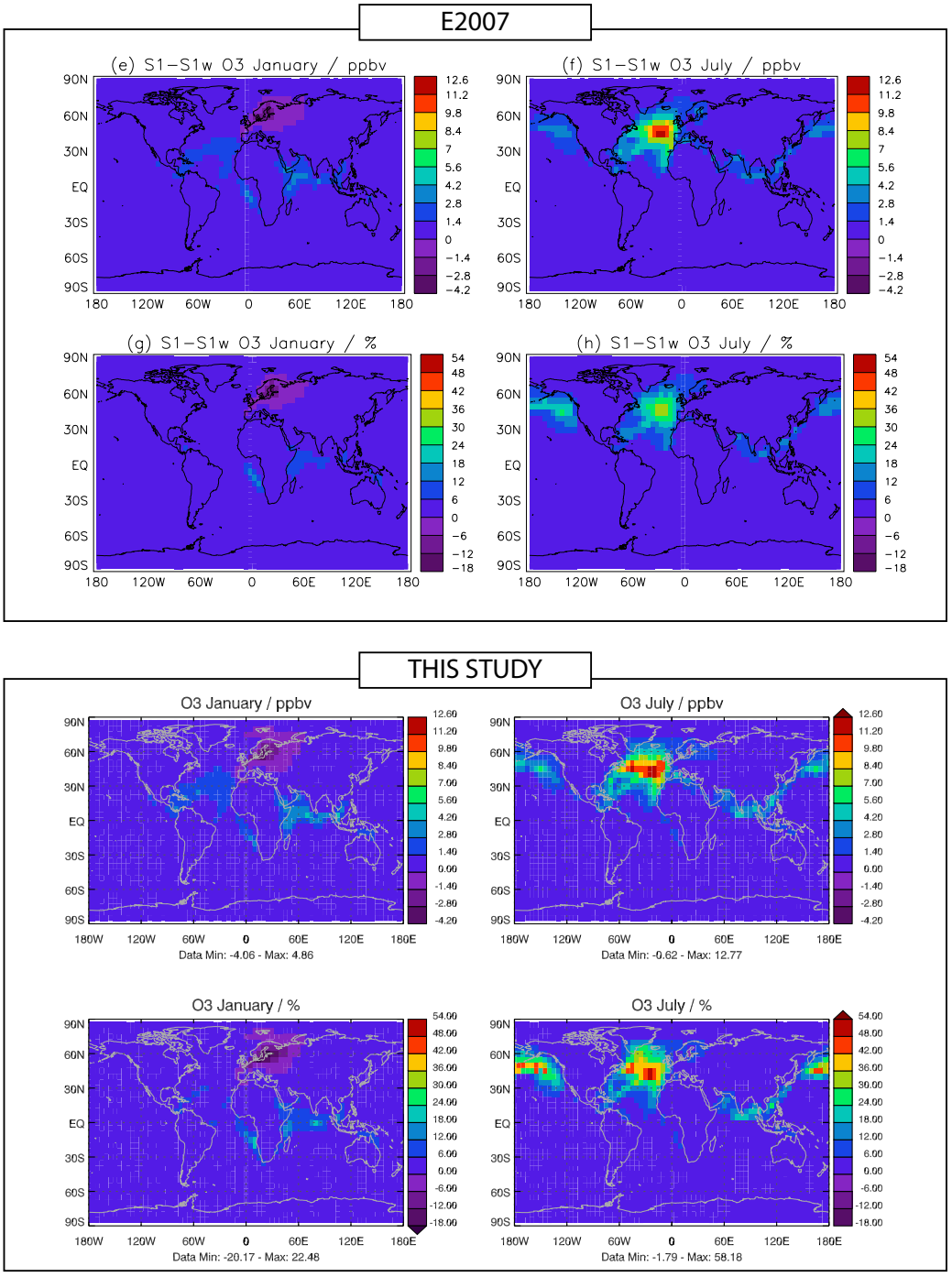

FIGURE 5.5: Comparison of near-surface shipping-induced O_3 volume mixing ratios and ratios with respect to background O_3 volume mixing ratios in January and July between E2007 and the present study. Note that arrows were collated to the original colour bar when values computed by MOZART-4 were found larger or smaller than the minimum and maximum levels of the colour bar.

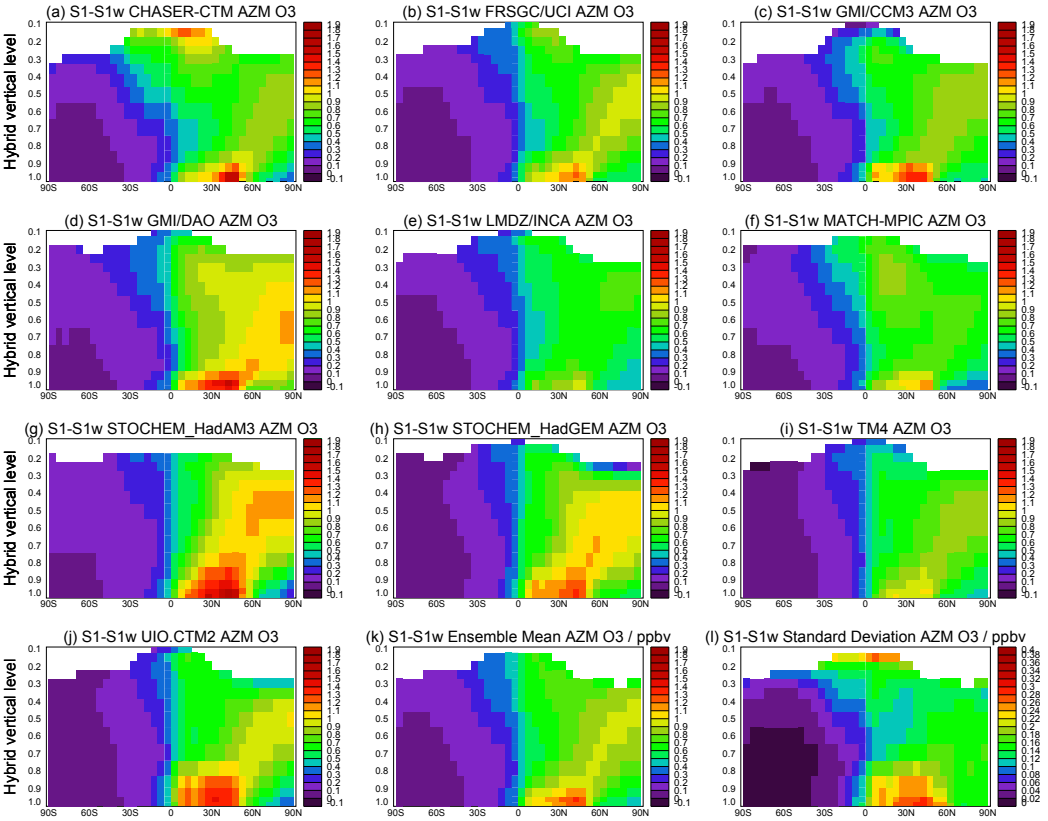

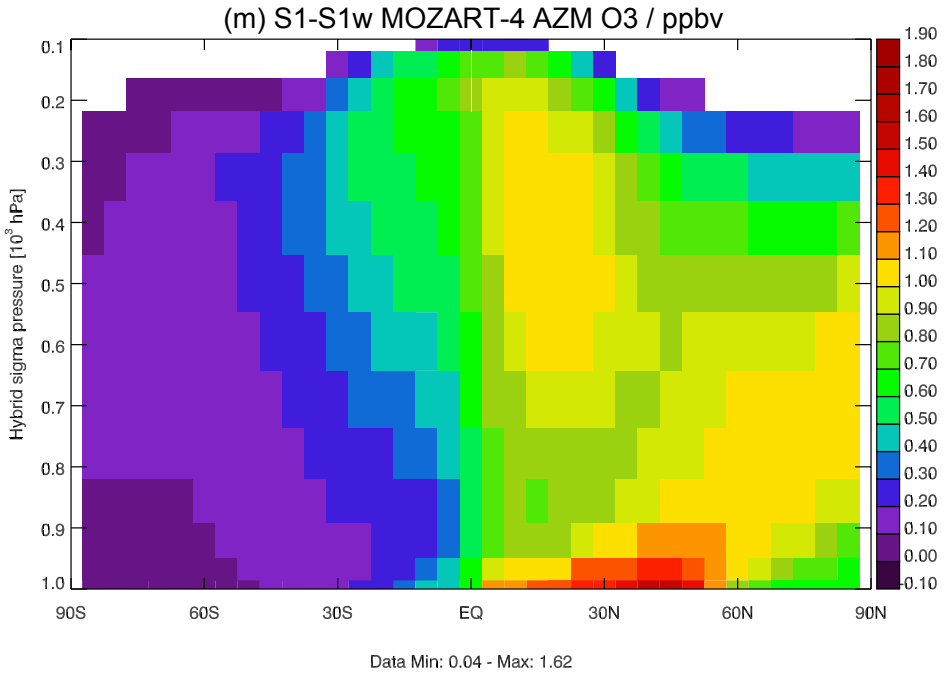

FIGURE 5.6: Comparison of annual zonal mean shipping-induced O_3 volume mixing ratios between E2007 and the present study.

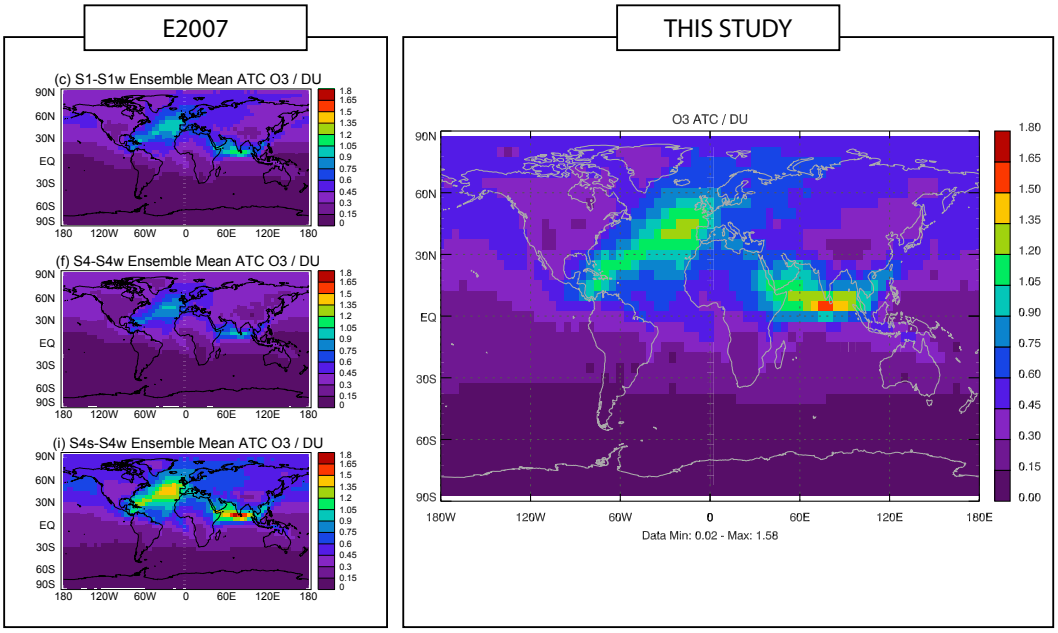

FIGURE 5.7: Comparison of annual shipping-induced tropospheric O_3 column between E2007 and the present study.

noting that differences between the peaks in the 100% and 5% removal cases are larger in summer than in winter. This emphasizes the non-linear character of the chemical mechanism.

As for the zonal mean plots in January and July, they are available on figure 5.9. The shape looks similar to that displayed in E2007. In general, the perturbation is stronger in the Northern hemisphere as a result of larger shipping emissions. A vertical gradient is also clearly noticeable with larger values at the bottom, near ship lanes. In January, maximum values peak at 2.88 ppbv, 2.23 ppbv and 17.55 ppbv and are located at the surface close to 30°N in the 100% and 5% removal cases. In July, they peak at 7.48 ppbv, 3.07 ppbv and 120.39 ppbv at higher latitudes compared with January. Again, differences between the peaks in the 100% and 5% removal cases are much larger in summer than in winter. Although the geographical distribution of shipping emissions has changed between EDGAR v3.2 and ACCMIP, the shape of annual zonal means remain similar: there is a slant in the lower troposphere of the Northern hemisphere which leans towards the North Pole and starts between 15°N and 30°N.

TABLE 5.3: Changes in global tropospheric O_3 burden owing to shipping emissions.

Study	Shipping NO_x emissions [Tg(N)/yr]	Global ΔO_3 burden [year]	Relative difference [%]
E2007	3.1	2.0-3.5	-
This study (EDGAR-100%-R)	3.1	4.10	1.24
This study (ACCMIP-5%-R)	5.4	8.78	2.65
This study (ACCMIP-100%-R)	5.4	10.70	3.23
This study (ACCMIP-O_3 tag)	5.4	24.22	7.32

Regarding tropospheric columns, they are shown on figure 5.10. On an annual average basis, values reach up to 2.36 DU, 1.95 DU and 18.71 DU in the North Pacific owing to the large NO_x and O_3 perturbations but also in the Indian Ocean where convective transport is more efficient and lifts O_3 up into the free troposphere. Perturbations in the 100% removal and 5% removal cases present similar patterns to that shown in E2007, except in the Pacific but is different from that shown in Dalsøren et al. [2009]. The magnitude of the tropospheric columns lays between 0.20 DU and 2.28 DU which is larger than that reported by Eyring et al. [2007] but somewhat smaller than that from Dalsøren et al. [2009]. Global annual averages equal 0.95 DU, 0.76 DU and 18.71 DU which for the first two values are in good agreement with that reported by Endresen et al. [2003].

Finally, global annual tropospheric O_3 burdens added by shipping emissions are presented in table 5.3. In the 100% removal case, the burden has a value of 10.70 Tg which is in good agreement with the value of 4.10 Tg obtained in the simulation with EDGAR v3.2 shipping emissions. There is more than a factor of 2 between these two values which result from the near doubling in shipping emissions and the spread shipping spatial distribution. Using the small perturbation approach reduces this value by 20%.

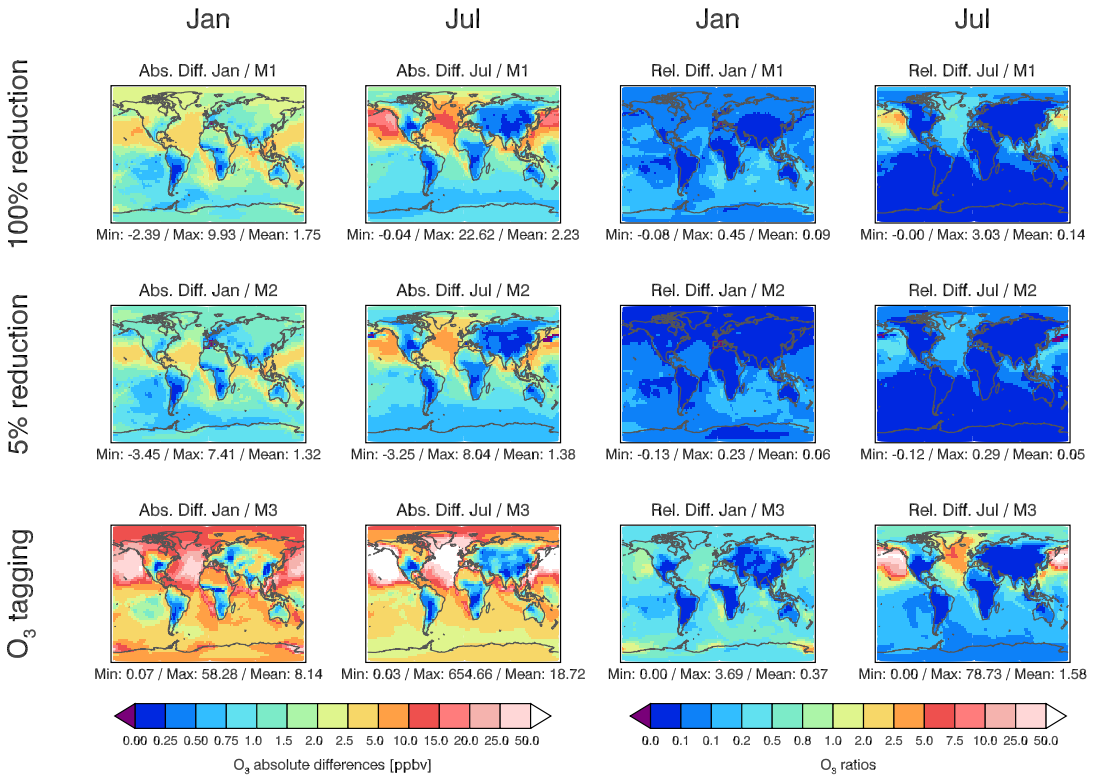

FIGURE 5.8: Near-surface shipping-induced O_3 volume mixing ratios and ratios with respect to background O_3 volume mixing ratios in January and July in the three cases using ACCMIP emissions. Note that the background concentrations used for the 5% removal case is the same as in the 100% removal case.

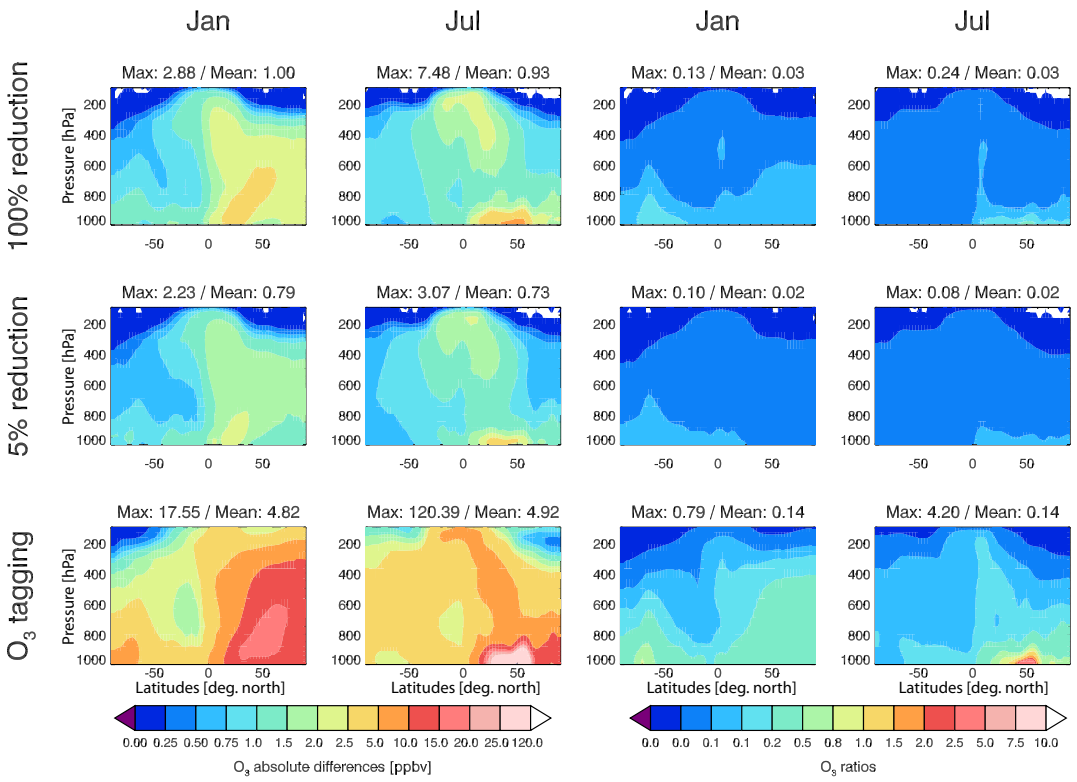

FIGURE 5.9: Annual zonal mean shipping-induced O_3 volume mixing ratios and ratios with respect to background O_3 volume mixing ratios in January and July in the three cases using ACCMIP emissions.

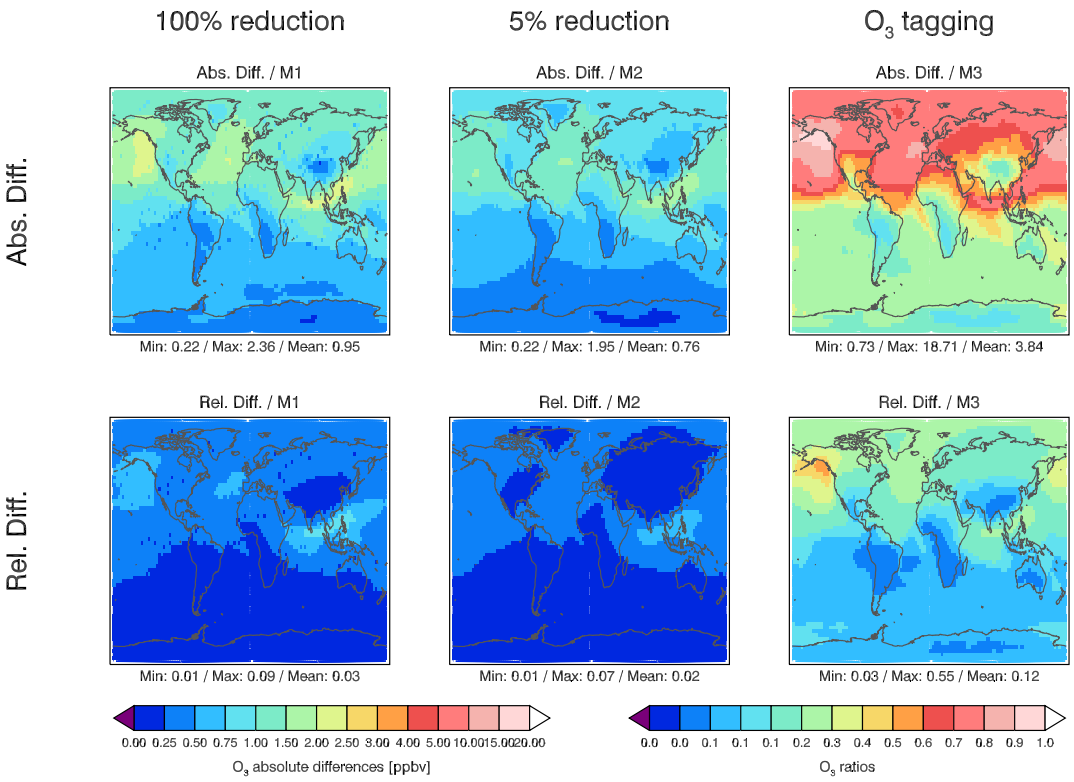

FIGURE 5.10: Annual tropospheric column shipping-induced O_3 volume mixing ratios and ratios with respect to background O_3 volume mixing ratios in January and July in the three cases using ACCMIP emissions.

5.3.3 Hydroxyl radical

In this section, only results from the three cases with different methodologies are displayed as no OH plot was provided in the multimodel study (see figures 5.11 and 5.12). The OH perturbation is tightly linked to that of O_3 and is more important in the tropics since the photolysis of O_3 followed by reaction with H_2O constitutes the main production path for OH. As a result, maximum values are expected to be located near the surface of tropical regions.

In January, OH concentrations up to 1.89x10^{6}molecules.cm^{-3}, 1.31x10^{6}molecules.cm^{-3} and 20.36x10^{6}molecules.cm^{-3} are simulated in tropical regions, particularly in the Asian region. Large values with a similar magnitude are also present off the west coast of Southern Africa. However, in the case with 100% removal, the maximum is located in Antarctica near scientific stations and equals 2.49x10^{6}molecules.cm^{-3} (factor of 7.09). These large OH concentrations result from the combination of shipping NO_x emissions, long daylight and the fact that Antarctica is a low-polluted region. In July, OH concentrations reach up to 4.42x10^{6}molecules.cm^{-3} (factor of 12.16) in the North Pacific ocean in the 100% removal case and up to 1.92x10^{6}molecules.cm^{-3} in the Pacific off the coast of China in the 5% removal case. Using the shipping spatial distribution and a magnitude of 3.0 Tg(N)/yr from the EDGAR v2 emission inventory, Lawrence and Crutzen [1999] reported that concentration differences are larger by 20% in the Northern hemisphere and by more than a factor of 5 in the main shipping lanes in summer. These local maximums are located at the surface between 40°N and 50°N where shipping emissions are the largest. Zonal means show that on average OH concentrations are increased in the tropical regions and are subject to a slight seasonal variability. In July, the vertical gradient is more pronounced than in January, which is in agreement with the O_3 perturbation. In January, maximums are located near 30°S and equal 0.32x10^{6}molecules.cm^{-3} in the 100% removal case and 0.28x10^{6}molecules.cm^{-3} in the 5% removal case. In July, values peak at 1.36 and 0.60x10^{6}molecules.cm^{-3} in these two cases, respectively. Again differences between January and July are more pronounced in the 100% removal case.

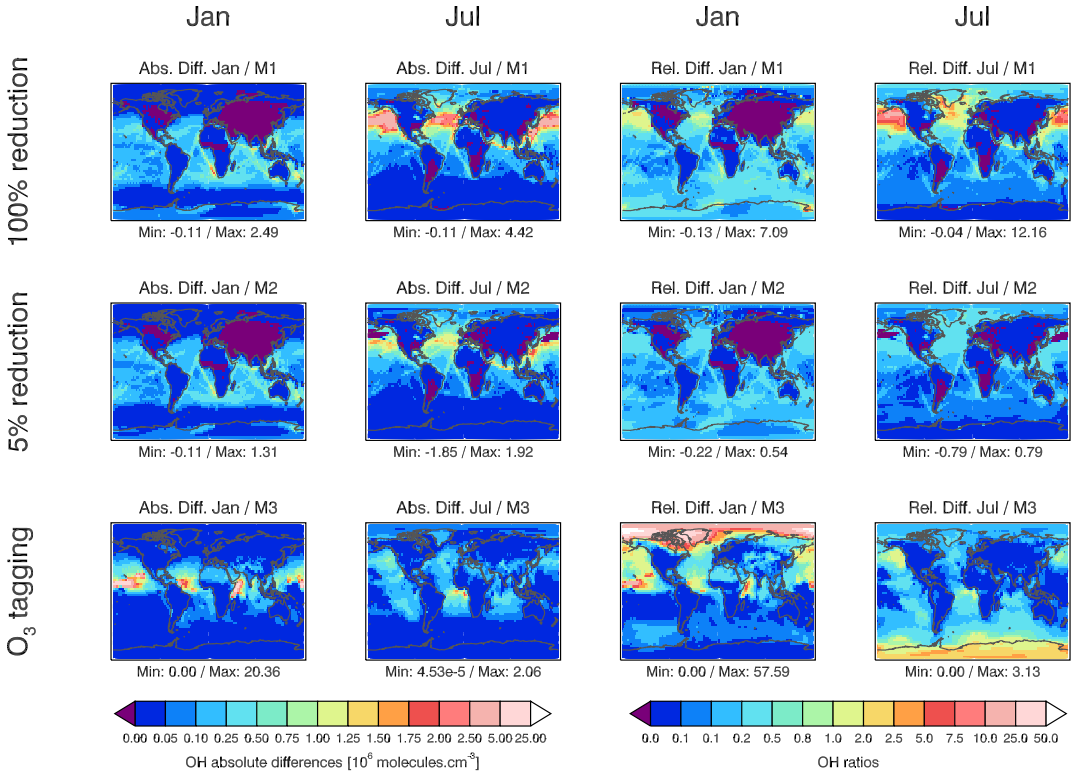

FIGURE 5.11: Near-surface shipping-induced OH volume mixing ratios and ratios with respect to background OH volume mixing ratios in January and July in the three cases using ACCMIP emissions.

The annual global average relative difference equals 7.22% in the 100% removal case and 5.43% in the 5% removal case which are 1.4 and 0.8 times more than the 3% values reported by Endresen et al. [2003] and Dalsøren et al. [2009] who used respectively a 3.0 Tg(N)/yr and a 5.0 Tg(N)/yr shipping emission with the Oslo CTM2 model run at different resolutions. These values are also more than 8.5 times larger than that reported by Dalsøren et al. [2007]. Nonetheless, the case including EDGAR emissions yields an annual global average relative difference of 2.74% which is in better agreement with the studies from Endresen et al. [2003] and Dalsøren et al. [2009].

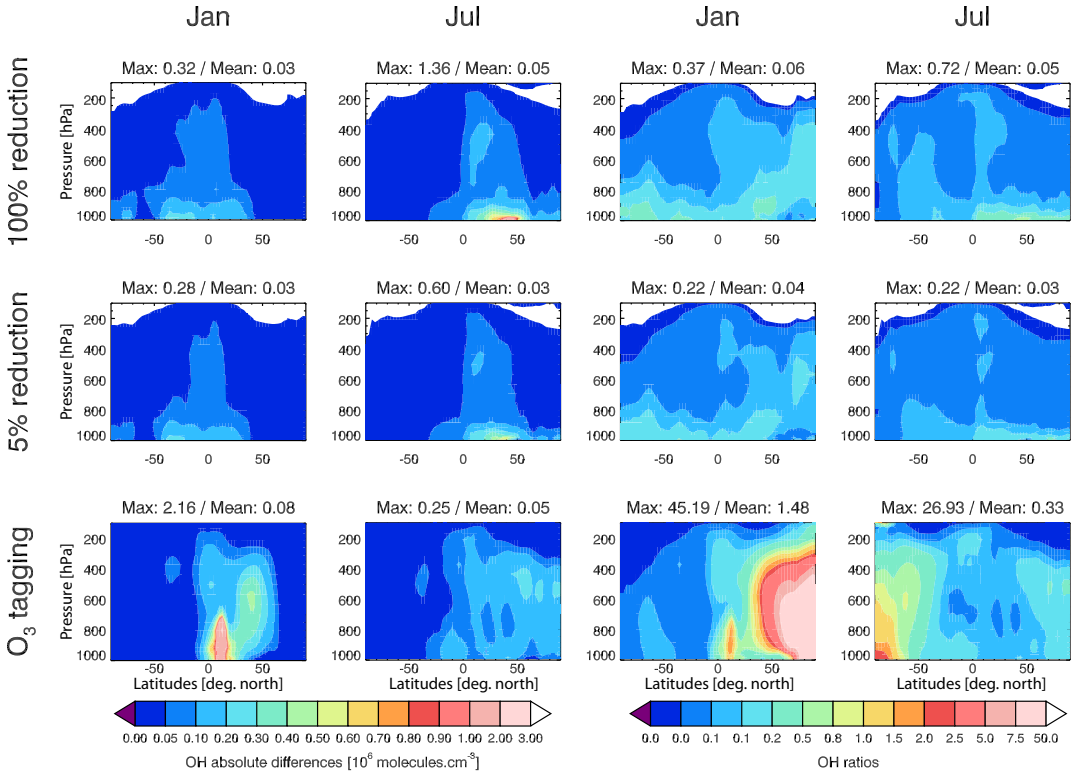

FIGURE 5.12: Annual zonal mean shipping-induced OH volume mixing ratios and ratios with respect to background OH volume mixing ratios in January and July in the three cases using ACCMIP emissions.

5.3.4 Methane

An increase in OH concentrations leads to a reduction of global CH_4 lifetime. Reductions in the four simulation cases are provided in table 5.4 together with values reported across the literature. The case with EDGAR v3.2 emissions is more than twice larger than the ensemble mean reported by Eyring et al. [2007] but 28% smaller than that reported by Lawrence and Crutzen [1999]. The former is expected since MOZART-4 produces more O_3 compared with the ensemble mean in Eyring et al. [2007]. This perturbation is equivalent to a 6.22% reduction which is similar to those reported in a few previous studies [Lawrence and Crutzen, 1999, Endresen et al., 2003, Dalsøren et al., 2009]. Indeed, both Lawrence and Crutzen [1999] and Endresen et al. [2003] reported a decrease of about 4.2% when shipping emissions are included with a magnitude of 3.0 Tg(N)/yr in their model, while

TABLE 5.4: Changes in global CH_4 lifetime owing to shipping emissions.

Study	Shipping NO_x emissions [Tg(N)/yr]	ΔCH_4 lifetime [year]	Relative difference [%]
[Lawrence and Crutzen, 1999]	3.0	-0.4	-4.2
[Endresen et al., 2003]	3.0	-	-4.2 (-5.9)
[Dalsøren et al., 2007]	3.0	-	-1.48
E2007	3.1	-0.13	-1.56±0.05
[Dalsøren et al., 2009]	5.0	-	-5.35 (-7.5)
This study (EDGAR-100%-R)	3.1	-0.29	-2.69 (-3.76)
This study (ACCMIP-5%-R)	5.4	-0.55	-5.09 (-7.13)
This study (ACCMIP-100%-R)	5.4	-0.73	-6.22 (-8.71)

Dalsøren et al. [2009] found that a magnitude of 5.0 Tg(N)/yr yields to a decrease of 5.35%. Nevertheless, it is important to mention that in two other studies published in 2007, this perturbation was about 1.5% for a shipping magnitude of about 3.0 Tg(N)/yr [Dalsøren et al., 2007, Eyring et al., 2007].

5.4 Discussion

In this chapter, MOZART-4's ability to simulate shipping perturbations was assessed by using two shipping emission inventories (EDGAR v3.2 and ACCMIP) and three methodologies (total removal, small-perturbation approach and O_3 tagging) and by comparing results to previous findings from the literature.

The version of the O_3 tagging scheme used in this chapter fails to reproduce shipping perturbations of O_3, OH and CH_4 when applied to shipping NO_x emissions. However, it could provide a useful framework for implementing the ship plume parameterisation from Cariolle et al. [2009] (see chapter 7).

Although anthropogenic background emissions used in this study were different compared with E2007, the case with EDGAR v3.2 shipping emissions revealed that MOZART-4 represents shipping perturbations of NO_x and O_3 within 1-σ standard deviation of the ensemble means with a slight tendency to overestimate concentrations by up to a factor of 2 for NO_x and up to 20% for O_3. The globally

and zonally averaged shape of the O_3 response is also in good agreement. For instance, the shape with a slant towards the north pole is reproduced by the model but somehow reaches lower altitudes in the Arctic region compared with the ensemble mean. There is also another region of overestimated O_3 in the upper and free troposphere of the northern tropics which is not shown on the ensemble mean plot.

The 100% removal and 5% removal cases with ACCMIP shipping emissions are also in good agreement with previous studies but in the North Pacific region, there is an overestimation which is likely to be stemming from the combination of low MBL with saturation of the NO_x-O_3-HO_x photochemical system. The PBL scheme used in MOZART-4 has been previously shown to trap atmospheric compounds in the lower part of the troposphere [Horowitz et al., 2003, van Noije et al., 2006]. In addition, O_3 levels simulated by MOZART-4 are slightly higher in the free troposphere which could be due to the deep convection scheme of the model [Horowitz et al., 2003].

MOZART-4 is very sensitive to shipping NO_x emissions and non-linear effects are clearly triggered when using the 100% removal methodology (especially during summer time). For instance, the large overestimations in the North Pacific are less pronounced in the 5% removal case. Nonetheless, it is not clear which methodology between the small-perturbation and the 100%-removal approaches provides the most realistic perturbations and for this reason, the total removal methodology will be employed in the next chapters.

Although comparisons between studies are interesting and useful, they cannot provide answers to all the differences arising from these comparisons. A sensitivity analysis of shipping perturbations simulated by MOZART-4 is therefore required to further understand.

Chapter 6

Sensitivity of shipping perturbations to current uncertainties from various atmospheric processes

In this chapter, the sensitivity of shipping perturbations of NO_x, O_3, OH and CH_4 was assessed with the help of MOZART-4. The following results were found:

- Depending on the metric, shipping perturbations are more or less sensitive to atmospheric processes and model resolution. For instance, changes in photochemical data have significant impacts on the vertical structure of shipping O_3 perturbations but their effect is reduced near the surface.
- Uncertainty ranges, maxima ranges and changes used in this chapter leads to changes at the global scale in the following order, from the largest to the smallest: shipping emission magnitude, photolysis scheme, shipping emission spatial distribution, lightning activity, photochemical

data, horizontal resolution, background anthropogenic emissions and dynamical data.

- On a global average, current uncertainties in shipping emissions yields to the largest effects on shipping perturbations. The upper end of the range of shipping emissions is nearly twice as large as the best-estimate value. This large uncertainty results in global O_3 burden, global OH concentration and CH_4 lifetime shipping perturbations of 67%, 66% and 59%, respectively.
- Differences resulting from the use of online and offline photolysis schemes suggest that shipping perturbations are very sensitive to it. However, it is unclear whether the version of the offline photolysis scheme used in this chapter is performing well.
- An increase in horizontal resolution reduce shipping O_3 levels in the tropics but augment them everywhere else. In addition, shipping CH_4 lifetime perturbation become larger by 14% between T21LR and T106LR.

6.1 Introduction

Once released into the atmosphere, NO_x molecules emitted by ships and their secondary products are subject to various physical and chemical processes, such as advection, convection, diffusion (or mixing), dry and wet depositions, photolysis reactions, gas-phase reactions and heterogeneous reactions [Seinfeld and Pandis, 2006]. These processes contribute in different ways to the magnitude and spatial distribution characteristics of the shipping O_3 and CH_4 responses. In addition, the magnitude and the location of shipping NO_x emissions as well as those of other anthropogenic and natural emissions play a role on the manner by which NO_x molecules are transported and transformed in the troposphere. For instance, background emissions modify background species concentrations which in turn

may affect the chemical production and destruction of NO_x, HO_x and O_3. It is important to stress that these transformations happen on different spatial and time scales and that some of them are non-linear [Lin et al., 1988].

In global models, these processes are represented by numerical schemes that solve ordinary differential equations and partial differential equations as well as parameterisations and empirical formulas. These may differ from one model to another and generally introduce numerical errors to the results. Furthermore, the discretisation of the troposphere is of particular interest since the size of grid cells, which can be several orders of magnitude larger than ship plumes, determines the concentration of species but also the rates of chemical production and destruction within them.

Overall, shipping O_3 and CH_4 perturbations resulting from shipping NO_x emissions and simulated by global models depend on atmospheric processes and the way they are represented in those models. It is therefore crucial to understand and quantify the extent of their impacts relatively to the shipping NO_x-O_3-HO_x-CH_4 chemical system in order to find where the largest uncertainties lie. In the past, a few modelling studies have partly looked at the sensitivity of shipping NO_x, O_3, OH and CH_4 perturbations to those physical and chemical processes. For instance, Endresen et al. [2003] realised that the use of different shipping emission inventories with the Oslo CTM2 model run at T21 horizontal resolution yields large regional perturbations but noticed that the temporal variability of the COADS-based shipping emission inventory had a small effect. Interestingly, the same model was run on two other occasions at a T63 horizontal resolution with different shipping and background emission inventories[1] and authors reported globally averaged OH increases of 0.64% [Dalsøren et al., 2007] and 3.67% [Dalsøren et al., 2009] compared with about 3% in Endresen et al. [2003]. Eyring et al. [2007] further addressed the uncertainties associated to shipping NO_x emissions on the O_3 and CH_4 perturbations by using ten state-of-the-art global atmospheric chemistry models in combination with three different shipping emission inventories. In their

[1] Dalsøren et al. [2007] used shipping emissions from Endresen et al. [2003] with the COADS spatial proxy and background emissions from POET whereas Dalsøren et al. [2009] used the RETRO emission inventory (Personal communication, 2011)

reference case using 2000 emissions, they found variabilities of 16% and 20% in the O_3 response in the free troposphere and at ground level respectively. They attributed these variabilities to inter-model differences[2] but also noted that these were "significantly smaller than estimated uncertainties stemming from the ship emission inventory". In any case, these differences were not resolved in terms of model characteristics or tropospheric processes. Collins et al. [2008] looked at the role of land-based emissions on global shipping O_3 burden and CH_4 lifetime perturbations and reported large differences in the MFR[3] and A2[4] cases in 2000. These differences displayed on Table 5 in that study yield a relative difference of +31.25% and -18.75% for the O_3 burden and +26% and -26% for CH_4 lifetime.

Furthermore, some of these modelling studies were carried out with the help of small-scale models which give further insight on the nature of the sensitivity. For example, with the help of a photochemical box model, von Glasow et al. [2003] looked at the influence of the magnitude, local time and NO_x partitioning of ship emissions as well as the importance of aerosol chemistry, mixing and background concentrations on the ship plume chemistry. They reported significant effects from the background concentrations of NO_x and O_3 on O_3 production as well as effects from background aerosols, such as sulphates and sea salts, on the gas phase chemistry. By contrast, NO_x partitioning does not seem to be of great influence. They also found that the local time of emissions have an impact on the photochemistry. Charlton-Perez et al. [2009] looked at the impact of different model resolutions using a small-scale ship plume model driven by dynamical data taken from the Large-Eddy simulation model. Between the highest (200 m x 200 m x 40 m) and the lowest (9600 m x 9600 m x 1920 m) resolutions, the perturbations of OH concentration, NO_x lifetime and O_3 production were found to follow a linear relationship and to equal 8%, 32% and 31%., respectively. Moreover,

[2]"There are notable differences in the magnitude of the response to ship emissions between the individual models which can be attributed to differences in the main characteristics of the models" [Eyring et al., 2007], pages 765-766

[3]Background anthropogenic emissions in the MFR case were 8.26 $Tg(N).year^{-1}$ corresponding to a decrease by about a factor of 0.3

[4]Background anthropogenic emissions in the A2 case were 52.50 $Tg(N).year^{-1}$ corresponding to an increase by about a factor of 2.

extrapolating this linear relationship to a typical GCTM resolution of 5°x5°, they reported increases of 15%, 55% and 59%.

The purpose of this chapter is thus to assess and quantify the impact of the some atmospheric processes as well as some modelling aspects on shipping perturbations by making use of MOZART-4. Being a global model, MOZART-4 represents these processes and has thus the ability to provide a good representation of their impacts on shipping perturbations at the global scale. However the coarse resolutions, required by GCTMs to run within a reasonable period of time, prevent them from resolving processes occurring at small scales. In particular, the dilution of ship plumes is not taken into account in this section, but will be studied in the next chapter (chapter 7).

Firstly, the methodology followed in this study is described. Then, results are presented and analysed going from detailed to global aspects of shipping perturbations. Finally, a discussion summarizes the significance of these processes.

6.2 Methodology

Although a Monte-Carlo approach would probably be preferable in this context, a simpler approach was chosen here owing to the complexity of the problem and the constraints imposed by the computing power that was available at the time of the study.

The present approach mainly consisted in running simulations using the bound values[5] of the uncertainty ranges associated to each physical or chemical process. In some cases, this was more difficult to achieve and a different approach was taken. For instance, in the case of changes in model resolution, a few typical resolutions recurrently used in the recent literature were chosen. Other cases without bound values are changes in dynamical data, changes in shipping emission spatial

[5]These can be either 1-σ standard deviations or minimum and maximum.

distribution and a change in photolysis scheme. In addition to these simplifications, each atmospheric process was studied independently from the others, again in order to lower the number of simulations to be run. MOZART-4 was chosen to perform a set of simulations required to quantify the sensitivity of shipping perturbations to various atmospheric processes and model resolutions. All these simulation cases were run with and without shipping emissions in order to calculate the impacts of each process on the shipping perturbation. They were then compared to a reference case of shipping perturbation corresponding to that analysed in the previous chapter (chapter 5). In other words, the model was run with and without the best-estimate shipping emissions included in the ACCMIP emission inventory representative of the year 2000 [Lamarque et al., 2010] and with the NCEP Reanalysis data of the year 2000 [Kalnay et al., 1996, Kistler et al., 2001]. Apart from the emissions, MOZART-4 was run in its default configuration with the default input data.

The diagram on figure 6.1 shows a basic description of the modelling framework employed here and displays the physical and chemical processes listed in the introduction while highlighting in yellow the few studied within this chapter.

The methodology employed for each case is first described below. Furthermore, each case is identified by two labels (a name and a letter) which both appear in bold characters. A table provides then a summary of the set of cases run in this study (table 6.3 and 6.4).

6.2.1 Dynamical data

In an offline GCTM, the modelling of advection, convection and diffusion processes relies on offline dynamical data. For instance, in MOZART-4, advection is resolved by a semi-Lagrangian flux form scheme which requires as input the meridional and zonal components of the wind speed [Lin and Rood, 1996], whereas convection is parameterised using temperature, specific humidity and pressure data [Hack, 1994, Zhang and McFarlane, 1995]. As for the diffusion process, it is resolved by

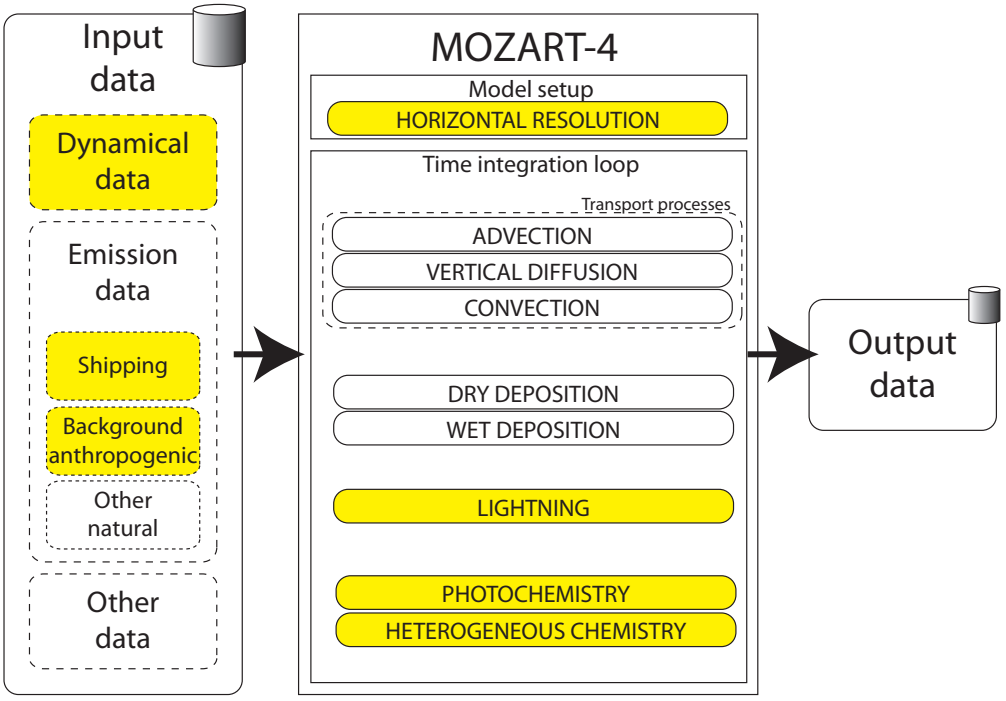

FIGURE 6.1: Flowchart representing the modelling framework employed in this chapter. The input data and model processes altered for the purpose of this study are highlighted in yellow.

the parameterisation from Hosltag and Boville [1993] using temperature, specific humidity, wind speed, surface heat flux and surface stress.

In order to reduce the number of simulations to be run, these transport processes were assessed simultaneously by using dynamical data from different years (2000, 2001, 2002). There is no particular reason why these specific years were chosen. In an ideal case, a few characteristic years would be extracted from a meteorological dataset containing a few decades. However, only these three years of NCEP Reanalysis were available at the time of the study and the available computing time did not allow for further simulations to be run. The years chosen in this study present different climatic characteristics (NAO index[6], ENSO index[7] ...) and provide therefore a basis for comparison. In addition to the NCEP Reanalysis dataset, data from the ECMWF-Interim dataset was also employed since the production of

[6]See http://www.cru.uea.ac.uk/~timo/datapages/naoi.htm
[7]http://www.esrl.noaa.gov/psd/enso/mei/

these datasets involve different methodologies and parameterisations[8]. This last comparison was done in order to highlight the differences that could arise from the use of various meteorological datasets.

The simulations associated with changes in dynamical data bear the identifiers (**DYN-[2001]**, **DYN-[2002]**, **DYN-[ECMWF2000]**, (**a**, **b**, **c**).

6.2.2 Shipping emissions

In the report of the ATTICA project [Eyring et al., 2009], authors calculated the uncertainty bounds corresponding to the magnitude of shipping emissions. They came up with a high bound value of 10.4 Tg(N).year^{-1} and a low bound value of 3.0 Tg(N).year^{-1} for shipping NO_x emissions in 2000, whereas the best estimate[9] was evaluated at 5.4 Tg(N).year^{-1}. This uncertainty range as well as those for other species emitted by ships were applied to the reference shipping emissions chosen in this study (ACCMIP 2000 emission dataset) (**SEM-[x2]**, **SEM-[/2]**, (**d**, **e**))[10].

Impacts from the different geographical distributions of shipping emissions were estimated with the help of the three spatial datasets developed by Wang et al. [2008] (**SESD-[AM]**, **SESD-[IC/AM]**, (**f**, **g**, **p**)). Among these datasets, two of them were produced using monitoring data taken from AMVER (Automated Mutual-Automated Vessel Rescue System)[11] and ICOADS (International Comprehensive Ocean-Atmosphere Data Set)[12] whereas the third one was calculated using a combination of the first two. In order to improve these datasets, ship-installed power was used as a proxy to shipping emissions rather than ship size. In addition, the ICOADS dataset was improved by averaging three years of data and removing redundant information. The combination of the AMVER and ICOADS datasets

[8]NCEP: http://www.esrl.noaa.gov/psd/data/gridded/data.ncep.reanalysis.html (last access: 08/06/2011) and ECMWF: www.ecmwf.int/research/era/do/get/era-interim (last access 08/06/2011)

[9]The best estimate is the value used in the ACCMIP emission inventory.

[10]Since the high and low bound values are very close to a doubling and halving of the best estimate, the labels "x2" and "/2" were chosen.

[11]http://www.amver.com (last access 08/06/2011)

[12]http://dss.ucar.edu/pub/coads (last access 08/06/2011)

corresponds to the average of the ship emission allocation factor of the two proxies at each grid cell. Figure 6.2 shows the differences between the three datasets.

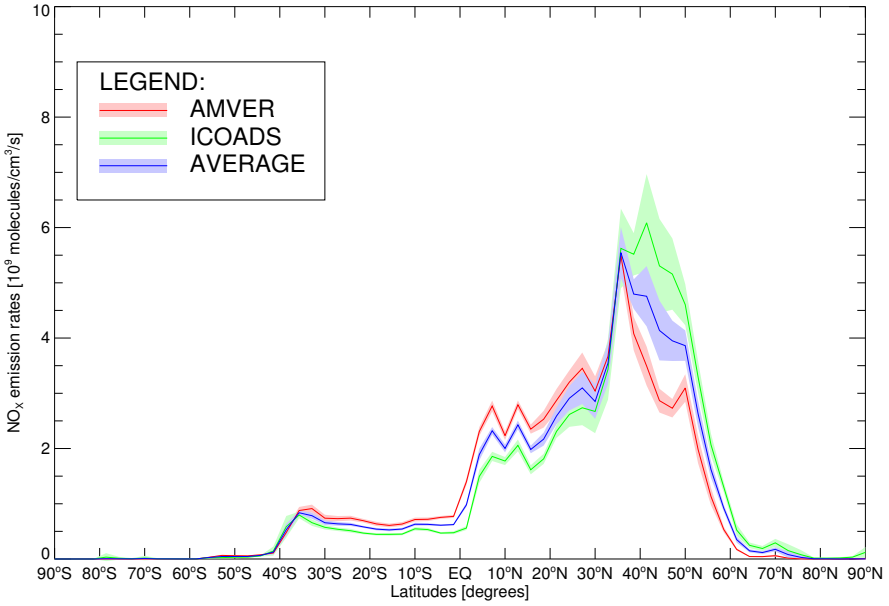

FIGURE 6.2: Zonal plot of shipping NO_x emissions from 3 different emissions inventories. The shaded areas represent the 1-σ standard deviation of the monthly temporal variability.

6.2.3 Background anthropogenic emissions

In this chapter, background anthropogenic emissions are defined as anthropogenic emissions other than shipping emissions. Changes in anthropogenic and natural background emissions alter the background concentrations of various species. These alterations have both local and global reaches [Auvray and Bey, 2005, Sudo and Akimoto, 2007] and as a result, perturb the environment in which ship emissions are released. Because the production and destruction from photochemical reactions depend on species concentrations, the NO_x-HO_x-O_3 photochemical system will be affected by changes in background emissions.

In the present study, natural emissions have been assumed to remain constant. The Asian, European and North American regions have been chosen since they present one of the largest emissions and changes over the next 100 years. They are

displayed on figure 6.3. The potential future anthropogenic emissions for these re-

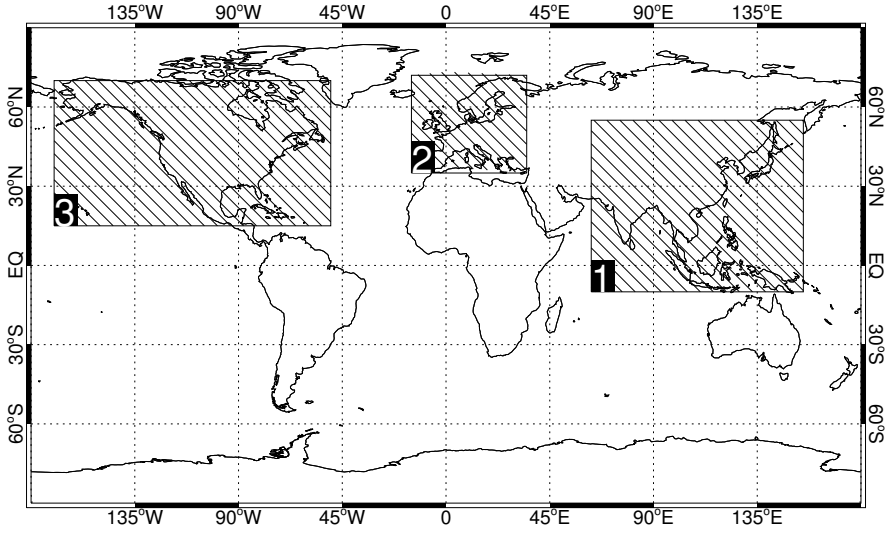

FIGURE 6.3: Regions defined in the background emission cases. (1.Asia (AS), 2.Europe (EU), 3.North America (NA))

gions were investigated by looking at the RCP scenarios[13]. The bar plot on figure 6.4 shows these changes for the years 2010, 2020, 2050 and 2100 for the three regions. Emissions decrease over time in the European and North American regions whereas they are still increasing in the Asian region in 2020. As a consequence, background anthropogenic emissions were multiplied and divided by a factor of 2 in the three selected regions with a view to provide realistic changes. Although no anthropogenic emissions have been forecast to increase two-fold under these scenarios, this factor was retained to better analyse non-linear effects (**BAE-[ASx2]**, **BAE-[EUx2]**, **BAE-[NAx2]**, **BAE-[AS/2]**, **BAE-[EU/2]**, **BAE-[NA/2]** (**h**, **i**, **j**, **k**, **l** and **m**)).

6.2.4 Photolysis and chemical activity

The relatively large number of photolysis and chemical reactions defined in MOZART-4 makes it difficult to analyse the sensitivity of shipping perturbations to all of

[13] www.iiasa.ac.at/web-apps/tnt/RcpDb/ (last access 08/06/2011)

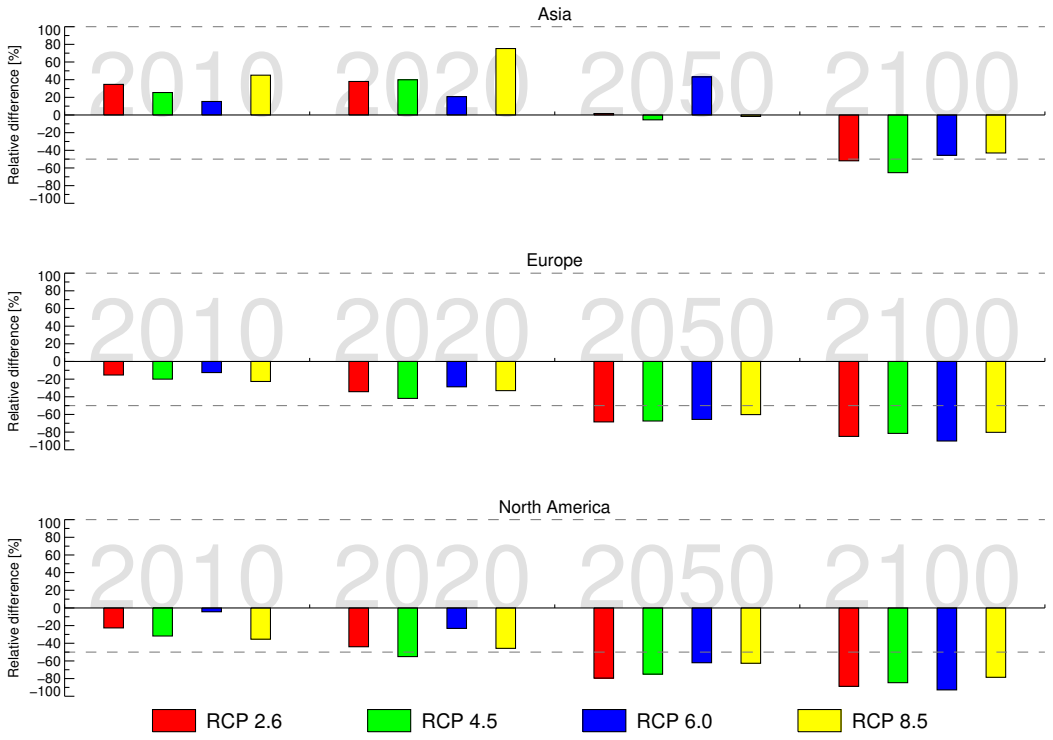

FIGURE 6.4: Proportions of anthropogenic NO_x emissions excluding aviation and shipping compared to 2000 emissions taken from IIASA RCP database. The grey dotted lines show the values chosen in this study.

them. Since results from chapter 4 suggested that O_3 photolysis could be underestimated while those from chapter 5 showed that the CH_4 lifetime perturbation from shipping is at the upper end of present estimates, the focus was set on O_3 photolysis and some reactions controlling OH levels in the troposphere. Besides, as mentioned in chapter 2, O_3 photolysis is an important process in ship plumes because it leads to OH production which in turn reduces NO_x and CH_4 lifetime. So are the chemical reaction of NO with HO_2 and that of NO_2 with OH which correspond respectively to the main pathway to O_3 production and the main sink for NO_x. These reactions are actually some of the most important in the marine boundary layer regarding NO_x molecules [Song et al., 2003b]. Background aerosol uptake was also pointed out by von Glasow et al. [2003] to be an important process.

O_3 photolysis was tested following two approaches. On the one hand, uncertainties

in the $O(^1D)$ quantum yield were taken from the chemical kinetics and photochemical data assessment from NASA/JPL [Sander et al., 2006][14] and were applied to the online photolysis scheme which calculates these quantum yields by using the parameterisation of Matsumi et al. [2002] (see figure 6.5, **PC-[O_3+hν] (n)**). In the NASA/JPL assessment uncertainties are provided in the form of a wavelength-dependent reliability factor which reflects a consensus among authors[15]. On the other hand, the impact of photolysis was further assessed by switching to the offline photolysis scheme which consists in using look-up tables of normalised actinic flux [Kinnison et al., 2007] (**PC-[OffPhot]**, (**q**)). These look-up tables were calculated from the TUV 2-stream radiative transfer model by Dr. Doug Kinnison (version 2.3 was used in this study).

Uncertainty functions of chemical kinetics data were also drawn out from the 2006 JPL assessment in order to calculate the 1-σ standard deviations of the reaction between NO and HO_2 and the reaction between NO_2 and OH. These functions reflect again a consensus among the expert panel in charge of writing the report and read:

$$f(T) = f(298K) \exp \left| g \left(\frac{1}{T} - \frac{1}{298} \right) \right|$$

$f(298K)$ represents the rate constant uncertainty at a temperature of 298 K and g modulates this rate constant uncertainty across a range of temperatures found in the atmosphere. The 1-σ standard deviations are then obtained by multiplying and dividing the rate constant by this uncertainty function (see figure 6.6).

A last sensitivity test was carried out to diagnose effects of aerosol chemistry by removing aerosol species and their reactions with gas species from the chemical

[14] It is important to note that since this study has been done, a new JPL assessment is available with new coefficients and uncertainty functions [Sander et al., 2009]. In particular, the coefficients of the reaction between NO and HO_2 have been reviewed as well as the values and uncertainties of the $O(^1D)$ quantum yield function.

[15] As stated in the report, "The error estimates are not rigorous numbers resulting from a detailed error propagation analysis of statistical manipulations of the different sets of literature values; they merely represent a consensus among the panel members as to the reliability of the data for atmospheric photo-dissociation calculations, taking into account the difficulty of the measurements, the agreement among the results reported by various groups, etc."

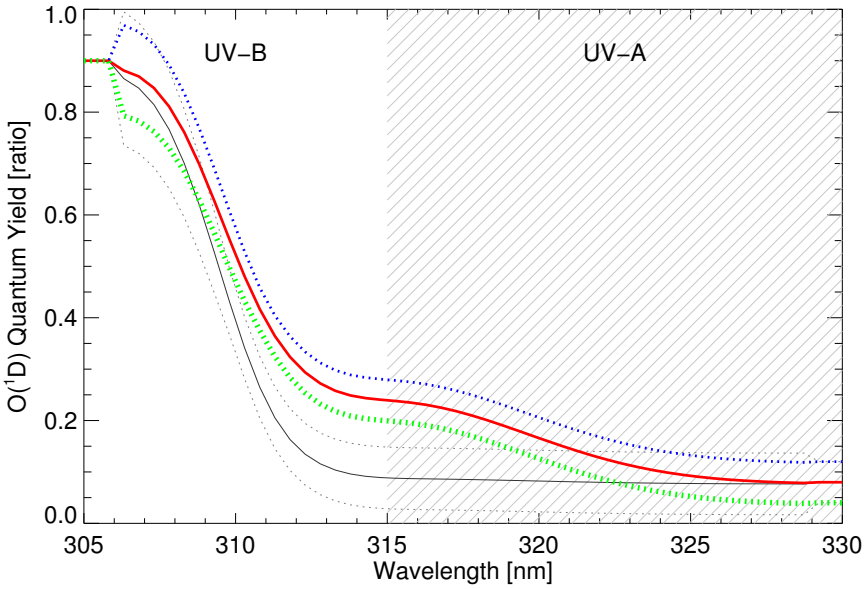

FIGURE 6.5: Uncertainty in $O(^1D)$ quantum yield as a function of wavelength [Sander et al., 2006]. The three coloured lines indicate the best estimate values (red) and the uncertainty of the quantum yield function at 298K (blue and green) whereas the grey lines present these estimates for a temperature of 263K. The green dotted line corresponds to the uncertainty applied in this study.

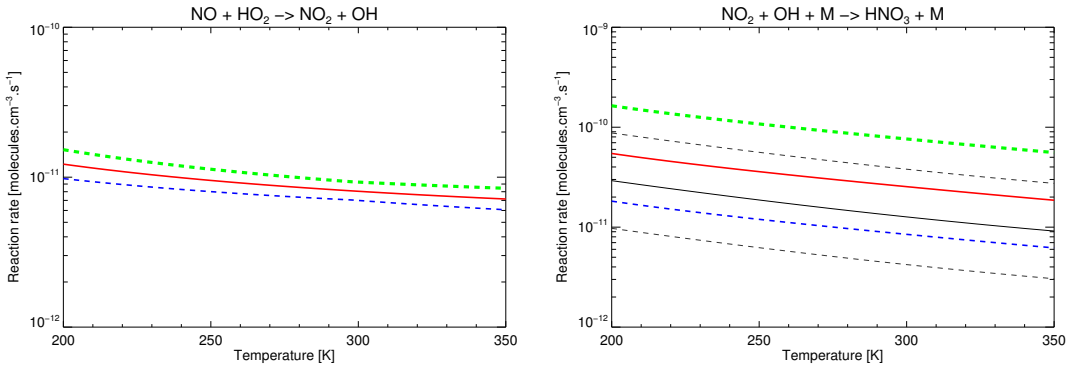

FIGURE 6.6: Uncertainties in the $NO+HO_2$ and NO_2+OH reactions as a function of temperature [Sander et al., 2006]. As in figure 6.5, the plain lines give the best estimates whereas the dotted lines provide the 1-σ uncertainty. The green dotted lines correspond to the uncertainties applied in this study.

mechanism. These include nitrates (NH_3, NH_4, NH_4NO_3), sulphates (SO_4), sea salts (SA), black and organic carbons (CB, OC) and secondary organic aerosols (SOA) (**PC-[NoAero] (r)**). SO_4 and SA have been found to affect sensitively the gas phase chemistry of ship plumes [von Glasow et al., 2003].

TABLE 6.1: Scaling factors used in the study and associated global lightning NO_x productions (default value in bold).

Scaling factor	Global lightning NO_x production [Tg(N).year^{-1}]
0.15	2.89
0.25	**4.82**
0.43	8.29

6.2.5 Lightning

Lightning is one of the largest contributor of NO_x emissions in the atmosphere [Galloway et al., 2004]. Yet, this process is still not very well understood and uncertainties related to it remain as a result significant [Solomon et al., 2007]. Schumann and Huntrieser [2007] summarised the work of nearly twenty-five teams and confirmed the previous consensus estimate of global NO_x production from lightning which equal 5 $\pm$3 Tg(N).year^{-1}. This translates into a $\pm$60% uncertainty.

In MOZART-4, the global NO_x production by lightning is defined by a scaling factor, which in the default case yields a production of 4.82 Tg(N).year^{-1} for the year 2000. The scaling factor was adjusted to obtain values close to 2 Tg(N).year^{-1} and 8 Tg(N).year^{-1} (**LGT-[3], LGT-[8] (s, t)**). Because at a given resolution the global NO_x production by lightning responds almost linearly to a change of scaling factor, a simple linear relationship was employed to find a scaling factor leading to a global production of NO_x close to the expected value. The scaling factors used in this case are given in table 6.1 and the global lightning NO_x productions were taken from the output log file.

6.2.6 Horizontal resolution

Previous studies on shipping NO_x impacts have underlined the importance of model resolution on the production of O_3 [Kasibhatla et al., 2000, Davis et al., 2001, Charlton-Perez et al., 2009]. In addition, a more general study further supported this argument by analysing the effects of model resolution changes on the

TABLE 6.2: Horizontal resolutions used in this study (default value and reference case in bold).

#	Ref. name	Spectral-like resolution	Number of longitude and latitude divisions	Degrees
u	R-[T21]	T21LR	64x32	∼5.6°x∼5.6°
v	R-[T31]	T32LR	96x48	∼3.8°x∼3.8°
c	**R-[T42]**	**T42LR**	**128x64**	**∼2.8°x∼2.8°**
w	R-[T63]	T63LR	192x96	∼1.9°x∼1.9°
x	R-[T106]	T106LR	320x160	∼1.1°x∼1.1°

NO_x-HO_x-O_3 chemical system [Wild and Prather, 2006]. Indeed, the production and destruction of chemical species is driven by the concentrations of available reactants. Because grid boxes in a large-scale model, such as a GCTM, can be as large as hundreds of kilometres, it cannot reproduce the very large concentrations of NO_x available at the early stages of ship plumes. Franke et al. [2008] estimated that a ship plume under neutral stability conditions takes about 46 hours to expand to 60 kilometres. Instead, ship NO_x are emitted instantaneously in the grid boxes which leads to smaller NO_x concentrations than found in ship plumes and therefore may overestimate O_3 production in GCTM. Although changes in currently available resolutions in large scale models are unlikely to resolve the physics and chemistry of ship plumes, several coarser and finer resolutions have been employed in order to estimate the impacts from a change in resolution at such scales (**R-[T21], R-[T31], R-[T63], R-[T106], (u, v, w, x)**). The different resolutions employed in this study are given in table 6.2. Lightning NO_x production scaling factor was updated for each resolution case to yield a value similar to that in the reference case (4.82 $Tg(N).year^{-1}$). Relative differences remain within 0.005% of the reference value. It is important to note that results from MOZART-4 were here assumed to converge with increasing resolution, as in Wild and Prather [2006]. In fact, shipping and background emission inventories were refined with resolution as they would be if someone was to carry out research at a specific resolution.

6.2.7 Summary of the simulations

TABLE 6.3: Summary of the simulation cases run in this study (continue on the next page).

#	Ref. name	Modification	Description/Comments
RF1	Reference	-	Reference case NCEP Reanalysis 2000 / IPCC-AR5 historic 2000
a	DYN-[2001]	Dynamical data	Using NCEP Reanalysis data representative of the year 2001
b	DYN-[2002]	Dynamical data	Using NCEP Reanalysis data representative of the year 2002
RF2/c	DYN-[ECMWF2000]	Dynamical data	Using ECMWF-INTERIM data representative of the year 2000. This case also corresponds to the reference case of the resolution cases.
d	SEM-[/2]	Magnitude of shipping emissions	Scaling IPCC-AR5 historic 2000 shipping emissions by the low uncertainty bound.
e	SEM-[x2]	Magnitude of shipping emissions	Scaling IPCC-AR5 historic 2000 shipping emissions by the high uncertainty bound.
f	SESD-[AM]	Spatial distribution of shipping emissions	Distributing ship emissions according to the averaged AMVER ship traffic proxy.
g	SESD-[IC/AM]	Spatial distribution of shipping emissions	Distributing ship emissions according to the averaged ICOADS/AMVER ship traffic proxy.
h	BAE-[AS/2]	Background anthropogenic emissions	Increasing Asian anthropogenic emissions by a factor of 2.
i	BAE-[EU/2]	Background anthropogenic emissions	Increasing European anthropogenic emissions by a factor of 2.
j	BAE-[NA/2]	Background anthropogenic emissions	Decreasing North American anthropogenic emissions by a factor of 2.
k	BAE-[ASx2]	Background anthropogenic emissions	Decreasing Asian anthropogenic emissions by a factor of 2.
l	BAE-[EUx2]	Background anthropogenic emissions	Decreasing European anthropogenic emissions by a factor of 2.
m	BAE-[NAx2]	Background anthropogenic emissions	Decreasing North American anthropogenic emissions by a factor of 2.
n	PC-[O_3+hμ]	Photolysis and chemical activity	Applying the JPL06 low uncertainty bound to the O_3 photolysis.
o	PC-[NO_2+OH]	Photolysis and chemical activity	Applying the JPL06 high uncertainty bound to the reaction between NO_2 and OH yielding HNO_3.
p	PC-[NO+HO_2]	Photolysis and chemical activity	Applying the JPL06 high uncertainty bound to the reaction between NO and HO_2 yielding NO_2.
q	PC-[OffPhot]	Photolysis and chemical activity	Switching to offline photolysis instead of online photolysis.
r	PC-[NoAero]	Photolysis and chemical activity	Removing aerosol chemistry of nitrate species.
s	LGT-[8]	Lightning NO_x production	Scaling the model global lightning NO_x production to the high uncertainty bound of 8 Tg(N).year^{-1}.
t	LGT-[3]	Lightning NO_x production	Scaling the model global lightning NO_x production to the low uncertainty bound of 3 Tg(N).year^{-1}.

TABLE 6.4: Summary of the simulation cases run in this study (continued).

#	Ref. name	Modification	Description/Comments
u	R-[T21]	Model resolution	Running model on a T21LR grid (64x32) with ECMWF-INTERIM data.
v	R-[T31]	Model resolution	Running model on a T31LR grid (96x48) with ECMWF-INTERIM data.
w	R-[T63]	Model resolution	Running model on a T63LR grid (192x96) with ECMWF-INTERIM data.
x	R-[T106]	Model resolution	Running model on a T106LR grid (320x160) with ECMWF-INTERIM data.

6.3 Results

Results are given in the form of different metrics, starting with detailed concentrations changes at the surface and in the vertical extent and going into more aggregated values as the chapter unfolds. First, near-surface maps of NO_x and O_3 as well as zonal means of O_3 and OH are analysed. Then, effects on tropospheric O_3 columns are discussed. Finally, changes in global O_3 burden, OH concentration and CH_4 lifetime are presented.

6.3.1 Changes in shipping perturbations of NO_x and O_3 near the surface

Statistical summaries of relative differences between perturbed and reference cases at the lower vertical level of the model are provided for both NO_x and O_3 on figures 6.7 and 6.8 respectively. These figures come to support near-surface maps of NO_x and O_3 ratios between the perturbed and reference cases which are displayed on figures D.1 and D.2 in appendix D[16]. Please note that shipping perturbations of NO_x and O_3 smaller than 10% and 5% of their respective background concentrations were filtered out for all cases prior to calculations. Filtered-out values are displayed in grey colour superimposed by diagonal hatched regions on the map plots. 45° diagonal hatched regions are reserved for the perturbed cases (**a**-**x**) whereas 135° diagonal hatched regions are reserved for the reference cases (**RF1** and **RF2**). This operation results in a variable selection of grid cells that, out of 2048, lie between 1062 and 1485 for NO_x and between 773 and 1304 for O_3. Zonal means of annually-averaged NO_x and O_3 have also been plotted on figures 6.9 and 6.10 to provide further information on the impacts of each perturbed case. Results are described by order of importance and come as follow: shipping emission magnitude (SEM), shipping emission spatial distribution (SESD), model resolution (R), dynamical (DYN), photolysis and other photochemical (PC), lightning (LGT) and background anthropogenic emissions (BAE).

[16]Note that these maps are also available on the thesis' website http://hilaire.jerome.free.fr/PhD_thesis/

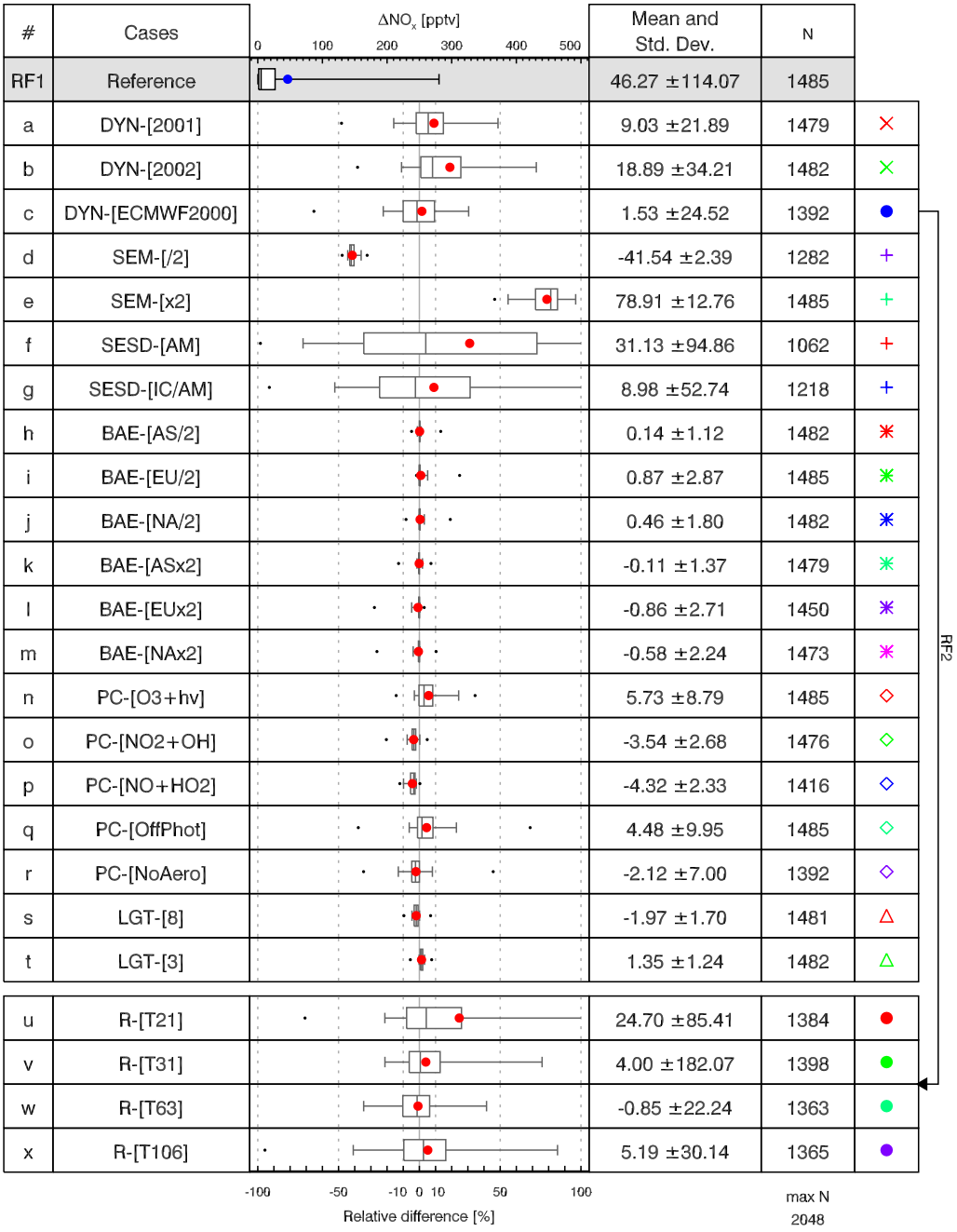

FIGURE 6.7: Statistical summary of annually averaged near-surface NO_x shipping perturbations and relative differences between cases. The blue-and-red coloured filled circles display mean values while the small black dots present the minimum and maximum values. The box-and-whisker plots show further statistics: bars display medians, box extents show the lower and upper quartiles and the ends of the whiskers present the 5^{th} and 95^{th} percentiles. Statistical information about shipping perturbations in the reference case (**RF1**) is provided at the top of the table in the shaded row. Statistical information about relative differences between shipping perturbations in the perturbation and reference cases (**RF1** & **RF2**) are listed below. N is the number of values used to performed the statistical calculations. The coloured symbols identify the zonal mean curves on figures 6.9 and 6.10.

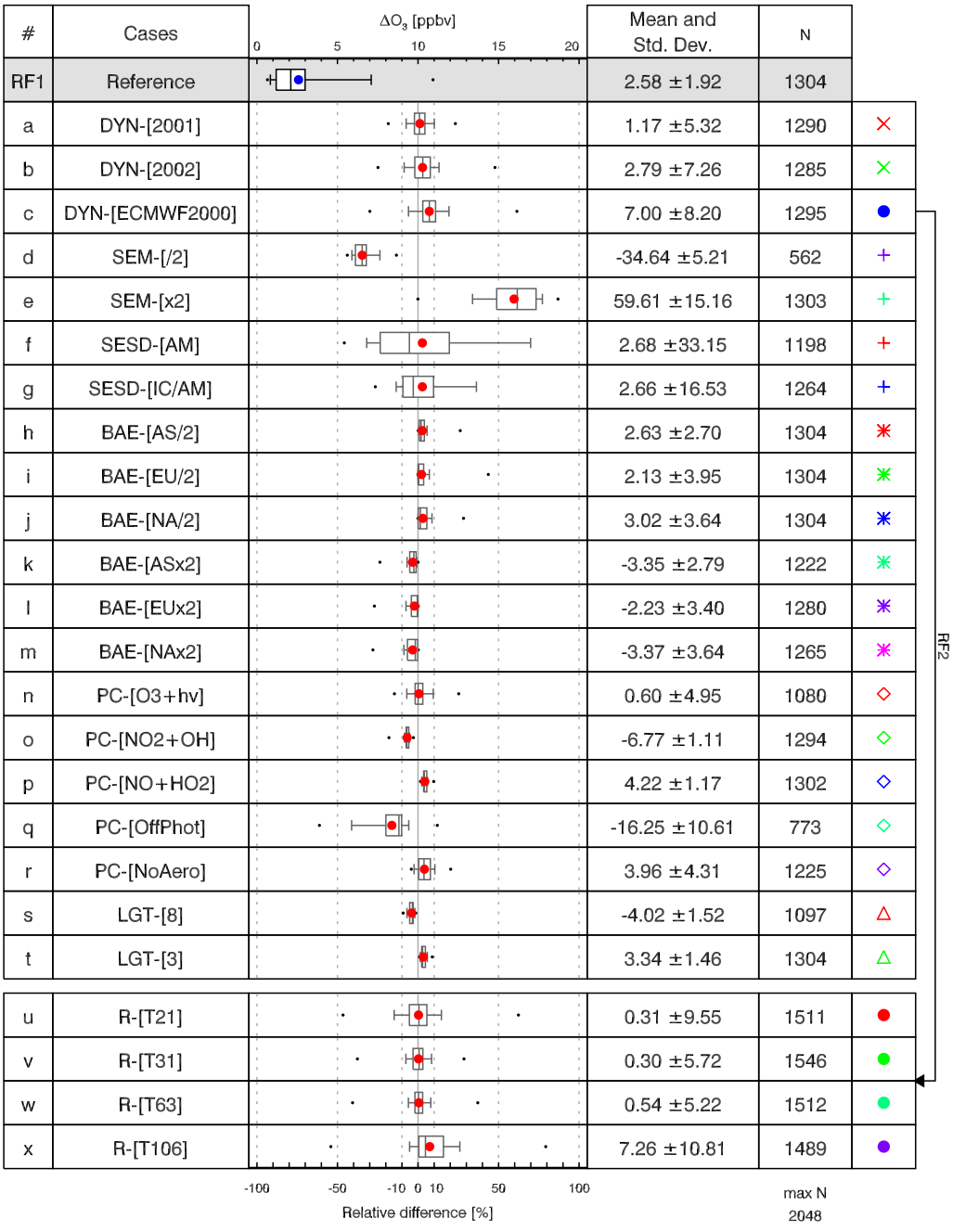

FIGURE 6.8: Same as figure 6.7 for O_3

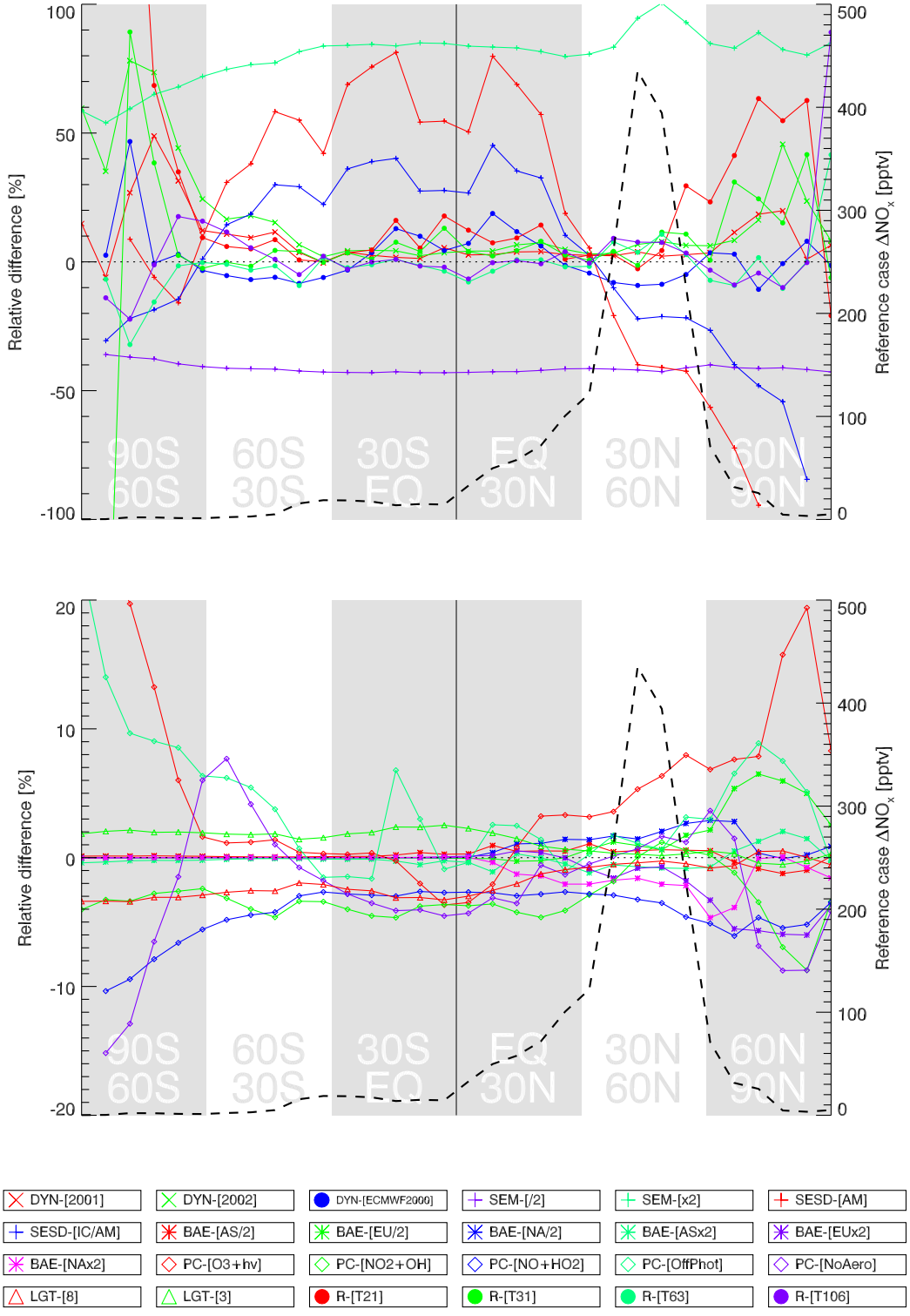

FIGURE 6.9: Annually averaged NO_x zonal means at the model lowest level. The left plots show cases with global means or standard deviations larger than 10% while the right plots display the remaining cases. The symbol and colour codes are also given on figures 6.7 and 6.8.

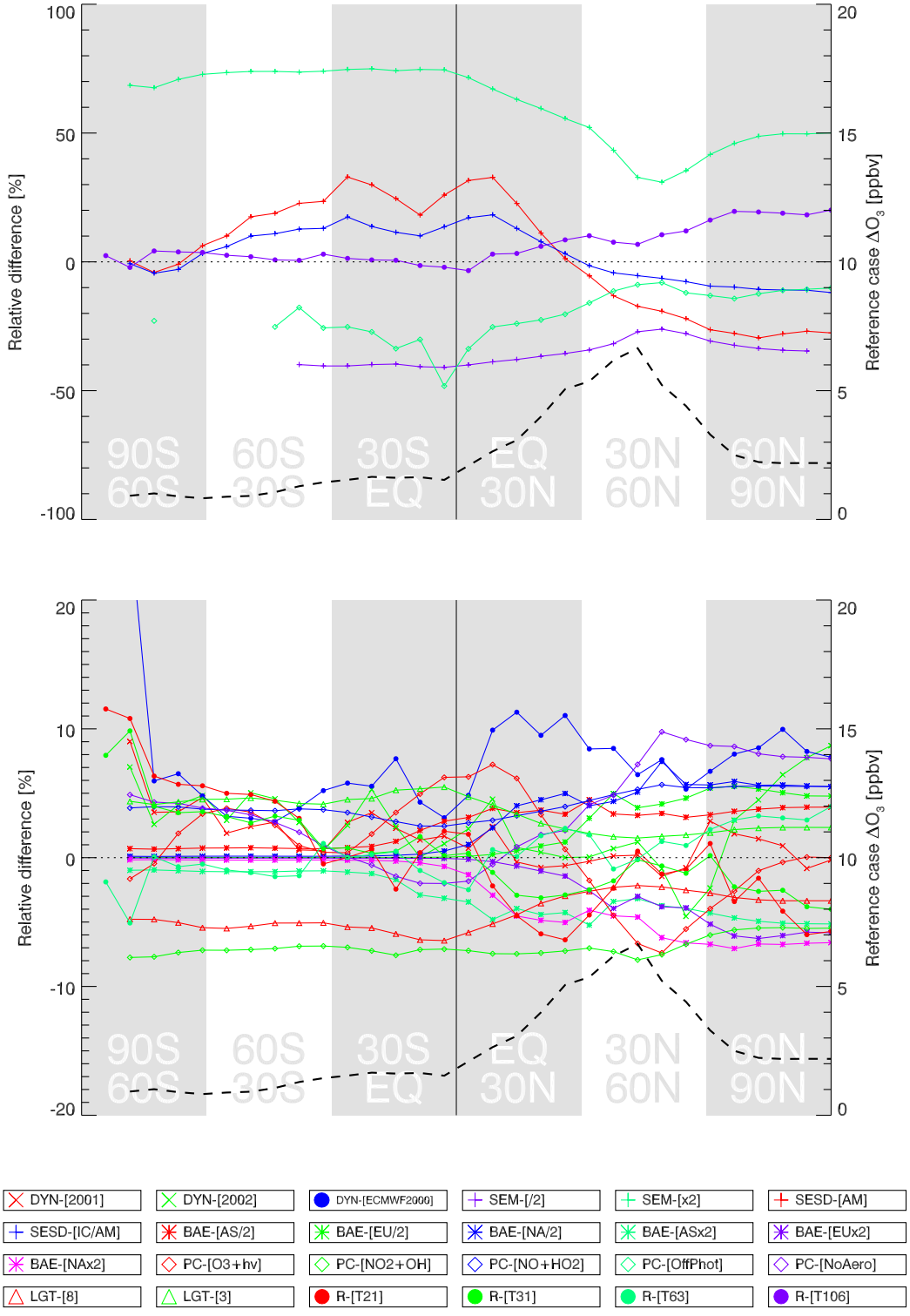

FIGURE 6.10: Annually averaged O_3 zonal means at the model lowest level. The left plots show cases with global means or standard deviations larger than 10% while the right plots display the remaining cases. The symbol and colour codes are also given on figures 6.7 and 6.8.

6.3.1.1 Shipping emission magnitude

From the statistical summaries provided on figures 6.7 and 6.8, it is clear that current uncertainties in shipping emissions produce the largest changes in NO_x and O_3 surface perturbations. Indeed, the two cases with changes in the magnitude of shipping emissions present annually and globally averaged relative differences of 78.9% and -41.5% for NO_x and 59.6% and -34.6% for O_3 (**d** & **e**).

Although emission magnitudes have been uniformly scaled up and down, the NO_x and O_3 responses are not exactly proportional to these changes. In particular, the NO_x and O_3 curves of the SEM-[x2] case vary much more than that of the SEM-[/2] case, reflecting the complexity and non-linearity in the production and destruction of these two species (figures 6.9 and 6.10).

Interestingly, the shipping-induced NO_x maximum seen in the Northern Pacific in the reference case (see chapter 5) is increased by more than a factor of 2 during the month of July, but also on an annual average when emissions are increased by a factor of 2 confirming then that NO_x production terms are larger than sink terms (figures 6.11 and D.1 **e.3**). In addition, a decrease in shipping O_3 concentrations is also visible at the same location (figures 6.11 and D.2 **e.3**). This decrease is undoubtedly related to the NO_x maximum and indicates that O_3 production has reached saturation which is followed by a build-up of NO_x that induces O_3 destruction. Although it is not obvious on the maps, a similar decrease is situated near the port of Marseilles in July in the SEM-[x2] case. In fact, the largest changes in O_3 are found in the tropics in July where relative differences lie between 2.0 and 0.5 between these two cases. Interestingly, the SEM-[x2] case also leads to level enhancements in the Arctic regions where shipping perturbations can be increased by up to a factor of 1.88 also in July.

6.3.1.2 Shipping emission spatial distribution

The picture is slightly different for the two cases related to changes in the spatial distribution of shipping emissions (**f** & **g**). These differ on average by up to 31.1%

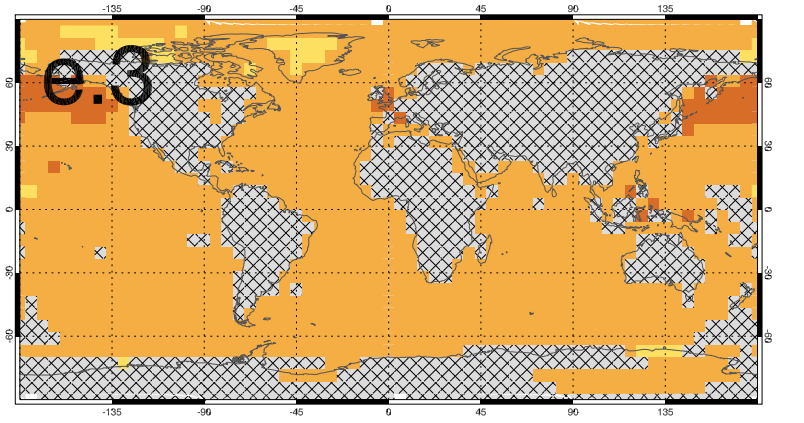

(a) NO_x

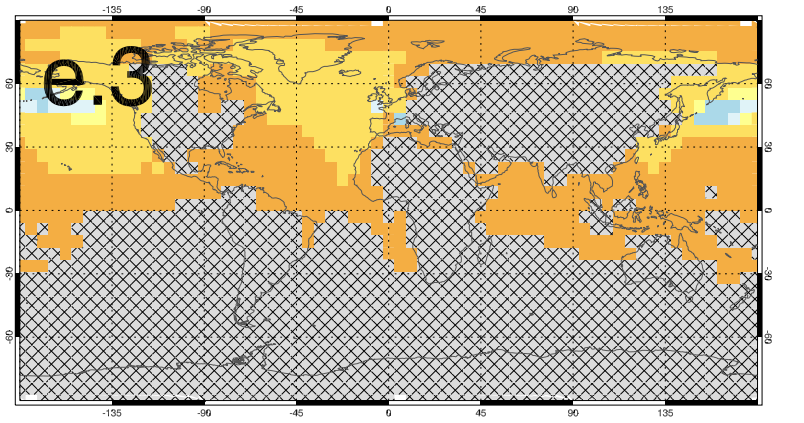

(b) O_3

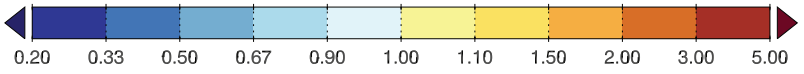

FIGURE 6.11: NO_x (a) and O_3 (b) relative differences between the SEM-[x2] and RF1 cases in July.

for NO_x but only up to 2.7% for O_3 (figures 6.7 and 6.8). In addition, the large standard deviations on those figures provide evidence for the spatial extent of the changes.

In fact, one can verify on figures 6.9 and 6.10 that the southern shift of shipping traffic in AMVER and AMVER-ICOADS yields a corresponding shift in NO_x and O_3 concentrations.

A closer look at the maps on figure 6.12 as well as those in the appendix D.1 **f.*** &

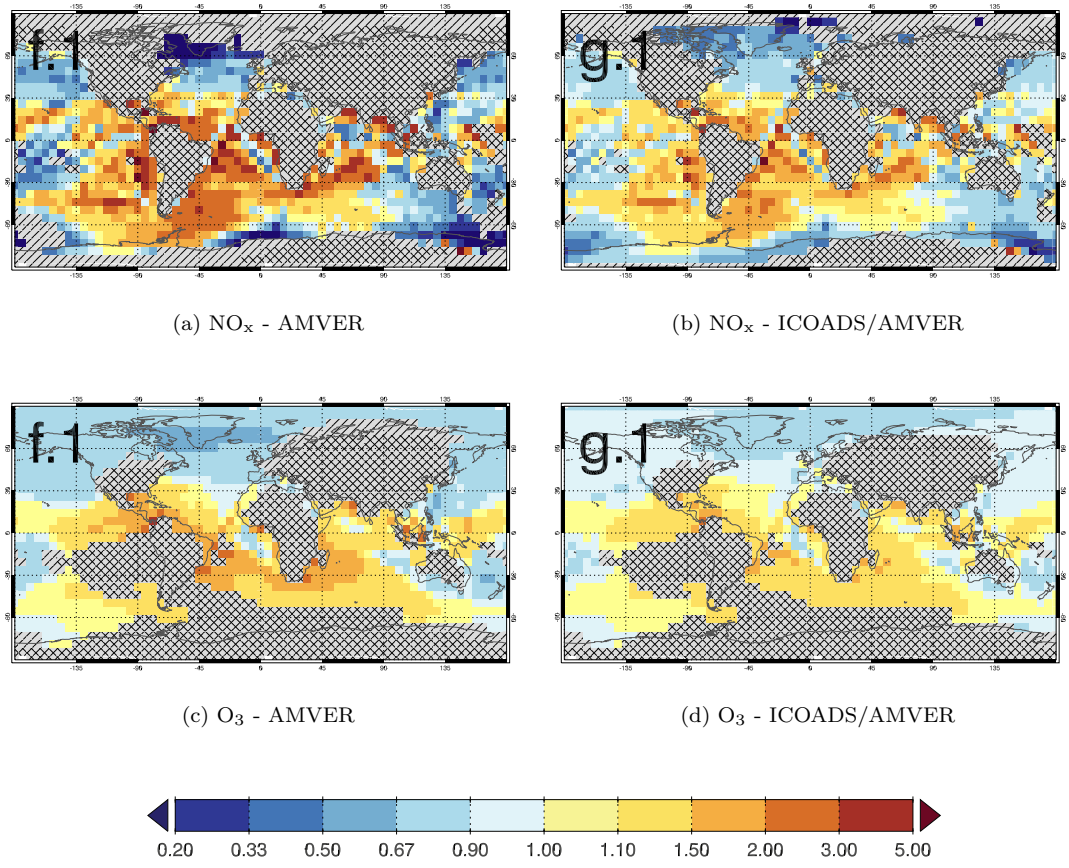

(a) NO_x - AMVER (b) NO_x - ICOADS/AMVER

(c) O_3 - AMVER (d) O_3 - ICOADS/AMVER

FIGURE 6.12: Annually averaged NO_x (a,b) and O_3 (c,d) relative differences between the SESD-[AM], SESD-[IC/AM] and RF1 cases.

g.* and D.2 **f.*** & **g.*** show that this shift entails lower NO_x and O_3 levels at latitudes above 30°N. Furthermore, the largest differences are located along the main ship lanes where levels can be enhanced by up to a factor of 5. In the SESD-[AM] case, the NO_x perturbation maximum in the Northern Pacific region is found to decrease by a maximum factor of 3. These differences remain similar in magnitude and spatial distribution throughout the year. Again, the O_3 perturbation is correlated to that of NO_x. Maximum and minimum perturbations are both found in July when the AMVER spatial distribution is used and correspond to factors of 2.97 and 0.21 respectively.

6.3.1.3 Horizontal resolution

As for the four cases focusing on changes in horizontal resolution, their annual and global means form interesting curves that span over [-0.9%, 24.7%] for NO_x and [0.3%, 7.3%] for O_3 (figures 6.7 and 6.8). In the case of NO_x, a C-shape can be noticed suggesting that an increase or a decrease of horizontal resolution result overall in NO_x increases whilst averaged O_3 seems to increase relatively steadily with resolution changes. The NO_x minimum is reached in the R-[T63] case. It is also interesting to note that standard deviations become larger as resolution increase or decrease.

The explanation for the odd-shaped NO_x curve is given on figure 6.9 which reveals that two competing factors determine NO_x changes. On the one hand, the use of coarse resolutions induces smaller shipping NO_x concentrations over large regions but allows shipping perturbations to reach further locations. On the other hand, fine resolutions enable shipping inventories to become more precise with larger emission rates in smaller grid cells. This will lead to larger NO_x concentrations in regions with high traffic.

However, one has to look at the January and July map plots to fully understand this behaviour (figures 6.13, D.1 **u.2**, **x.2**, **u.3** & **x.3**). These maps show that the largest impacts are located in the polar regions where an increase in resolution decreases NO_x concentrations during summertime but increases them during wintertime. A reduction in NO_x concentrations is also visible along the main ship lanes in the tropical regions in the Indian Ocean and off the West coast of Africa where values can be reduced by more than a factor of 0.8. In the European, Atlantic and Pacific regions no clear pattern can be discerned.

In the polar regions, the O_3 behaviour is similar to that of NO_x. A reduction of O_3 can also be noticed over most of the oceans with increasing resolution, except during the month of January when O_3 concentrations are increased by more than 10% between R-[T106] and R-[T42] cases. At a T21LR resolution, net decreases in O_3 concentrations are revealed close to coastal locations (figures 6.14 and D.2 **u.***).

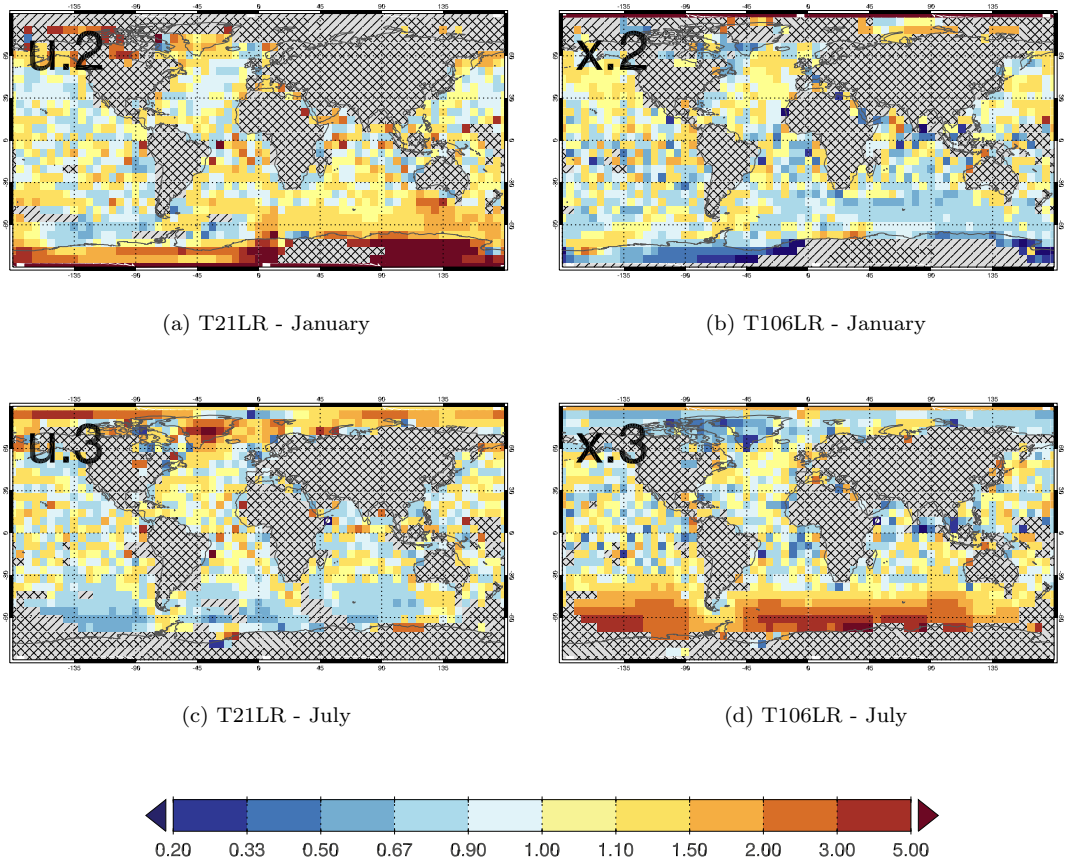

(a) T21LR - January

(b) T106LR - January

(c) T21LR - July

(d) T106LR - July

FIGURE 6.13: NO_x relative differences between the R-[T21], R-[T106] and RF2 cases in January and July.

This phenomenon emphasizes the impact of inland pollution on coastal locations at coarse resolutions.

6.3.1.4 Dynamical data

NO_x and O_3 changes resulting from the use of different years of dynamical data are sparsely distributed and mainly affect NO_x. In the case with maximum impact (DYN-[2002]), the annually and globally averaged NO_x difference equals 18.9% while its corresponding O_3 value is only 2.8% (figure 6.7). In DYN-[2001], these figures represent 9.0% and 1.2% respectively. The turbulent motion of the PBL generate noisy patterns which are noisier on the NO_x plots than on the O_3 plots because of the different lifetimes of these gas species. NO_x standard deviations equal to $\pm$34.2% in 2002 while those of O_3 equal to $\pm$7.3%.

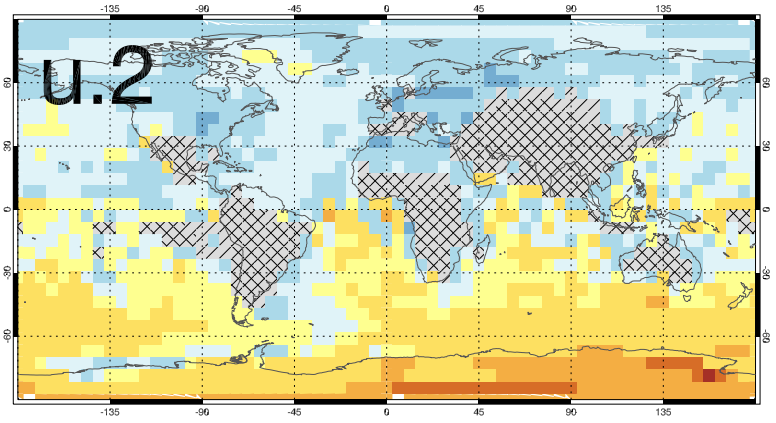

(a) January

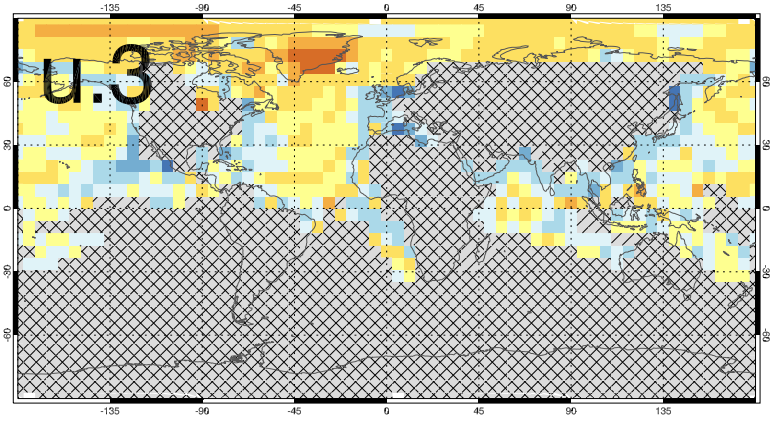

(b) July

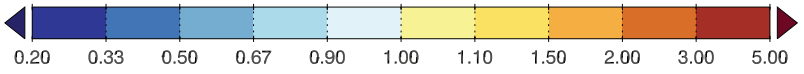

FIGURE 6.14: O_3 relative differences between the R-[T21] and RF2 cases in January (a) and July (b).

For NO_x, the zonal mean plot (figure 6.9) and map plots (figures 6.15 and D.1 **a.*** & **b.***) show that the largest increases are in the polar regions where levels are enhanced by more than a factor of 3 at some locations (Northern coast of Scandinavia and near the Antarctic coast line at 45°W and 140°E, see figure D.1 **b.1**). Between 60°N and 60°S, some regions see a maximum increase by 1.5 while other see a maximum decrease by 0.38.

As for O_3, perturbations are similar to those of NO_x. Interestingly, the 5%-cut-off

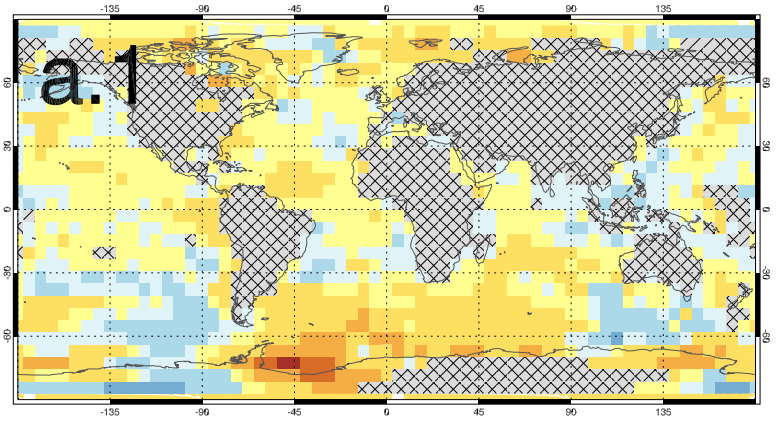

(a) 2001

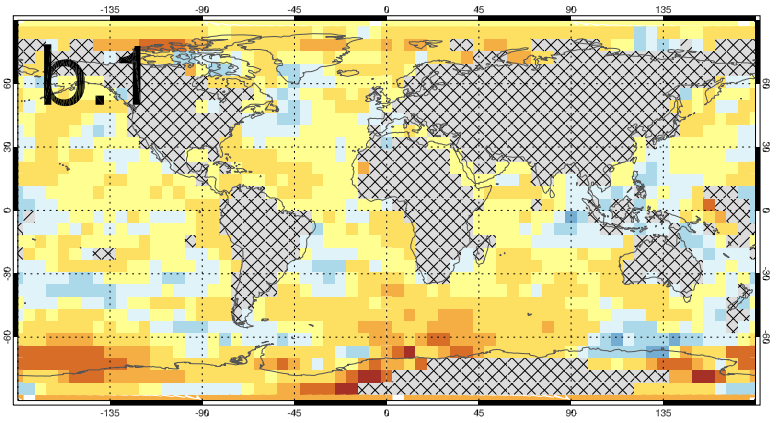

(b) 2002

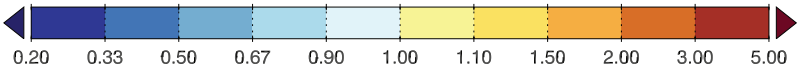

FIGURE 6.15: Annually averaged NO_x relative differences between the D-[2001], D-[2002] and RF1 cases.

reveals that the oceanic areas located to the East of continents have a weaker O_3 production owing to the pollution outflows coming from urbanised areas. In January, larger O_3 concentrations seen along the coastline of Antarctica in 2001 and 2002 can be increased by a factor of 3.14 (figures 6.16 and D.2 **a.2** & **b.2**). For both years in July, there is an increase of O_3 concentrations by up to a factor of 2.5 whereas these concentrations decrease in the North Pacific and the Arctic region above Europe. The smallest decreases are simulated in the North Pacific in July 2001 and in the Arctic region in July in 2002 and equal 0.29 and 0.40

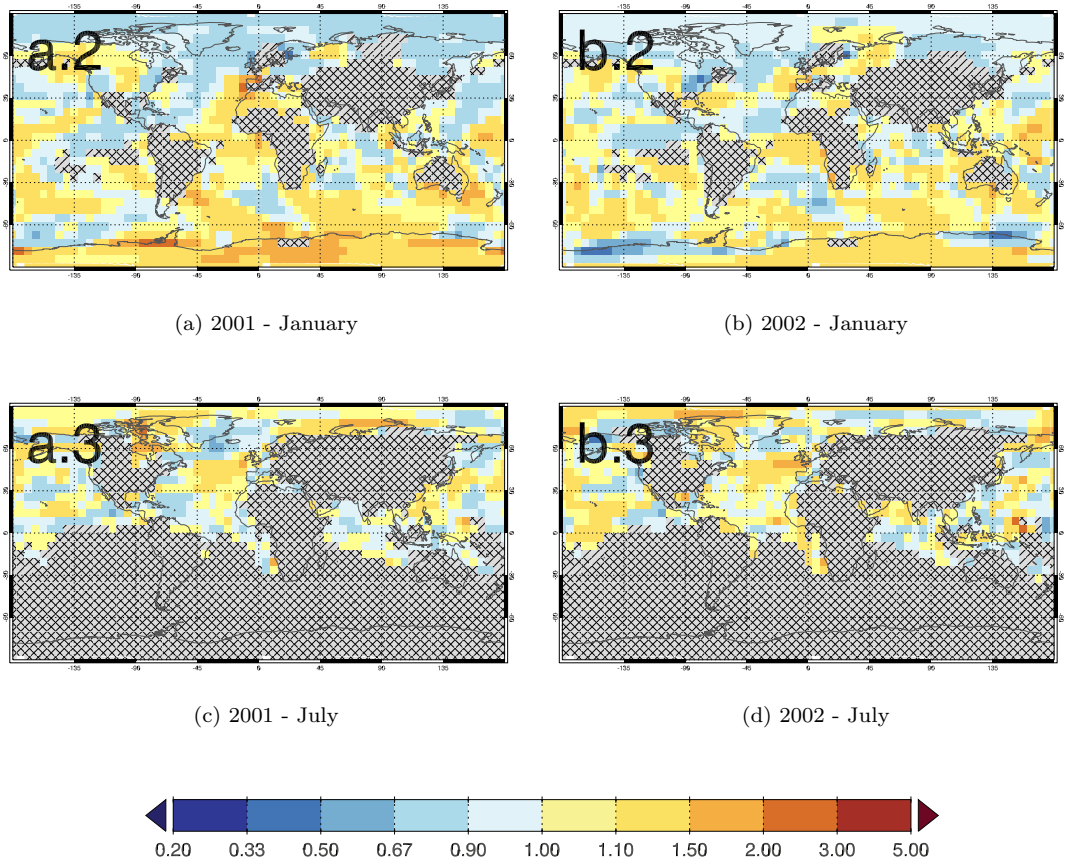

(a) 2001 - January

(b) 2002 - January

(c) 2001 - July

(d) 2002 - July

FIGURE 6.16: O_3 relative differences between the D-[2001], D-[2002] and RF1 cases in January and July.

respectively (figures 6.16 and D.2 **a.3** & **b.3**).

Compared to the DYN-[2001] and DYN-[2002], the NO_x global mean in DYN-[ECMWF2000] case is much smaller (1.5%). However, the O_3 global mean is larger (7.0%) (figures 6.7 and 6.8). It is also interesting to note that the NO_x standard deviation is in the same order of magnitude than the 2 NCEP cases ($\pm$24%). In addition, the zonal mean plot shows that there are NO_x increases in the tropical regions and decreases in the midlatitudes (figures 6.9 and 6.10). O_3 concentrations rise as a consequence in the tropical and midlatitudinal regions.

6.3.1.5 Offline photolysis scheme

The switch to offline photolysis scheme leads to an annually and globally averaged decrease in O_3 of -16.3% and to a small increase in NO_x of 4.5% (figures 6.7 and 6.8). The zonal mean plots show moderate NO_x increases of about 10% in the polar regions but also in the southern tropics (figure 6.9). In contrast, O_3 levels are decreased by more than a factor of 0.7 in the tropics and by about a factor of 0.9 in the northern midlatitudes and polar region (figure 6.10). In this case, it is interesting to see that the distributions of NO_x and O_3 look poorly related indicating that the NO_x-O_3-HO_x chemical system does not play a significant role in these changes. Maps on figures 6.17 as well as those in the appendix (D.1 **q.*** and D.2 **q.***) confirm these results.

6.3.1.6 Other photochemistry

The large effects presented in the previous sections are followed by less substantial ones that fall on a global average into the [-10%, 10%] range. For instance, impacts from changes in the photochemical system range between [-4.3%, 5.7%] and [-6.8%, 4.2%] for NO_x and O_3 respectively.

Effects of the O_3 photolysis are overall not significant for NO_x concentrations, except in the North Pacific Ocean and the Antarctic Ocean where they can increase by up to 50% (figures 6.18 and D.1 **n.***). Conversely, the shipping O_3 perturbation is quite sensitive to O_3 photolysis. Minimum ratios of 0.69 and 0.63 can be seen in the South hemisphere in January and in the North hemisphere in July respectively (figures 6.18 and D.2 **n.***).

Increasing the termolecular reaction rate constant between NO_2 and OH has a moderate effect on the shipping NO_x perturbation yielding a relative difference of -3.54%. In the tropics, NO_x concentrations tend to be enhanced by more than 1.1 and up to 1.33 (figures 6.19 and D.1 **o.***). In the Northern hemisphere, NO_x concentrations are decreased by up to 0.67 off the North American and European

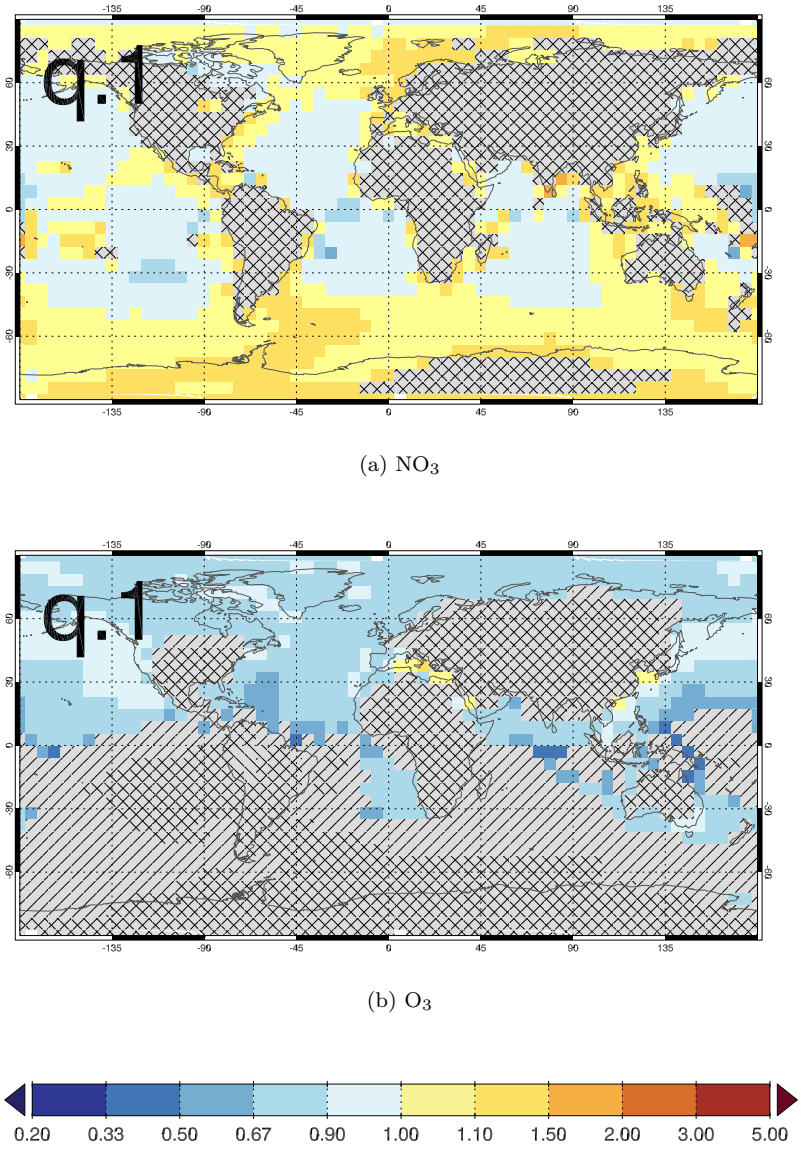

(a) NO_3

(b) O_3

FIGURE 6.17: Annually averaged NO_x and O_3 relative differences between the PC-[OffPhot] and RF1 cases.

coasts. In the case of O_3, annually and globally averaged relative differences are nearly doubled and equal -6.77%.

The decrease in the rate of the reaction between NO and HO_2 also has a moderate effect of -4.32% for NO_x and 4.22% for O_3. These opposite magnitudes may be understood by the fact that this reaction increases the ratio NO_2/NO_x which yields more NO_x destruction but at the same time increases the ratio OH/HO_x which leads to enhanced O_3 levels.

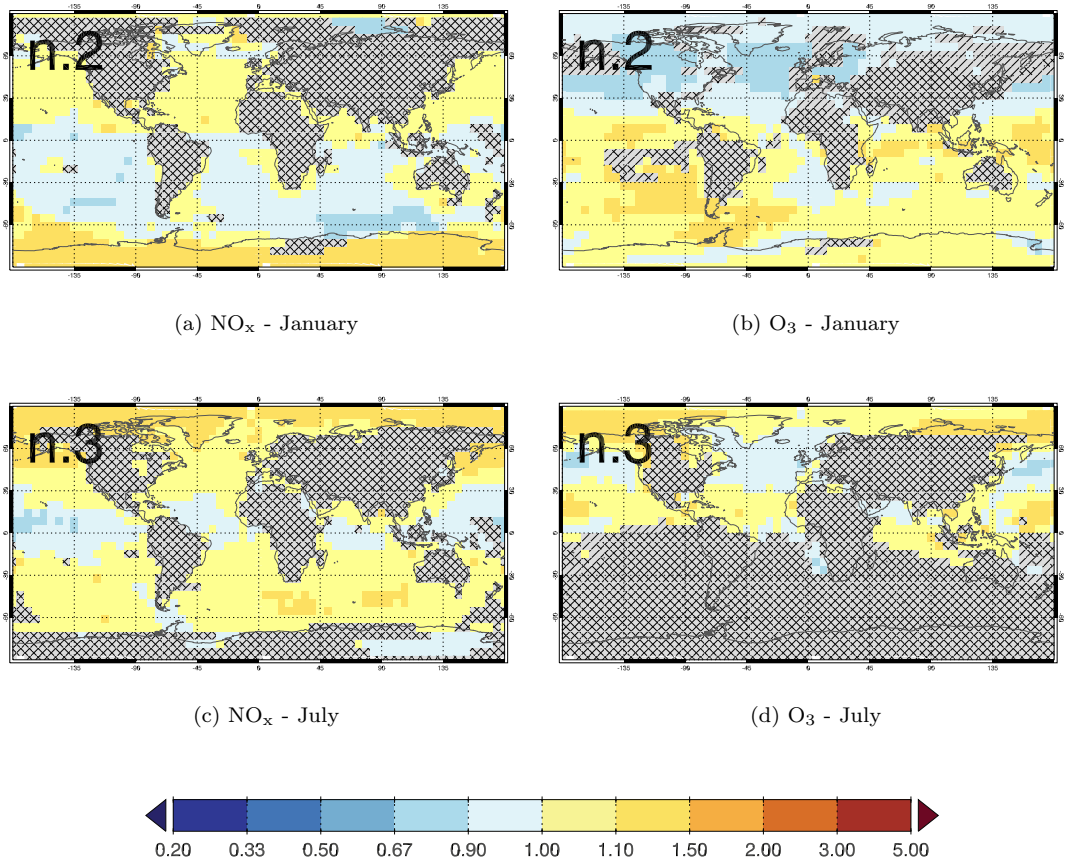

(a) NO_x - January

(b) O_3 - January

(c) NO_x - July

(d) O_3 - July

FIGURE 6.18: NO_x and O_3 relative differences between the PC-[O3+hv] and RF1 cases in January and July.

Finally, the PC-[NoAero] case presents substantial effects that can reach more than a factor of 2 in the polar regions and which sometimes extend to the midlatitudes (figures 6.20 and D.2 **r.***).

6.3.1.7 Lightning activity

NO_x and O_3 perturbations are relatively small since lightning NO_x is produced over tropospheric vertical columns. Consequently, O_3 perturbations are not significantly affected at the surface and globally and annually averaged relative differences lie between -1.97% and 1.35% for NO_x and between -4.02% and 3.34% for O_3 (figures 6.7 and 6.8). The largest impacts are found for both cases in the tropics between 15°N and 15°S where lightning activity is strong but relative differences remain in the range [0.8, 1.2] (figures 6.21 and D.2 **s.*** & **t.***). Interestingly,

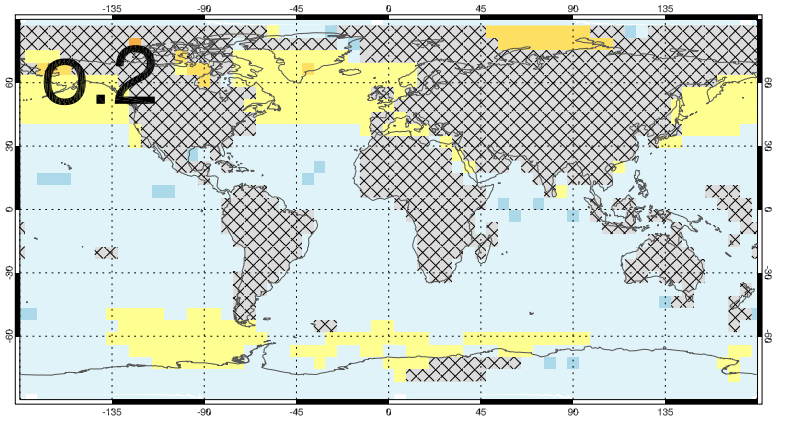

(a) January

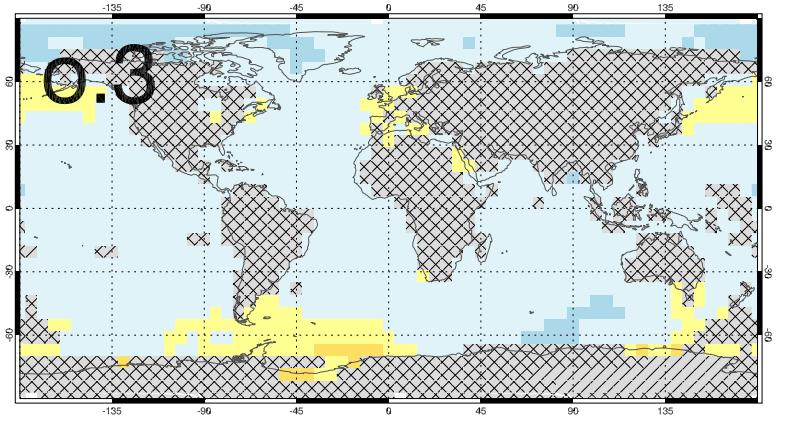

(b) July

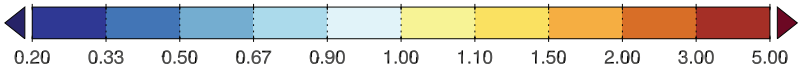

FIGURE 6.19: NO_x relative differences between the PC-[NO2+OH] and RF1 cases.

the result from a decrease in lightning activity is symmetrically opposed to those resulting from an increase (figures 6.9 and 6.10).

6.3.1.8 Background anthropogenic emissions

Changes in background anthropogenic emissions (BAE) remain smaller than ±3.5% on average (figures 6.7 and 6.8). Zonal mean plots of NO_x and O_3 show that shipping perturbations respond symmetrically to a doubling or halving in regional

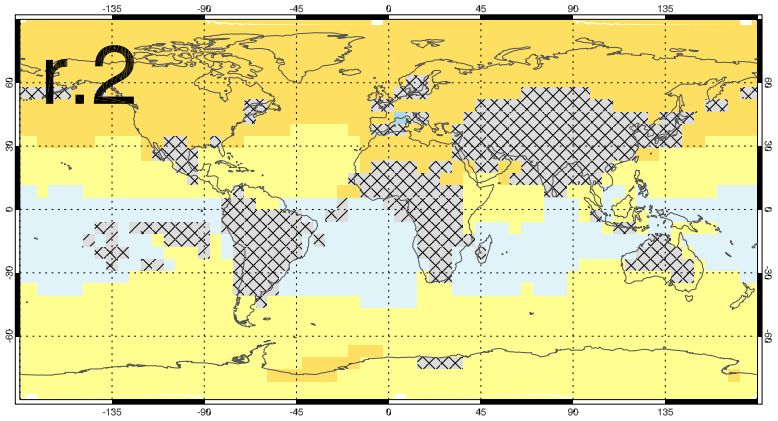

(a) January

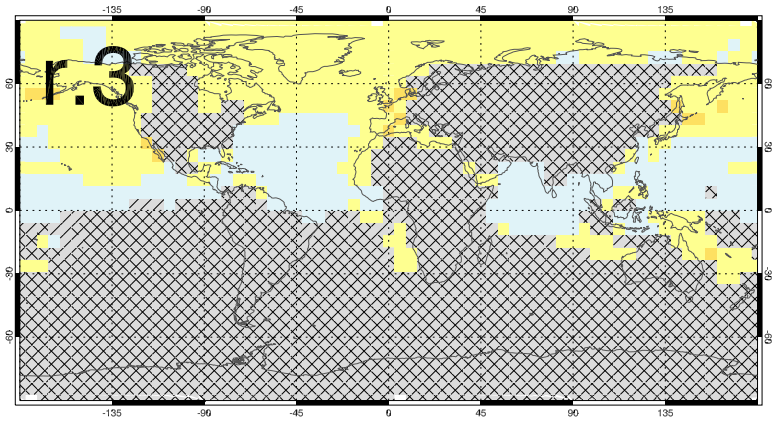

(b) July

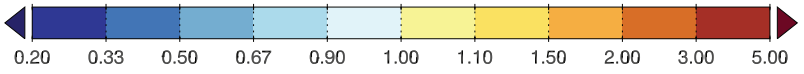

FIGURE 6.20: O_3 relative differences between the PC-[NoAero] and RF1 cases.

background emissions (figures 6.9 and 6.10). They also reveal that much of the Asian and European perturbations of NO_x and O_3 are located in the north polar region whilst that of North America peaks at 60° (relative differences remain in the range [0.93, 1.07]). These spatial characteristics are also displayed on the maps (figures 6.22 and D.1 and D.2 **h-m.***). For instance, one can see the extend of the perturbation resulting from a doubling or halving background anthropogenic emissions in the Asian and European regions that spreads over the Arctic region. It is also interesting to note that these perturbations mainly affect oceanic regions

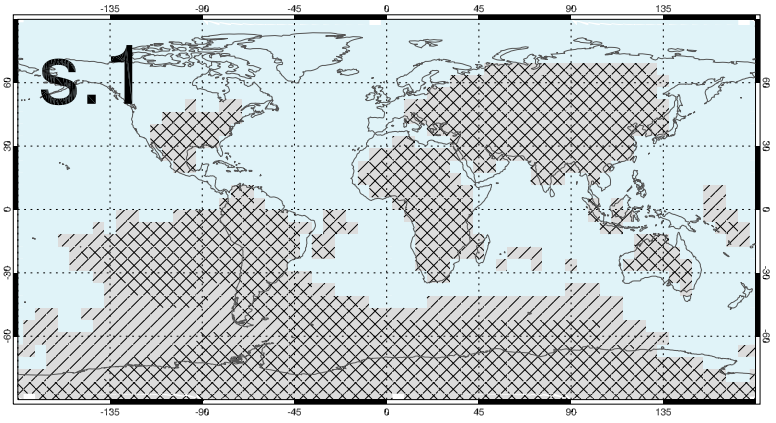

(a) Lightning x2

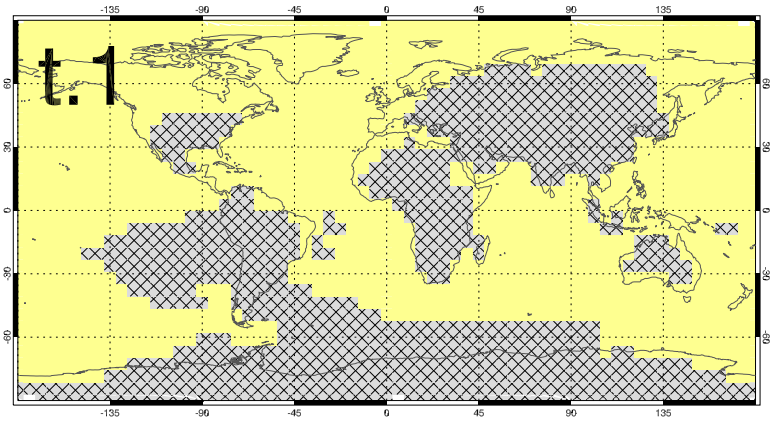

(b) Lightning /2

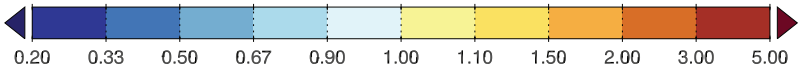

FIGURE 6.21: O_3 relative differences between the LGT-[8], LGT-[3] and RF1 cases.

close to coasts but in the case of O_3, its longer lifetime allows the perturbation to reach further in land in January (figures 6.23 and D.2 **h-m.2**).

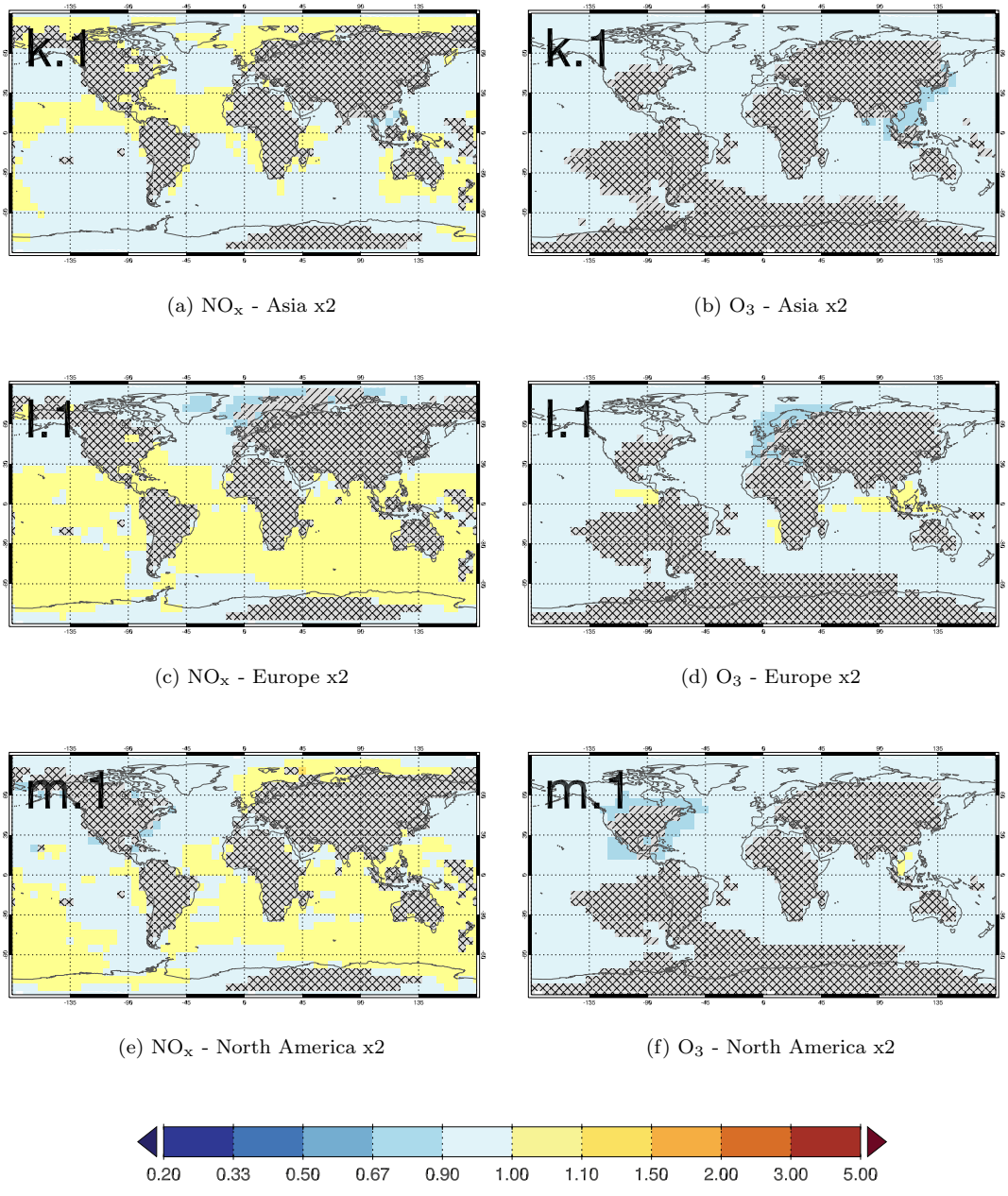

(a) NO_x - Asia x2

(b) O_3 - Asia x2

(c) NO_x - Europe x2

(d) O_3 - Europe x2

(e) NO_x - North America x2

(f) O_3 - North America x2

FIGURE 6.22: Annually averaged NO_x and O_3 relative differences between the BAE-[ASx2], BAE-[EUx2], BAE-[NAx2] and RF1 cases.

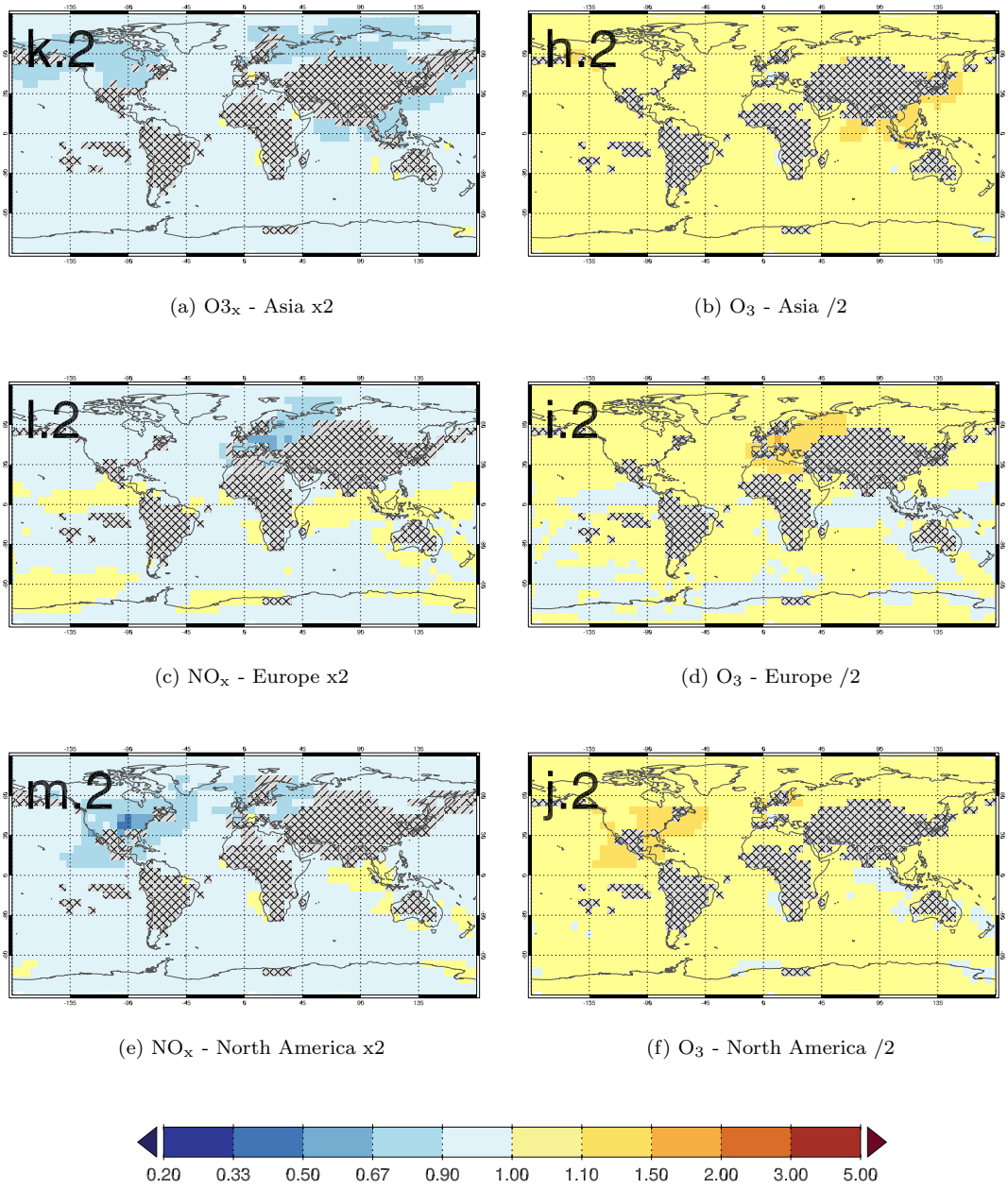

(a) $O3_x$ - Asia x2

(b) O_3 - Asia /2

(c) NO_x - Europe x2

(d) O_3 - Europe /2

(e) NO_x - North America x2

(f) O_3 - North America /2

FIGURE 6.23: and O_3 relative differences between the BAE-[ASx2], BAE-[AS/2], BAE-[EUx2], BAE-[EU/2], BAE-[NAx2], BAE-[NA/2] and RF1 cases in January.

6.3.2 Vertical structure of the changes of shipping perturbations of O_3 and OH

As in the previous section, statistical summaries of annual zonal means of O_3 and OH changes are provided (figures 6.24 and 6.25). This time, O_3 and OH perturbed and reference shipping perturbations lower than 1% relative difference were filtered out. This allows to get nearly the whole tropospheric domain and results in a selection of 522 to 552 grid cells out of 896. Globally and annually averaged vertical profiles are also displayed on figures 6.26 and 6.27. All zonal mean plots are available in appendix D. Results from the different cases are presented in a similar fashion as the previous section and follow this order: shipping emission magnitude (SEM), Offline photolysis (PC-[OffPhot]), shipping emission spatial distribution (SESD), photolysis and other photochemical (PC), lightning (LGT), dynamical (DYN), model resolution (R), and background anthropogenic emissions (BAE).

6.3.2.1 Shipping emission magnitude

On figures 6.24 and 6.25 one can see that changes in the magnitude of shipping emissions remain the dominant contributor with global mean relative differences ranging between 67.24% and -39.15% for O_3 and 65.86% and -37.86% for OH. Interestingly, O_3 relative differences are slightly larger in comparison with those calculated near the surface which indicate again a saturation of the NO_x-HO_x-O_3 chemical system close to shipping emissions. This can be seen on the globally and annually averaged vertical profile where the curve of the SEM-[x2] case bends slightly towards lower differences as it reaches the surface (figure 6.26). Zonal mean plots displayed on figures D.3 **d**.* & **e**.* show that when shipping emissions are multiplied by a factor of 2, shipping O_3 levels are enhanced by ratios ranging between 1.11 and 1.81 depending on the time of the year and the region considered. It is clear that the bottom of the atmosphere in the northern hemisphere

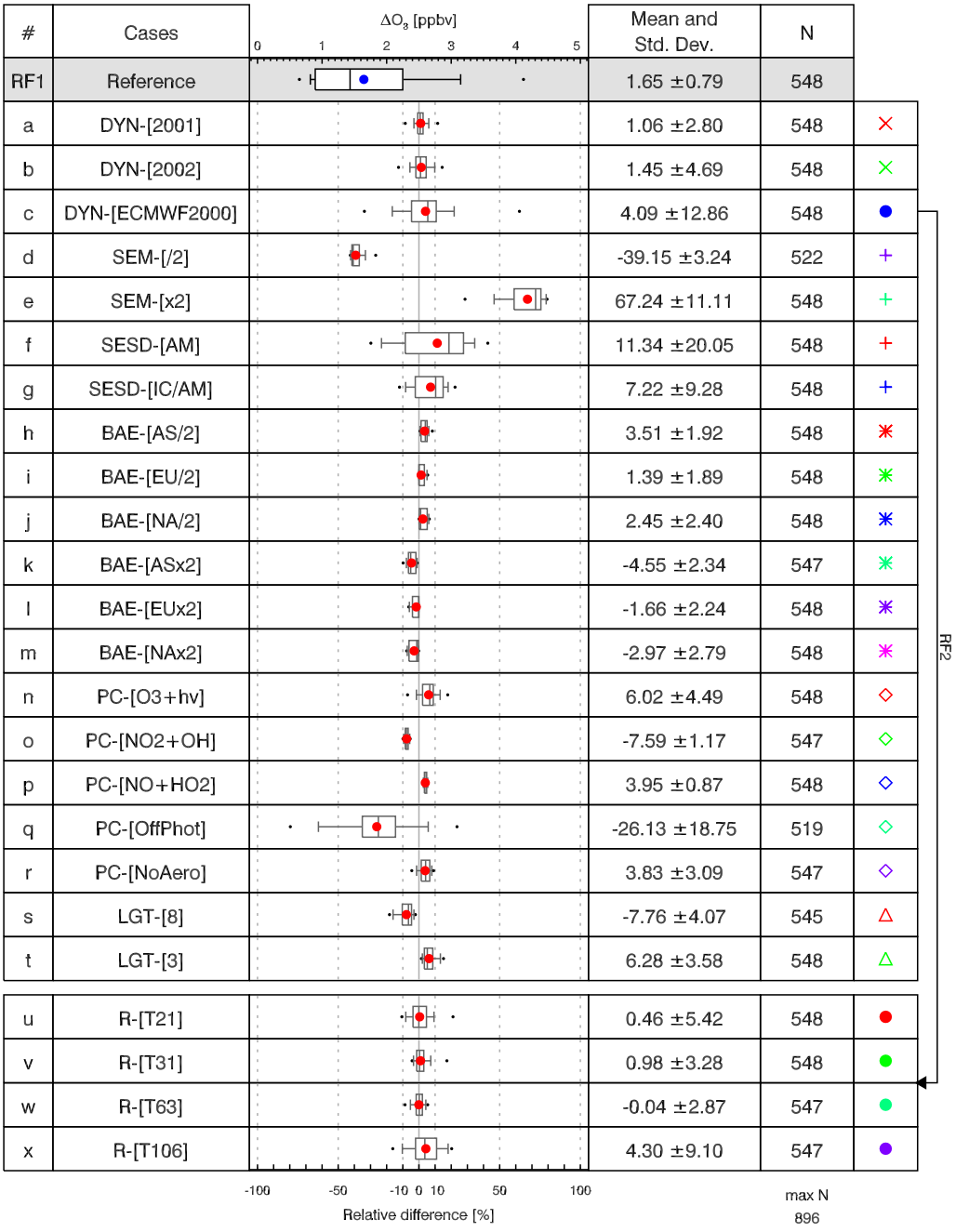

FIGURE 6.24: Statistical summary of annually averaged zonal mean O_3. Statistical information about shipping perturbations in the reference case (**RF1**) is provided at the top of the table in the shaded row. Statistical information about relative differences between shipping perturbations in the perturbation and reference cases (**RF1** & **RF2**) are listed below. N is the number of values used to performed the statistical calculations. The coloured symbols identify the zonal mean curves on figures 6.26 and 6.27.

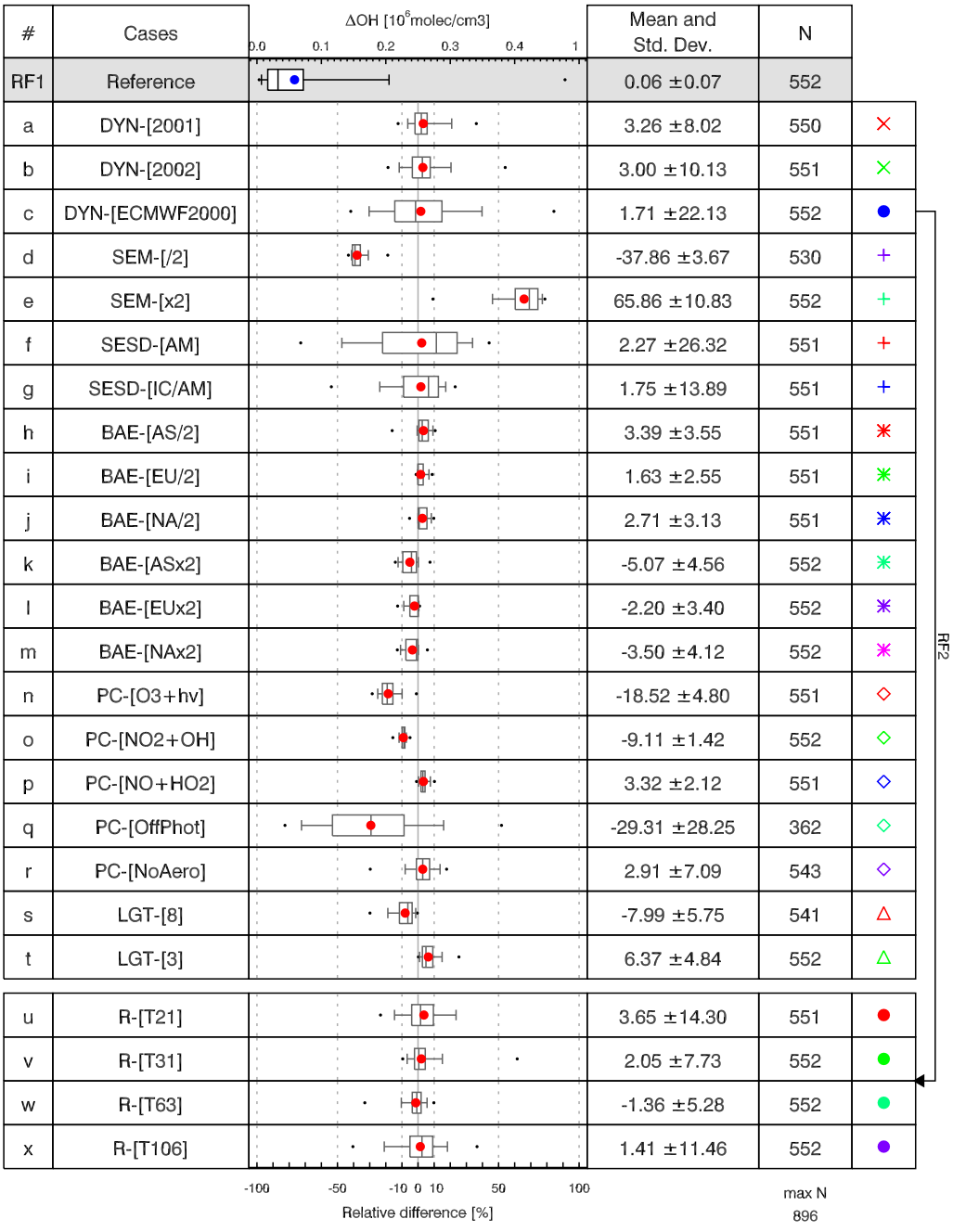

FIGURE 6.25: Same as figure 6.24 for OH

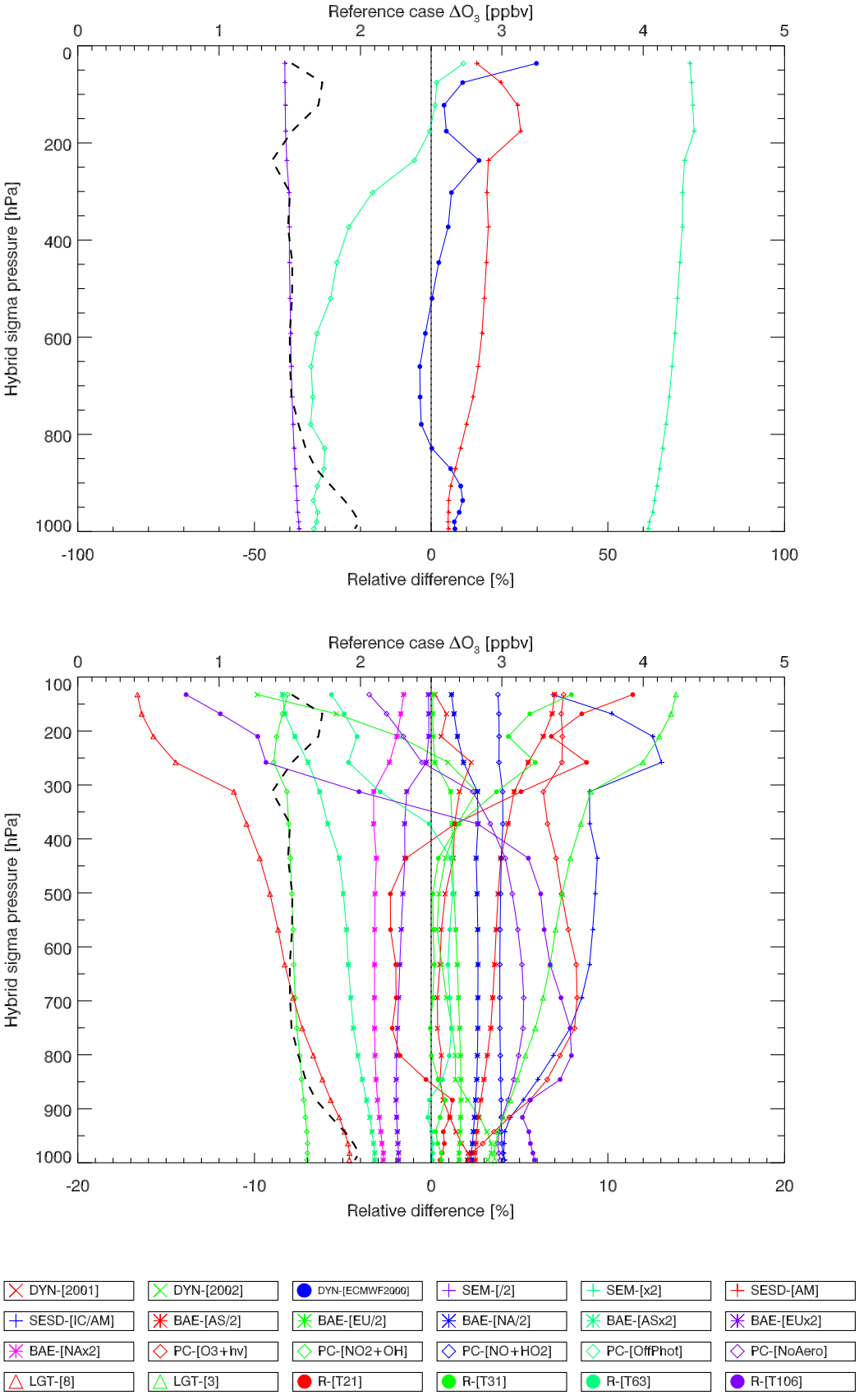

FIGURE 6.26: Annually and spatially averaged O_3 vertical profiles. The left plots show cases with global means or standard deviations larger than 10% while the right plots display the remaining cases. The symbol and colour codes are also given on figures 6.24 and 6.25.

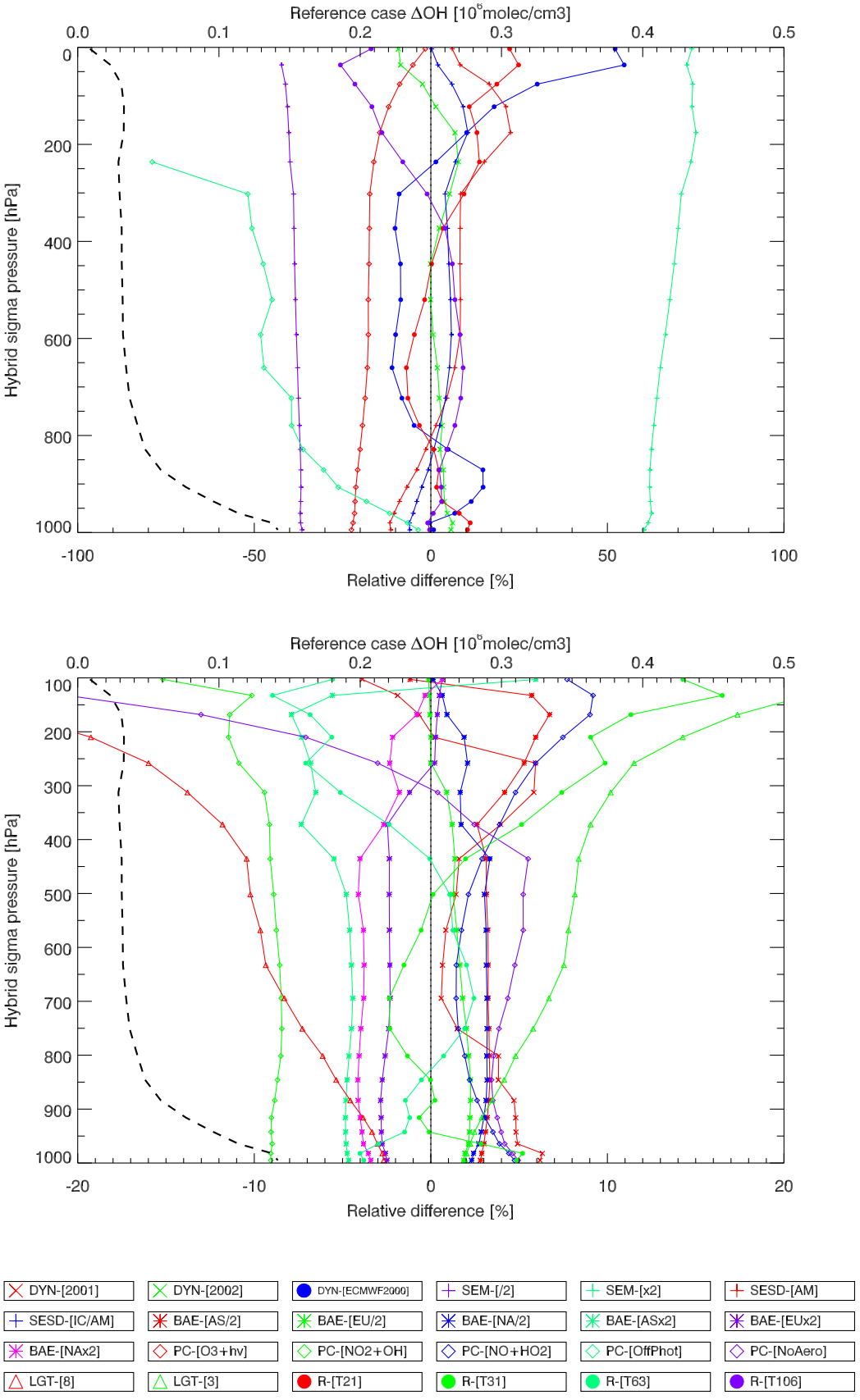

FIGURE 6.27: Annually and spatially averaged OH vertical profiles. The left plots show cases with global means or standard deviations larger than 10% while the right plots display the remaining cases. The symbol and colour codes are also given on figures 6.24 and 6.25.

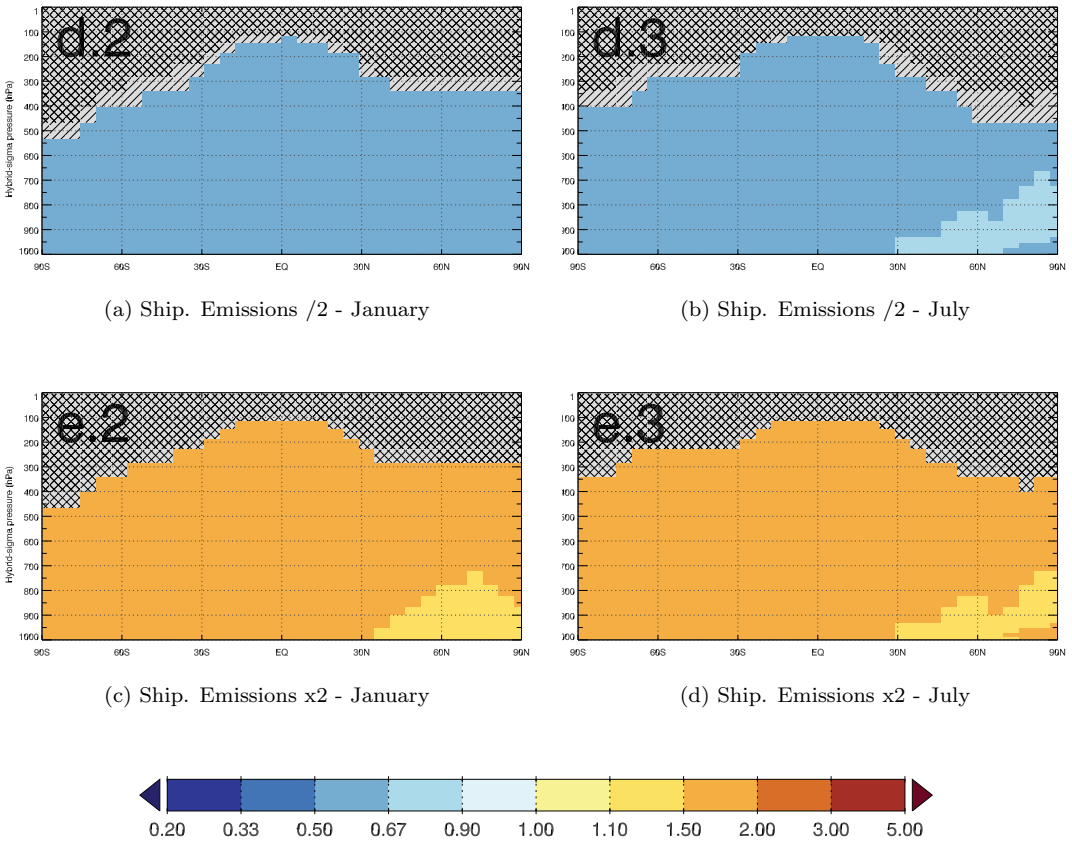

(a) Ship. Emissions /2 - January

(b) Ship. Emissions /2 - July

(c) Ship. Emissions x2 - January

(d) Ship. Emissions x2 - July

FIGURE 6.28: O_3 relative differences between the SEM-[/2], SEM-[x2] and RF1 cases in January and July.

is affected by saturation. When these emissions are decreased, shipping O_3 concentrations drop between 0.57 and 0.83. Again, the bottom of the atmosphere in the northern hemisphere shows a lower effect indicating that the current best estimate of shipping emissions is likely to be close to the optimum O_3 production of the NO_x-HO_x-O_3 chemical system. Regarding the changes in OH concentrations, decreases as large as 0.44 can be seen in January and as large as 0.38 in July in the SEM-[/2] case whereas increases as large as 2.01 can be seen in January and as large as 2.28 in July in the SEM-[x2] case (figures 6.28 as well as D.3 **d.2-3** and **e.2-3**).

6.3.2.2 Offline photolysis scheme

The switch to offline photolysis affects O_3 and OH concentrations substantially across the troposphere with global mean values of -26.13% ±18.75 and -29.31% ±28.25 respectively (figures 6.24 and 6.25). O_3 and OH ratios smaller than 0.5 are found across nearly the whole troposphere and in particular the southern tropical free troposphere on an annual average. Hatched regions emphasises the fact that the shipping O_3 perturbation in the PC-[OffPhot] case is small (relative difference becomes smaller than 1%, figures 6.29 and D.3 **q.***). Actually, absolute differences reveal that this perturbation even reaches negative values of up to -0.4 ppbv in the southern tropical mid-troposphere. Such negative values have never been reported in the literature which could indicate a problem either with the scheme or the way it is currently implemented.

6.3.2.3 Shipping emission spatial distribution

When either the AMVER or the AMVER-ICOADS spatial proxies are applied, the shift in shipping traffic towards the southern hemisphere that was displayed on the map plots in the previous section is also visible in the free troposphere (figures 6.30 and D.3 **f.*** & **g.***). Up to a 1.24 and a 1.45 increase in O_3 concentrations can be seen nearly everywhere between 90°S and 30°N in the AMVER-ICOADS and AMVER cases respectively. Concentrations decrease by less than 0.9 and up to 0.72 above 30°N for these two cases. Concerning the changes in OH concentration, the pattern is very similar on the exception of a larger decrease in the Antarctic region which appears on the annually averaged zonal mean plots of the AMVER and AMVER-ICOADS cases. The OH concentration changes range between 0.21 and 1.45 in January and between 0.18 and 4.44 in July in the AMVER case. Globally and annually averaged vertical profiles of O_3 and OH clearly show that this shift has brought the NO_x-O_3-HO_x chemical system into a higher regime of O_3 production leading to an increase in OH concentrations (figures 6.26 and 6.27). It is also worthy to note that O_3 and OH concentrations are increased by more than a factor of 1.20 in the upper troposphere above 200 hPa (figure 6.27). This

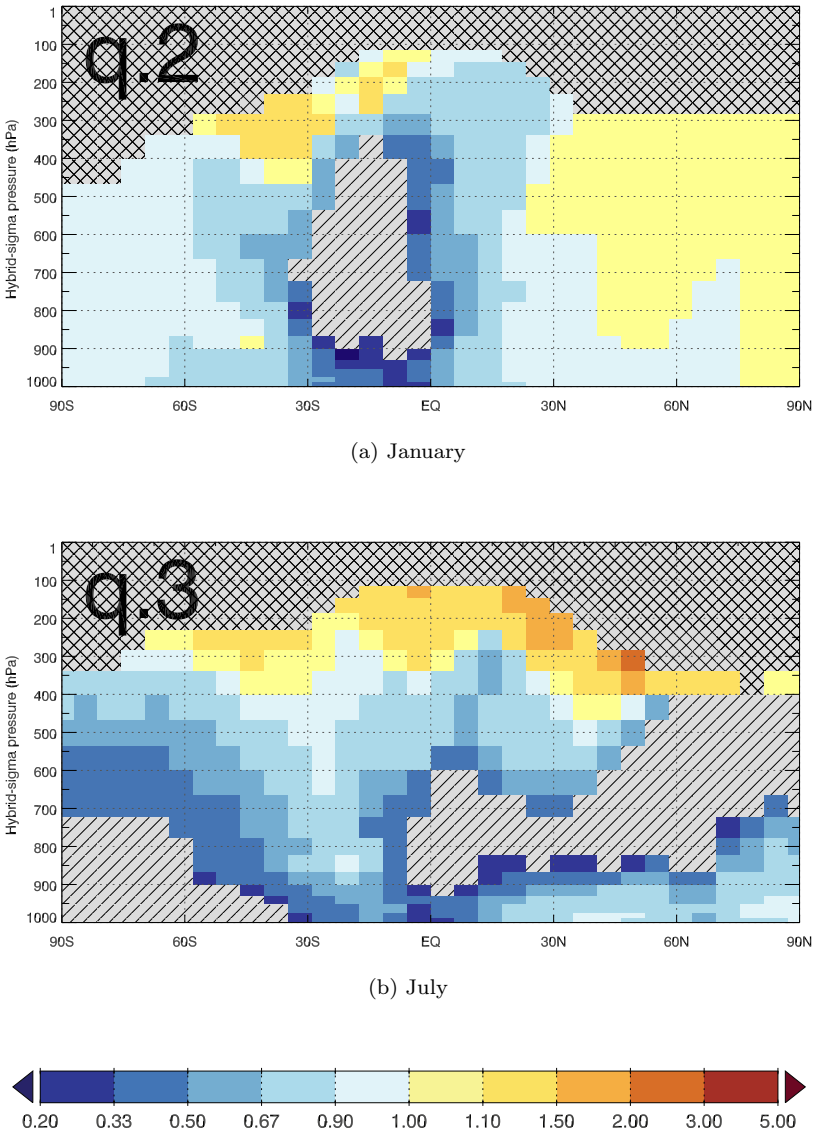

(a) January

(b) July

FIGURE 6.29: O_3 relative differences between the PC-[OffPhot] and RF1 cases in January and July.

increase demonstrates that the deep convection scheme of the model effectively lifts up O_3 precursors released by ships as noted by Horowitz et al. [2003].

6.3.2.4 Lightning activity

Although the O_3 and OH global figures of the lightning cases presented on the statistical summaries are smaller than ±10%, lightning effects lead to changes in shipping O_3 concentrations ranging between 0.7 and 1.3 in the free troposphere

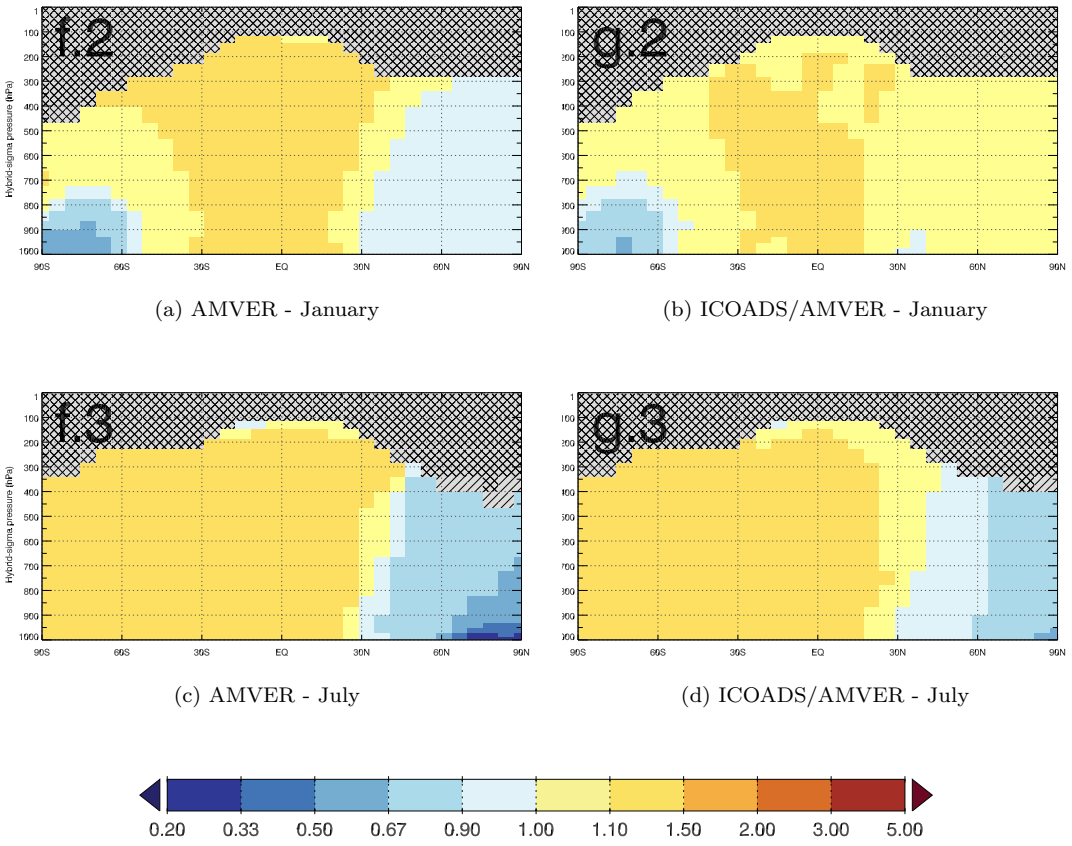

(a) AMVER - January

(b) ICOADS/AMVER - January

(c) AMVER - July

(d) ICOADS/AMVER - July

FIGURE 6.30: O_3 relative differences between the SESD-[AM], SESD-[IC/AM] and RF1 cases in January and July.

between 60°S and 30°N and changes in OH concentrations ranging between 0.6 and 1.4 (figures 6.31 and D.3 **s.*** & **t.*** and D.4 **s.*** & **t.***). The extent of lightning is wider in July than in January owing to the difference in NO_x concentrations in the background atmosphere in the Northern and the Southern hemispheres. In addition, the symmetry between the two cases can be appreciated on the globally and annually averaged vertical profiles of O_3 and OH (figures 6.26 and 6.27).

6.3.2.5 Other photochemistry

The effects of the O_3 photolysis on the O_3 concentrations present a vertical gradient in which large decreases peaking at 0.81 are found near the surface and small increases up to 1.12 in July lay near the tropopause. Regarding OH, the effects are smaller and correspond mainly to a ratio of 0.87 near the surface of the tropics.

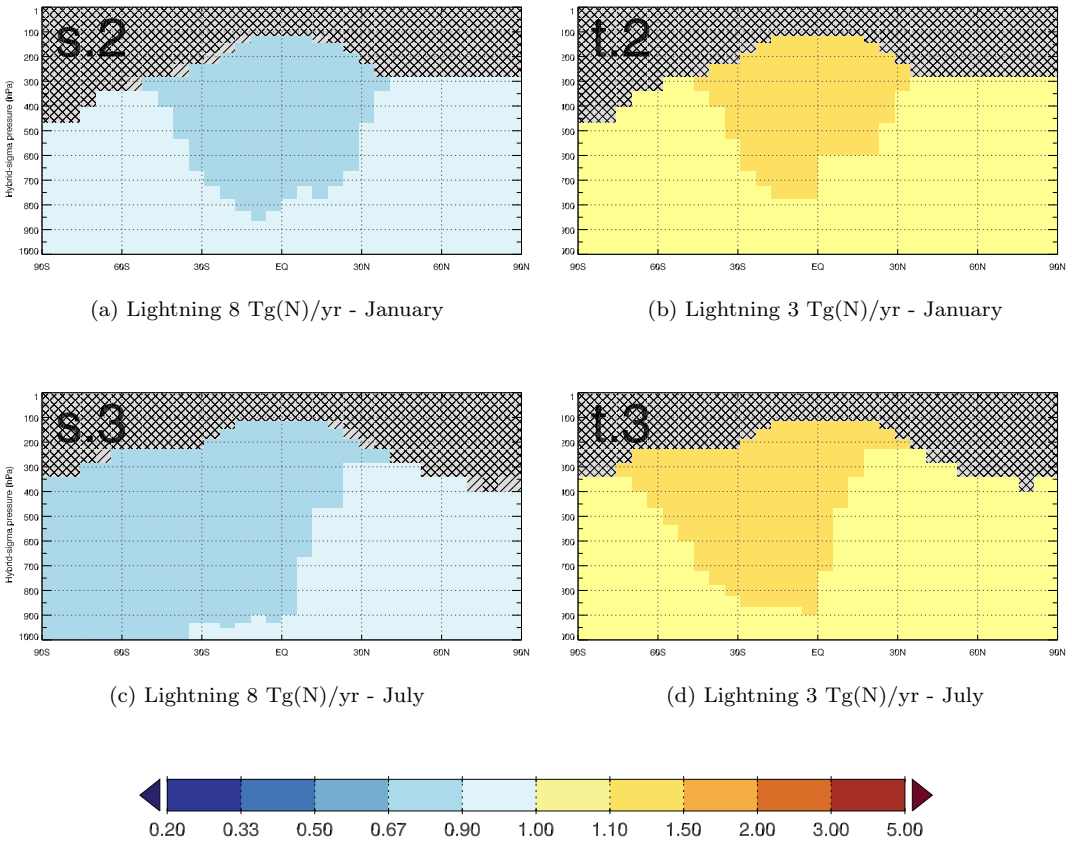

(a) Lightning 8 Tg(N)/yr - January

(b) Lightning 3 Tg(N)/yr - January

(c) Lightning 8 Tg(N)/yr - July

(d) Lightning 3 Tg(N)/yr - July

FIGURE 6.31: O_3 relative differences between the LGT-[8], LGT-[3] and RF1 cases in January and July.

Impacts of the termolecular reaction on O_3 and OH are not significant: -7.59% for O_3 and -9.11% for OH. O_3 concentration changes are usually below ±10%. The polar regions show a maximum of decrease of 0.7 in OH concentration changes in January (figures 6.32 and D.4 **o.3**).

The bimolecular reaction between NO and HO_2 does not have significant effects either. Global means on figures 6.24 and 6.25 show that it yields a 3.95% increase in O_3 and a 3.32% increase in OH.

Finally, removing aerosol chemistry from the model leads to moderate changes in global O_3 and OH zonal mean averages: 3.83% and 2.91% respectively. The zonal mean plots suggest that O_3 and OH are increased across the whole troposphere in the winter hemisphere (figures 6.33 as well as D.3 **r.2-3** and D.4 **r.2-3**).

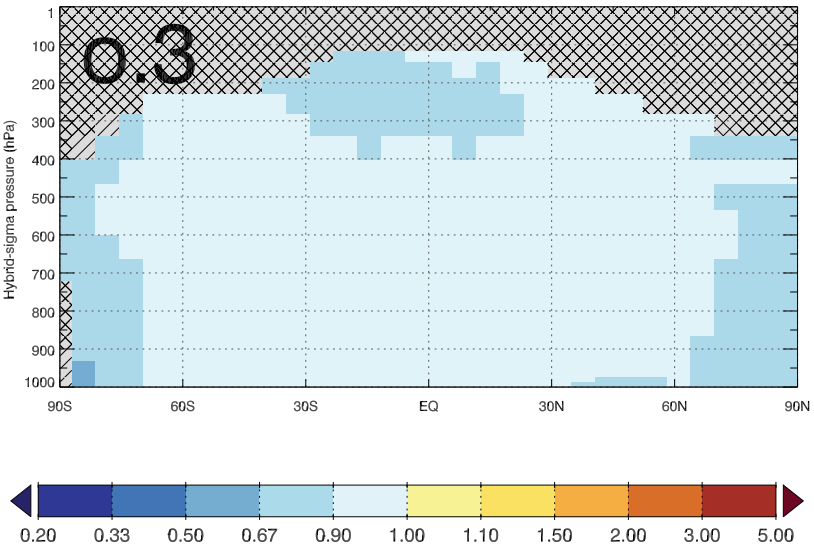

FIGURE 6.32: OH relative differences between the PC-[NO2+OH] and RF1 cases in July.

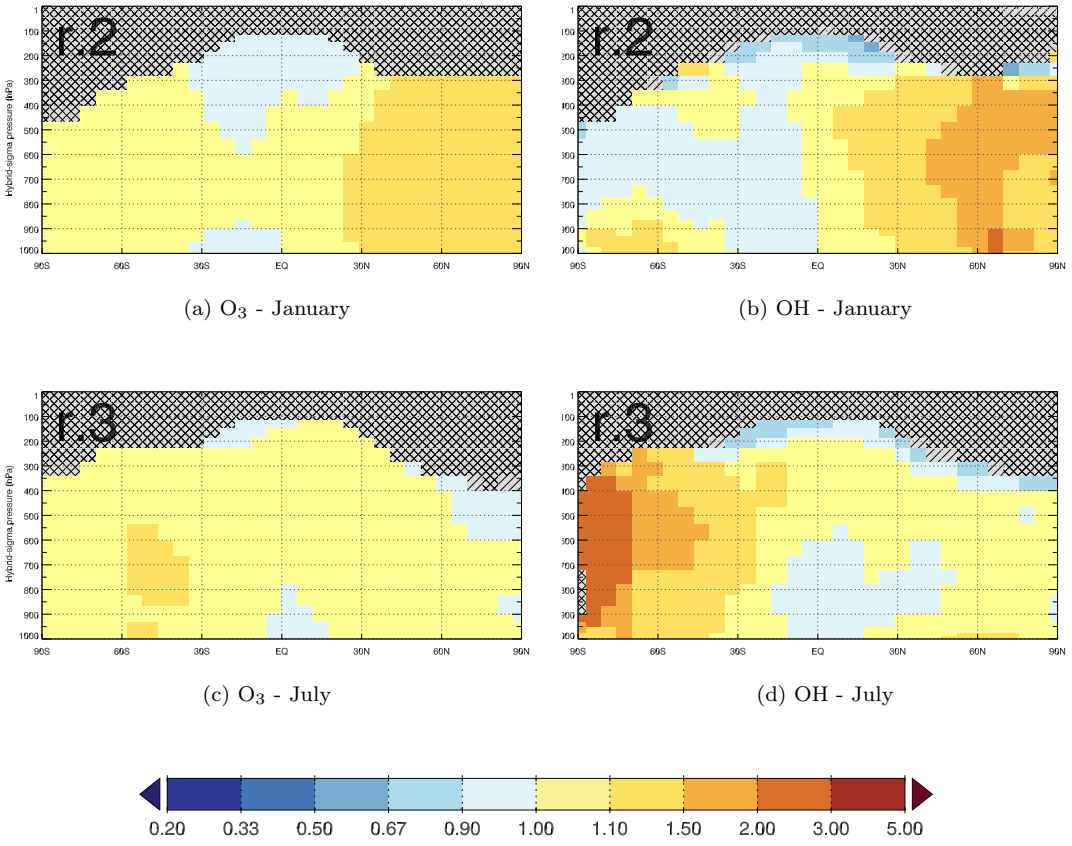

(a) O_3 - January

(b) OH - January

(c) O_3 - July

(d) OH - July

FIGURE 6.33: O_3 and OH relative differences between the PC-[NoAero] and RF1 cases in January and July.

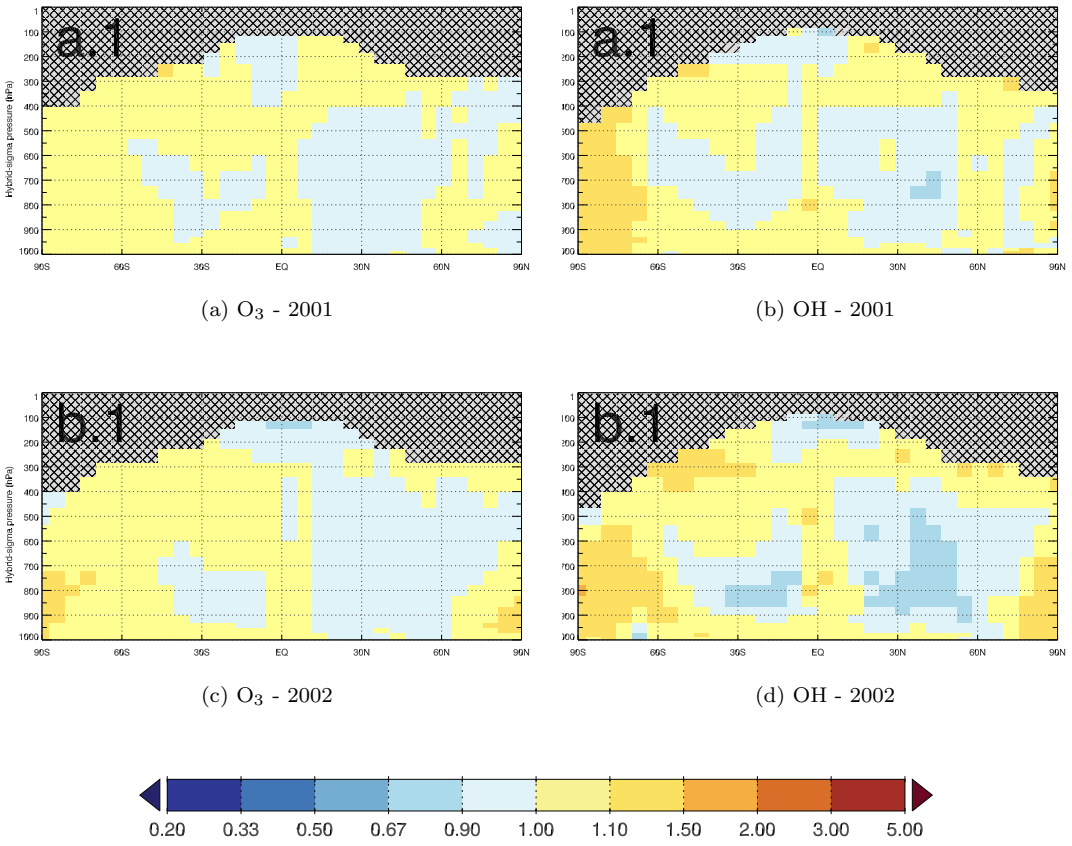

(a) O_3 - 2001 (b) OH - 2001

(c) O_3 - 2002 (d) OH - 2002

FIGURE 6.34: Annually averaged O_3 and OH relative differences between the D-[2001], D-[2002] and RF1 cases.

6.3.2.6 Dynamical data

A change in dynamical data results in changes of several factors such as temperature and relative humidity that sensibly affect the concentrations of O_3 and OH across the troposphere. Global mean figures presented on the statistical summaries equal 1.06% in 2001 and 1.45% in 2002 for O_3 and 3.26% in 2001 and 3.00% in 2002 for OH (figures 6.24 and 6.25). O_3 and OH zonal mean plots displayed on figures 6.34 as well as D.3 **a**.* and **b**.* and D.4 **a**.* and **b**.* show that the 2001 and 2002 meteorological data present similarities.

In January, O_3 and OH increases and decreases may be seen depending on the location. For instance, decreases in shipping O_3 concentrations up to 0.82 in 2001 and 0.84 in 2002 are present in the tropical regions above 700 hPa. Another region affected by a decrease but to a lesser extent is the Arctic region. Shipping

OH concentrations present a more dramatic change which shares some similarities with the change in shipping O_3. For example, there is also a decrease in OH concentrations larger than 0.9 in the tropical regions. However, the largest OH decrease is seen in 2002 above 60°N and equals 0.37. The boundary layer of the Antarctic region and the free and upper tropospheric regions in mid-latitude and polar regions all show an increase in O_3 concentrations. The largest effects reside in the Antarctic where ratios can be as large as 2.18 but increases larger than 1.10 also lie at the top of the troposphere. This is similar for OH concentrations but the largest effect are found in the Arctic region where an increase by a factor of 2.55 can be seen.

The picture is different in July. For instance, a large decrease of 0.68 in O_3 concentrations occurs between 30°N and 60°N in 2002. The top of the atmosphere at 30°N and the free troposphere at 60°N are usually regions of increasing O_3 concentrations which seems to indicate that general circulation patterns are the main factor responsible for it. In July 2002, an additional region of increase can be noticed at the equator from the surface to 600 hPa. As for OH concentrations, maximum increases are located in the Antarctic region and equal respectively 2.59 and 4.03 in 2001 and 2002. The large decrease in O_3 concentrations between 30°N and 60°N corresponds to a large decrease in OH concentration as well. This decrease can reach up to 0.48 in 2002.

Regarding the DYN-[ECMWF2000] case, it presents larger differences compared to the reference case. Global mean figures equal 4.09% ±12.86 for O_3 and 1.71% ±22.13 for OH. Furthermore, the globally and annually averaged vertical profiles reveal that O_3 and OH concentrations increase at the top and the bottom of the troposphere whereas they decrease in the middle troposphere (figures 6.26 and 6.27). In fact, the zonal mean plots show that the decrease mainly occurs in the middle troposphere of the tropics which could indicate that the change in the number of vertical levels (from 28 to 47) can significantly affect the convection or lightning parameterisations.

6.3.2.7 Horizontal resolution

Annually and globally averaged relative differences in the case of changes in model resolution are quite small with a maximum value of 4.30% ±9.10 for O_3 in the R-[T106] case and 3.85% ±14.30 for OH in the R-[T21] case. Globally and annually averaged relative differences of O_3 profiles displayed on figure 6.26 show that O_3 concentrations increase at the surface and the top of troposphere while they decrease in the middle troposphere. For OH, the variability is greater and the vertical profiles of R-[T21] and R-[T42] show an opposite trend compared with R-[T106]. These trends suggest that an increase in resolution increase concentrations in the middle troposphere but decrease them at the bottom and at the top of the troposphere. The zonal mean plots on figures 6.35 and D.3 **u.*-x.*** confirm that the model simulates less O_3 in the upper troposphere. This occurs however in the tropical regions only while the mid-latitudes and polar regions both see an increase. In addition, the model also simulates a decrease in O_3 concentrations at the surface of the summer hemisphere. Ratios remain within a range of [0.67, 1.50]. It is interesting to note the symmetrical aspect of the O_3 and OH changes resulting from model resolution alterations. Concentrations of these species decrease in tropical regions with an increase in resolution while they increase in the mid-latitude and polar regions.

6.3.2.8 Background anthropogenic emissions

Regarding changes in background anthropogenic emissions, their effects on the annually and globally averaged zonal means of O_3 and OH remain smaller than or equal to ±5% (figures 6.24 and 6.25). Furthermore, figures 6.26 and 6.27 reveal that regions have a similar impact close to the ground but have a greater impact in the free troposphere and upper troposphere when all or part of the emissions are located in tropical regions (Asian and North-American regions). This is confirmed by the zonal mean plots that show that a doubling or halving in Asian emissions alter O_3 concentrations at the top of the tropical troposphere by more (less) than 1.1 (0.9) (figures 6.36 and D.3 **h.*-m.***). OH changes are similar to those of O_3

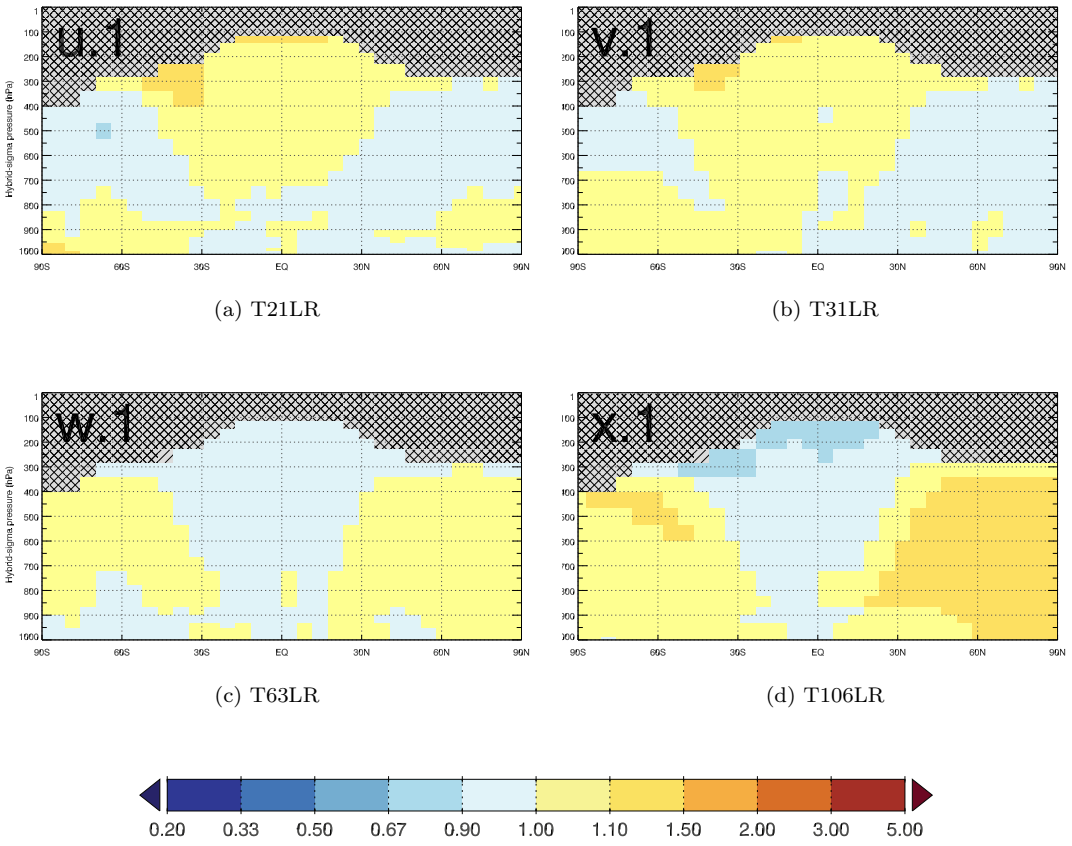

(a) T21LR (b) T31LR

(c) T63LR (d) T106LR

FIGURE 6.35: Annually averaged O_3 relative differences between the R-[T21], R-[T31], R-[T63], R-[T106] and RF2 cases.

in spatiality and magnitude (figures D.4 **h.*-m.***). It is worth noting the changes in background emissions in Europe which affects the Arctic region.

6.3.3 Changes in tropospheric O_3 columns of shipping perturbations

Relative differences of tropospheric O_3 columns are displayed on figure D.5 in appendix D. In addition, global averages and zonal mean plots of perturbed and reference tropospheric O_3 columns are shown on figure 6.37 in this section for all simulation cases. A threshold value of 0.02 was used to remove insignificant shipping perturbations. This value is consistent with the global shipping O_3 column of about 1 DU and the globally averaged tropospheric O_3 column of about 35

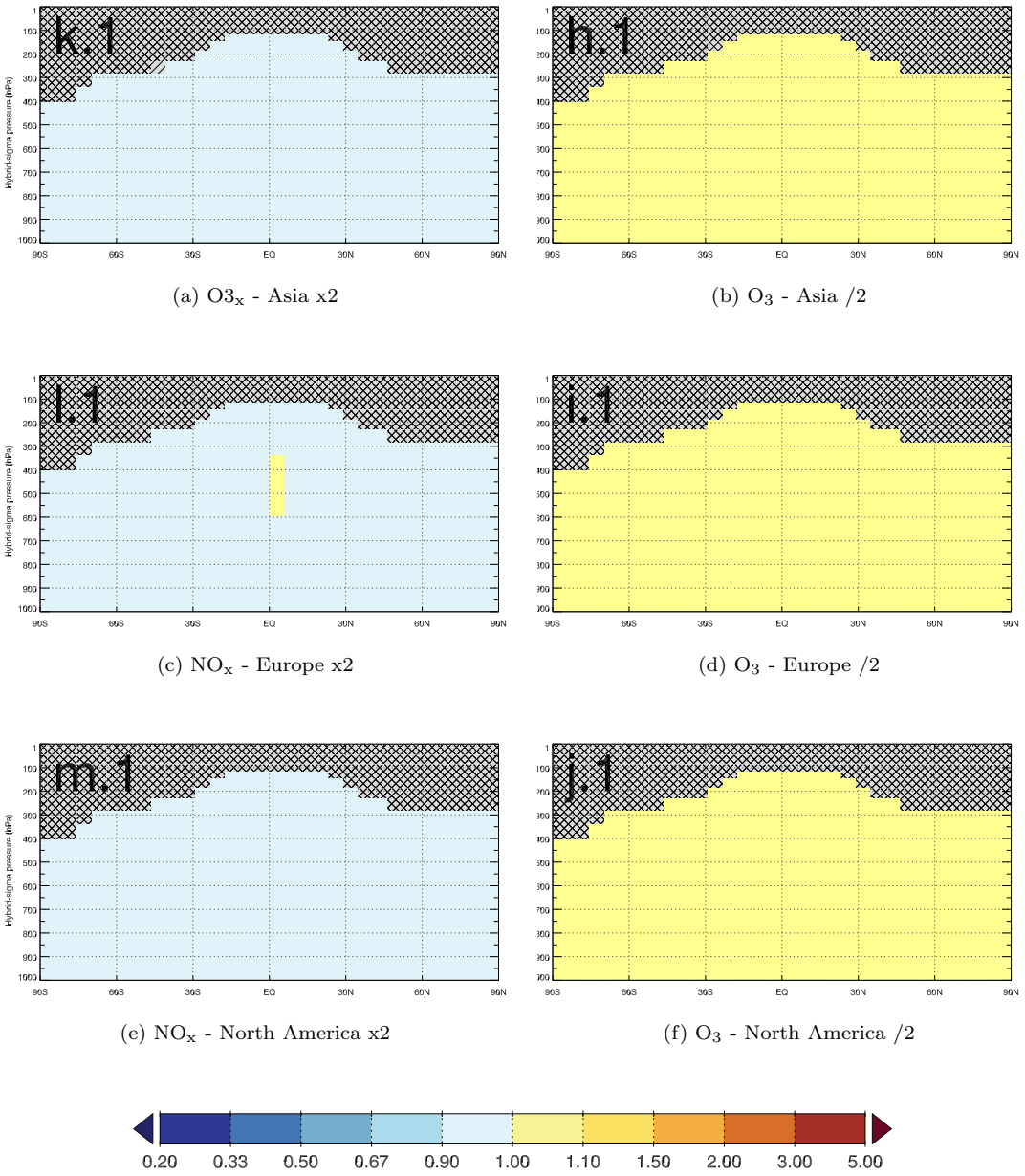

(a) $O3_x$ - Asia x2

(b) O_3 - Asia /2

(c) NO_x - Europe x2

(d) O_3 - Europe /2

(e) NO_x - North America x2

(f) O_3 - North America /2

FIGURE 6.36: and O_3 relative differences between the BAE-[ASx2], BAE-[AS/2], BAE-[EUx2], BAE-[EU/2], BAE-[NAx2], BAE-[NA/2] and RF1 cases in January.

DU reported in the literature [Endresen et al., 2003, Eyring et al., 2007, Dalsøren et al., 2007, Houghton et al., 2001].

6.3.3.1 Shipping emission magnitude

In the SEM-[x2] case, a global annual average of 1.56 DU is found, corresponding to a 65% increase (figure 6.37 β**.***). The largest effects are clearly located in the southern hemisphere and especially in the tropics where values can become larger than 81% in both January and July (figures 6.38 **(a,c)** and D.5 **e.2** and **e.3**). The trend prevails on the annual mean plots where values lie between 67% and 80% in the southern hemisphere, whereas they lie between 52% and 70% in the northern hemisphere. Conversely, shipping tropospheric O_3 columns are reduced by 38% on average in the SEM-[/2] case. Again, the largest effects are located in the tropics but they have a similar magnitude of -43% in both the northern and southern tropics in January and July (figures 6.38 **(b,d)** and D.5 **d.2** and **d.3**). As for annual mean relative differences, they range between -42% and -39% in the southern hemisphere and between -42% and -34% in the northern hemisphere. This emphasizes once again the saturation of the NO_x-O_3-HO_x chemical system that occurs when shipping emissions become too large.

6.3.3.2 Offline photolysis scheme

Figures 6.37 δ**.*** also show that the third case with largest impacts is PC-[OffPhot] with an annually and globally averaged increase of -27%. The maps associated to this case reveal that the tropics contain the largest ratios and that a strong seasonal variation exists (figures 6.39 and D.5 **q.***). The minimum relative difference is found in January in the Southern tropics and equals -90%. It is interesting to note that MOZART-4 simulates a depletion of O_3 over land (South America, Africa and Indonesia) owing to shipping emissions when the photolysis is calculated offline. Despite a negative annual global mean some tropical regions of the pacific also present positive ratios that peak at 56%. It seems that the pattern of large changes

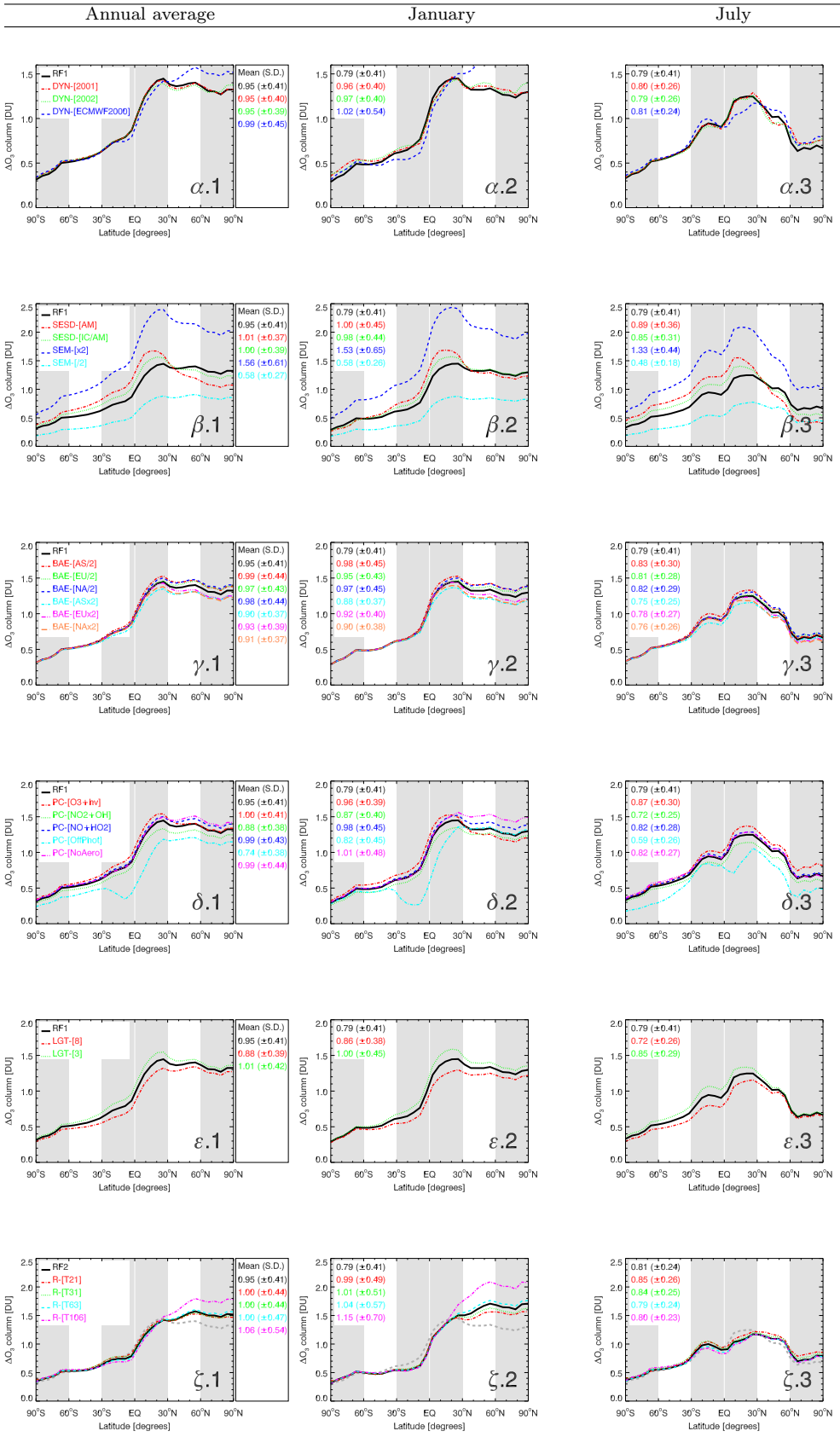

FIGURE 6.37: Zonal average of O_3 columns for the different perturbation cases in January, July and on an annual average. The cases are gathered by type: α for the dynamical data, β for shipping emissions, γ for background emissions, δ for photochemistry, ϵ for lightning and ζ for resolution.

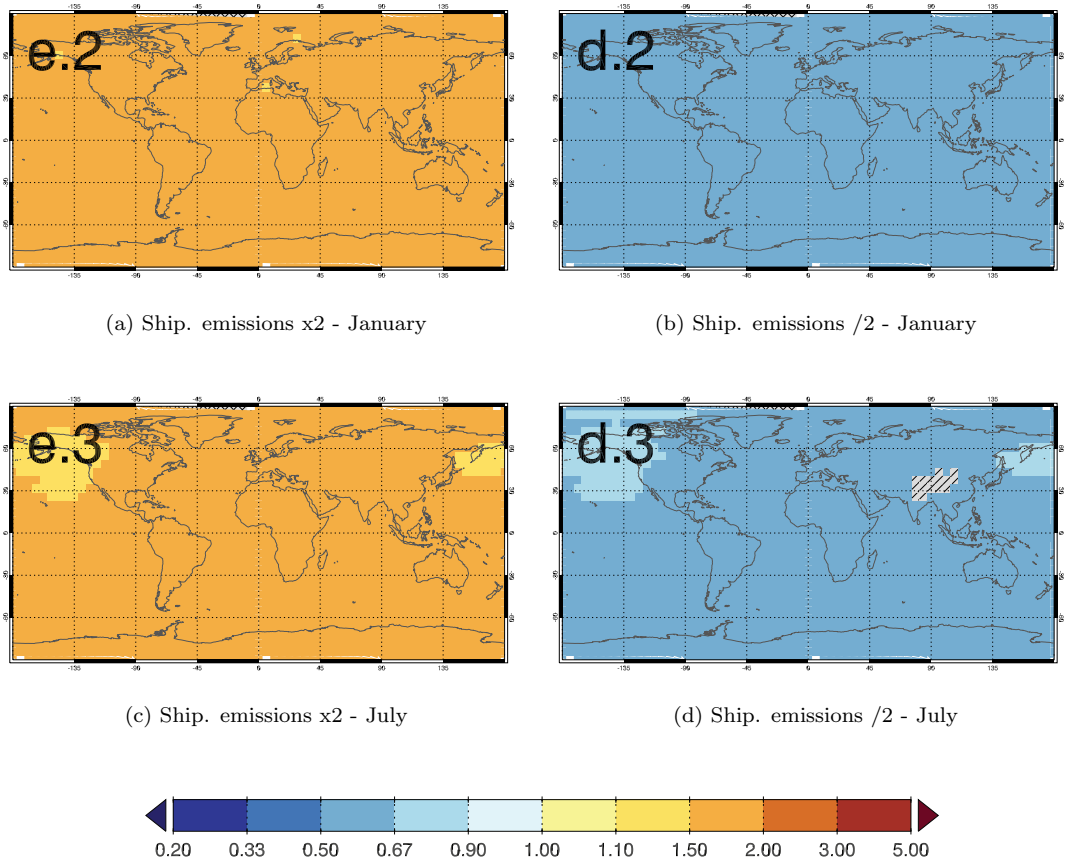

(a) Ship. emissions x2 - January

(b) Ship. emissions /2 - January

(c) Ship. emissions x2 - July

(d) Ship. emissions /2 - July

FIGURE 6.38: O_3 relative differences between the SEM-[x2], SEM-[/2] and RF1 cases in January and July.

in the tropics resemble that of the ISCCP cloud coverage[17] suggesting that the offline photolysis scheme computes larger cloud effects compared with the online photolysis scheme. Outside the tropics, values are generally negative and below -10% .

6.3.3.3 Horizontal resolution

An interesting effect of model resolution change can be seen on figures 6.37 ζ.*. The annual average and January zonal mean plots show that an increase in model resolution leads to a large increase in shipping tropospheric O_3 column in the northern mid-latitudes and polar region. This is especially true for the case with a T106LR resolution which sees columns being increased by 48% in January in the

[17] http://isccp.giss.nasa.gov/

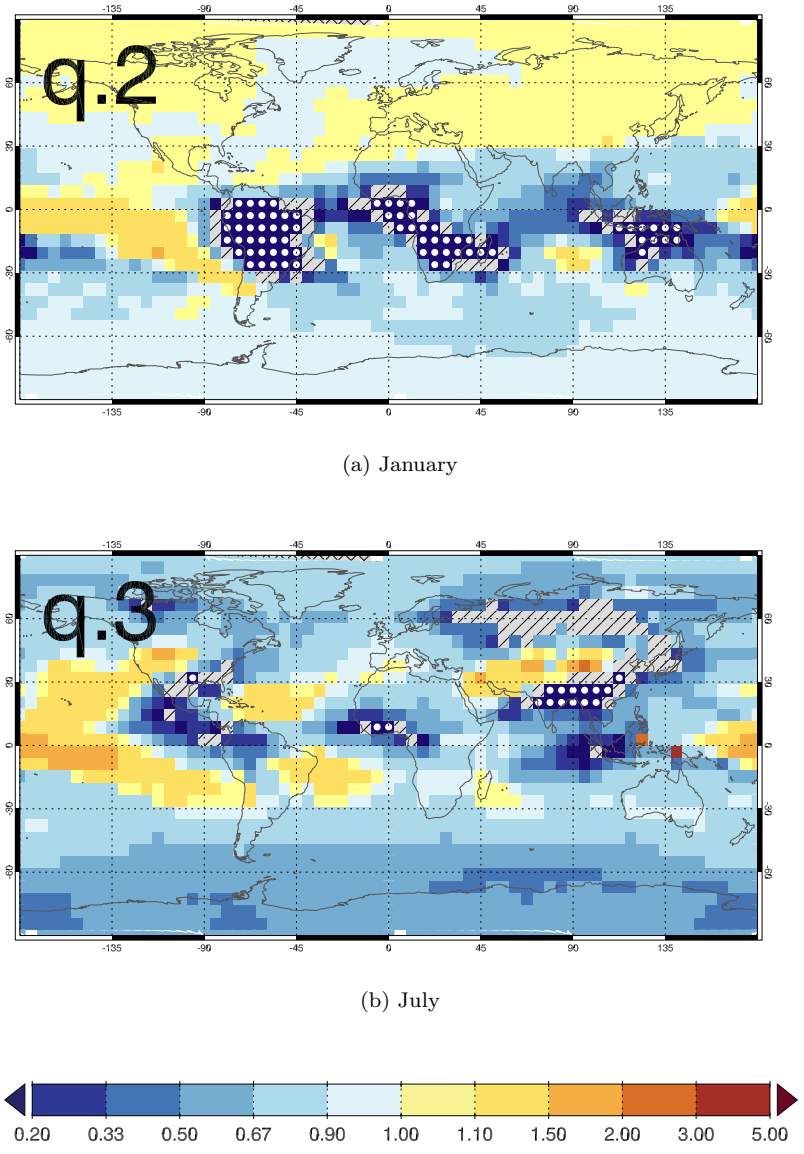

(a) January

(b) July

FIGURE 6.39: O_3 relative differences between the PC-[OffPhot] and RF1 cases in January and July.

mid-latitudes. A perceptible trend can also be seen on this figure. When model resolution increase, shipping O_3 columns increase in the mid-latitudes and polar regions but decrease in the tropics.

6.3.3.4 Lightning activity

Differences arising from uncertainties in lightning activity remain on average smaller than 6% for the LGT-[3] case and -7% for the LGT-[8] case and are clearly larger

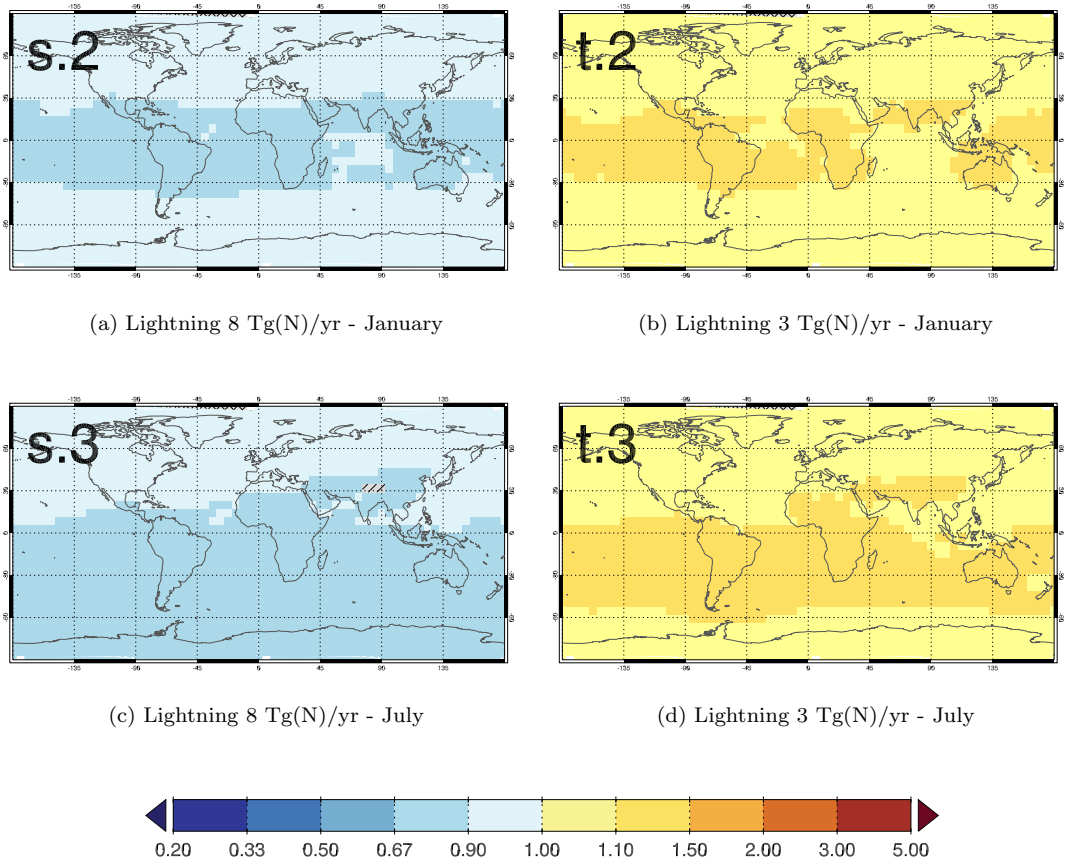

(a) Lightning 8 Tg(N)/yr - January

(b) Lightning 3 Tg(N)/yr - January

(c) Lightning 8 Tg(N)/yr - July

(d) Lightning 3 Tg(N)/yr - July

FIGURE 6.40: O_3 relative differences between the LGT-[8], LGT-[3] and RF1 cases in January and July.

in the tropics (figure 6.37 ϵ**.***). The maps on figures 6.40 as well as D.5 **s.*** and **t.*** show that differences up to 20% and as small as -23% can be reached in the southern tropics in January for these two cases respectively. On an annual basis, tropical shipping O_3 column means range between -14% and 11% across the southern tropics and between -10% and 9% in the northern hemisphere.

6.3.3.5 Shipping emission spatial distribution

Similarly, changes in the spatial distribution of shipping emissions increase shipping O_3 column by 7% and 5% in the SESD-[AM] and SESD-[IC/AM] cases respectively (figures 6.37 β**.***). The shift of shipping emissions towards southern latitudes results in shipping emissions being released in regions affected by convection but also in regions where anthropogenic pollution is low, explaining the

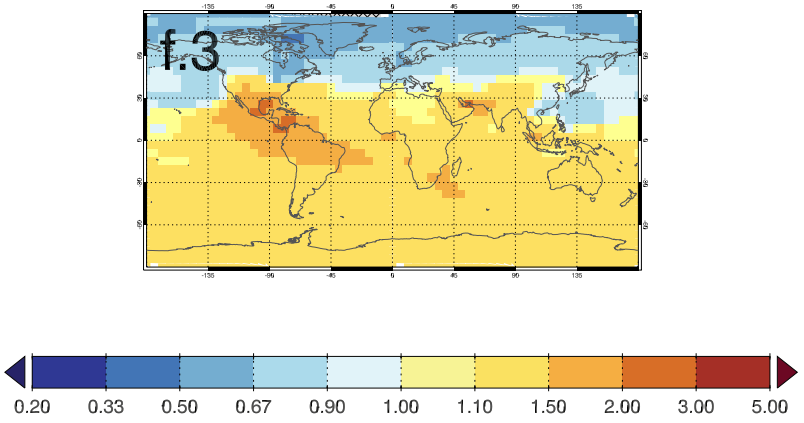

FIGURE 6.41: O_3 relative differences between the SESD-[AM] and RF1 cases in July.

larger column. The maximum difference is found in the Gulf of Mexico (northern tropics) in July and equals 140% (figures 6.41 and D.5 **f.3**).

6.3.3.6 Background anthropogenic emissions

Differences smaller than ±6% are found for the changes in background anthropogenic emissions (figures 6.37 γ.*). The largest effects are produced in the BAE-[ASx2] and BAE-[AS/2] cases where differences can be as small as ±20% in the northern tropics and mid-latitudes in January and July. The second largest effects come from emissions changed in North America and range between -4.21% and 3.16% . Finally, impacts resulting from emissions changes in Europe lie between -2.11% and 2.11%.

6.3.3.7 Other photochemistry

Other changes in photochemistry remain smaller than 5% on an annual global average (figures 6.37 δ.*). An increase in the reaction rate constant between NO_2 and OH yields less shipping O_3 column whereas a decrease in the reaction rate constants of reactions 1 and 2 yields more shipping O_3 column. The PC-[NoAero] case also yields more shipping O_3 column and especially on the northern mid-latitudes and polar region (figures 6.42 and D.5 **r.2**).

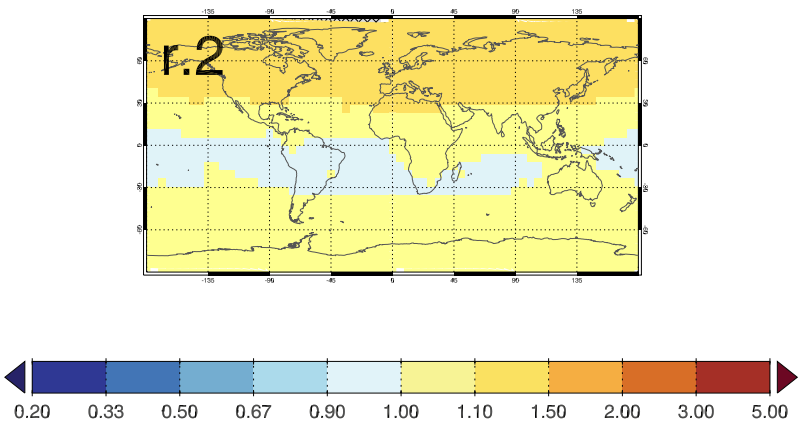

FIGURE 6.42: O_3 relative differences between the PC-[NoAreo] and RF1 cases in January.

6.3.3.8 Dynamical data

A change in dynamical data does not sensibly affect tropospheric O_3 columns (figures 6.37 α.*). For the 2001 and 2002 cases, the annual global mean is less than 1% but differences can reach up to $\pm$50% on a monthly basis. It is interesting to see that the 2002 meteorology tends to displace the shipping O_3 perturbation into the polar regions more efficiently (figures 6.43 as well as 6.37 **a.*** & **b.***). This could be explained by the different NAO pattern compared to that of 2000 and 2001, although more simulations would be required to be fully conclusive. Also, in the Northern Hemisphere in winter, differences induced by the use of the NCEP and ECMWF dynamical datasets are substantial. This reflects again the importance of vertical levels in simulations and their influence on models' parameterisations.

6.3.4 Changes in global O_3 burden, global OH concentrations and global CH_4 lifetime

Absolute and relative differences of global ozone burden, global OH concentrations and global methane lifetime resulting from shipping perturbations are given in table 6.5 for all simulation cases performed in this chapter.

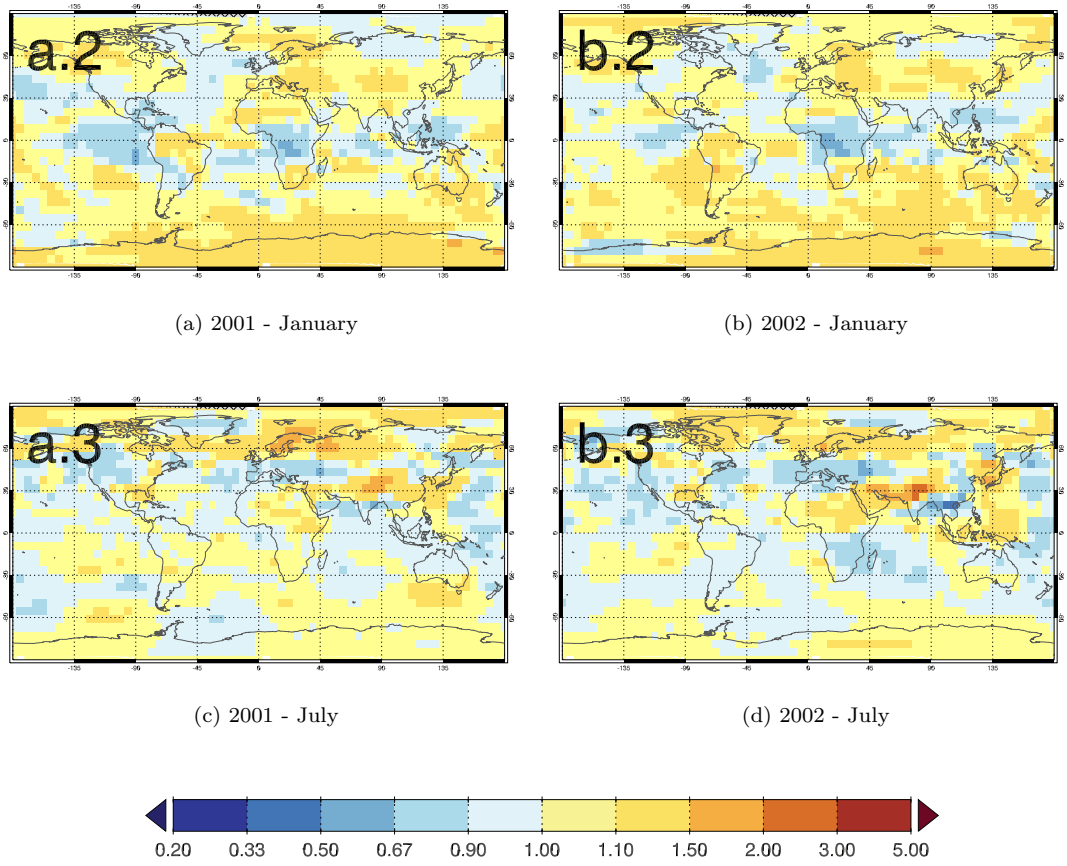

(a) 2001 - January

(b) 2002 - January

(c) 2001 - July

(d) 2002 - July

FIGURE 6.43: O_3 relative differences between the D-[2001], D-[2002] and RF1 cases in January and July.

6.3.4.1 Shipping emission magnitude

It comes as no surprise that global O_3 burden, OH concentration and CH_4 lifetime differences resulting from uncertainties in shipping emission magnitude dominate over the rest of the results (cases **d** & **e**). Indeed, relative differences are about -40% and 70% for the O_3 burden, -38% and 66% for OH concentration and about -35% and 60% for the CH_4 lifetime in the SEM-[/2] and SEM-[x2] cases respectively. It is interesting to note that when shipping emissions are increased by 92%, only 70% of O_3 burden is added to the system resulting in a difference of 22 percentage points, whereas when shipping emissions are decreased by 44%, a similar amount of O_3 is removed from the system and the difference is only 4 percentage points. The same behaviour is reflected by the OH concentration and CH_4 lifetime figures though with a smaller magnitude. This emphasizes again the non-linear

TABLE 6.5: Global ΔO_3 burdens, ΔOH concentrations and ΔCH_4 lifetimes in the perturbed and reference cases. The cases leading to the maximum and minimum differences are shown in bold characters.

#	Simulation name	Global ΔO_3 burden [$Tg.year^{-1}$]	Relative difference [%]	Global ΔOH [10^{-4}#.cm^{-3}]	Relative difference [%]	Global ΔCH_4 lifetime [year]	Relative difference [%]
RF1	Reference	10.93	-	7.33	-	-0.74	-
a	DYN-[2001]	10.94	0.08	7.30	-0.33	-0.73	-0.62
b	DYN-[2002]	10.84	-0.89	7.24	-1.17	-0.75	1.24
c	DYN-[ECMWF2000]	11.13	1.79	7.67	4.67	-0.78	6.16
d	**SEM-[/2]**	**6.64**	**-39.30**	**4.54**	**-38.00**	**-0.47**	**-36.54**
e	**SEM-[x2]**	**18.29**	**67.29**	**12.16**	**66.00**	**-1.18**	**59.31**
f	SESD-[AM]	12.39	13.28	8.33	13.63	-0.83	12.98
g	SESD-[IC/AM]	11.82	8.14	7.93	8.23	-0.80	7.84
h	BAE-[AS/2]	11.43	4.57	7.73	5.51	-0.77	4.00
i	BAE-[EU/2]	11.08	1.37	7.43	1.34	-0.75	0.89
j	BAE-[NA/2]	11.25	2.92	7.55	3.07	-0.76	3.11
k	BAE-[ASx2]	10.30	-5.78	6.77	-7.67	-0.72	-3.16
l	BAE-[EUx2]	10.76	-1.62	7.20	-1.77	-0.73	-0.61
m	BAE-[NAx2]	10.55	-3.55	7.03	-4.08	-0.72	-3.04
n	PC-[O3+hν]	11.65	6.51	5.96	-18.69	-0.82	11.52
o	PC-[NO2+OH]	10.08	-7.77	6.70	-8.61	-0.82	11.19
p	PC-[NO+HO2]	11.37	3.95	7.55	3.01	-0.70	-4.76
q	**PC-[OffPhot]**	**8.10**	**-25.96**	**3.10**	**-57.69**	**-0.29**	**-61.11**
r	PC-[NoAero]	11.32	3.50	7.54	2.91	-0.61	-17.32
s	LGT-[8]	9.94	-9.05	6.82	-6.86	-0.60	-18.89
t	LGT-[3]	11.73	7.32	7.72	5.41	-0.86	16.88
RF2	DYN-[ECMWF2000]	11.13	-	7.67	-	-0.78	-
u	R-[T21]	11.24	0.99	7.49	-2.40	-0.71	-9.64
v	R-[T31]	11.27	1.23	7.58	-1.22	-0.76	-2.76
w	R-[T63]	11.06	-0.62	7.71	0.51	-0.81	3.03
x	R-[T106]	11.42	2.63	7.92	3.32	-0.81	2.96

character of the NO_x-O_3-HO_x-CH_4 chemical system which implies the saturation of O_3 production at high NO_x levels.

6.3.4.2 Offline photolysis scheme

The two emission cases are followed by that corresponding to the change from online to offline photolysis scheme (**q**). This change yields a reduction of more than 25% in shipping-induced O_3 burden and subsequent decreases of about 58% in shipping-induced OH concentration and 61% in shipping-induced CH_4 lifetime. Interestingly, these relative differences translate into an O_3 burden perturbation of 7.10 $Tg(N).year^{-1}$ and a CH_4 lifetime perturbation of -0.29 year which scales well with that reported in Dalsøren et al. [2007] (-0.11 year for a shipping NO_x emission

magnitude of 3.6 Tg(N)/year[18]) but more importantly with the multi-model study of Eyring et al. [2007] (-0.13 year for a shipping NO_x emission magnitude of 3.1 Tg(N)/year).

6.3.4.3 Shipping emission spatial distribution

Changes in the shipping emission spatial distribution come next with O_3 burden and CH_4 lifetime relative differences being equal to about 13% in the cases SESD-[AM] (**f**) and about 8% in SESD-[IC/AM] (**g**). These increases in O_3 burden, OH concentration and CH_4 lifetime reflect the shift of shipping traffic into regions with a higher O_3 production efficiency such as the tropical regions as noted by Endresen et al. [2003].

6.3.4.4 Lightning activity

Regarding the effects of the current uncertainty range in lightning activity, their relative difference lie between -9% and 7% for the O_3 burden, between -6% and 5% for the OH concentration and between -19% and 17% for the CH_4 lifetime in the cases LGT-[8] (**s**) and LGT-[3] (**t**) respectively.

6.3.4.5 Other photochemistry

Effects from the three photochemical reactions are moderately significant and range between -7.76% and 6.40% for O_3, between -18.69% and 3.01% for OH concentration and between -4.90% and 10.96% for CH_4 lifetime (**n**, **o**, **p** and **r**).

6.3.4.6 Horizontal resolution

A step-by-step increase in horizontal model resolution yields a steady decrease in the shipping-induced CH_4 lifetime but a non-linear response of the O_3 burden. As

[18]Using the 1.48% decreased mentioned in this study in conjunction with the 8-year CH_4 lifetime of the Oslo CTM2 model reported in Shindell et al. [2006].

shown in the previous sections, since emissions are refined as resolution increase, species concentrations change, affect photochemical activity which results in these responses in multiple ways (**u-x**).

6.3.4.7 Background anthropogenic emissions

Changes in background anthropogenic emissions also have a moderate effect on these global figures since relative differences are all smaller than 8%. The Asian and North American cases present the largest effects since their emission regions cover larger domains that extend to tropical regions (**h-m**). Maximum differences can be seen in the BAE-[AS/2] and BAE-[ASx2] cases which yield differences of 4.57% and -5.78% for ΔO_3 burden, 5.54% and -7.67% for ΔOH concentration and 4.00% and -3.16% for ΔCH_4 lifetime (**h** and **k**).

6.3.4.8 Dynamical data

Changes in dynamical input data remain smaller than $\pm 2\%$ and consequently, do not have a substantial effect on the shipping signal with respect to these global figures (**a** and **b**). The use of a different meteorological dataset such as ECMWF instead of NCEP has nonetheless a larger impact compared with interannual variability presented in this study. This is likely to be related to the difference in vertical levels as discussed previously (**c**).

6.4 Discussion

Results from this chapter provide evidence that the shipping NO_x-O_3-HO_x-CH_4 chemical system is largely sensitive to current uncertainties in the magnitude and the spatial distribution of shipping emissions. In both cases, the non-linear character of the chemical system is brought out in many ways by the various metrics used in this chapter, even though it is clearly more important near the surface of the model. For instance, the magnitude of O_3 changes near the surface is larger

when shipping emissions are reduced than when they are increased. In addition, O_3 differences are much larger in all cases when one looks at zonal means, tropospheric columns and global burden compared to the near-surface. This last example explains the smaller change in CH_4 lifetime in the case of a near-doubling in emissions, since about 75% of CH_4 is oxidised near the surface in the Northern hemisphere [Lawrence et al., 2001]. This finding supports that reported in the multimodel study by Eyring et al. [2007] who found that intermodel standard deviations of shipping-induced NO_2 and O_3 remain smaller than 20% and much smaller than those arising from uncertainties in shipping emission inventories.

It is not clear whether the offline photolysis scheme provided with the version of MOZART-4 used in this study is calculating the right O_3 photolysis rates, since shipping O_3 perturbations are negative in some regions. Nonetheless, results obtained with the offline scheme are in better agreement with previous assessments of shipping impacts. Tie et al. [2003] demonstrated the high sensitivity of the global budgets of O_3, OH and CH_4 to photolysis rate calculations under clear-sky and cloudy-sky conditions. In the present study, global OH concentration was increased by more than 80% in December and June while CH_4 lifetime was decreased by more than 40% when the photolysis scheme of global model was switched from offline to online.

Effects of horizontal resolution changes are generally limited to the surface where NO_x and O_3 concentrations can be increased or decreased by more than a factor of 10. However, shipping-induced global O_3 burden, global OH concentration and CH_4 lifetime remain smaller than $\pm 10\%$. These results are in very good agreement with those reported in [Hodnebrog et al., 2011b] where it was found that the impacts of resolution changes was mostly relevant to air quality problems. Another point of interest is the study of Dalsøren et al. [2007] in which the authors claimed that the large reduction in global OH concentration compared to the study of Endresen et al. [2003] originates from the use of a finer resolution. Nonetheless, a later study reported global OH concentration much in line with previous estimates from Endresen et al. [2003]. Interestingly, the present study suggests that changes in resolution might not be the primary factor for this change.

Current uncertainties in lightning NO_x production have a small impact near the surface ($< \pm 5\%$) but can lead to substantial CH_4 lifetime perturbations lying between [-20%, -15%] and [15%, 20%]. O_3 metrics defined across the whole troposphere are larger than $\pm 5\%$ and smaller than $\pm 10\%$.

The three photochemical reactions tested here present effects that are overall smaller than $\pm 10\%$ throughout the troposphere. This provides some degree of confidence regarding the precision of the chemical mechanism embedded in MOZART-4. Exceptions are the OH and CH_4 lifetime perturbations resulting from the application of the uncertainty function in O_3 photolysis (-18.5% and -18.7%) as well as the CH_4 lifetimes perturbation in the case without aerosol chemistry (-17.3%). This second warning regarding O_3 photolysis suggests that further investigation should be made to try to reduce the uncertainties linked to it. The large negative CH_4 lifetime difference stemming from the removal of aerosol chemistry in the model is an interesting case since this drop is much larger than that of the case focusing on the reaction between OH and HO_2, although the OH perturbations are relatively similar. Actually, impacts of aerosol chemistry mechanism removal on OH are much larger than that of the bimolecular reaction at the surface and in the free troposphere of the northern midlatitudes resulting in this large CH_4 lifetime change.

A doubling or halving of background anthropogenic emissions does not perturb substantially the chemical system since most differences remain smaller than $\pm 5\%$. These results contradict those found by Collins et al. [2008] who reported large changes of shipping O_3 burden (-18.8% under the A2 scenario and +31.3% under the MFR scenario) and CH_4 lifetime (-26.1% under the A2 scenario and +26.1% under the MFR scenario).

It is important to note that some processes, such as dynamical data, horizontal resolution and background anthropogenic emissions, have a larger impact at the surface which makes them particularly relevant to the context of air quality.

Chapter 7

Effects of including a ship plume parameterisation

Summary

This chapter is divided into two main sections in which the concept of effective reaction rates was studied. In the first section, the parameterisation developed by Huszár et al. [2010] was implemented in MOZART-4 in order to assess it further. This parameterisation rests basically upon two parameters: τ which defines the characteristic time of the high-concentration phase of the ship plume and K_{eff} which accounts for the loss by reaction between NO_x and O_3. The main findings are:

- The current version of the parameterisation artificially reduces NO_x concentrations via horizontal and vertical transport at the global scale.
- The parameterisation is insensitive to K_{eff} but very sensitive to τ.
- The O_3 titration term becomes less important as τ increases.
- Shipping O_3 perturbations are not reduced homogeneously across the globe and are even increased by the parameterisation in some regions.
- This parameterisation might not be suitable for use in global models.

In the second section, an attempt to improve the parameterisation was made by taking into account the different ship plume chemistry and dynamical characteristics. This second part led to the following findings:

- Shipping NO_x and O_3 levels decrease by more than 20% at the surface of the oceans.
- Allowing the ship exhaust tracer to be transported might lead to unrealistic distributions of shipping NO_x and its secondary products.
- In particular, large shipping O_3 decreases are simulated in the free and upper troposphere by the global model.
- This new approach is heading towards the right direction but it needs refinement.

7.1 Introduction

The necessity to implement a ship plume parameterisation into large-scale chemistry-transport models was first suggested by Kasibhatla et al. [2000] and Davis et al. [2001] after they found that the GCTM they were using was overestimating NO_x concentrations by a factor of 10 in the Pacific MBL when shipping emissions were included. A number of following studies has provided further support to this idea. For instance, Endresen et al. [2003] found similar results in the same oceanic region even though they noticed a good agreement between modelled and observed NO_x levels in the North Atlantic. As explained earlier in this thesis, larger shipping NO_x concentrations can lead to larger shipping O_3 concentrations. With the help of a box-model, von Glasow et al. [2003] estimated that shipping O_3 perturbations could be overestimated by 50% in global models. These simulated overestimations of NO_x and O_3 were further confirmed by measurements taken during the ITCT2K2 campaign over the Pacific [Chen et al., 2005]. Other studies such as the multi-model study from Eyring et al. [2007] and those from Dalsøren et al.

[2007] and Dalsøren et al. [2009] showed however that the global models employed were simulating NO_x and O_3 concentrations that were in agreement with several observations throughout the troposphere, but agreed that NO_x lifetime reductions within ship plumes could not be represented realistically by global models and that a parameterisation should be included in such models to palliate this problem.

A number of studies responded to this problem and developed frameworks and parameterisations to account for the chemical processes occurring at the ship plume scale. Esler [2003] proposed an interesting scheme based on the concept of effective emission indices but the idea has never been implemented. A few years later, Franke et al. [2008] came up with a parameterisation drawn from the concept of effective emissions which had originally been tried out with aircraft emissions [Petry et al., 1998]. It was developed for a specific case of atmospheric conditions and this idea has again not been taken further. A simple parameterisation was developed upon the OPE observations reported by [Chen et al., 2005] and consisted in replacing NO_x molecules emitted by ships by 1 HNO_3 molecule and 10 O_3 molecules (GEOS-chem wiki[1]). The main problems with this approach are: first, the OPE was specific to atmospheric conditions of the measurement campaign, secondly this parameterisation largely underestimates shipping NO_x concentrations and more importantly it generates O_3 at night. An improved version of this scheme in which O_3 production is multiplied by normalised NO_2 photolysis was developed by Duncan et al. [2008]. Although this new approach is able to simulate daily variations and stop O_3 production at night, it was again specific to a restricted set of atmospheric conditions and underestimating NO_x concentrations. More recently, Huszár et al. [2010] (H2010, hereafter) developed a ship plume parameterisation based on the effective reaction rate (ERR) parameterisation formulated by Cariolle et al. [2009] and implemented it in CAMx. They reported NO_x reductions of up to 25% while O_3 production was decreased by up to 15% to 30% over Europe. Lately, Vinken et al. [2011] followed a plume-in-grid approach to develop and implement another parameterisation. They found that NO_x was overestimated by 50% and O_3 by 10% to 25% at the surface of the globe.

[1] http://wiki.seas.harvard.edu/geos-chem/index.php/Ship_emissions, last access 08/08/2011

The merit of the ERR method is that its original version does not require the use of a look-up table compared to the methods proposed by Franke et al. [2008] and Vinken et al. [2011]. In addition, the ERR method is mass conservative, according to its authors. For these reasons, the focus of this study was set on the ERR method.

The structure of this chapter differs a little bit compared with the previous chapters since it embraces two consecutive steps. Huszár's work is first extended to the global scale and further analysed. This analysis leads then to the modification and attempt to improve the scheme, in a second section.

7.2 Extension of Huszár's work

In this first section, the work of Dr. Huszár was extended to the global scale using MOZART-4 and a thorough comparison is made between results from the two modelling studies.

7.2.1 Methodology

The parameterisation developed by H2010 and defined by the set of partial differential equations ((7.1) to (7.4)) was implemented in MOZART-4. The same approach taken by Dr. Huszár[2] and described in his article has been followed in this study. First, the ship plume inert tracer is added to the model by defining it via MOZART's pre-processor. Shipping NO_x emissions can be then channelled through this newly-defined tracer by specifying it in the pre-processor as well (see figure 3.3 in chapter 3). Furthermore, the Crank-Nicholson implicit scheme was employed to integrate the set of ordinary differential equations in time (Personal communication with Dr. Huszár, 2009). The ship plume solver was then implemented in a new FORTRAN routine which was further embedded into the model as a new step process after surface processes (emissions and dry deposition) but

[2]huszarpet@gmail.com, Charles University, Prague, Czech Republic

before vertical diffusion (figure 3.3 in chapter 3, please note that the step order is different in CAMx).

$$\frac{\partial \overline{r_{SHIPTR}}}{\partial t} = E - \frac{\overline{r_{SHIPTR}}}{\tau} + \langle T \rangle \tag{7.1}$$

$$\frac{\partial \overline{r_{NO}}}{\partial t} = \frac{\overline{r_{SHIPTR}}}{\tau} \times \alpha_{NO} \times EI_{NO} + \langle T \rangle \tag{7.2}$$

$$\frac{\partial \overline{r_{NO_2}}}{\partial t} = \frac{\overline{r_{SHIPTR}}}{\tau} \times \alpha_{NO_2} \times EI_{NO_2} + \langle T \rangle \tag{7.3}$$

$$\begin{aligned} \frac{\partial \overline{r_{O_3}}}{\partial t} = &- \frac{\overline{r_{SHIPTR}}}{\tau} \times \alpha_{NO_x} \times EI_{NO_x} \left(\frac{\overline{r_{NO_2}}}{\overline{r_{NO_x}}} - E_{r_{NO_2}/r_{NO_x}} \right) \times \delta \\ &- K_{eff} \times \overline{r_{SHIPTR}} \times \rho \times \alpha_{NO_x} \times EI_{NO_x} \times \overline{r_{O_3}} \times \delta + \langle T \rangle \end{aligned} \tag{7.4}$$

Where r_{SHIPTR}, r_{NO}, r_{NO_2} and r_{O_3} are volume mixing ratios of the plume tracer, NO, NO_2 and O_3 respectively. E is the shipping emission rate, τ determines the lifetime of the plume tracer, α_{NO} and α_{NO_2} are the ratios of NO and NO_2 to NO_x respectively (hence, $\alpha_{NO_x} = 1$). EI_{NO} and EI_{NO_2} are emission factors of NO and NO_2. $E_{r_{NO_2}/r_{NO_x}}$ is a ratio equal to the proportion of NO_2 in the NO_x emissions. K_{eff} is the pre-calculated effective reaction rate. ρ is the air density. δ equals 1 during daytime and 0 over night. $\langle T \rangle$ represents the contribution of transport processes. All overlined quantities refer to GCTM grid cell averages.

As in the previous chapters, MOZART-4 was run for 24 months but only the last 12 months were selected for analysis. Simulations with and without shipping emissions were directly taken from chapter 5. The set of simulations is summarised in table 7.1.

7.2.2 Results

It is first important to emphasize the fact that shipping emissions are different in H2010 and in this study. H2010 used the EMEP regional inventory whereas the ACCMIP emissions were inputted into MOZART-4. A comparison of shipping NO_x emissions between these two inventories is provided on figure 7.1. Several differences are visible on the maps. Firstly, emission fluxes are constant over a

TABLE 7.1: Summary of the simulations performed in the first section of this chapter.

#	ID	Description
1	NS	Simulation without shipping emissions. As in chapter 5.
2	SNP	Simulation with shipping emissions. As in chapter 5.
3	SPP	Simulation including Huszár's shipping parameterisation
4	SPP_keff	Simulation including Huszár's shipping parameterisation. K_{eff} term removed.
5	SPP_t25	Simulation including Huszár's shipping parameterisation. $\tau = 25$min
6	SPP_t120	Simulation including Huszár's shipping parameterisation. $\tau = 120$min
7	SPP_t300	Simulation including Huszár's shipping parameterisation. $\tau = 300$min

year in EMEP but change every month in those defined in the ACCMIP emission inventory. Secondly, some regions of the ACCMIP emission inventory such as remote regions of the Atlantic ocean, the main ship lanes in the Atlantic and those close to the port of Marseilles are characterised by larger emission fluxes compared to EMEP's. This is compensated to some extend by smaller fluxes in the North and Baltic seas as well as in the Eastern part of the Mediterranean sea. In addition, the regridding process from a 0.5°x0.5° grid to a T42LR grid results in an averaging of emission fluxes over large areas which decreases them (Differences between the maximums in the original and regridded ACCMIP inventories are separated by factors ranging between 5.7-9.6).

Since shipping NO_x emission fluxes are smaller, NO_x absolute differences between simulations with and without shipping emissions are also diminished in the present study. For instance in Europe, maximum differences larger than 2 ppbv in winter and larger than 4 ppbv in summer were simulated by the regional model whereas they are smaller than 2 ppbv in the present study (figures 7.2 and 7.3). In addition, relative differences are simulated with larger differences in MOZART-4 of more than 90% over much of the remote regions, indicating that background NO_x concentrations are much smaller in the global model. This behaviour is also reflected on the meridional vertical cross-sections on figure 7.4. This effect was already mentioned in chapter 5 where relative differences where found to increase

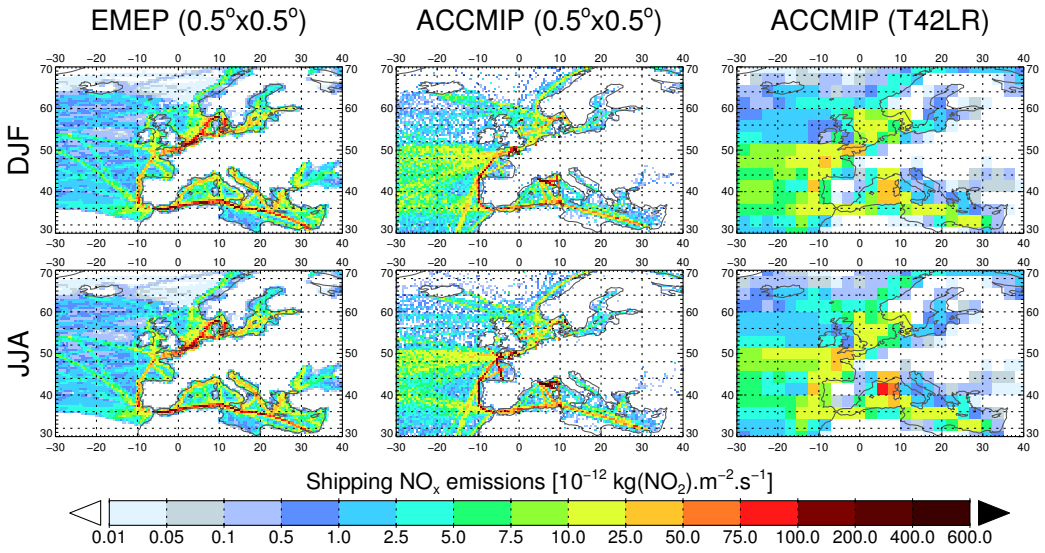

FIGURE 7.1: Comparison between the EMEP and ACCMIP shipping emission inventories in 2000. EMEP data was downloaded from www.ceip.at

by more than one order of magnitude in remote regions. Seasonal variations and gradients are however in good agreement between the two studies.

Regarding the effects of the parameterisation, ship exhaust tracer concentrations are also smaller than in H2010 as testified by figure 7.5. The annually averaged concentrations of ship exhaust tracer have a global peak of 0.57 ppbv near Marseilles (where shipping emissions are the largest) and a local one of 0.37 ppbv in the English Channel. In contrast, the concentration peak in the English Channel observed by H2010 was larger than 1.4 ppbv or about 4 times that found in the present study. Similar differences are noticeable for the NO_x reduction stemming from the parameterisation (figures 7.6 and 7.7). Interestingly, the pattern of shipping NO_x emissions displayed on figure 7.1 is still perceptible on the ship exhaust and NO_x tracer maps which is expected given the short lifetimes of these species. Outside of Europe, SHIPTR concentrations between 100 pptv and 200 pptv and NO_x concentration absolute differences between -100 pptv and -50 pptv are computed by the global model along the main ship lanes in the Atlantic, Indian and Pacific Oceans. Other oceanic regions polluted by shipping emissions see differences smaller than 100 pptv and larger than -50 pptv for SHIPTR concentrations and NO_x concentration differences respectively.

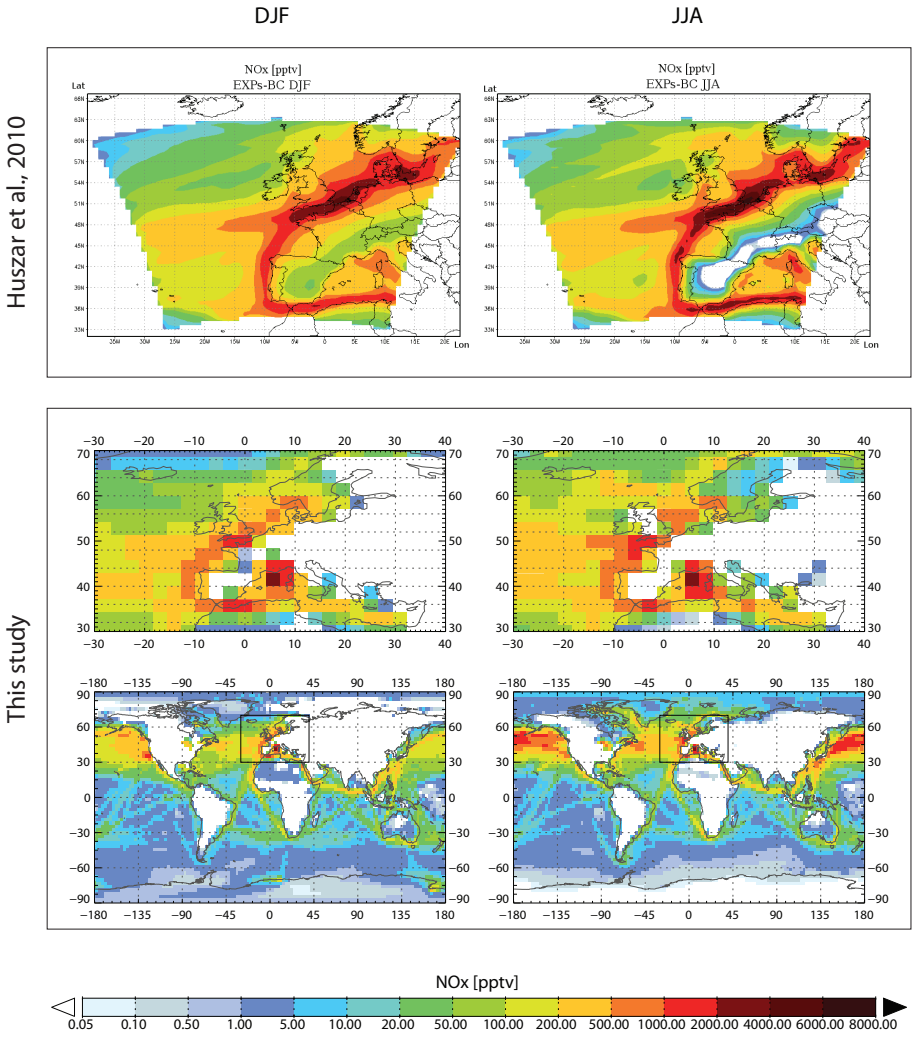

FIGURE 7.2: Comparison between seasonal background NO_x absolute differences in H2010 and this study.

O_3 concentrations are reduced over much of the oceans but also over some continental regions as reported by H2010 (figures 7.8 and 7.9). This is intrinsic to the nature of the ship exhaust tracer which is only removed by its decay into NO_x and results in transport processes moving it further over land. In absolute terms, effects are more important during summer than during winter in the Northern Hemisphere. In Europe, O_3 concentration absolute differences range between -300 pptv and 50 pptv in winter with minimum values located in the Bay of Biscay, off the strait of Gibraltar and in the Mediterranean between the Balearic islands and Sicily. In summer, these absolute differences are larger than -300 pptv along the main ship lanes and reach up to -1.7 ppbv near Marseilles. Impacts remain

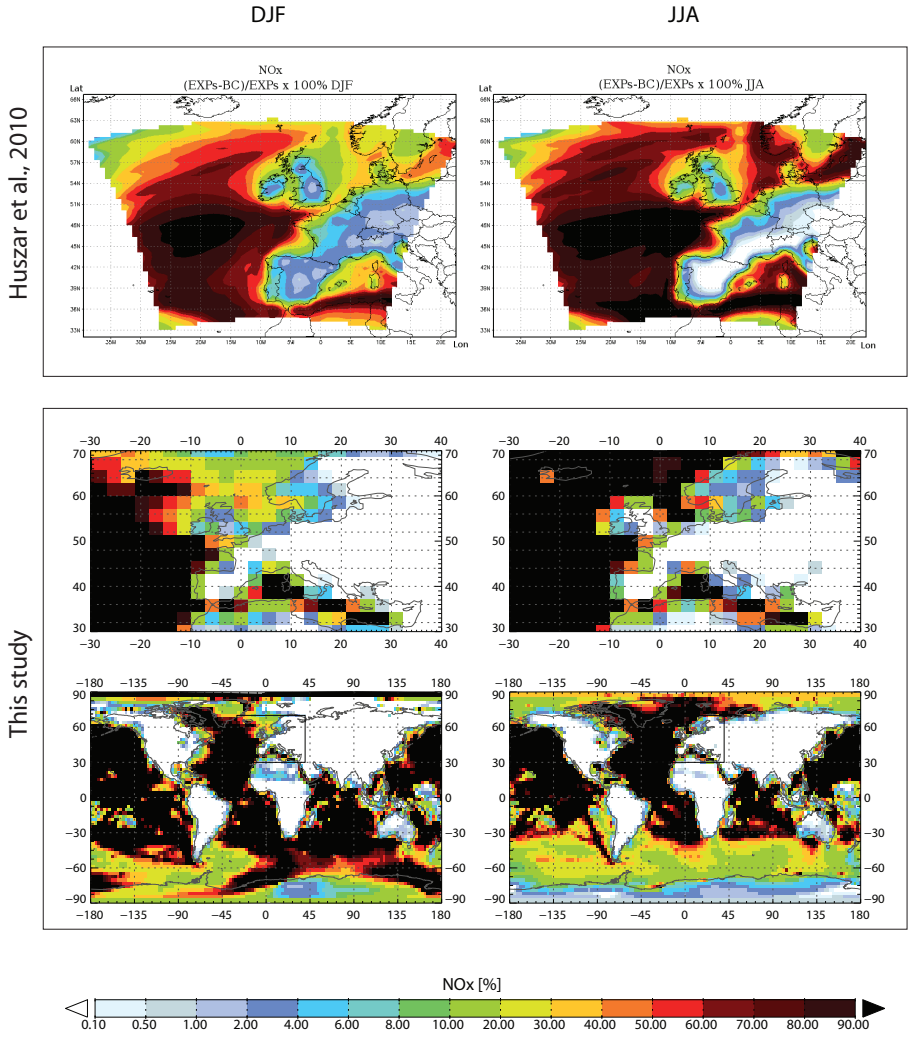

FIGURE 7.3: Comparison between seasonal background NO_x relative differences in H2010 and this study.

similar at coastal locations to those in winter but are smaller than -50 pptv further in land. In terms of relative differences the picture looks different because impacts are larger during winter (up to -26%) than during summer (up to -17%). This effect was also reported by H2010. The O_3 destruction simulated by the regional model in the English Channel in summer is however not reproduced by MOZART-4 since emissions are not large enough, but a similar phenomenon is simulated by the global model near Marseilles in winter instead (where emissions are the largest). Outside of Europe, large absolute changes between -200 pptv and -1 ppbv in summer and below -200 pptv in winter are found near the main ship lanes in remote regions. Relative changes remain smaller than -15% in these regions in winter and smaller than 5% in summer.

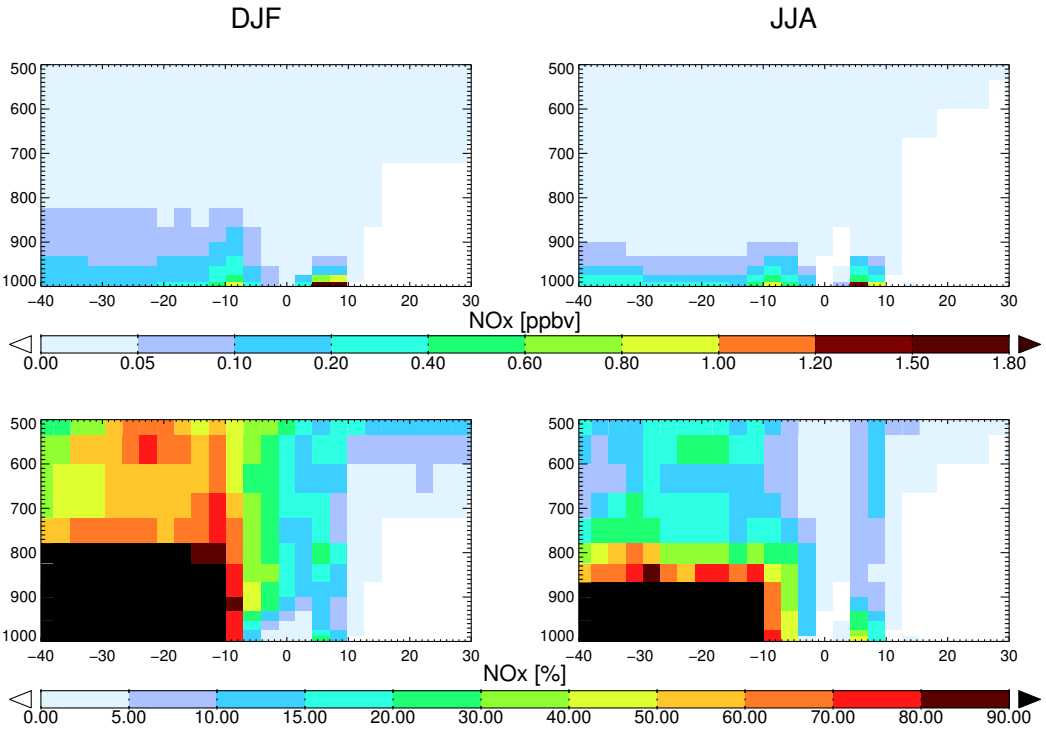

FIGURE 7.4: Meridonal cross-sections at 45.2°N showing absolute and relative NO_x differences between the SNP and NS simulations performed with MOZART-4.

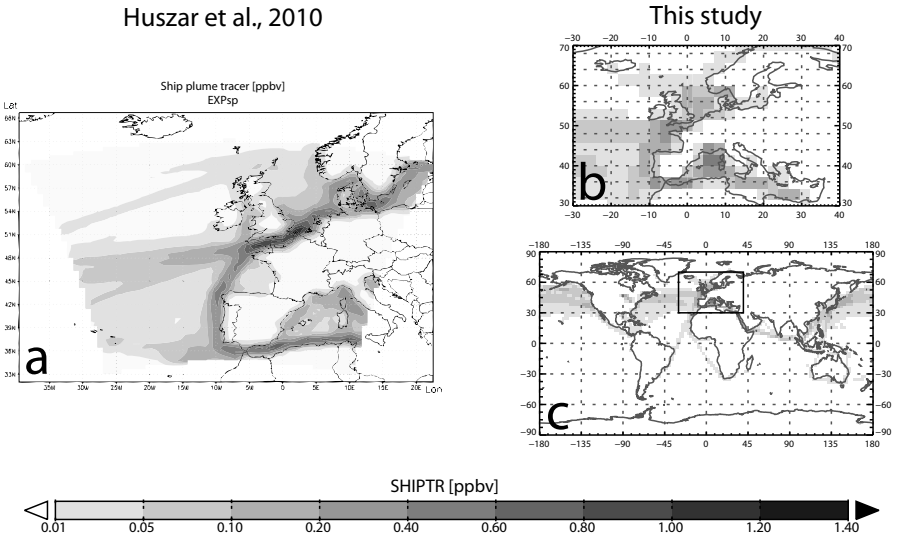

FIGURE 7.5: Comparison between annually averaged SHIPTR volume mixing ratios in H2010 and this study.

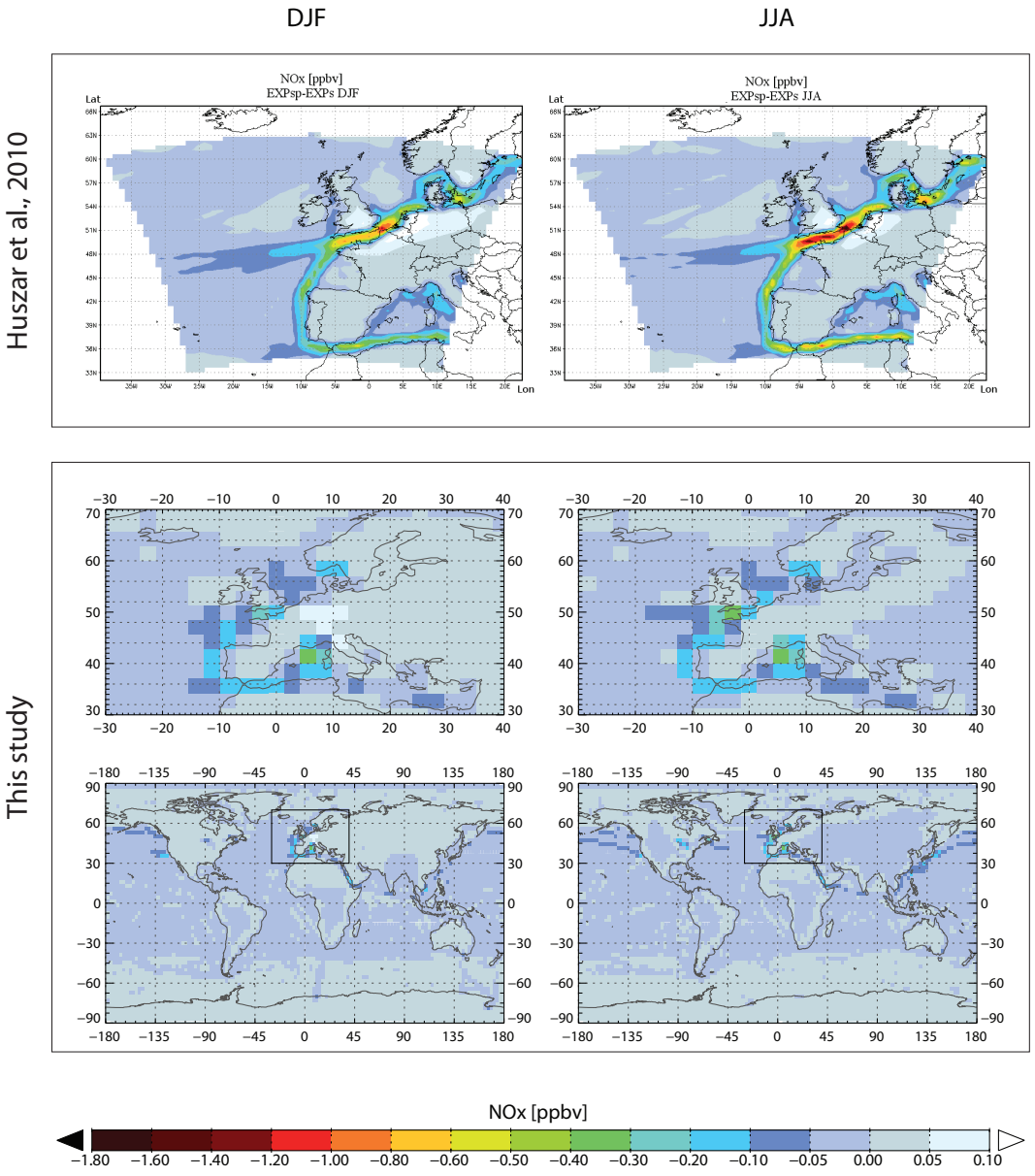

FIGURE 7.6: Comparison between seasonal NO_x absolute differences in H2010 and this study.

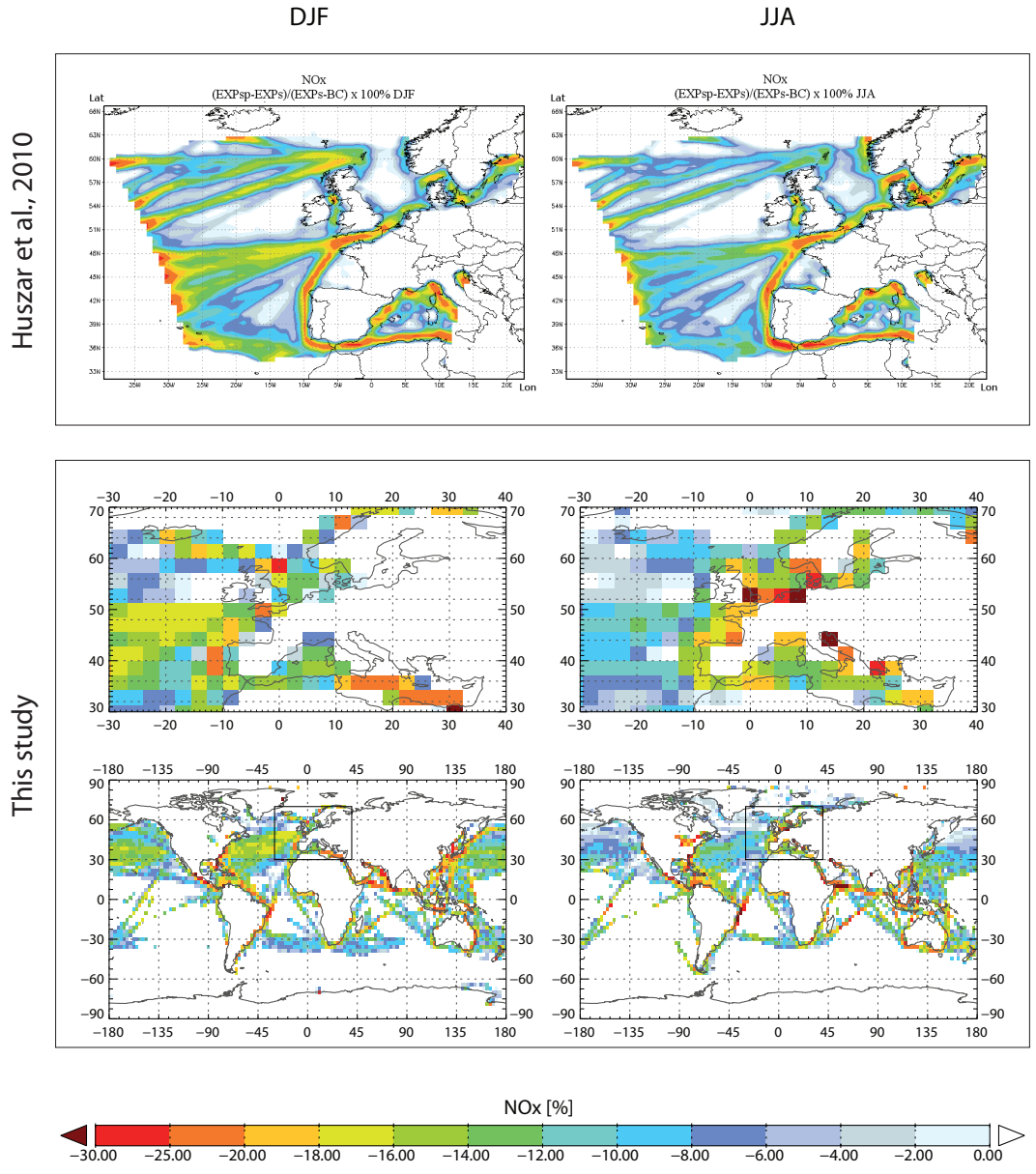

FIGURE 7.7: Comparison between seasonal NO_x relative differences in H2010 and this study.

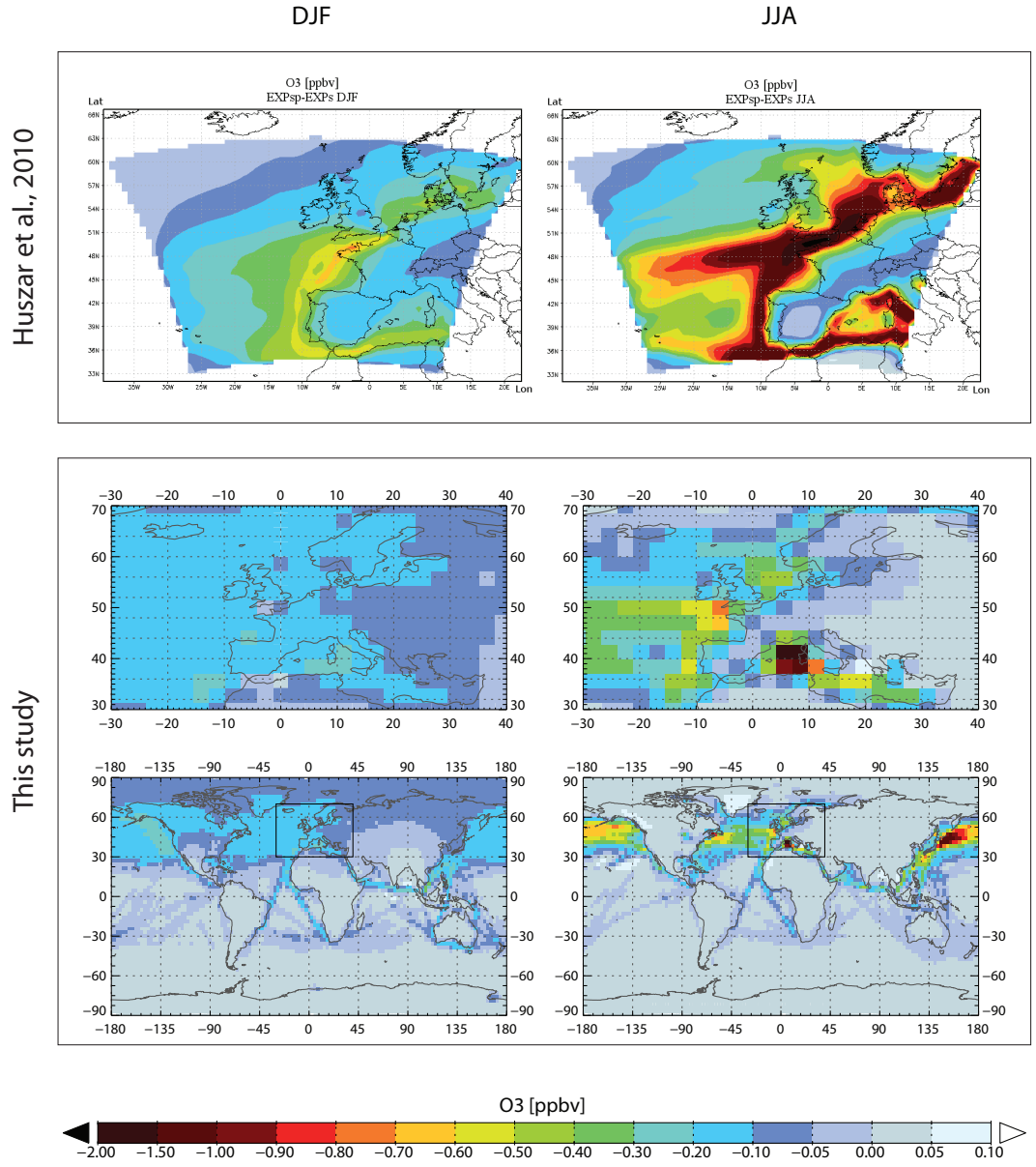

FIGURE 7.8: Comparison between seasonal O_3 absolute differences in H2010 and this study.

The meridional cross-sections at 45.2°N presented in H2010 are also plotted here on figures 7.10 and 7.11. MOZART-4 does not reproduce the decrease of NO_x simulated by CAM-x. In fact, the global model simulates larger NOx concentrations in the upper MBL and free troposphere when the shipping parameterisation is included than the CAM-x. This effect results in a larger production of O_3 in the troposphere compare to a simulation with instantaneous dilution of shipping emissions.

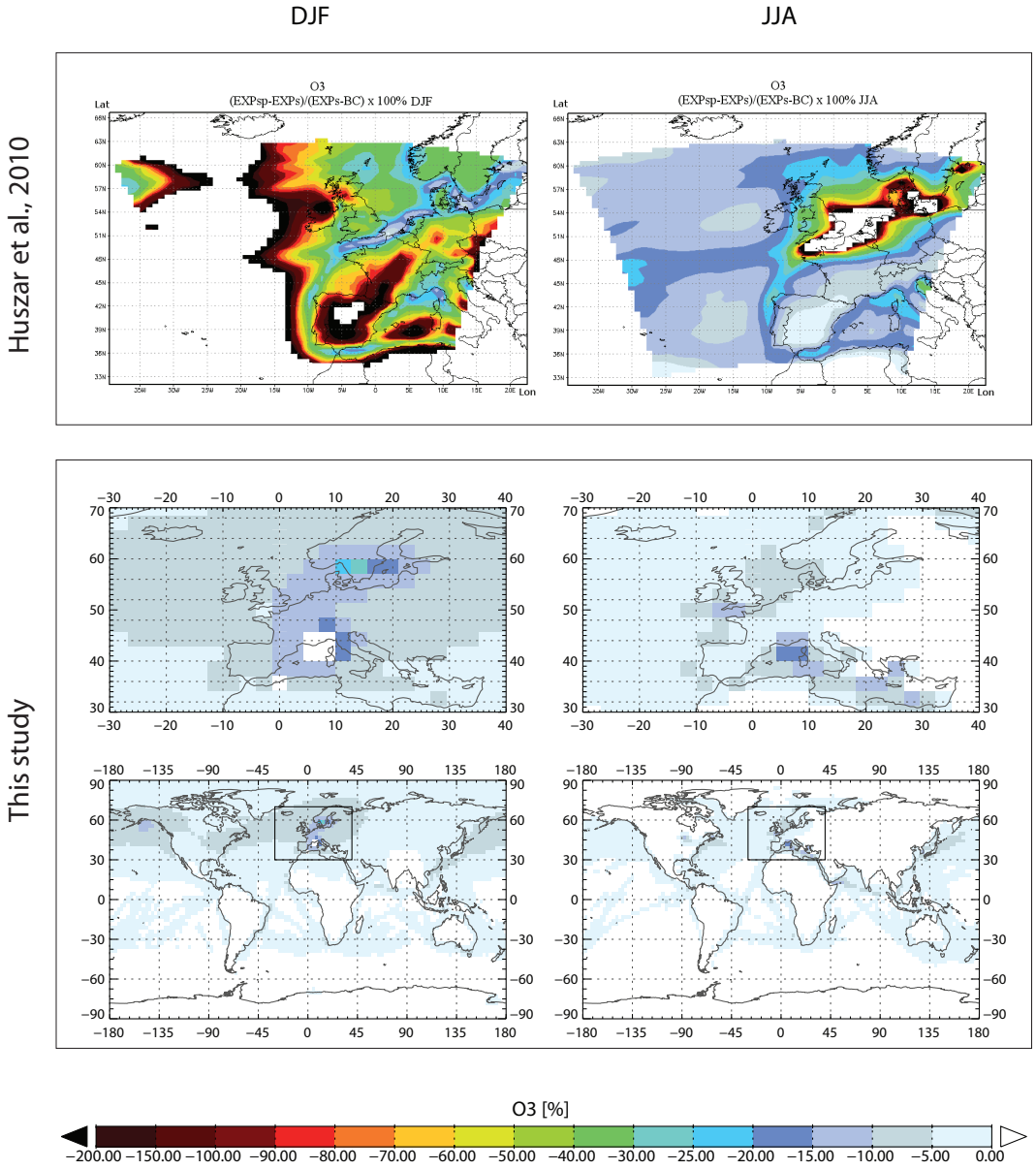

FIGURE 7.9: Comparison between seasonal O_3 relative differences in H2010 and this study.

Sensitivity tests were also carried out and extended compared with H2010. Firstly, the sensitivity to K_{eff} was assessed. H2010 tested the sensitivity to this parameter by changing its original value by ±14%. They commented that this parameter had little effect on shipping O_3 concentrations (maximum of 4-5 pptv in summer (about 0.5%)). Here, the term of the parameterisation corresponding to the effective reaction was simply removed from equation (7.4) and results are displayed on figure 7.12. It is clear that the parameterised effective reaction is insignificant compared to the O_3 titration term. According to the results of the present study,

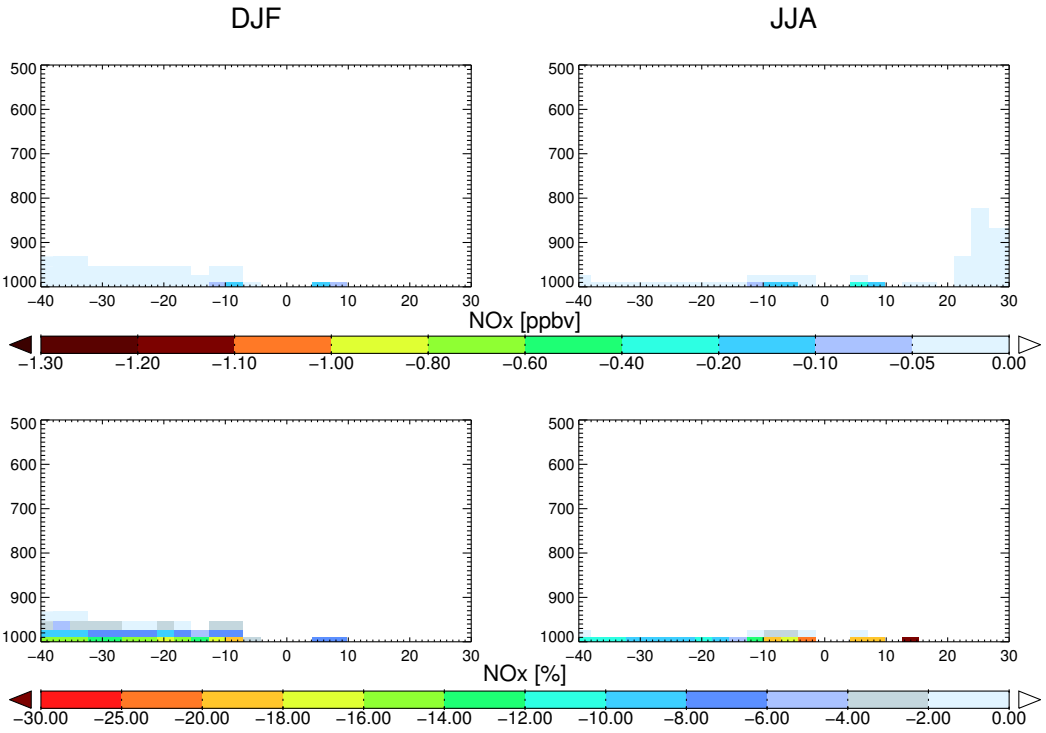

FIGURE 7.10: Meridional cross-sections at 45.2°N showing the absolute and relative NO_x differences between the SPP and SNP simulations performed with MOZART-4

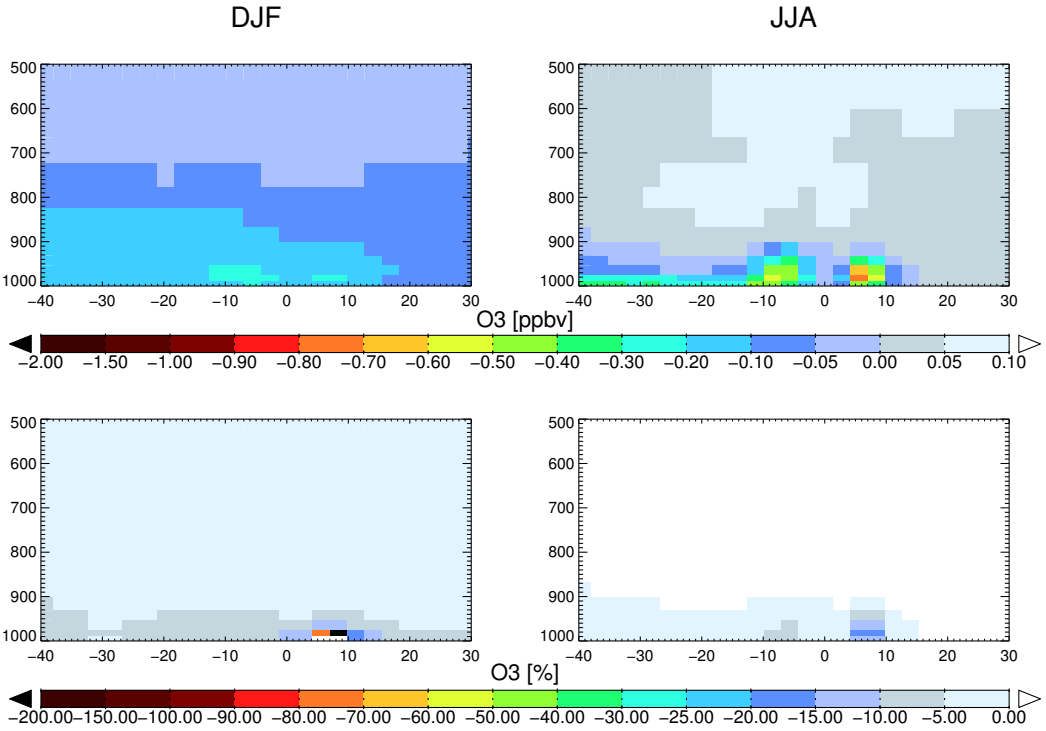

FIGURE 7.11: Same as figure 7.10 but for O_3

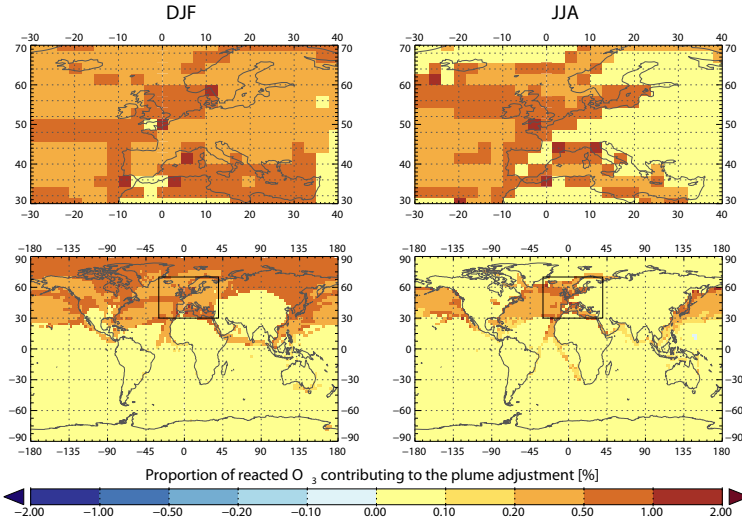

FIGURE 7.12: Sensitivity of the parameterised O_3 removal to the K_{eff} parameter.

the proportion of O_3 removed by this term represent less than 2% of the total removal corresponding to a few parts per trillion in volume of O_3. This effect can be explained by the fact that the parameterised chemical reaction considered here is that between NO_2 and O_3 which is not significant in the MBL. A simple calculation confirms that this parameter has a small contribution over a model time step:

$$\Delta t \times K_{eff} \times \rho \times O_3 \times NO_x = 1200.0 \times 7.0 \times 10^{-19} \times 2.5 \times 10^{19} \times 20 \times 10^{-9} \times 1 \times 10^{-9} \tag{7.5}$$

$$= 4.2 \times 10^{-13}$$

Secondly, the sensitivity to the parameter τ was tested by setting its value to: 25 minutes, 120 minutes and 300 minutes (figure 7.13). As the lifetime of the ship exhaust tracer (τ) augments, its concentrations increase as well. Moreover, concentrations are larger in summer than in winter owing to the lower MBL height (see chapter 4). Shipping NO_x concentrations tend to decrease linearly with the increase of τ. However, some grid cells see an increase in shipping NO_x concentrations compared to the reference simulation. This is especially true in winter and is largely associated to the transport of ship exhaust tracer above land. These

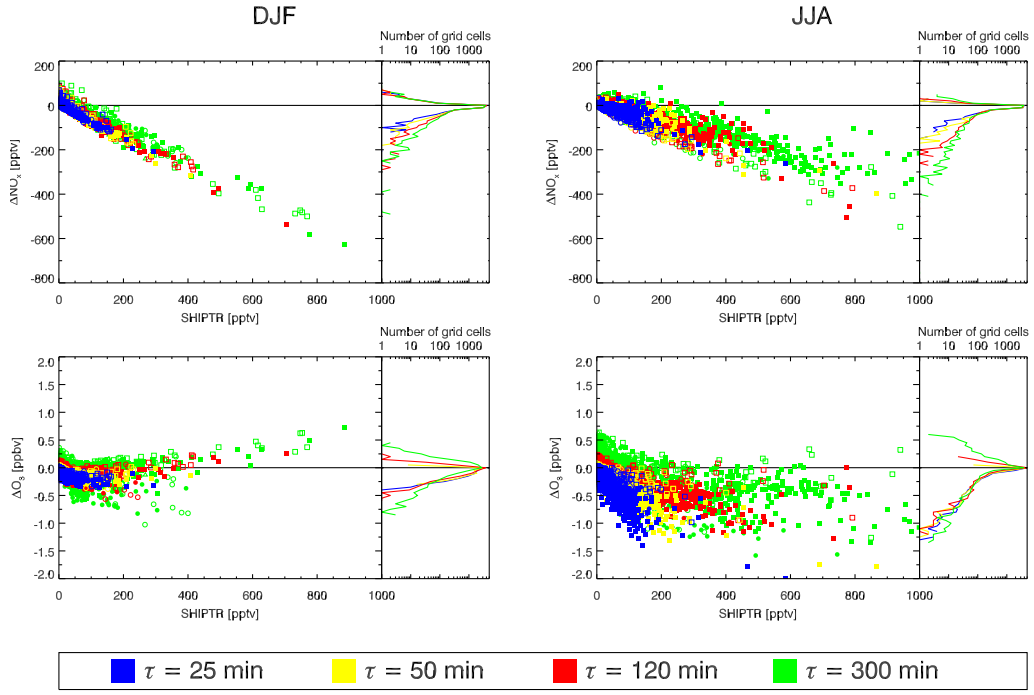

FIGURE 7.13: Sensitivity of NO_x and O_3 concentrations to the τ parameter at the bottom level. ΔNO_x and ΔO_3 represent concentration differences between the simulation with and without the shipping emission parameterisation. Filled symbols display grid cells found above oceans and influenced by shipping emissions whereas empty ones display the remaining grid cells. Tropical regions are shown with circles, mid-latitudes are displayed with a square symbol and polar regions are represented by triangles.

changes in shipping NO_x concentrations result in changes in shipping O_3 concentrations. As τ increases, two phenomena compete against each other. On the one hand, changes in shipping NO_x concentrations shift the NO_x-O_3-HO_x system into various regimes of O_3 production. The non-linearity of this system is emphasized on the winter and summer plot where parabola-shaped curves can be seen. H2010 in the English Channel where a decrease in τ leads to a recovery in O_3 production. On the other hand, the transport of SHIPTR into further locations previously unaffected by shipping NO_x emissions results in a larger O_3 production. It is important to realise that this transport occurs also vertically and that O_3 builds up also in the free troposphere. Overall, this study shows that there is more O_3 removed when τ equals 25 minutes. Strangely, H2010 displayed this effect on figure 12 in their publication but seemed to get confused by this finding and hardly commented about it.

In order to understand this peculiar effect of the parameterisation, it is interesting to look more closely at the effects of the parameterisation at steady state[3]. Under this condition, (7.1) becomes :

$$\frac{\partial \overline{r_{SHIPTR}}}{\partial t} = 0 \quad \Leftrightarrow \quad E + \langle T \rangle = \frac{\overline{r_{SHIPTR}}}{\tau} \tag{7.6}$$

If transport processes ($\langle T \rangle$) were not included in (7.6), one can see that the decaying fraction of SHIPTR ($\frac{\overline{r_{SHIPTR}}}{\tau}$) would equal the shipping NO_x emissions (E) at steady state. Consequently, the NO and NO_2 tracers would receive the same amount of shipping NO_x molecules as in the instantaneous dilution case with the only difference stemming from a temporal shift defined by τ. Decreases of shipping NO_x concentrations in ship lanes are thus driven by transport processes. Nonetheless, these transport processes are also responsible for artificially increasing NO_x concentrations away from shipping lanes horizontally and vertically. This effect will result in both O_3 production and destruction depending on the region considered.

7.2.3 Discussion

The implementation of Huszár's parameterisation results in shipping concentration reductions of about 15% to 20% for NO_x and of about 5% to 10% for O_3 in the main ship lanes. Compared with H2010, O_3 reductions are much smaller since they were previously found to lie between -25% and -20% in the main ship lanes.

A number of problems have been identified in the first section of this chapter which focuses on implementing the parameterisation developed by Dr. Huszár. Firstly, the parameterisation exhibits a dependency on model resolution that arises from the regridding of shipping emissions. The coarser resolution used in here leads to smaller concentrations of ship exhaust tracer which in turn reduces the effect of the parameterisation in terms of NO_x and O_3 removal.

[3]Steady state can be assumed to be reached after 5τ which roughly equals to 4 hours when τ equals 50 minutes.

In addition, the way NO and NO_2 are released at the global scale is not realistic since after 50 minutes the proportion of NO is much closer to background NO ratio than shipping emission NO ratio.

Furthermore, the ship exhaust tracer is allowed to be transported across the model by advection, convection and vertical diffusion. The results presented here suggest that this introduces a non-physical behaviour in the system by displacing shipping NO_x emissions not only temporally but also spatially.

Sensitivity studies revealed that the second term in equation (7.4) is clearly insignificant since it represents the loss of O_3 driven by a chemical reaction that is unimportant in the MBL. Moreover, the parameter τ controls the concentrations of ship exhaust tracer as expected but does not necessarily lead to decreases in both NO_x and O_3 shipping perturbations. This phenomenon stems from the combined effects of transport and the lack of removal processes of the ship exhaust tracer.

Finally, K_{eff} and τ depend both on external conditions such as temperature, wind shear, MBL height and stability as underlined by H2010.

The next section of this chapter will seek to address some of the problems encountered with the current version of this parameterisation.

7.3 Implementing Moldanová's approach

One of the problems arising from Huszár's parameterisation is the fact that the parameterisation does not account for NO_x transformation into HNO_3 which constitutes a major loss of NO_x in the MBL and results in less O_3 molecules being produced. Cariolle et al. [2009] extended the parameterisation for the case of aircraft by using two coefficients that represent this loss. Dr. Jana Moldanová[4] proposed a different approach based on an effective reaction between SHIPTR[5] and background OH ([Moldanová, 2010] and collaborative work, 2011).

7.3.1 Methodology

In this section, Moldanová's approach is assessed by implementing the scheme into MOZART-4. The principle of this approach is summarised on figure 7.14. During a 1-week collaborative work at IVL, the sensitivity of this new scheme was tested against various parameters such as the magnitude and time of emissions and τ. It appeared that the parameterisation was producing spurious data over night and for this reason the scheme was switched on during daytime only. The effective reaction rate K_{eff} was pre-calculated with the SPM-2D model (see chapter 3) for typical oceanic conditions found above clear-sky oceanic midlatitudes in spring at midday (atmospheric stability D, relative wind speed 5 m.s$_{-1}$, temperature 280 K, Julian day 96). This simple factor was then applied uniformly across the the model's domain. A factor of about 3 was found between the effective and the usual rates of the reaction between NO_2 and OH.

7.3.2 Results

Shipping NO_x concentrations are clearly reduced over ship lanes as a result of implementing this new approach (figure 7.15). In winter, these concentrations

[4] jana.moldanova@ivl.se, IVL, Sweden
[5] SHIPTR represents shipping NO_x exhaust

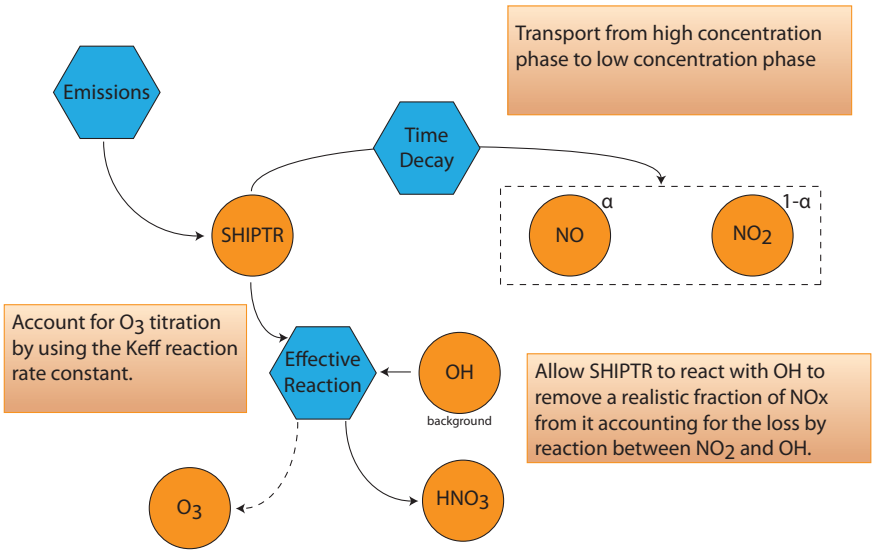

FIGURE 7.14: Flowchart displaying the functioning of the ship emission parameterisation proposed by Dr. Jana Moldanová. Processes are displayed with hexagon symbols while gas species are shown with circles.

TABLE 7.2: Summary of the simulations performed in the first section of this chapter.

#	ID	Description
1	NS	Simulation without shipping emissions. As in chapter 5.
2	SNP	Simulation with shipping emissions. As in chapter 5.
3	SPPM	Simulation including Moldanová's shipping parameterisation
4	SPPM_keff	Simulation including Moldanová's shipping parameterisation. K_{eff} tuned.

are reduced by a few tenth of pptv across most of the oceans and reductions can reach more than 200 pptv in areas affected by large shipping emissions (Europe, Eastern coast of USA, Asia), corresponding to reductions between -20% and -50% compared to background NO_x. In summer, these reductions are even larger, especially in the northern mid-latitudes where OH production is stimulated by increased sunlight. The main ship lanes linking Asia, Europe and the USA see decreases between 200 pptv and 400 pptv and up to 700 pptv. In the Atlantic and Pacific Oceans, this translates into reductions larger than 20-30%. Nonetheless, an extra few hundreds of pptv can be seen above land, especially in Winter above

those hosting developed economies (South East Asia, Europe, North America). This effect cannot be solely attributed to the transport of SHIPTR over land since Vinken et al. [2011] reported similar behaviour with their parameterisation, although their increase is smaller. It could also stem from the general reduction of O_3 and its subsequent effects on OH which also occurs over land. However, as Vinken et al. [2011] mentioned, this increase is small in terms of relative differences.

Shipping O_3 concentrations are reduced across the surface of the model. In winter, reductions are about -1 ppbv above the northern oceans whereas further reductions of -2 ppbv are simulated by the model. These translate into reductions of more than 20% above the northern oceans. Compared with Huszár's parameterisation, no O_3 molecules are produced. Over land, O_3 relative differences can reach substantial amounts (more than 50% in developed countries), but it should be reminded that the shipping O_3 perturbation in this region is small.

Zonal averages of absolute differences show that shipping NO_x levels are enhanced in most of the troposphere by more than 10 pptv and less than 50 pptv (figure 7.17). However, the vertical gradient of shipping NO_x is such that these increases are only significant near the surface of the model between 700 hPa and 1000 hPa. Effects are again stronger during winter than during summer.

As for shipping O_3, substantial decreases of up to 5 ppbv can be seen at the top of the tropical region. Remembering that the shipping O_3 perturbation induced by instantaneous dilution was peaking at about 2 ppbv. These results shows that the parameterisation removes more O_3 than expected. The location of these changes indicates again a problem with the transport of SHIPTR which can be effectively lift up into the upper troposphere in tropical regions. The ship exhaust tracer has then the potential to remove O_3 via the parameterised O_3 titration term. Overall the shipping O_3 response is significantly reduced and very likely unrealistic.

The sensitivity of the shipping NO_x and O_3 concentrations was assessed by setting K_{eff} to the default rate calculated by MOZART-4. Figure 7.19 shows that further NO_x and O_3 are removed from the system as a result of this change, especially in summer.

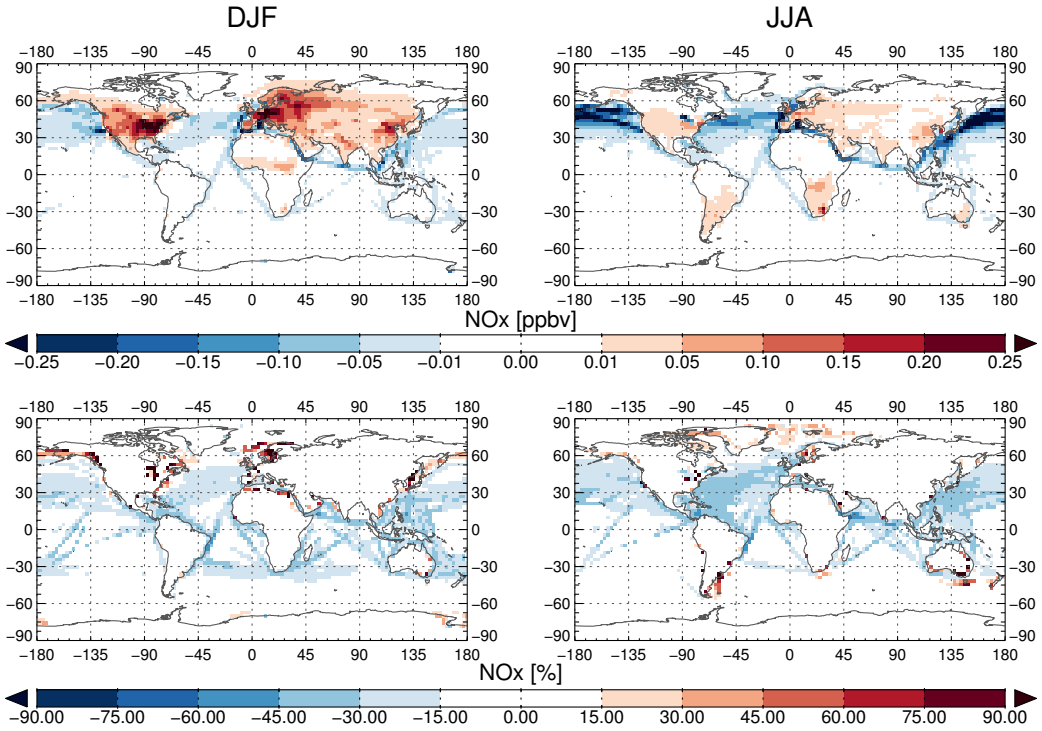

FIGURE 7.15: Absolute and relative differences of shipping NO_x concentrations between simulations SPPM and SNP at the bottom level.

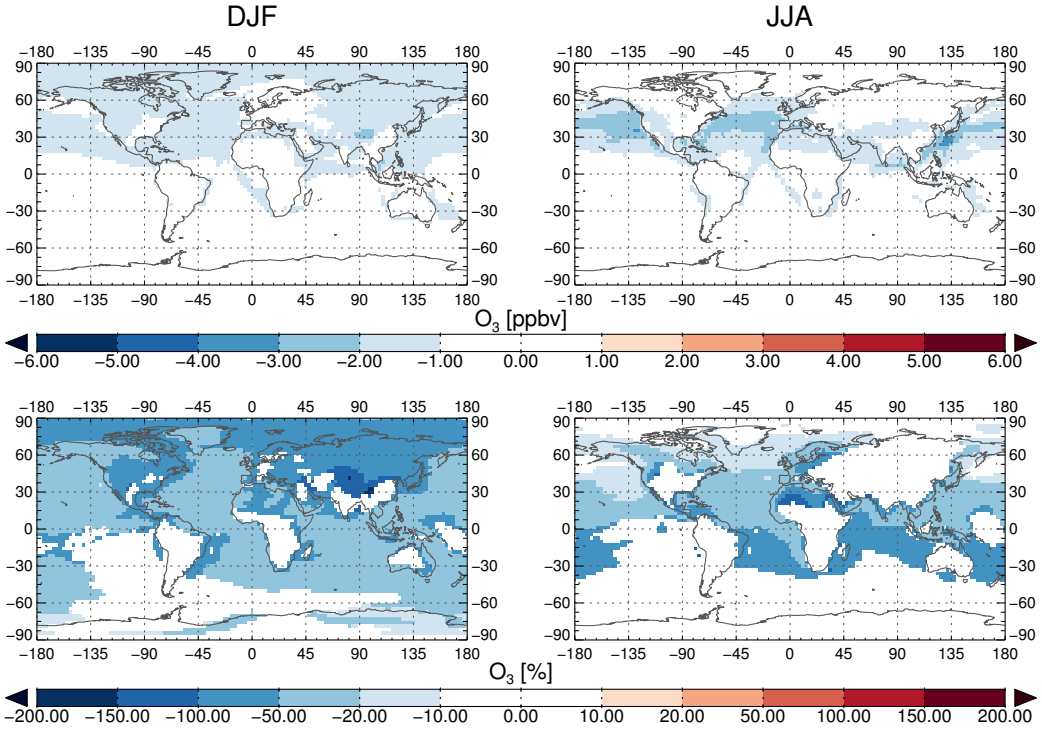

FIGURE 7.16: Absolute and relative differences of shipping O_3 concentrations between simulations SPPM and SNP at the bottom level.

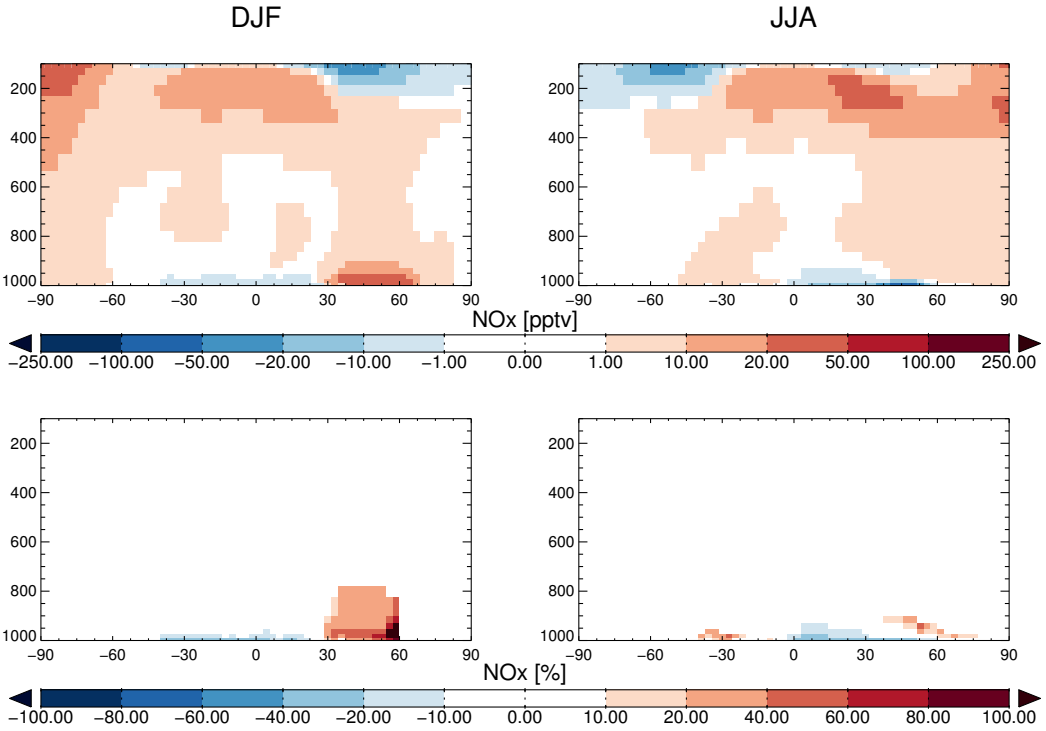

FIGURE 7.17: Absolute and relative differences of shipping NO_x zonal averages between simulations SPPM and SNP.

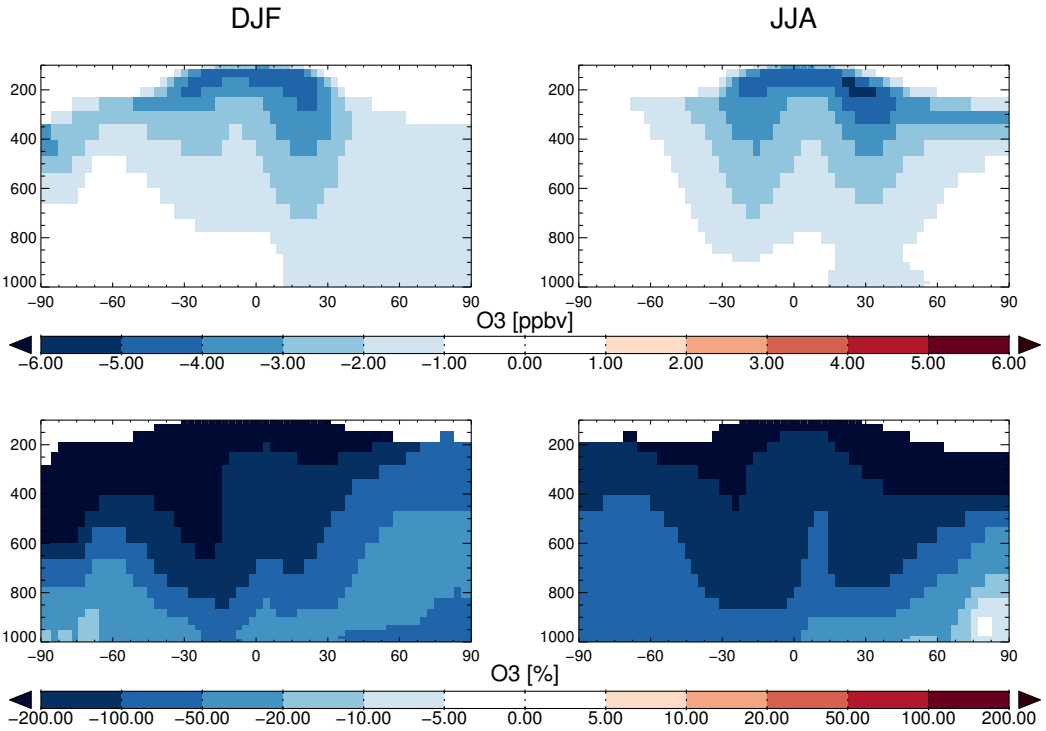

FIGURE 7.18: Absolute and relative differences of shipping O_3 zonal averages between simulations SPPM and SNP.

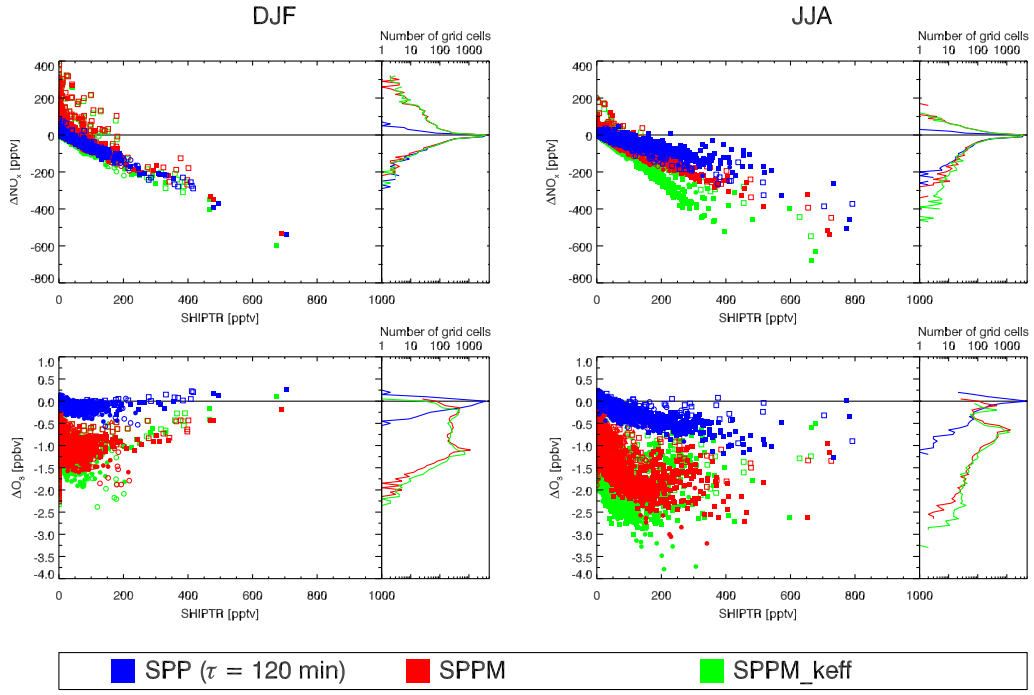

FIGURE 7.19: Sensitivity of shipping NO_x and O_3 concentrations to K_{eff}. Filled symbols display grid cells found above oceans and influenced by shipping emissions whereas empty ones display the remaining grid cells. Tropical regions are shown with circles, mid-latitudes are displayed with a square symbol and polar regions are represented by triangles.

7.3.3 Discussion

In this second section, the parameterisation was brought a step closer to reality by taking into account the removal of SHIPTR by OH and its subsequent conversion into HNO_3. This sink reaction allows to account for the loss of shipping NO_x which is a crucial characteristic of ship plumes. This was done by implementing Moldanová's approach into MOZART-4, in a similar fashion to the implementation of Huszár's approach.

Shipping NO_x and O_3 reductions are larger than 20% at the surface of the Northern Oceans and are in better agreement with the recent work of Vinken et al. [2011]. Shipping NO_x reductions are particularly similar in the two studies where values reach -0.2 ppbv in the main ship lanes in summer time. However, O_3 reductions remain smaller in the present study. For instance, Vinken et al. [2011] reported

decrease smaller than -3 ppbv over much of the oceans whereas they are here larger than -3 ppbv.

The large shipping O_3 decreases present in the free and upper troposphere are likely to be unrealistic. Park et al. [2004] showed that the monsoon region in MOZART is affected by a strong uplift which could result in SHIPTR being quickly and efficiently transported in upper regions of the troposphere. Unfortunately, Vinken et al. [2011] did not show the vertical extent of the impacts of their parameterisation, so that no comparison is possible at the moment.

As in Huszár et al. [2010], the value for τ was calculated for specific dynamical conditions. In the future, this parameter should be made dependent upon atmospheric stability, temperature, ... The same argument applies to the parameter K_{eff}.

Chapter 8

Radiative forcing of ozone and methane in 2000 and in the future

In this chapter, MOZART-4 and Edwards-Slingo were used together to estimate the future radiative forcing of shipping O_3 and CH_4 in 2000 and under the RCP scenarios. The following results were found:

- In 2000, the net radiative forcing from shipping NO_x emissions equals -60 $mW.m^{-2}$. The O_3 RF is 31 $mW.m^{-2}$ whereas the CH_4 RF is -60 $mW.m^{-2}$, showing that the CH_4-induced O_3 RF and stratospheric H_2O RF balance out the O_3 RF.
- Under the RCP scenarios, shipping emissions do not grow much (+23% maximum) yielding similar changes in shipping perturbations.
- The net radiative forcing from shipping NO_x emissions ranges between -96 $mW.m^{-2}$ and -15 $mW.m^{-2}$.
- A linearisation of the shipping NO_x-O_3-CH_4 system was calculated and the shipping O_3 and CH_4 radiative forcing can now be expressed in terms

of NO_x, CO and VOC emissions as well as background CH_4 concentrations. This is also the case for global O_3 tropospheric column and CH_4 lifetime

8.1 Introduction

A number of studies has discussed the radiative forcing (RF) impacts arising from shipping NO_x in 2000. The range of RF values in 2000 available from the literature was recently compiled by Eyring et al. [2009] and lies between 8 $mW.m^{-2}$ and 41 $mW.m^{-2}$ for O_3 RF and between -56 $mW.m^{-2}$ and -11 $mW.m^{-2}$ for CH_4 RF. Latterly, Myhre et al. [2011] estimated these values to equal 24 $mW.m^{-2}$ for O_3 RF and -27±8 $mW.m^{-2}$ for CH_4 RF. The relatively large spread of RF values stems from the use of different models as well as from significant uncertainties in shipping emissions inventories, as noted in chapter 6.

The development of future emission scenarios is an important process to address the problem of anthropogenic climate change. It is particularly relevant to the context of policy making which seeks to establish solutions[1] in order to prevent dangerous climate change, but also to the industry which will have to adapt to new regulations and face new challenges related to climatic perturbations. In 2000, a collection of forty emission scenarios was presented and published in the IPCC Special Report on Emissions Scenarios (SRES) [Nakicenovic et al., 2000]. These emission scenarios comprise four main families: A1, A2, B1 and B2 which result from the combination of two dimensions: economy versus environment and regionalisation versus globalisation. The A1 family is further split into A1F1 (fossil fuel intensive), A1T (predominantly non-fossil fuel) and A1B (balanced) (figure 8.1). The SRES scenarios have been extensively used since their creation, particularly in the Third Assessment Report and the Assessment Report 4 of the IPCC. However, they have been criticised on several occasions for overestimating energy

[1] These solutions include for instance regulations, market-based instruments and behavioural approaches.

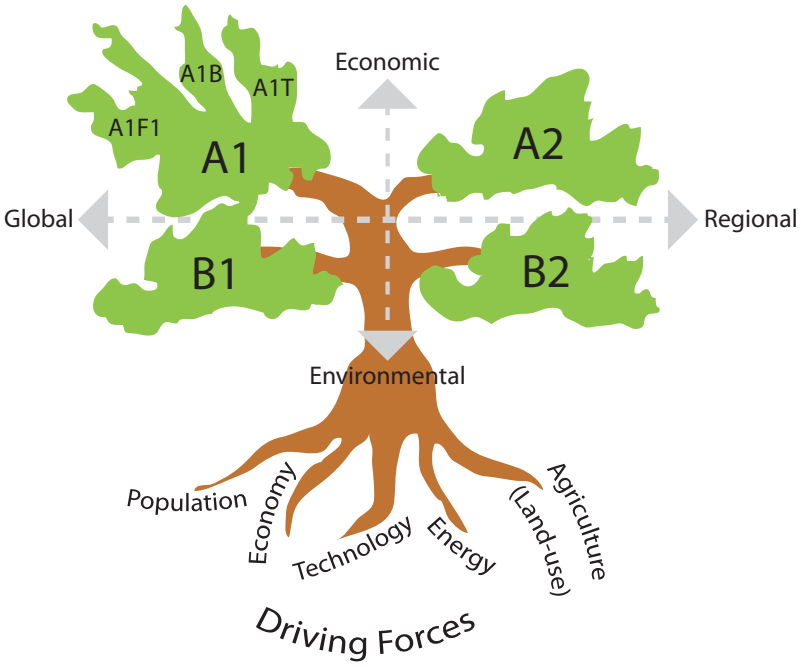

FIGURE 8.1: SRES families against the two main dimensions. Figure adapted from figure 1.4 of section 1.7.2 in Nakicenovic et al. [2000].

resources and anthropogenic emissions and therefore not representing plausible futures [Höök et al., 2010, Patzek and Croft, 2010].

Scenarios are used by three different communities in the framework of the IPCC, namely the climate modelling community (CMC), the integrated assessment modelling community (IAMC) and the vulnerability, impacts and adaptation community (VIAC). Another criticism of the SRES scenarios was that they were designed for the CMC but were hardly suitable for the VIAC. More recently, the creation process of emission scenarios has been reviewed and a new framework was adopted [Moss et al., 2010]. This new framework consists of four Representative Concentration Pathways (RCP) drawn from the literature and calculated by means of four integrated assessment models (IAM): IMAGE, GCAM, AIM and MESSAGE that resolve economics, technology, and physical processes [Van Vuuren et al., 2007, 2010, Clarke et al., 2007, Thomson et al., 2010, Masui et al., 2010, Riahi et al., 2007, 2010]. These new scenarios aim at providing consistent views of the future that can be used by the three communities. Figure 8.2 illustrates the similarities and differences between the SRES and RCP emission scenarios and suggests

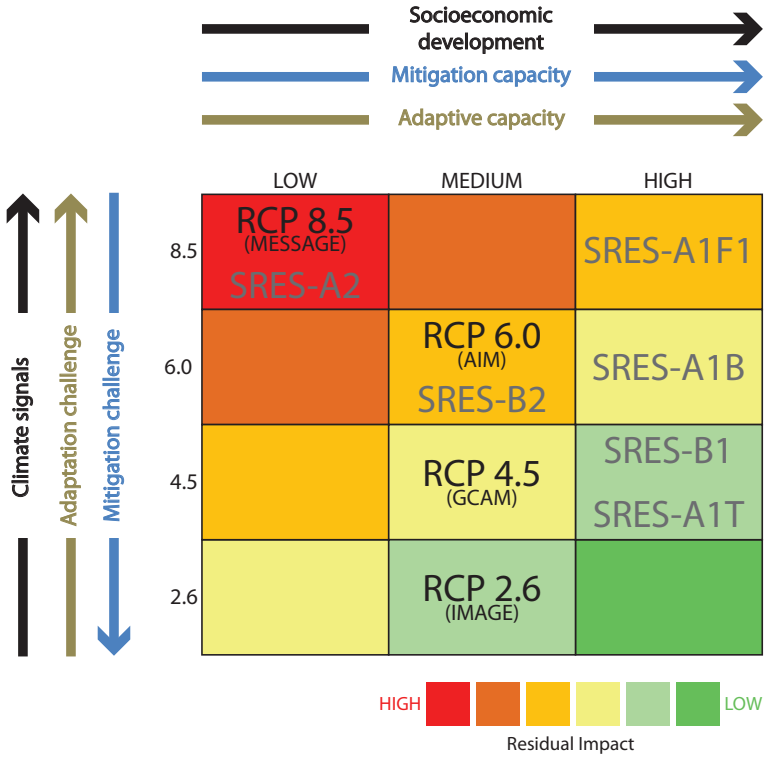

FIGURE 8.2: Similarities between the SRES (grey) and RCP (black) scenarios. The names of the IAMs are provided in brackets below RCP scenarios names. Figure adapted from figures 5 and 7 in van Vuuren et al. [2010].

that previous SRES scenarios were expecting too large adaptive and mitigation capacities under carbon-intensive scenarios. Four scenarios have been constructed in total and they describe different possible futures in terms of RF stabilisation. For instance, in the RCP 2.6[2], the temporal variation of anthropogenic emissions entails a RF stabilisation at 2.6 $mW.m^{-2}$ whereas in the RCP 4.5, 6.0 and 8.5 it leads to stabilisations at 4.5 $mW.m^{-2}$, 6.0 $mW.m^{-2}$ and 8.5 $mW.m^{-2}$ respectively. These scenarios will be employed in the Assessment Report 5 (AR5) of the IPCC by the three communities identified previously.

A few studies have looked at future impacts of the shipping sector on radiative forcing. For instance, Lee et al. [2006] used the future shipping emission scenarios constructed by Eyring et al. [2005a] and forecasted a range of possible CO_2 RF between 80 $mW.m^{-2}$ and 90 $mW.m^{-2}$ in 2050. However, this study did not assess the impacts of shipping NO_x emissions in the future. Furthermore, the use of a

[2]Note that this scenario is also called RCP-3PD in the literature because of its peak-and-decline characteristic.

simple linearised formula to estimate the perturbation of OH failed to provide a realistic depletion of CH_4 in 2000. Later on, Eyring et al. [2007] simulated for the first time a case of future shipping emissions in 2030 (assuming a flat emission increase of 2.2% from 2000) using a combination of GCTM, GCM and RTM. They estimated the O_3 and CH_4 RF to be 13.6±2.3 $mW.m^{-2}$ and -21 $mW.m^{-2}$ respectively in 2030. Lately, Hodnebrog et al. [2011a] forecast these RF under a B1 scenario with the help of a collection of GCTM, GCM and RTM in 2025 and 2050. They followed the work of Myhre et al. [2011] to account for the long-term effects of CH_4 on O_3 and reported the following values for 2025: O_3 (short-term) 23.6±8.4 $mW.m^{-2}$, CH_4 -37.8±4.1 $mW.m^{-2}$ and O_3 (long-term) -13.8±1.5 $mW.m^{-2}$ and the following ones for 2050: O_3 (short-term) 25.2±9.6 $mW.m^{-2}$, CH_4 -41.0±5.0 $mW.m^{-2}$ and O_3 (long-term) -15.0±1.8 $mW.m^{-2}$.

The present study seeks to estimate NO_x radiative forcing resulting from the full range of possible futures of shipping emissions from 2010 up to 2100 using the four different RCP scenarios. For the first time, a multi-linear parametrisation of the NO_x-O_3-CH_4 shipping system is produced. Such parametrisation could help the shipping industry as well as policy makers to facilitate taking decisions in the future.

8.2 Methodology

In order to estimate impacts of shipping NO_x emissions on the respective O_3 and CH_4 radiative forcings in 2000 and in the future, two models were utilised in conjunction with the ACCMIP 2000 and RCP emission inventories. On the one hand, MOZART-4 computed the perturbations of O_3 and CH_4 in the troposphere. On the other hand, the offline RTM Edwards Slingo calculated the O_3 and CH_4 radiative forcings arising from these perturbations. The next two sections will describe the modifications made to each model and their respective input data.

8.2.1 MOZART-4: Calculating ozone and methane concentration perturbations

The model setup used to performed simulations in 2000 was the same as that described in chapter 5. Historical shipping emissions in 2000 were taken from the ACCMIP emission inventory and the model was run with NCEP-Reanalysis dynamical data representative of the year 2000 on a T42LR horizontal grid with 28 vertical levels.

As shown on figure 3.3 in chapter 3, MOZART-4 requires various input data to run. In order to perform future scenario simulations, these input data need to be updated. In particular, it is mandatory to change initial concentrations of prescribed long-lived species such as CH_4 and N_2O provided at the beginning of each simulation as well as concentrations defined at the lower and upper boundary conditions (LBC and UBC). In the present study, the meteorology was fixed to 2000 conditions and so were the natural emissions of isoprenes and terpenes depending on them.

The concentrations of CH_4 and N_2O were updated using data available from the IIASA RCP database[3]. These data were used to scale the concentrations of the two gas species in the initial condition, UBC and LBC files. In addition, the future stratospheric concentrations of O_3 were set to the forecast values reported by [Cionni et al., 2011].

As for anthropogenic and biomass burning emissions, they were also updated by regridding the RCP emission inventories[4] to the T42LR resolution used to perform the simulations. For each of the four RCP scenarios, only the years 2010, 2020, 2050 and 2100 were picked out of the decadal emission inventories, totalling a number of sixteen cases, with a view to reduce the computing load. Emissions totals of NO_x are provided in table 8.2 while the remaining species are available in appendix B.

[3]Data available from http://www.iiasa.ac.at/web-apps/tnt/RcpDb. Last access 17/06/2010

[4]Data available on ftp-ipcc.fz-juelich.de. Last access 17/06/2011

TABLE 8.1: Concentrations of long-lived species in the future according to the RCP scenarios. Source: IIASA RCP database.

Case	Year	CO_2 [ppmv]	N_2O [ppbv]	CH_4 [ppbv]
Historic	**2000**	**368.87**	**315.85**	1751.02
RCP 2.6	2010	389.29	322.96	1773.13
	2020	412.07	329.21	1730.52
	2050	442.70	341.90	1451.54
	2100	420.90	344.02	**1253.63**
RCP 4.5	2010	389.13	322.97	1767.10
	2020	411.13	329.98	1801.43
	2050	486.54	350.61	1785.79
	2100	538.36	372.27	1923.67
RCP 6.0	2010	389.07	323.07	1768.69
	2020	409.36	330.20	1785.79
	2050	477.67	354.59	1894.85
	2100	669.72	406.27	1649.40
RCP 8.5	2010	389.32	323.06	1778.68
	2020	415.78	331.51	1923.67
	2050	540.54	367.22	2739.99
	2100	**935.87**	**435.11**	**3750.69**

TABLE 8.2: Future NO_x emissions. Source: IIASA RCP database.

Case	Year	Total Tg(N)/yr	Anthropogenic and Biomass burning Tg(N)/yr	Shipping Tg(N)/yr	Proportion shipping %
Historic	2000	42.45	31.02	5.43	17.50
RCP 2.6	2010	43.34	37.24	6.11	16.41
	2020	40.47	34.26	6.21	18.13
	2050	32.87	26.43	6.44	24.37
	2100	21.11	20.57	**0.54**	**2.63**
RCP 4.5	2010	42.00	36.23	5.78	15.95
	2020	39.84	33.88	5.96	17.59
	2050	32.70	26.52	6.19	23.34
	2100	20.86	17.21	3.64	21.18
RCP 6.0	2010	42.01	37.02	4.99	13.49
	2020	39.34	34.96	4.38	12.54
	2050	20.03	19.09	0.94	4.94
	2100	20.03	19.09	0.94	4.94
RCP 8.5	2010	43.60	37.57	6.03	16.05
	2020	46.04	39.57	6.07	15.18
	2050	36.73	30.05	**6.68**	22.24
	2100	27.82	22.21	5.61	**25.25**

The methodology employed to run the simulation cases is identical to that in the previous chapters. From each of the sixteen cases, shipping emissions were removed so that shipping perturbations could be estimated under each scenario and for the four different years. As for the simulations described in the previous chapters, each one was run for two years but only the twelve last months were kept for analysis, allowing the model to spin-up over one year.

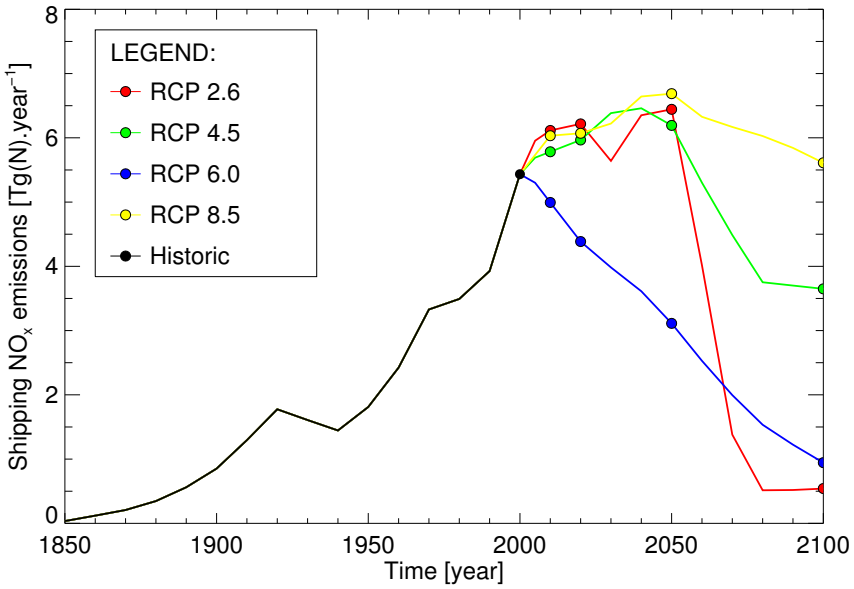

FIGURE 8.3: Past and future shipping NO_x emissions as calculated in the ACCMIP project. The filled circles indicate those used in this chapter. Source: IIASA RCP Database http://www.iiasa.ac.at/web-apps/tnt/RcpDb/

8.2.2 Edwards-Slingo: Calculating ozone and methane radiative forcing

The Edwards-Slingo RTM model was set up in the same configuration as in [Myhre et al., 2009] and a description of it is available in chapter 3.

Shipping RF in 2000 was calculated by using shipping perturbations of O_3 and CH_4 resulting from the MOZART-4 runs including the ACCMIP 2000 emission inventory.

Regarding future impacts, the model's input data were set to the future values predicted by IIASA in a similar fashion as in MOZART-4. For instance, the files containing the concentrations of long-lived gaseous species such as CO_2 and N_2O were scaled to the concentrations provided by the IIASA RCP database. In addition, the resulting O_3 and CH_4 perturbations and background concentrations from the MOZART-4 simulations were used as input to the RTM. The ISCCP cloud climatology used by default in this version of the model was left to its original 2000 values.

The available version of Edwards-Slingo did not take into account any stratospheric adjustment. A reduction of 20% was thus applied to the obtained O_3 RF following the work of Stevenson et al. [1998]. In addition, the methodology undertaken by Myhre et al. [2011] to calculate CH_4-induced O_3 RF and stratospheric water vapour RF was applied. Furthermore, the factor accounting for historical CH_4 concentrations resulting from the shipping NO_x emissions was calculated and employed [Grewe and Stenke, 2008, Myhre et al., 2011]. This last aspect of the methodology to calculate CH_4 RF is important since shipping NO_x emissions are not constant in time as shown on figure 8.3. The CH_4 feedback factor was assumed to be constant and equal to 1.4 in this study as in Houghton et al. [2001][5].

8.3 Results

8.3.1 RF estimates of O_3 and CH_4 in 2000 and in the future

Results from the simulations are summarised in table 8.3 and zonal averages of O_3 and CH_4 RF are displayed on figure 8.5.

The estimate of shipping short-lived O_3 RF in 2000 is found to equal 31.1 $mW.m^{-2}$ and is in very good agreement with recent studies which used similar shipping emissions[6]: 32 ± 9 $mW.m^{-2}$ [Fuglestvedt et al., 2008], 27.3 ± 2.2 $mW.m^{-2}$ [Hoor et al., 2009] and 24 $mW.m^{-2}$ [Myhre et al., 2011]. Furthermore, Lee et al. [2006] reported a value of 21 $mW.m^{-2}$ resulting from the use of a simple climate model with an input shipping NO_x emission magnitude of 6.51 Tg(N)/yr.

[5] "The possibility that future emissions of CH_4 and CO overwhelm the oxidative capacity of the troposphere is tested (Case E, see Table 4.3 footnote c) with a +10% increase in CH_4 on top of Y2100-A2x (Case B). Even at 4,300 ppb CH_4, the decrease in OH calculated by two CTMs is only slightly larger than in Case A, and thus, at least for SRES A2p, the CH_4-feedback factor does not become as large as in the runaway case (Prather, 1996). This report assumes that the CH_4 feedback remains constant over the next century; however, equivalent studies for the low-NO_x future scenarios are not assessed."

[6] These studies are part of the QUANTIFY project in which a shipping emission inventory based on the ICOADS spatial proxy and with a magnitude of 4.39 Tg(N)/yr was developed.

It comes as no surprise that the shipping CH_4 RF estimated in this study with a value of -60.3 mW.m^{-2} is much smaller than that calculated in all previous studies: -43±13 mW.m^{-2} [Fuglestvedt et al., 2008], -37.2±9.3 mW.m^{-2} [Hoor et al., 2009] and -27±8 mW.m^{-2} [Myhre et al., 2011]. Indeed, the strong impact of shipping emissions on CH_4 lifetime noticed in the previous chapters (5, 6 and 7) result in a shipping CH_4 RF with a larger magnitude. As a consequence, the CH_4-induced O_3 and stratospheric H_2O RF have also a larger magnitude of -21 mW.m^{-2} and -9 mW.m^{-2} respectively, compared with -14 mW.m^{-2} and -4 mW.m^{-2} in Myhre et al. [2011].

It is interesting to note that the shape of the annual O_3 RF zonal average is very similar to those presented in the multi-model study from Myhre et al. [2011] which further support the results found in this study. The two maxima present in the Northern and Southern tropics are clearly visible, with that in the northern hemisphere being larger (figure 8.5).

Regarding results from the future scenarios, the spread of O_3 and CH_4 RF is quite substantial and lies between 4.3 mW.m^{-2} and 42.4 mW.m^{-2} for O_3 and between -12.1 mW.m^{-2} and -94.5 mW.m^{-2} for CH_4 (figure 8.5). Minimum and maximum O_3 and CH_4 RF perturbations are found in the RCP 2.6 in 2100 and RCP 8.5 in 2050. Estimates in 2050 range between 20.0 mW.m^{-2} and 42.4 mW.m^{-2} for O_3 and between -108.7 mW.m^{-2} and -62.1 mW.m^{-2} CH_4 including impacts on stratospheric H_2O while Hodnebrog et al. [2011a] reported inter-model mean values of 25.2±9.6 mW.m^{-2} and -41±5.0 mW.m^{-2} respectively. Again, O_3 and CH_4 RF estimates computed in this study are overestimated in comparison with Hodnebrog et al. [2011a].

Interestingly, the RCP 2.6 scenario in 2100 leads to a CH_4 lifetime perturbation of -0.14 year which is close to the value reported by Eyring et al. [2007]. However, there is nearly a factor of 6 between the magnitude of shipping NO_x emissions in this study and that of Eyring et al. [2007], and more than a factor of 2 between the resulting global shipping O_3 burdens. This large discrepancy emphasizes the strong oxidising capacity simulated by MOZART-4 in its present configuration.

TABLE 8.3: Global shipping figures : total NO_x emissions, global O_3 burden, CH_4 lifetime, global O_3 and CH_4 radiative forcings, CH_4-induced O_3 and stratospheric H_2O radiative forcings and net radiative forcing Bold format indicates the minimum and maximum values of a specific metric.

Case	Year	Shipping NO_x emis. [Tg(N)/yr]	Global ΔO_3 burden [Tg/yr]	ΔCH_4 lifetime [year]	ΔO_3 RF [mW.m^{-2}]	ΔCH_4 RF [mW.m^{-2}]	ΔCH_4-induced O_3 RF [mW.m^{-2}]	ΔStrat. H_2O RF [mW.m^{-2}]	Net RF [mW.m^{-2}]
Historic	2000	5.43	10.93	-0.74	31.05	-60.32	-21.37	-9.05	-59.70
RCP 2.6	2010	6.11	11.61	-0.79	32.83	-72.87	-25.87	-10.93	-76.83
	2020	6.21	12.12	-0.83	33.64	-80.03	-28.62	-12.00	-87.01
	2050	6.44	13.03	-0.93	35.38	-86.74	-32.84	-13.01	-97.21
	2100	**0.54**	**1.71**	**-0.14**	**4.32**	**-12.06**	**-5.01**	**-1.81**	**-14.56**
RCP 4.5	2010	5.78	11.05	-0.74	31.20	-70.28	-25.02	-10.54	-74.64
	2020	5.96	11.70	-0.77	32.39	-74.84	-26.47	-11.23	-80.15
	2050	6.19	13.35	-0.87	36.64	-86.81	-30.46	-13.02	-93.66
	2100	3.65	9.11	-0.62	24.75	-60.43	-22.60	-9.06	-67.34
RCP 6.0	2010	4.99	9.77	-0.68	27.90	-68.33	-24.41	-10.25	-75.09
	2020	4.38	8.99	-0.63	25.31	-64.85	-23.19	-9.73	-72.45
	2050	3.11	7.38	-0.54	20.01	-54.02	-19.11	-8.10	-61.23
	2100	0.94	3.00	-0.25	7.65	-25.06	-9.45	-3.76	-30.61
RCP 8.5	2010	6.03	11.30	-0.75	32.06	-69.71	-24.76	-10.46	-72.87
	2020	6.07	11.81	-0.76	32.94	-75.46	-26.14	-11.32	-79.98
	2050	**6.68**	**15.29**	**-0.97**	**42.38**	**-94.53**	**-29.22**	**-14.18**	**-95.55**
	2100	5.61	14.94	-0.94	40.37	-92.23	-26.33	-13.83	-92.02

One may also notice that the maximum emission case has a value of 6.68 Tg(N)/yr (RCP 8.5 - 2050). This value is 23% larger than the reference case in 2000 presented in chapters 5 and corresponds only to a shipping sector growth of 0.46% each year against 2.2% in Eyring et al. [2007]. This underlines once again the differences in resource availability between the SRES and RCP scenarios.

Finally, the minimum shipping O_3 RF is found under the RCP 2.6 scenario in 2100 whereas the maximum shipping O_3 RF occurs under the RCP 8.5 scenario in 2050. These minimum and maximum values correspond to the minimum and maximum values of shipping NO_x emissions respectively and conversely for shipping CH_4 RF. This simple fact raises the question of whether the O_3 and CH_4 RF responses to shipping NO_x emissions are linear.

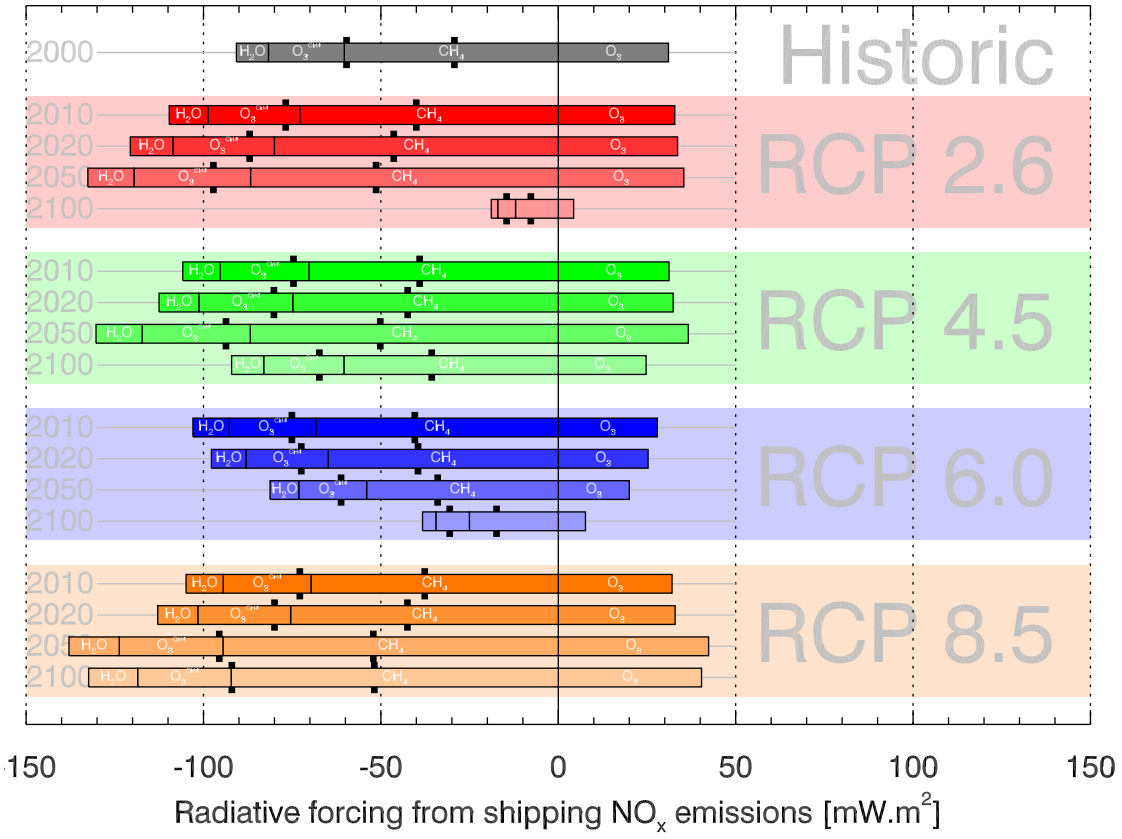

FIGURE 8.4: Bar plots showing radiative forcing from shipping NO_x emissions in 2000, 2010, 2020, 2050 and 2100 following the RCP scenarios. The contribution from O_3 RF, CH_4 RF, CH_4-induced O_3 RF and stratospheric H_2O are plotted in independent rectangles. The 2 black vertical bars behind the rectangles indicate 2 net radiative forcings. Those on the right are the result of combining O_3 RF and CH_4 RF while those on the left correspond to the sum of all contributions.

8.3.2 Linear relationships between global metrics of shipping perturbations and parameterisation of the O_3 and CH_4 RF responses to shipping NO_x emissions

In order to verify whether linear relationships exist between shipping NO_x emissions, shipping O_3 column, shipping CH_4 lifetime perturbation and shipping O_3 and CH_4 RF, correlations between these different metrics are computed and the results are shown on figures 8.6 **a**, **b** and **c** as well as on figures 8.7 **a** and **b**. There is a strong correlation between the radiative forcings of shipping O_3 and shipping CH_4 (r=0.98) (figure 8.6 **c**) as well as between global tropospheric shipping O_3

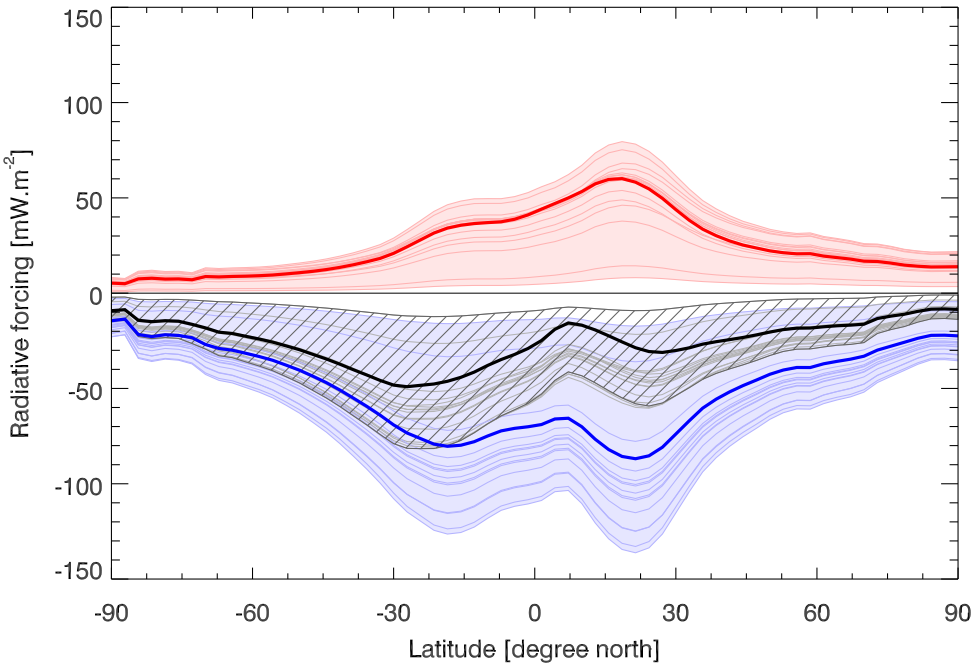

FIGURE 8.5: Zonal average of annually-averaged O_3 (red) and CH_4 (blue) RF in 2000 (thick lines) and in the RCP scenarios (thin lines). The net forcing is displayed in black while the spread is hatched.

column and shipping O_3 radiative forcing (r=0.99) (figure 8.6 **b**) and shipping CH_4 lifetime and shipping CH_4 radiative forcing (r=0.99) (figure 8.7 **b**). However, the variability between total shipping NO_x emissions and global tropospheric shipping O_3 column (figure 8.6 **a**) and that between total shipping NO_x emissions and shipping CH_4 lifetime (figure 8.7 **a**) are larger. They equal r=0.94 and r=0.96, respectively. In particular, one may notice that there are two outliers on the top right of the plot on figure 8.6 **a** which correspond to the two simulations with the largest background concentrations of CH_4 (RCP 8.5 - 2050: 2739.99 ppbv, RCP 8.5 - 2100: 3750.69 ppbv, see table 8.1 for comparison). The linear regressions found between total shipping NO_x emissions and global tropospheric shipping O_3 column and shipping CH_4 lifetime will be called **LR models** in the rest of this chapter.

Since the relation between the shipping O_3 and CH_4 RF follows a linear trend, two linear regressions are performed on the results reported in Eyring et al. [2007] and Hodnebrog et al. [2011a]. Although these two studies provide only three and two

data points respectively, the slopes of these trends remain similar to that found in the present study (figure 8.6 **c**).

Because shipping emissions under the RCP scenarios only increase by a maximum of 23% compared with 2000, the whole shipping NO_x-O_3-CH_4 system appears to be weakly affected by this change and this is why the relationships between shipping O_3 column, shipping CH_4 lifetime and shipping NO_x emissions exhibit linear tendencies. With a view to improve estimates from the **LR models**, multi-linear regression models of the form $\mathcal{C}^t_{O_3^{ship}} = \sum_i \alpha_i X_i^t + \beta$ and $\mathcal{L}^t_{CH_4^{ship}} = \sum_i \alpha_i X_i^t + \beta$ are tested in order to verify the influence of other factors on the global shipping O_3 column, where $\mathcal{C}^t_{O_3^{ship}}$ is the shipping O_3 column in DU, $\mathcal{L}^t_{CH_4^{ship}}$ is the shipping CH_4 lifetime in years, α_i are the linear coefficients, X_i^t are the factors influencing global tropospheric shipping O_3 column and shipping CH_4 lifetime. β is a constant. Remembering that the NO_x-O_3-HO_x-CH_4 system also depends upon background NO_x, CO and VOC concentrations and therefore on background NO_x, CO and VOC emissions, the shipping and background NO_x, CO and VOC emission variables as well as CH_4 concentrations are added to the simple LR model. In fact, the logarithm of CH_4 background concentrations replaces CH_4 background concentrations in the model as in Wigley et al. [2002]. This new approach which follows that employed in Houghton et al. [2001] will be called **MLR model**. In the MLR case, the following linear system has to be solved for the global tropospheric shipping O_3 column:

$$\begin{pmatrix} \mathcal{C}^{ACCMIP\ 2000}_{O_3^{ship}} \\ \mathcal{C}^{RCP26\ 2010}_{O_3^{ship}} \\ \mathcal{C}^{RCP26\ 2020}_{O_3^{ship}} \\ \vdots \\ \mathcal{C}^{RCP85\ 2100}_{O_3^{ship}} \end{pmatrix} = \begin{pmatrix} E^{ACCMIP\ 2000}_{NO_x^{ship}} & E^{ACCMIP\ 2000}_{NO_x^{other}} & \dots & C^{ACCMIP\ 2000}_{CH_4^{bg}} & 1 \\ E^{RCP26\ 2010}_{NO_x^{ship}} & E^{RCP26\ 2010}_{NO_x^{other}} & \dots & C^{RCP26\ 2010}_{CH_4^{bg}} & 1 \\ E^{RCP26\ 2020}_{NO_x^{ship}} & E^{RCP26\ 2020}_{NO_x^{other}} & \vdots & C^{RCP26\ 2020}_{CH_4^{bg}} & 1 \\ \vdots & \vdots & \ddots & \vdots & \vdots \\ E^{RCP85\ 2100}_{NO_x^{ship}} & E^{RCP85\ 2100}_{NO_x^{other}} & \dots & C^{RCP26\ 2100}_{CH_4^{bg}} & 1 \end{pmatrix} \begin{pmatrix} \alpha_{NO_x^{ship}} \\ \alpha_{NO_x^{other}} \\ \vdots \\ \alpha_{CH_4^{bg}} \\ \beta \end{pmatrix} \tag{8.1}$$

All combinations of X_i^t are tested in order to find the best parameterisation. The number of factor combinations total 127. In order to assess which combination provides the best estimation, root-mean square error (RMSE) calculations are

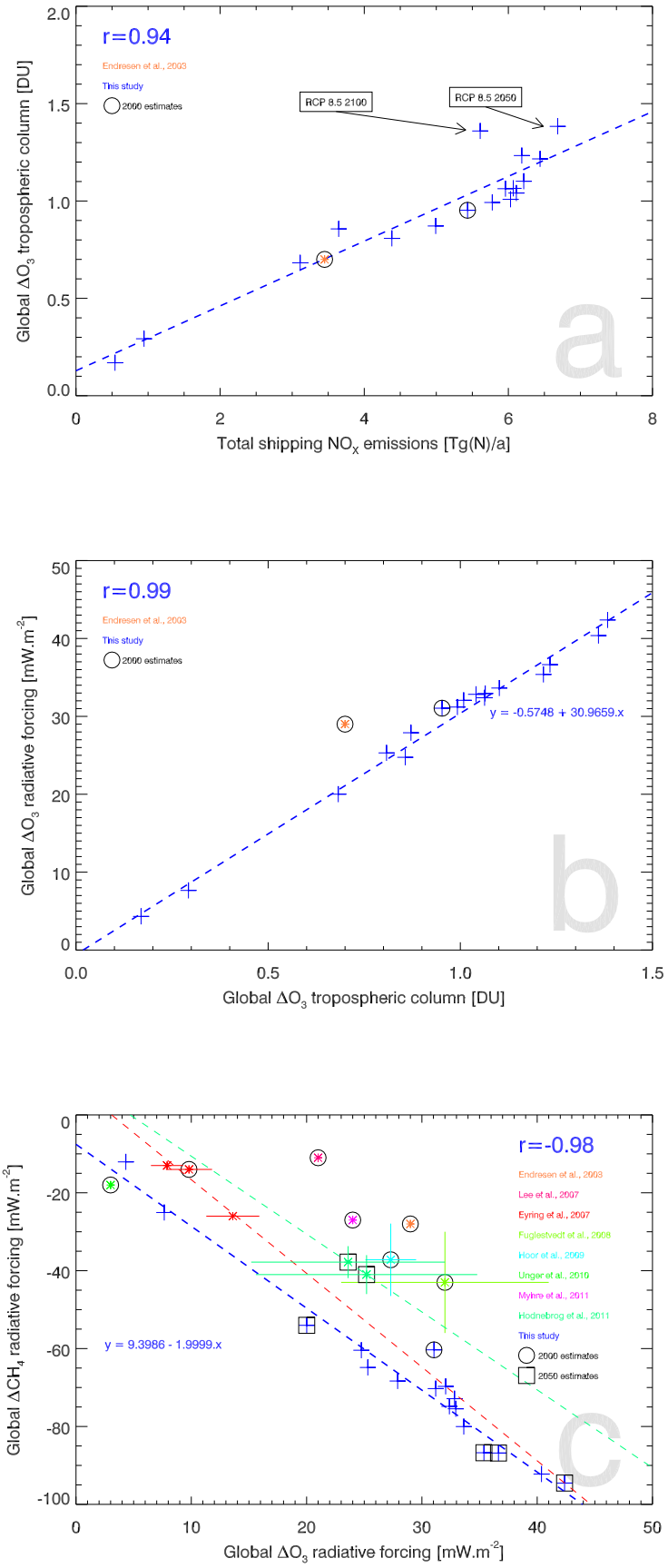

FIGURE 8.6: Plots showing the correlations between different global figures such as total shipping NO_x emissions, global shipping O_3 column, global shipping CH_4 lifetime, global shipping O_3 radiative forcing and global shipping CH_4 radiative forcing.

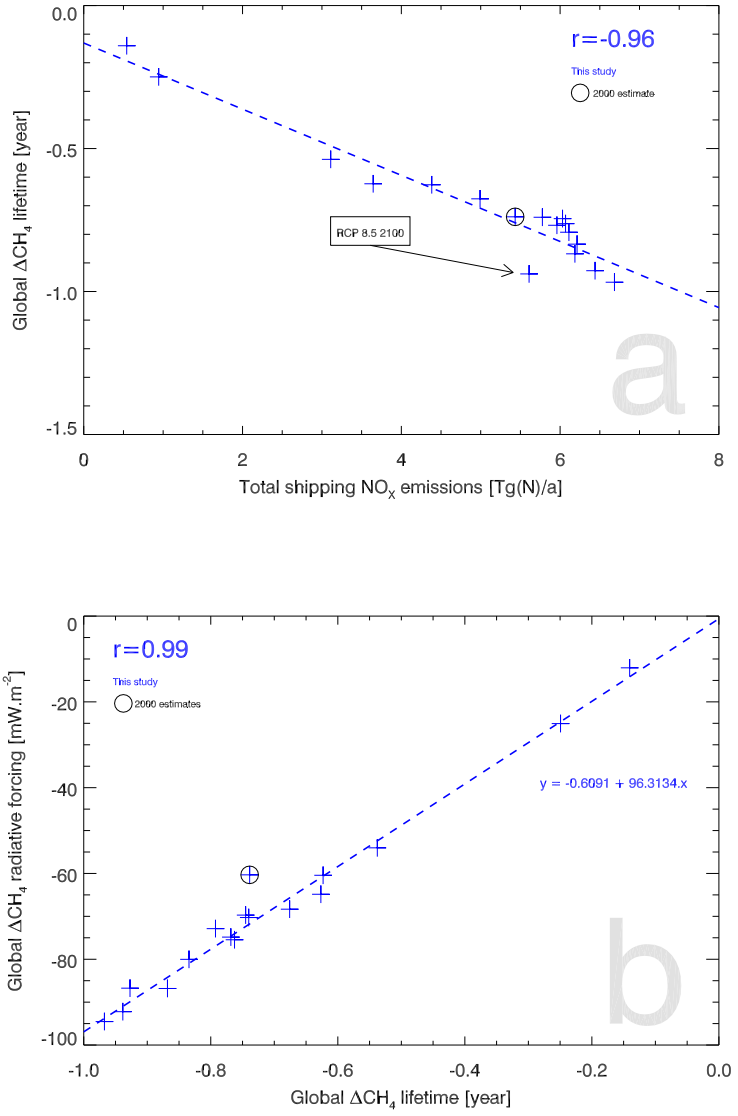

FIGURE 8.7: Plots showing the correlations between different global figures such as total shipping NO_x emissions, global shipping O_3 column, global shipping CH_4 lifetime, global shipping O_3 radiative forcing and global shipping CH_4 radiative forcing.

TABLE 8.4: Root-mean square errors (RMSE) of the Linear and Multi-linear models (**LR** & **MLR**) for global tropospheric shipping O_3 column and shipping CH_4 lifetime.

Model	RMSE	
	O_3	$CH4_4$
LR model	0.109	0.063
MLR model	0.009	0.021

performed between values estimated with the **MLR model** and those computed in the GCTM/RTM framework. The models that includes all factors are found to provide the best estimates and have RMSE of 0.009 and 0.063 for O_3 and CH_4 respectively, compared with 0.109 and 0.021 in the **LR model** (table 8.4). The **MLR model** clearly improves estimations, especially for O_3 since its RMSE drops by more than an order of magnitude compared with the simple linear regression.

The resulting estimates calculated by the new models are further plotted on figures 8.8(a) and 8.8(b). Compared with a simple linear regression, the new model is able to reproduce all cases within ±3.5% and ±35.5% of the values estimated with the GCTM/RTM for O_3 and CH_4 respectively. One may notice that the inclusion of factors other than shipping NO_x emissions clearly provides enough information to the models to estimate the global tropospheric shipping O_3 column and shipping CH_4 lifetime when background CH_4 concentrations become large. There is however an outlier in

The equations describing the global tropospheric shipping O_3 column and shipping CH_4 lifetime as a function of shipping NO_x emissions and other factors reads:

$$\begin{aligned}\mathcal{C}_{O_3}^{Ship} =& 1.7496\times E_{NO_x}^{Ship} - 0.1370\times E_{NO_x}^{Other} + 2.5030\times E_{CO}^{Ship} - 0.0079\times E_{CO}^{Other} \\ & - 1.6717\times E_{VOC}^{Ship} + 0.1199\times E_{VOC}^{Other} + 3.1736\times ln\left(C_{CH_4}^{Bg}\right) - 17.6631 \quad (8.2)\end{aligned}$$

$$\begin{aligned}\mathcal{L}_{CH_4}^{Ship} =& -0.1051\times E_{NO_x}^{Ship} + 0.0139\times E_{NO_x}^{Other} - 0.2147\times E_{CO}^{Ship} + 0.0004\times E_{CO}^{Other} \\ & + 0.1184\times E_{VOC}^{Ship} - 0.0090\times E_{VOC}^{Other} - 0.1044\times ln\left(C_{CH_4}^{Bg}\right) + 0.4202 \quad (8.3)\end{aligned}$$

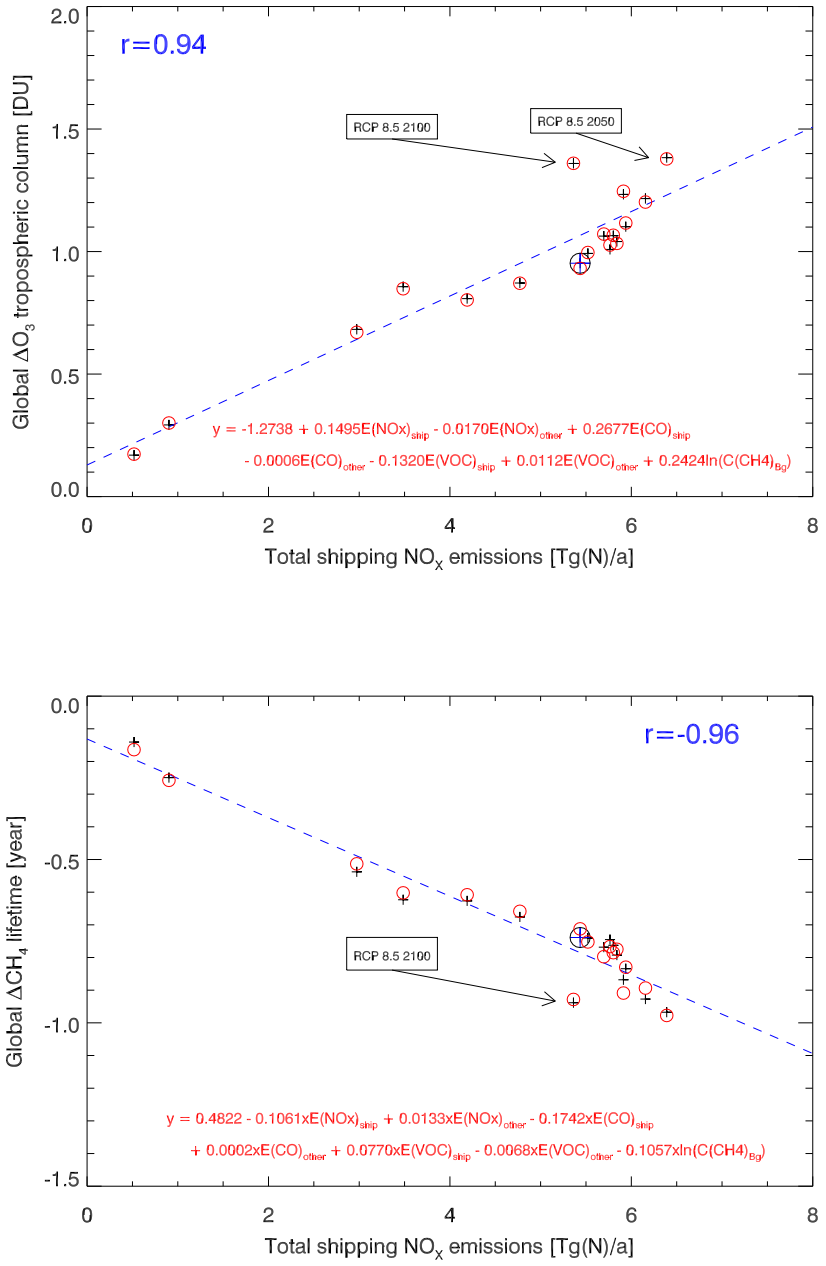

FIGURE 8.8: Results from the two multi-linear regression models using 4 variables: Total shipping NO_x emissions, background CH_4 concentrations, background NO_x emissions and background CO emissions.

TABLE 8.5: Comparisons between shipping O_3 burden and CH_4 lifetime calculated by the GCTM/RTM and by the MLR models.

Case	Year	Shipping NO_x emis. [Tg(N)/a]	Global ΔO_3 column [DU]	Estimated Global ΔO_3 column [DU]	Error [%]	Global ΔCH_4 lifetime [yr]	Estimated Global ΔCH_4 lifetime [yr]	Error [%]
Historic	2000	5.44	0.95	0.93	-2.21	-0.74	-0.71	-3.58
RCP 2.6	2010	5.84	1.04	1.03	-0.72	-0.79	-0.77	-2.25
	2020	5.94	1.10	1.12	1.35	-0.83	-0.83	-0.56
	2050	6.16	1.22	1.20	-1.16	-0.93	-0.89	-3.64
	2100	0.52	0.17	0.17	2.39	-0.14	-0.16	16.53
RCP 4.5	2010	5.52	0.99	1.00	0.37	-0.74	-0.75	1.63
	2020	5.70	1.06	1.07	0.77	-0.77	-0.80	3.80
	2050	5.91	1.23	1.25	1.03	-0.87	-0.91	4.68
	2100	3.48	0.86	0.85	-0.99	-0.62	-0.60	-3.37
RCP 6.0	2010	4.77	0.87	0.87	-0.09	-0.68	-0.66	-2.54
	2020	4.19	0.81	0.80	-0.67	-0.63	-0.61	-2.98
	2050	2.97	0.68	0.67	-1.73	-0.54	-0.51	-4.55
	2100	0.90	0.29	0.30	2.67	-0.25	-0.26	3.33
RCP 8.5	2010	5.76	1.01	1.03	1.78	-0.75	-0.77	2.88
	2020	5.80	1.06	1.07	0.17	-0.76	-0.79	2.96
	2050	6.39	1.38	1.38	-0.37	-0.97	-0.98	1.02
	2100	5.36	1.36	1.36	0.05	-0.94	-0.93	-1.08

Where $\mathcal{C}_{O_3}^{Ship}$ is the global shipping O_3 column in DU, $\mathcal{L}_{CH_4}^{Ship}$ is the shipping CH_4 lifetime in years, $E_{species}^{Ship}$ corresponds to the total magnitude of shipping NO_x, CO and VOC emissions in Tg(N)/yr, Tg(CO) or Tg(C)/yr, $E_{species}^{Other}$ represents the total of other NO_x, CO and VOC emissions in Tg(N)/yr, Tg(CO) or Tg(C)/yr and $C_{CH_4}^{Bg}$ is the global-mean tropospheric CH_4 background concentration in ppbv.

Finally, the shipping O_3 and CH_4 RF could be calculated by combining the expressions for global tropospheric shipping O_3 column and shipping CH_4 lifetime with those relating them to their respective RF. However, a multi-linear model was constructed in a similar way to those for $\mathcal{C}_{O_3}^{Ship}$ and $\mathcal{L}_{CH_4}^{Ship}$. The resulting shipping O_3 and CH_4 RF can be expressed as a function of shipping NO_x emissions and the

TABLE 8.6: Comparisons between shipping O_3 RF and CH_4 RF calculated by the GCTM/RTM and by the MLR models.

Case	Year	Shipping NO_x emis. [Tg(N)/a]	Global ΔO_3 RF [mW.m^{-2}]	Estimated ΔO_3 RF [mW.m^{-2}]	Error [%]	ΔCH_4 RF [mW.m^{-2}]	Estimated ΔCH_4 RF [mW.m^{-2}]	Error [%]
Historic	2000	5.44	31.05	29.91	-3.68	-60.32	-69.75	15.62
RCP 2.6	2010	5.84	32.83	32.71	-0.37	-72.87	-76.12	4.46
	2020	5.94	33.64	34.17	1.58	-80.03	-80.79	0.96
	2050	6.16	35.38	35.22	-0.45	-86.74	-85.72	-1.17
	2100	0.52	4.32	4.12	-4.70	-12.06	-13.66	13.29
RCP 4.5	2010	5.52	31.20	31.23	0.10	-70.28	-73.42	4.47
	2020	5.70	32.39	33.14	2.34	-74.84	-77.85	4.02
	2050	5.91	36.64	36.51	-0.35	-86.81	-87.46	0.75
	2100	3.48	24.75	24.52	-0.93	-60.43	-58.77	-2.74
RCP 6.0	2010	4.77	27.90	27.50	-1.44	-68.33	-64.55	-5.54
	2020	4.19	25.31	24.96	-1.37	-64.85	-59.14	-8.81
	2050	2.97	20.01	19.71	-1.50	-54.02	-48.31	-10.57
	2100	0.90	7.65	8.34	8.99	-25.06	-22.41	-10.56
RCP 8.5	2010	5.76	32.06	32.61	1.70	-69.71	-75.68	8.56
	2020	5.80	32.94	33.56	1.90	-75.46	-77.59	2.82
	2050	6.39	42.38	42.01	-0.86	-94.53	-95.53	1.05
	2100	5.36	40.37	40.41	0.09	-92.23	-89.71	-2.73

other variables used in the previous MLR models, they read:

$$\begin{aligned}\mathcal{RF}_{O_3}^{ship} =& 5.5721\times E_{NO_x}^{Ship} - 0.2049\times E_{NO_x}^{Other} + 3.3287\times E_{CO}^{Ship} - 0.0229\times E_{CO}^{Other} \\ & - 4.5201\times E_{VOC}^{Ship} + 0.2756\times E_{VOC}^{Other} + 9.5314\times ln\left(C_{CH_4}^{Bg}\right) - 54.3622\end{aligned} \tag{8.4}$$

$$\begin{aligned}\mathcal{RF}_{CH_4}^{ship} =& -11.7351\times E_{NO_x}^{Ship} + 0.9227\times E_{NO_x}^{Other} - 13.1597\times E_{CO}^{Ship} + 0.0427\times E_{CO}^{Other} \\ & + 10.0102\times E_{VOC}^{Ship} - 0.7319\times E_{VOC}^{Other} - 12.4200\times ln\left(C_{CH_4}^{Bg}\right) + 57.4357\end{aligned} \tag{8.5}$$

The MLR models provide good estimations of global tropospheric shipping O_3 column (within ±3%) and global shipping O_3 RF (within ±9%). Errors in estimated shipping CH_4 lifetime and shipping CH_4 RF are however larger but remain within ±17%. Estimates of shipping CH_4 lifetime are actually within ±5% of the global-model computed data, expect for the RCP 2.6 case in 2100 where the relative error reach 17%. It should be noted that the absolute difference remain small with 0.02 year. Furthermore, It seems that most of the errors larger than ±10% are found in the cases with small shipping NO_x emissions (<3 Tg(N)/yr).

8.4 Discussion

The framework employed in this study of using MOZART-4 in conjunction with Edwards-Slingo in order to estimate 2000 and future RF under the RCP scenarios was found to compute O_3 RF in good agreement with previous studies. CH_4 RF is however on the high-end of the range of values published in the literature owing to the large CH_4 lifetime perturbation calculated by the GCTM. According to recent publication from the QUANTIFY project [Fuglestvedt et al., 2008, Hoor et al., 2009, Myhre et al., 2011], CH_4 RF calculated in this study could be overestimated between 8% and 217% in 2000. The use of RCP scenarios results in a range of shipping NO_x emissions lying between 0.94 and 6.68 Tg(N)/yr. On the one hand, future impacts of shipping under the RCP scenarios are quite small. On the other hand, this small emission range ensures that the global shipping O_3 and CH_4 perturbations respond linearly to shipping NO_x emissions.

It is important to emphasize the fact that although the RCP scenarios are reasonably well depicted in the literature, the emission inventories that have been build upon them and used in this study remain poorly described. In addition, shipping emissions included in the RCP emission inventories are much smaller than those which come from better-documented activities [Eyring et al., 2005a, Buhaug et al., 2009].

The parameterisation of the shipping O_3 column resembles that given in Wigley et al. [2002]. Differences reside in the inclusion of shipping emissions of NO_x, CO and VOC that sensibly improves estimations. Results suggest that the MLR model is currently able to provide shipping O_3 RF within $\pm 10\%$. As for CH_4 RF, errors remain in general within $\pm 16\%$. The linearisation of the shipping NO_x-CO-VOC-O_3-CH_4 system provides first-order estimates of global tropospheric shipping O_3 column, shipping CH_4 lifetime and shipping O_3 and CH_4 RF resulting from shipping emissions of NO_x, CO and VOC and background concentrations of CH_4 which could be used in a simple climate model to forecast future changes in global mean surface temperature. Further work should look at the possibility to apply

the method of principal component analysis in order to reduce the number of factors included in the equations.

In the future, changes in dynamics and chemistry are expected to influence shipping O_3 and CH_4 perturbations. For instance, deep convection could be increased in the tropics leading to a more efficient uplift of O_3 precursors in the upper troposphere where the OPE is greater. Since O_3 molecules have a greater RF impact near the tropopause [Lacis et al., 1990], global warming could be further enhanced by this phenomenon. Additionally, water vapour concentrations are expected to increase in the troposphere as a result of warming. This increase would affect both O_3 and CH_4 levels. This should be taken into account in further studies.

Chapter 9

Summary of the results

1. **Is MOZART-4 able to reproduce the composition of the environment in which shipping perturbations occur?**

   Results from chapter 4 showed that MOZART-4 is suitable for the analysis of global shipping perturbations stemming from NO_x emissions. In particular, the GCTM is able to simulate the global composition of the NO_x-HO_x-CO-CH_4-O_3 system in the troposphere in good agreement with respect to the WDCGG, WOUDC, Aircraft composite and TES datasets. Discrepancies in CO levels in the Northern and Southern hemispheres suggest that some of the anthropogenic and biomass burning sources may still be missing or not properly represented in the global model. In the upper troposphere, modelled O_3 concentrations differ quite largely from the WDCGG and TES datasets. However, prescribed O_3 concentrations in the stratosphere as well as stratospheric-tropospheric O_3 exchange and the simulated tropopause height could well be responsible for these differences. Furthermore, it has been shown previously that the deep convection scheme used in the MOZART models since MOZART-2 leads to a larger O_3 production in the upper troposphere [van Noije et al., 2006]. The absence of a tropospheric halogen chemistry mechanism is very likely to be responsible for the O_3 overestimates in the Arctic region in Spring. This could have an influence on

the shipping O_3 perturbations at the surface of this region and potentially on the radiative forcing.

2. **Is MOZART-4 able to reproduce shipping perturbations of NO_x, O_3 and CH_4?**

   In chapter 5, MOZART-4 was shown to reproduce shipping perturbations of NO_x, O_3 and CH_4 in good agreement with previous studies. The main differences lie in a larger production of O_3 in the free and upper troposphere as well as in a tendency to trap more NO_x molecules in the MBL. These differences are likely to result from the parameterisation of convection and MBL processes. In the case of O_3, concentrations can be increased by 25%. In addition, shipping CH_4 lifetime perturbation is at the upper end of the range of values reported across the literature. In particular, a factor of 2 is found between the value simulated by MOZART-4 and the ensemble mean computed in [Eyring et al., 2007].

3. **How sensitive are these shipping perturbations to current uncertainties in various atmospheric processes and changes in some model characteristics?**

   The sensitivity of shipping perturbation was assessed by looking at various metrics in chapter 6. At the global scale, current uncertainties in shipping emissions produce the largest effects and this is followed by change in photolysis scheme, uncertainties in lightning activity, uncertainties in photochemical data, changes in horizontal resolution, changes in background anthropogenic emissions and changes in dynamical data. Current uncertainties in shipping emissions, and especially in shipping emission magnitude, have the largest impacts on these perturbations regardless of the metric considered. Current uncertainties in shipping emission magnitudes are about a factor of 2 which translates into global O_3 burden, global OH concentration and CH_4 lifetime shipping perturbations of 67%, 66% and 59%, respectively. Interestingly, an increase in horizontal resolution between T21LR and T106LR does not reduce O_3 production everywhere as one may expect. On a yearly

average, O_3 levels drop in the tropical regions but increase in the rest of the troposphere when horizontal resolution increase. Interestingly, shipping perturbations of CH_4 lifetime increase by 14% between T21LR and T106LR. In addition, changes in vertical resolution induced by a change in dynamical data suggest that an increase in the number of vertical levels could increase O_3 levels too.

4. **What are the effects of including a ship plume parameterisation?**

   In chapter 7, the focus was set on the effects of including the ERR concept in MOZART-4 to account for the chemical non-linearities occurring at the plume scale. On the one hand, Huszár's approach was shown to be unsuitable for use in MOZART-4. The main reasons for this are the weak effect of the parameterised chemical reaction which is not very important in the MBL, and the absence of NO_x loss through reaction with OH. In the present study, MOZART-4, including the parameterisation, computed shipping O_3 reduction lying between -10% and -5% (compared with -25% and -20% in [Huszár et al., 2010]). Furthermore, these characteristics of Huszár's approach leads to larger shipping NO_x and O_3 concentrations in the free troposphere. These problems were addressed and partially solved by implementing Moldanová's approach that takes the NO_x-OH reaction into account. Shipping NO_x and O_3 concentration reductions larger than 20% were simulated by MOZART-4 as a result of including this new parameterisation. However, large O_3 decreases were also computed by the global model in the free and upper troposphere, most probably because of the strong deep convection scheme used in MOZART-4.

5. **What are the 2000 and future radiative forcing impacts of shipping NO_x emissions?**

   In 2000, net radiative forcing from shipping NO_x emissions was estimated with MOZART-4 and Edwards-Slingo to equal -60 $mW.m^{-2}$. Owing to the large shipping CH_4 lifetime perturbation, the CH_4-induced O_3 RF and stratospheric H_2O RF balance out the O_3 RF. Under the RCP scenarios, the net

radiative forcing stemming from shipping NO_x emissions has been found in chapter 8 to range between -96 $mW.m^{-2}$ and -15 $mW.m^{-2}$. Net radiative forcings were calculated as a combination of direct O_3 RF, direct CH_4 RF, CH_4-induced O_3 RF and CH_4-induced H_2O RF. The relatively small change in net RF result from a relatively small increase of shipping NO_x emissions under the RCP scenarios (+23% between 2000 emissions and RCP 8.5 emission in 2050).

6. **Is it possible to simplify and linearise the shipping NO_x-O_3-CH_4 system?**

   The 16 scenario cases performed in chapter 8 were also employed to analyse correlations between the main global metrics of the shipping NO_x-O_3-CH_4 system. It was found that shipping perturbations of global tropospheric O_3 column, CH_4 lifetime, O_3 and CH_4 RF were all exhibiting a linear relationship to shipping NO_x emissions. The shipping NO_x-O_3-CH_4 system was successfully linearised under the RCP scenarios and radiative forcing of shipping O_3 and CH_4 can be now explained in terms of NO_x, CO, VOC emissions and background CH_4 concentrations. O_3 and CH_4 RF estimates calculated with this linearisation remain within $\pm 6\%$ and $\pm 15\%$ of the values computed with the global models respectively.

Chapter 10

Conclusions and recommendations for further work

The framework employed in this work was found to be suitable for the analysis of shipping NO_x emissions impacts on the tropospheric composition and radiative forcing. In particular, MOZART-4 was able to reproduce NO_x, O_3, OH and CH_4 shipping perturbations as well as the environment in which they occur in good agreement with previous studies. In addition, the O_3 and CH_4 radiative forcings computed by Edwards-Slingo were also found to be in good accord with the existing literature. Global 3D models such as MOZART-4 and Edwards-Slingo are able to provide detailed shipping O_3 and CH_4 responses which are crucial to analyse and understand the impacts of short-lived climate agents and how they compare against long-lived ones (e.g. CO_2).

Recent improvements in GCTMs could have substantial effects on the O_3, OH and CH_4 global budgets. For instance, a new dry deposition scheme which exhibits a different seasonal variation over the oceans compared to previous schemes could lead to significant changes in the shipping O_3 budget [Ganzeveld et al., 2009]. Furthermore, the new cloud scavenging parameterisation proposed by Neu and

Prather [2011] revealed the importance of ice phase scavenging and HNO_4 lifetime on the tropospheric O_3 budget in the upper troposphere. Another recent finding is the new HNO_3 forming channel resulting from the reaction between NO and HO_2 [Butkovskaya et al., 2005] which has been shown to lead to a reduction in tropospheric O_3 burden of 11%, a decrease of global mean OH of about 13% to 14% and an increase in CH_4 lifetime of 5% to about 11% [Cariolle et al., 2008, Svøde et al., 2011]. It should also be noted that while the N_2O_5 hydrolysis parameterisation developed by Jacob [2000] is currently implemented in MOZART-4, a new parameterisation by Evans and Jacob [2005] has been shown to yield important changes in global tropospheric concentrations of NO_x (7%), O_3 (4%) and OH (8%). Impacts from these changes could be assessed in the future to complete the picture of shipping perturbation sensitivity.

So far, the only two studies focusing on the impacts of shipping NO_x emissions in the Arctic region have not discussed the potential effects of halogen chemistry on O_3 [Granier et al., 2006, Ødemark et al., 2011]. Preliminary results from this study showed that this could be significant, especially at the surface in Spring but also in September. With the predicted opening of the Northern routes in the near future and the increase in shipping traffic, O_3 RF impacts from shipping could be significantly diminished by halogen chemical activity. Interestingly, a tropospheric halogen mechanism has been recently developed for CAM-chem which is a model related to MOZART-4 [Ordóñez et al., 2011]. This halogen mechanism should be implemented and taken into account in future calculations.

Under the RCP scenarios, it was shown that shipping emissions grow by a maximum of 23% in 2050. This estimate is quite small compared with those forecast within the SRES scenarios that could be increased by 168% under a A1F scenario in 2050. It is very likely that global shipping perturbations of O_3 and CH_4 would exhibit a saturation effect under such emission scenarios and it would be interesting to analyse under which conditions the system starts to saturate. In addition, the linearisation calculated in the present study might not be valid under the SRES scenarios. It would be worth extending the work to those scenario cases in order to derive a more robust model to estimate O_3 and CH_4 RF as a function

of shipping NO_x emissions and potentially other emissions and background concentrations. In any case, the linearisation of the shipping NO_x-O_3-CH_4 system is of great importance since it could be introduced in simple climate models to help policy makers design effective policy instruments to curb shipping emissions.

As for shipping emission parameterisations, a crucial aspect of the problem is the lack of measurements which are key to their assessment. Up to now, observations were made with aircraft. In the future, one may consider the use of airships or drones such as the Octocopter to perform Lagrangian measurements of ship plumes. This solution could appear to be less expensive. Regarding the ERR concept, the focus should be first set upon the legitimisation of allowing SHIPTR to be transported by advection, diffusion and convection in MOZART-4. Moreover, further control over O_3 production could be obtained by implementing the parameterisation displayedlatex on figure E.1 in Appendix E. This approach takes into account the three ship-plume phases described in Song et al. [2003b]: O_3 titration, O_3 recovery and O_3 net production. The O_3 titration term defined in the original parameterisation could be kept to avoid having to reduce the model timestep to a few minutes. The next two phases could then be tagged in the global model using two shipping NO_x tracers with characteristic decaying times determined by the ship plume model and defined as NO_x regions greater than 1 ppbv and regions smaller than 1 ppbv and larger than 500 pptv for instance. The use of multiple tracers was suggested by Cariolle et al. [2009]. NO_x concentrations smaller than 1 ppbv should not introduce non-linearity in the system of the global model (Personal communication with D. Cariolle, 2010 and Song et al. [2003b]). The rate of O_3 productions and SHIPTR decays should be then tuned with the ship-plume model (SPM-2D) to account for the various atmospheric conditions encountered in grid cells. O_3 productions could be defined as the reaction rates between NO and RO_2 (HO_2 and CH_3O_2) while NO_x loss would be defined with the approach designed by Dr. Moldanová.

Appendix A

Description of the dynamical data used in MOZART-4

Two different datasets were employed in this study: NCEP reanalysis [Kalnay et al., 1996, Kistler et al., 2001] and ECMWF INTERIM. The former was employed in the majority of the simulations performed in this work since it is the dataset that comes by default with the model. Another advantage is the smaller number of vertical levels compared with ECMWF-INTERIM data which result in simulations taking less time to run. The latter was used in the chapter on sensitivity (see chapter 6) to assess the effect of horizontal and vertical model resolution on shipping perturbations. More details about these datasets may be found in the following sections.

A.1 NCEP Reanalysis

NCEP Reanalysis data was downloaded off the Community Data Portal (CDP) website for the years 2000 (chapters 4, 5, 6, 7 and 8), 2001, 2002 (chapter 6) and 2005 (chapter 4).

TABLE A.1: NCEP Reanalysis variables used as input to MOZART-4.

#	Variable name	Dimension	Units	Description
1	U	3	$m.s^{-1}$	Zonal wind
2	V	3	$m.s^{-1}$	Meridional wind
3	T	3	K	Temperature
4	Q	3	$kg.kg^{-1}$	Specific humidity
5	PS	2	Pa	Surface pressure
6	TS	2	K	Surface temperature
7	LAND	2	FLAG	Orography (land, ocean, sea ice)
8	PHI	2	$m^2.s^{-2}$	Surface geopotential
9	HFLX	2	$W.m^{-2}$	Surface heat flux
10	QFLX	2	$kg.m^{-2}.s^{-1}$	Surface moisture flux
11	TAUX	2	$N.m^{-2}$	Surface zonal stress
12	TAUY	2	$N.m^{-2}$	Surface meridional stress
13	SNOWH	2	m	Snow height
14	FSDS	2	$W.m^{-2}$	Surface downward direct shortwave radiation
15	SOILW	2	ratio	Soil moisture
16	TS_avg	2	K	Averaged surface temperature
17	FSDS_avg	2	$W.m^{-2}$	Averaged FSDS

TABLE A.2: ECMWF-INTERIM variables used as input to MOZART-4.

#	Variable name	Dimension	Units	Description
1	U	3	$m.s^{-1}$	Zonal wind
2	V	3	$m.s^{-1}$	Meridional wind
3	T	3	K	Temperature
4	Q	3	$kg.kg^{-1}$	Specific humidity
5	PS	2	Pa	Surface pressure
6	TS	2	K	Surface temperature
7	ORO	2	FLAG	Orography (land, ocean, sea ice)
8	PHIS	2	$m^2.s^{-2}$	Surface geopotential
9	SHFLX	2	$W.m^{-2}$	Surface heat flux
10	QFLX	2	$W.m^{-2}$	Surface moisture flux
11	TAUX	2	$N.m^{-2}$	Surface zonal stress
12	TAUY	2	$N.m^{-2}$	Surface meridional stress
13	SD	2	m	Snow height
14	SSRD	2	$W.m^{-2}$	Surface downward direct shortwave radiation
15	SOILW	2	ratio	Soil moisture
16	W	2	$m.s^{-1}$	Vertical speed

A.2 ECMWF INTERIM

The ECMWF INTERIM dataset for the year 2000 was downloaded off the MARS server at ECMWF using NCO and CDO scripts provided by Dr. Olaf Stein and modified to suits MOZART-4 needs. It was used in chapter 6.

Appendix B

ACCMIP and RCP emission inventories

In this appendix are given the total emissions for each species used as input to the various MOZART-4 simulations performed within this study. The data were taken from the ACCMIP and RCP datasets for anthropogenic and biomass burning emissions in conjunction with the (Precursors of Ozone and their Effect on the Troposphere) POET and Global Emissions Inventory Activity (GEIA) datasets for natural emissions. These were downloaded from the Jülich FTP server `ftp://ftp-ipcc.fz-juelich.de` as well as from the ACCENT emission data portal `http://accent.aero.jussieu.fr/`(Please note that the ACCMIP and RCP datasets are also available from the ACCENT emission data portal now).

The ACCMIP emission inventory has been developed by Lamarque et al. [2010] and correspond to a combination of existing global and regional inventories. Emissions representative of the year 2000 resulted from the aggregation of the EDGAR-v4, Cofala et al. [2007], EMEP, Environment Canada, REAS, EPA, UNFCCC, Smith et al. [2011], Bond et al. [2007], Junker and Liousse [2008] emission inventories. Regional inventories generally replace global inventories where applicable and no assumption is made regarding the treatment of possible discontinuities between inventories. Shipping estimates in 2000 come from the ATTICA study by Eyring

et al. [2009] which is based on the work of Corbett and Köhler [2003], Endresen et al. [2003, 2007], Eyring et al. [2005b], Buhaug et al. [2009]. They are further distributed using the ICOADS spatial proxy [Wang et al., 2008]. Emissions from crude oil transport are taken into account following the work of Endresen et al. [2003].

The RCP emission inventories are emission scenarios that were produced by four different integrated assessment modelling teams (MESSAGE, IMAGE, GCAM, AIM) and were forced to agree with 2000 estimates. More details can be found in van Vuuren et al. [2010]. The emission datasets used in this study are provided in the next sections. It is important to note that the RCP emission inventories have no change in geographical distribution in the future and in particular, there is no opening of Arctic routes.

The POET emission inventory was developed by Granier et al. [2005] and was used to obtain estimates of soil, biogenic and oceanic emissions of NO_x, NH_3, CO, VOC, CH_3OH, CH_3COCH_3, DMS.

GEIA was created in 1990 under the International Geosphere-Biosphere Program and gather a community of scientists who seek to develop and distribute global anthropogenic and natural emissions of gas and aerosol species. The GEIA emission inventory was employed in this study for its volcanic emissions of SO_2 created by Andres and Kasgnoc [1998].

B.1 Comparison of the ACCMIP emission inventory with the POET emission inventory

TABLE B.1: Comparison between the ACCMIP and POET emission inventories, each representative of the years 2000 and 2006 respectively. The POET inventory was taken from [Emmons et al., 2010b].

Species	POET Tg/a	ACCMIP Tg/a	Difference %
NO	99.8	91.1	−8.7
CO	1210.7	1248.9	+3.2
C2H6	11.9	7.5	−37.0
C3H8	11.0	7.7	−30.0
C2H4	18.1	19.1	+5.5
C3H6	5.8	8.4	+45.8
BIGALK	78.9	41.0	−48.0
BIGENE	9.1	6.3	−30.8
TOLUENE	34.3	29.3	−14.6
ISOP	469.6	469.6	0.0
C10H16	90.7	90.7	0.0
CH3OH	237.6	245.5	+3.3
C2H5OH	5.8	5.8	0.0
CH2O	4.0	9.0	+125.0
CH3CHO	7.6	6.1	−19.7
CH3COCH3	27.2	30.9	+13.6
MEK	6.6	8.0	+21.1
SO2	151.4	117.2	−22.6
DMS	27.4	27.5	+0.4
NH3	67.5	58.6	−13.2
CB1+CB2	7.6	7.8	+2.6
OC1+OC2	38.1	36.0	−5.5

B.2 Historical inventory representative of the year 2000 (ACCMIP)

Species	Total	Anthro.	Aviati.	Shippi.	Soils.	Biomas.	Biogen.	Oceans.	Volcan.
NO_x *Tg(N)/a*	**42.52**	26.50	0.85	5.44	5.22	4.52	-	-	-
CO *Tg(CO)/a*	**1248.87**	608.56	-	1.19	-	459.29	159.96	19.87	-
C_2H_4 *Tg(C)/a*	**8.18**	3.21	-	0.11	-	2.71	2.14	-	-
C_3H_6 *Tg(C)/a*	**2.40**	0.91	-	0.08	-	1.13	0.29	-	-
BIGENE *Tg(C)/a*	**5.38**	4.14	-	0.02	-	1.21	-	-	-
C_2H_6 *Tg(C)/a*	**3.00**	1.28	-	0.06	-	1.26	0.40	-	-
C_3H_8 *Tg(C)/a*	**2.13**	0.94	-	0.12	-	0.53	0.55	-	-
BIGALK *Tg(C)/a*	**34.16**	32.52	-	0.94	-	0.70	-	-	-
TOLUENE *Tg(C)/a*	**26.77**	22.19	-	0.36	-	4.22	-	-	-
CH_2O *Tg(CH2O)/a*	**9.03**	3.18	-	-	-	5.85	-	-	-
CH_3OH *Tg(CH3OH)/a*	**245.50**	3.95	-	-	-	11.92	229.62	-	-
C_2H_5OH *Tg(C2H5OH)/a*	**5.75**	5.68	-	-	-	0.07	-	-	-
CH_3CHO *Tg(CH3CHO)/a*	**6.07**	1.23	-	-	-	4.84	-	-	-
CH_3COCH_3 *Tg(CH3COCH3)/a*	**30.89**	2.20	-	-	-	4.22	24.47	-	-
SO_2 *Tg(S)/a*	**58.64**	46.41	-	5.54	-	1.92	-	-	4.77
DMS *Tg(DMS)/a*	**27.52**	-	-	-	-	-	-	27.52	-
NH3 *Tg(NH3)/a*	**58.60**	37.53	-	-	2.43	10.53	-	8.12	-
MEK *Tg(MEK)/a*	**7.97**	2.73	-	-	-	5.24	-	-	-
BC *Tg(C)/a*	**7.78**	5.02	0.01	0.13	-	2.62	-	-	-
OC *Tg(C)/a*	**35.98**	12.57	-	0.14	-	23.27	-	-	-

TABLE B.2: Emission inventory used as input to MOZART-4 and generated from the ACCMIP historical 2000 dataset (anthropogenic and biomass burning emissions), the POET dataset (soil, biogenic and oceanic emissions) and the GEIA dataset (volcanic emissions).

B.3 RCP emission inventories

Species	Total	Anthro.	Aviati.	Shippi.	Soils.	Biomas.	Biogen.	Oceans.	Volcan.
NO_x *Tg(N)/a*	**42.76**	25.13	1.05	5.84	5.27	5.47	-	-	-
CO *Tg(CO)/a*	**1189.14**	543.13	-	1.31	-	464.93	159.84	19.91	-
C_2H_4 *Tg(C)/a*	**8.24**	3.24	-	0.14	-	2.73	2.14	-	-
C_3H_6 *Tg(C)/a*	**2.42**	0.91	-	0.10	-	1.12	0.29	-	-
BIGENE *Tg(C)/a*	**5.66**	4.06	-	0.02	-	1.57	-	-	-
C_2H_6 *Tg(C)/a*	**3.04**	1.30	-	0.07	-	1.27	0.40	-	-
C_3H_8 *Tg(C)/a*	**2.17**	0.95	-	0.14	-	0.53	0.55	-	-
BIGALK *Tg(C)/a*	**33.94**	32.12	-	1.12	-	0.71	-	-	-
TOLUENE *Tg(C)/a*	**27.36**	22.53	-	0.43	-	4.39	-	-	-
CH_2O *Tg(CH2O)/a*	**9.19**	3.33	-	-	-	5.86	-	-	-
CH_3OH *Tg(CH3OH)/a*	**245.13**	4.14	-	-	-	11.63	229.36	-	-
C_2H_5OH *Tg(C2H5OH)/a*	**22.68**	5.96	-	-	-	16.72	-	-	-
CH_3CHO *Tg(CH3CHO)/a*	**6.11**	1.26	-	-	-	4.85	-	-	-
CH_3COCH_3 *Tg(CH3COCH3)/a*	**31.15**	2.34	-	-	-	4.27	24.54	-	-
SO_2 *Tg(S)/a*	**56.47**	45.61	-	3.73	-	1.92	-	-	5.21
DMS *Tg(DMS)/a*	**27.52**	-	-	-	-	-	-	27.52	-
NH3 *Tg(NH3)/a*	**62.75**	41.09	-	-	2.41	11.17	-	8.08	-
MEK *Tg(MEK)/a*	**8.20**	2.90	-	-	-	5.30	-	-	-
BC *Tg(C)/a*	**8.45**	5.67	0.01	0.14	-	2.63	-	-	-
OC *Tg(C)/a*	**37.35**	14.07	-	0.15	-	23.13	-	-	-

TABLE B.3: Emission inventory generated with the RCP 2.6 2010 and POET datasets and used as input to MOZART-4.

Species	Total	Anthro.	Aviati.	Shippi.	Soils.	Biomas.	Biogen.	Oceans.	Volcan.
NO_x *Tg(N)/a*	**40.08**	22.24	1.24	5.94	5.27	5.40	-	-	-
CO *Tg(CO)/a*	**1142.13**	504.51	-	1.36	-	456.50	159.84	19.91	-
C_2H_4 *Tg(C)/a*	**7.97**	3.00	-	0.13	-	2.70	2.14	-	-
C_3H_6 *Tg(C)/a*	**2.34**	0.85	-	0.10	-	1.11	0.29	-	-
BIGENE *Tg(C)/a*	**5.38**	3.80	-	0.02	-	1.56	-	-	-
C_2H_6 *Tg(C)/a*	**2.93**	1.21	-	0.07	-	1.25	0.40	-	-
C_3H_8 *Tg(C)/a*	**2.12**	0.92	-	0.13	-	0.52	0.55	-	-
BIGALK *Tg(C)/a*	**33.09**	31.31	-	1.08	-	0.70	-	-	-
TOLUENE *Tg(C)/a*	**26.78**	22.02	-	0.42	-	4.35	-	-	-
CH_2O *Tg(CH2O)/a*	**9.12**	3.32	-	-	-	5.80	-	-	-
CH_3OH *Tg(CH3OH)/a*	**245.05**	4.17	-	-	-	11.51	229.36	-	-
C_2H_5OH *Tg(C2H5OH)/a*	**22.55**	6.00	-	-	-	16.55	-	-	-
CH_3CHO *Tg(CH3CHO)/a*	**5.99**	1.20	-	-	-	4.79	-	-	-
CH_3COCH_3 *Tg(CH3COCH3)/a*	**31.29**	2.51	-	-	-	4.24	24.54	-	-
SO_2 *Tg(S)/a*	**46.24**	37.75	-	1.38	-	1.89	-	-	5.21
DMS *Tg(DMS)/a*	**27.52**	-	-	-	-	-	-	27.52	-
NH3 *Tg(NH3)/a*	**67.64**	46.10	-	-	2.41	11.05	-	8.08	-
MEK *Tg(MEK)/a*	**8.38**	3.12	-	-	-	5.26	-	-	-
BC *Tg(C)/a*	**8.18**	5.51	0.01	0.07	-	2.59	-	-	-
OC *Tg(C)/a*	**37.30**	14.41	-	0.09	-	22.80	-	-	-

TABLE B.4: Emission inventory generated with the RCP 2.6 2020 and POET datasets and used as input to MOZART-4.

Species	Total	Anthro.	Aviati.	Shippi.	Soils.	Biomas.	Biogen.	Oceans.	Volcan.
NO_x *Tg(N)/a*	**33.24**	15.49	1.23	6.16	5.27	5.10	-	-	-
CO *Tg(CO)/a*	**990.70**	385.81	-	1.49	-	423.64	159.84	19.91	-
C_2H_4 *Tg(C)/a*	**6.91**	2.06	-	0.12	-	2.59	2.14	-	-
C_3H_6 *Tg(C)/a*	**2.03**	0.60	-	0.09	-	1.06	0.29	-	-
BIGENE *Tg(C)/a*	**4.04**	2.52	-	0.02	-	1.50	-	-	-
C_2H_6 *Tg(C)/a*	**2.48**	0.84	-	0.07	-	1.18	0.40	-	-
C_3H_8 *Tg(C)/a*	**1.93**	0.78	-	0.12	-	0.48	0.55	-	-
BIGALK *Tg(C)/a*	**26.95**	25.27	-	1.01	-	0.68	-	-	-
TOLUENE *Tg(C)/a*	**20.97**	16.37	-	0.39	-	4.20	-	-	-
CH_2O *Tg(CH2O)/a*	**8.60**	3.07	-	-	-	5.53	-	-	-
CH_3OH *Tg(CH3OH)/a*	**243.90**	3.46	-	-	-	11.08	229.36	-	-
C_2H_5OH *Tg(C2H5OH)/a*	**20.90**	4.97	-	-	-	15.93	-	-	-
CH_3CHO *Tg(CH3CHO)/a*	**5.48**	0.92	-	-	-	4.56	-	-	-
CH_3COCH_3 *Tg(CH3COCH3)/a*	**30.77**	2.12	-	-	-	4.10	24.54	-	-
SO_2 *Tg(S)/a*	**21.01**	13.73	-	0.32	-	1.74	-	-	5.21
DMS *Tg(DMS)/a*	**27.52**	-	-	-	-	-	-	27.52	-
NH3 *Tg(NH3)/a*	**77.33**	56.17	-	-	2.41	10.68	-	8.08	-
MEK *Tg(MEK)/a*	**7.73**	2.64	-	-	-	5.09	-	-	-
BC *Tg(C)/a*	**4.84**	2.54	0.01	0.01	-	2.28	-	-	-
OC *Tg(C)/a*	**29.96**	9.57	-	0.01	-	20.38	-	-	-

TABLE B.5: Emission inventory generated with the RCP 2.6 2050 and POET datasets and used as input to MOZART-4.

Species	Total	Anthro.	Aviati.	Shippi.	Soils.	Biomas.	Biogen.	Oceans.	Volcan.
NO_x *Tg(N)/a*	**20.88**	10.00	0.10	0.52	5.27	4.99	-	-	-
CO *Tg(CO)/a*	**784.65**	190.45	-	0.43	-	414.01	159.84	19.91	-
C_2H_4 *Tg(C)/a*	**5.48**	0.75	-	0.03	-	2.56	2.14	-	-
C_3H_6 *Tg(C)/a*	**1.57**	0.23	-	0.02	-	1.04	0.29	-	-
BIGENE *Tg(C)/a*	**2.38**	0.89	-	0.01	-	1.49	-	-	-
C_2H_6 *Tg(C)/a*	**1.92**	0.34	-	0.02	-	1.16	0.40	-	-
C_3H_8 *Tg(C)/a*	**1.39**	0.35	-	0.03	-	0.47	0.55	-	-
BIGALK *Tg(C)/a*	**12.86**	11.96	-	0.23	-	0.67	-	-	-
TOLUENE *Tg(C)/a*	**11.96**	7.75	-	0.09	-	4.12	-	-	-
CH_2O *Tg(CH2O)/a*	**6.91**	1.45	-	-	-	5.47	-	-	-
CH_3OH *Tg(CH3OH)/a*	**242.28**	2.04	-	-	-	10.88	229.36	-	-
C_2H_5OH *Tg(C2H5OH)/a*	**18.58**	2.93	-	-	-	15.64	-	-	-
CH_3CHO *Tg(CH3CHO)/a*	**4.87**	0.39	-	-	-	4.48	-	-	-
CH_3COCH_3 *Tg(CH3COCH3)/a*	**30.23**	1.63	-	-	-	4.06	24.54	-	-
SO_2 *Tg(S)/a*	**11.62**	4.51	-	0.18	-	1.72	-	-	5.21
DMS *Tg(DMS)/a*	**27.52**	-	-	-	-	-	-	27.52	-
NH3 *Tg(NH3)/a*	**91.52**	70.40	-	-	2.41	10.64	-	8.08	-
MEK *Tg(MEK)/a*	**7.07**	2.03	-	-	-	5.04	-	-	-
BC *Tg(C)/a*	**3.32**	1.10	0.01	0.01	-	2.20	-	-	-
OC *Tg(C)/a*	**25.34**	5.48	-	0.03	-	19.83	-	-	-

TABLE B.6: Emission inventory generated with the RCP 2.6 2100 and POET datasets and used as input to MOZART-4.

Species	Total	Anthro.	Aviati.	Shippi.	Soils.	Biomas.	Biogen.	Oceans.	Volcan.
NO_x *Tg(N)/a*	**41.60**	24.85	0.93	5.52	5.27	5.03	-	-	-
CO *Tg(CO)/a*	**1221.37**	629.88	-	1.21	-	410.52	159.84	19.91	-
C_2H_4 *Tg(C)/a*	**8.16**	3.48	-	0.12	-	2.41	2.14	-	-
C_3H_6 *Tg(C)/a*	**2.33**	0.98	-	0.09	-	0.97	0.29	-	-
BIGENE *Tg(C)/a*	**5.83**	4.40	-	0.02	-	1.41	-	-	-
C_2H_6 *Tg(C)/a*	**2.93**	1.37	-	0.06	-	1.10	0.40	-	-
C_3H_8 *Tg(C)/a*	**2.02**	0.92	-	0.12	-	0.44	0.55	-	-
BIGALK *Tg(C)/a*	**35.02**	33.41	-	0.98	-	0.63	-	-	-
TOLUENE *Tg(C)/a*	**27.64**	23.39	-	0.38	-	3.87	-	-	-
CH_2O *Tg(CH2O)/a*	**8.32**	3.15	-	-	-	5.17	-	-	-
CH_3OH *Tg(CH3OH)/a*	**243.77**	4.18	-	-	-	10.23	229.36	-	-
C_2H_5OH *Tg(C2H5OH)/a*	**20.71**	6.01	-	-	-	14.70	-	-	-
CH_3CHO *Tg(CH3CHO)/a*	**5.52**	1.32	-	-	-	4.20	-	-	-
CH_3COCH_3 *Tg(CH3COCH3)/a*	**30.69**	2.31	-	-	-	3.85	24.54	-	-
SO_2 *Tg(S)/a*	**57.16**	45.23	-	5.09	-	1.62	-	-	5.21
DMS *Tg(DMS)/a*	**27.52**	-	-	-	-	-	-	27.52	-
NH3 *Tg(NH3)/a*	**61.24**	41.27	-	-	2.41	9.49	-	8.08	-
MEK *Tg(MEK)/a*	**7.64**	2.87	-	-	-	4.78	-	-	-
BC *Tg(C)/a*	**7.84**	5.30	0.01	0.14	-	2.39	-	-	-
OC *Tg(C)/a*	**34.60**	13.45	-	0.15	-	20.99	-	-	-

TABLE B.7: Emission inventory generated with the RCP 4.5 2010 and POET datasets and used as input to MOZART-4.

Species	Total	Anthro.	Aviati.	Shippi.	Soils.	Biomas.	Biogen.	Oceans.	Volcan.
NO_x *Tg(N)/a*	**39.56**	23.42	1.03	5.70	5.27	4.14	-	-	-
CO *Tg(CO)/a*	**1151.15**	671.65	-	1.25	-	298.49	159.84	19.91	-
C_2H_4 *Tg(C)/a*	**7.74**	3.76	-	0.13	-	1.71	2.14	-	-
C_3H_6 *Tg(C)/a*	**2.05**	1.06	-	0.10	-	0.61	0.29	-	-
BIGENE *Tg(C)/a*	**5.81**	4.73	-	0.02	-	1.05	-	-	-
C_2H_6 *Tg(C)/a*	**2.65**	1.47	-	0.07	-	0.71	0.40	-	-
C_3H_8 *Tg(C)/a*	**1.72**	0.83	-	0.13	-	0.22	0.55	-	-
BIGALK *Tg(C)/a*	**34.10**	32.57	-	1.06	-	0.47	-	-	-
TOLUENE *Tg(C)/a*	**27.33**	24.24	-	0.41	-	2.68	-	-	-
CH_2O *Tg(CH2O)/a*	**6.44**	2.77	-	-	-	3.67	-	-	-
CH_3OH *Tg(CH3OH)/a*	**240.60**	4.28	-	-	-	6.95	229.36	-	-
C_2H_5OH *Tg(C2H5OH)/a*	**16.16**	6.16	-	-	-	10.00	-	-	-
CH_3CHO *Tg(CH3CHO)/a*	**4.09**	1.40	-	-	-	2.69	-	-	-
CH_3COCH_3 *Tg(CH3COCH3)/a*	**29.78**	2.32	-	-	-	2.92	24.54	-	-
SO_2 *Tg(S)/a*	**52.94**	41.92	-	4.70	-	1.11	-	-	5.21
DMS *Tg(DMS)/a*	**27.52**	-	-	-	-	-	-	27.52	-
NH3 *Tg(NH3)/a*	**62.31**	45.65	-	-	2.41	6.18	-	8.08	-
MEK *Tg(MEK)/a*	**6.51**	2.88	-	-	-	3.62	-	-	-
BC *Tg(C)/a*	**7.52**	5.52	0.01	0.15	-	1.84	-	-	-
OC *Tg(C)/a*	**29.99**	13.96	-	0.16	-	15.87	-	-	-

TABLE B.8: Emission inventory generated with the RCP 4.5 2020 and POET datasets and used as input to MOZART-4.

Species	Total	Anthro.	Aviati.	Shippi.	Soils.	Biomas.	Biogen.	Oceans.	Volcan.
NO_x *Tg(N)/a*	**33.63**	16.72	1.57	5.91	5.27	4.16	-	-	-
CO *Tg(CO)/a*	**1025.91**	533.13	-	1.31	-	311.72	159.84	19.91	-
C_2H_4 *Tg(C)/a*	**7.01**	2.93	-	0.16	-	1.78	2.14	-	-
C_3H_6 *Tg(C)/a*	**1.87**	0.81	-	0.12	-	0.66	0.29	-	-
BIGENE *Tg(C)/a*	**5.06**	3.93	-	0.03	-	1.10	-	-	-
C_2H_6 *Tg(C)/a*	**2.31**	1.06	-	0.08	-	0.77	0.40	-	-
C_3H_8 *Tg(C)/a*	**1.83**	0.87	-	0.16	-	0.25	0.55	-	-
BIGALK *Tg(C)/a*	**36.94**	35.15	-	1.29	-	0.50	-	-	-
TOLUENE *Tg(C)/a*	**26.26**	22.89	-	0.50	-	2.87	-	-	-
CH_2O *Tg(CH2O)/a*	**7.34**	3.38	-	-	-	3.96	-	-	-
CH_3OH *Tg(CH3OH)/a*	**240.35**	3.72	-	-	-	7.26	229.36	-	-
C_2H_5OH *Tg(C2H5OH)/a*	**15.80**	5.35	-	-	-	10.44	-	-	-
CH_3CHO *Tg(CH3CHO)/a*	**4.00**	1.16	-	-	-	2.84	-	-	-
CH_3COCH_3 *Tg(CH3COCH3)/a*	**29.85**	2.31	-	-	-	3.00	24.54	-	-
SO_2 *Tg(S)/a*	**29.98**	20.34	-	3.28	-	1.15	-	-	5.21
DMS *Tg(DMS)/a*	**27.52**	-	-	-	-	-	-	27.52	-
NH3 *Tg(NH3)/a*	**66.05**	49.22	-	-	2.41	6.34	-	8.08	-
MEK *Tg(MEK)/a*	**6.59**	2.87	-	-	-	3.72	-	-	-
BC *Tg(C)/a*	**5.97**	3.87	0.01	0.19	-	1.90	-	-	-
OC *Tg(C)/a*	**26.38**	9.48	-	0.20	-	16.69	-	-	-

TABLE B.9: Emission inventory generated with the RCP 4.5 2050 and POET datasets and used as input to MOZART-4.

Species	Total	Anthro.	Aviati.	Shippi.	Soils.	Biomas.	Biogen.	Oceans.	Volcan.
NO_x *Tg(N)/a*	**22.98**	7.81	2.39	3.48	5.27	4.02	-	-	-
CO *Tg(CO)/a*	**651.04**	175.78	-	0.80	-	294.69	159.84	19.91	-
C_2H_4 *Tg(C)/a*	**5.06**	1.10	-	0.14	-	1.68	2.14	-	-
C_3H_6 *Tg(C)/a*	**1.31**	0.30	-	0.10	-	0.62	0.29	-	-
BIGENE *Tg(C)/a*	**2.98**	1.92	-	0.02	-	1.04	-	-	-
C_2H_6 *Tg(C)/a*	**1.59**	0.40	-	0.07	-	0.71	0.40	-	-
C_3H_8 *Tg(C)/a*	**1.55**	0.63	-	0.14	-	0.23	0.55	-	-
BIGALK *Tg(C)/a*	**26.42**	24.81	-	1.14	-	0.47	-	-	-
TOLUENE *Tg(C)/a*	**17.81**	14.67	-	0.44	-	2.69	-	-	-
CH_2O *Tg(CH2O)/a*	**6.40**	2.74	-	-	-	3.67	-	-	-
CH_3OH *Tg(CH3OH)/a*	**238.66**	2.40	-	-	-	6.89	229.36	-	-
C_2H_5OH *Tg(C2H5OH)/a*	**13.36**	3.45	-	-	-	9.91	-	-	-
CH_3CHO *Tg(CH3CHO)/a*	**3.19**	0.52	-	-	-	2.67	-	-	-
CH_3COCH_3 *Tg(CH3COCH3)/a*	**29.32**	1.93	-	-	-	2.85	24.54	-	-
SO_2 *Tg(S)/a*	**15.97**	8.28	-	1.37	-	1.11	-	-	5.21
DMS *Tg(DMS)/a*	**27.52**	-	-	-	-	-	-	27.52	-
NH3 *Tg(NH3)/a*	**62.49**	45.88	-	-	2.41	6.13	-	8.08	-
MEK *Tg(MEK)/a*	**5.94**	2.40	-	-	-	3.54	-	-	-
BC *Tg(C)/a*	**3.78**	1.76	0.02	0.21	-	1.80	-	-	-
OC *Tg(C)/a*	**19.33**	3.30	-	0.22	-	15.81	-	-	-

TABLE B.10: Emission inventory generated with the RCP 4.5 2100 and POET datasets and used as input to MOZART-4.

Species	Total	Anthro.	Aviati.	Shippi.	Soils.	Biomas.	Biogen.	Oceans.	Volcan.
NO_x *Tg(N)/a*	**41.50**	24.94	0.92	4.77	5.27	5.60	-	-	-
CO *Tg(CO)/a*	**1208.90**	556.59	-	1.07	-	471.48	159.84	19.91	-
C_2H_4 *Tg(C)/a*	**7.77**	2.73	-	0.10	-	2.80	2.14	-	-
C_3H_6 *Tg(C)/a*	**2.28**	0.76	-	0.08	-	1.16	0.29	-	-
BIGENE *Tg(C)/a*	**5.38**	3.75	-	0.02	-	1.61	-	-	-
C_2H_6 *Tg(C)/a*	**2.82**	1.05	-	0.05	-	1.31	0.40	-	-
C_3H_8 *Tg(C)/a*	**2.17**	0.96	-	0.10	-	0.56	0.55	-	-
BIGALK *Tg(C)/a*	**35.94**	34.37	-	0.84	-	0.73	-	-	-
TOLUENE *Tg(C)/a*	**26.59**	21.76	-	0.32	-	4.51	-	-	-
CH_2O *Tg(CH2O)/a*	**9.56**	3.53	-	-	-	6.03	-	-	-
CH_3OH *Tg(CH3OH)/a*	**245.00**	3.71	-	-	-	11.93	229.36	-	-
C_2H_5OH *Tg(C2H5OH)/a*	**22.49**	5.34	-	-	-	17.15	-	-	-
CH_3CHO *Tg(CH3CHO)/a*	**6.07**	1.08	-	-	-	4.99	-	-	-
CH_3COCH_3 *Tg(CH3COCH3)/a*	**31.16**	2.27	-	-	-	4.36	24.54	-	-
SO_2 *Tg(S)/a*	**55.55**	43.60	-	4.78	-	1.96	-	-	5.21
DMS *Tg(DMS)/a*	**27.52**	-	-	-	-	-	-	27.52	-
NH3 *Tg(NH3)/a*	**63.29**	41.54	-	-	2.41	11.27	-	8.08	-
MEK *Tg(MEK)/a*	**8.22**	2.81	-	-	-	5.41	-	-	-
BC *Tg(C)/a*	**7.76**	4.94	0.01	0.11	-	2.70	-	-	-
OC *Tg(C)/a*	**36.98**	12.96	-	0.12	-	23.90	-	-	-

TABLE B.11: Emission inventory generated with the RCP 6.0 2010 and POET datasets and used as input to MOZART-4.

Species	Total	Anthro.	Aviati.	Shippi.	Soils.	Biomas.	Biogen.	Oceans.	Volcan.
NO_x *Tg(N)/a*	**39.12**	22.93	1.02	4.19	5.27	5.72	-	-	-
CO *Tg(CO)/a*	**1183.42**	520.04	-	0.95	-	482.68	159.84	19.91	-
C_2H_4 *Tg(C)/a*	**7.53**	2.41	-	0.10	-	2.88	2.14	-	-
C_3H_6 *Tg(C)/a*	**2.22**	0.67	-	0.07	-	1.19	0.29	-	-
BIGENE *Tg(C)/a*	**5.14**	3.47	-	0.02	-	1.65	-	-	-
C_2H_6 *Tg(C)/a*	**2.71**	0.91	-	0.05	-	1.35	0.40	-	-
C_3H_8 *Tg(C)/a*	**2.12**	0.90	-	0.10	-	0.58	0.55	-	-
BIGALK *Tg(C)/a*	**35.90**	34.37	-	0.78	-	0.75	-	-	-
TOLUENE *Tg(C)/a*	**26.26**	21.32	-	0.30	-	4.63	-	-	-
CH_2O *Tg(CH2O)/a*	**9.60**	3.39	-	-	-	6.21	-	-	-
CH_3OH *Tg(CH3OH)/a*	**245.23**	3.61	-	-	-	12.26	229.36	-	-
C_2H_5OH *Tg(C2H5OH)/a*	**22.82**	5.19	-	-	-	17.63	-	-	-
CH_3CHO *Tg(CH3CHO)/a*	**6.11**	0.96	-	-	-	5.15	-	-	-
CH_3COCH_3 *Tg(CH3COCH3)/a*	**31.49**	2.48	-	-	-	4.47	24.54	-	-
SO_2 *Tg(S)/a*	**50.09**	39.00	-	3.89	-	1.99	-	-	5.21
DMS *Tg(DMS)/a*	**27.52**	-	-	-	-	-	-	27.52	-
NH3 *Tg(NH3)/a*	**62.11**	40.24	-	-	2.41	11.39	-	8.08	-
MEK *Tg(MEK)/a*	**8.63**	3.08	-	-	-	5.55	-	-	-
BC *Tg(C)/a*	**7.40**	4.53	0.01	0.10	-	2.77	-	-	-
OC *Tg(C)/a*	**36.62**	12.04	-	0.10	-	24.48	-	-	-

TABLE B.12: Emission inventory generated with the RCP 6.0 2020 and POET datasets and used as input to MOZART-4.

Species	Total	Anthro.	Aviati.	Shippi.	Soils.	Biomas.	Biogen.	Oceans.	Volcan.
NO_x *Tg(N)/a*	**34.19**	18.83	1.47	2.97	5.27	5.85	-	-	-
CO *Tg(CO)/a*	**1180.28**	504.21	-	0.69	-	495.63	159.84	19.91	-
C_2H_4 *Tg(C)/a*	**7.20**	2.00	-	0.09	-	2.97	2.14	-	-
C_3H_6 *Tg(C)/a*	**2.13**	0.54	-	0.07	-	1.24	0.29	-	-
BIGENE *Tg(C)/a*	**4.89**	3.17	-	0.02	-	1.71	-	-	-
C_2H_6 *Tg(C)/a*	**2.56**	0.71	-	0.05	-	1.40	0.40	-	-
C_3H_8 *Tg(C)/a*	**2.05**	0.81	-	0.09	-	0.60	0.55	-	-
BIGALK *Tg(C)/a*	**38.14**	36.64	-	0.72	-	0.77	-	-	-
TOLUENE *Tg(C)/a*	**27.35**	22.26	-	0.28	-	4.80	-	-	-
CH_2O *Tg(CH2O)/a*	**9.65**	3.23	-	-	-	6.42	-	-	-
CH_3OH *Tg(CH3OH)/a*	**245.78**	3.73	-	-	-	12.69	229.36	-	-
C_2H_5OH *Tg(C2H5OH)/a*	**23.61**	5.36	-	-	-	18.25	-	-	-
CH_3CHO *Tg(CH3CHO)/a*	**6.13**	0.80	-	-	-	5.33	-	-	-
CH_3COCH_3 *Tg(CH3COCH3)/a*	**32.40**	3.26	-	-	-	4.60	24.54	-	-
SO_2 *Tg(S)/a*	**39.70**	30.23	-	2.22	-	2.03	-	-	5.21
DMS *Tg(DMS)/a*	**27.52**	-	-	-	-	-	-	27.52	-
NH3 *Tg(NH3)/a*	**74.29**	52.26	-	-	2.41	11.55	-	8.08	-
MEK *Tg(MEK)/a*	**9.77**	4.05	-	-	-	5.72	-	-	-
BC *Tg(C)/a*	**6.87**	3.96	0.01	0.06	-	2.85	-	-	-
OC *Tg(C)/a*	**36.47**	11.17	-	0.06	-	25.24	-	-	-

TABLE B.13: Emission inventory generated with the RCP 6.0 2050 and POET datasets and used as input to MOZART-4.

Species	Total	Anthro.	Aviati.	Shippi.	Soils.	Biomas.	Biogen.	Oceans.	Volcan.
NO_x *Tg(N)/a*	**20.99**	7.13	1.16	0.90	5.27	6.54	-	-	-
CO *Tg(CO)/a*	**954.52**	212.12	-	0.22	-	562.42	159.84	19.91	-
C_2H_4 *Tg(C)/a*	**6.54**	0.92	-	0.04	-	3.43	2.14	-	-
C_3H_6 *Tg(C)/a*	**2.00**	0.24	-	0.03	-	1.44	0.29	-	-
BIGENE *Tg(C)/a*	**3.48**	1.51	-	0.01	-	1.96	-	-	-
C_2H_6 *Tg(C)/a*	**2.36**	0.31	-	0.02	-	1.63	0.40	-	-
C_3H_8 *Tg(C)/a*	**1.64**	0.34	-	0.04	-	0.72	0.55	-	-
BIGALK *Tg(C)/a*	**20.97**	19.72	-	0.35	-	0.89	-	-	-
TOLUENE *Tg(C)/a*	**17.79**	12.12	-	0.14	-	5.53	-	-	-
CH_2O *Tg(CH2O)/a*	**8.86**	1.43	-	-	-	7.43	-	-	-
CH_3OH *Tg(CH3OH)/a*	**246.23**	2.20	-	-	-	14.67	229.36	-	-
C_2H_5OH *Tg(C2H5OH)/a*	**24.26**	3.16	-	-	-	21.10	-	-	-
CH_3CHO *Tg(CH3CHO)/a*	**6.57**	0.37	-	-	-	6.21	-	-	-
CH_3COCH_3 *Tg(CH3COCH3)/a*	**32.16**	2.35	-	-	-	5.27	24.54	-	-
SO_2 *Tg(S)/a*	**15.90**	7.96	-	0.48	-	2.24	-	-	5.21
DMS *Tg(DMS)/a*	**27.52**	-	-	-	-	-	-	27.52	-
NH3 *Tg(NH3)/a*	**84.80**	62.00	-	-	2.41	12.31	-	8.08	-
MEK *Tg(MEK)/a*	**9.46**	2.91	-	-	-	6.55	-	-	-
BC *Tg(C)/a*	**4.32**	1.04	0.00	0.01	-	3.26	-	-	-
OC *Tg(C)/a*	**32.18**	3.27	-	0.01	-	28.90	-	-	-

TABLE B.14: Emission inventory generated with the RCP 6.0 2100 and POET datasets and used as input to MOZART-4.

Species	Total	Anthro.	Aviati.	Shippi.	Soils.	Biomas.	Biogen.	Oceans.	Volcan.
NO_x *Tg(N)/a*	**43.47**	25.74	1.25	5.76	5.27	5.45	-	-	-
CO *Tg(CO)/a*	**1191.29**	553.49	-	1.30	-	456.75	159.84	19.91	-
C_2H_4 *Tg(C)/a*	**7.97**	3.00	-	0.12	-	2.70	2.14	-	-
C_3H_6 *Tg(C)/a*	**2.34**	0.86	-	0.09	-	1.10	0.29	-	-
BIGENE *Tg(C)/a*	**5.43**	3.84	-	0.02	-	1.57	-	-	-
C_2H_6 *Tg(C)/a*	**2.93**	1.21	-	0.07	-	1.26	0.40	-	-
C_3H_8 *Tg(C)/a*	**2.15**	0.96	-	0.12	-	0.53	0.55	-	-
BIGALK *Tg(C)/a*	**34.24**	32.53	-	1.00	-	0.71	-	-	-
TOLUENE *Tg(C)/a*	**27.19**	22.48	-	0.39	-	4.31	-	-	-
CH_2O *Tg(CH2O)/a*	**9.29**	3.46	-	-	-	5.83	-	-	-
CH_3OH *Tg(CH3OH)/a*	**245.07**	4.27	-	-	-	11.44	229.36	-	-
C_2H_5OH *Tg(C2H5OH)/a*	**22.58**	6.13	-	-	-	16.44	-	-	-
CH_3CHO *Tg(CH3CHO)/a*	**5.99**	1.21	-	-	-	4.77	-	-	-
CH_3COCH_3 *Tg(CH3COCH3)/a*	**31.34**	2.56	-	-	-	4.24	24.54	-	-
SO_2 *Tg(S)/a*	**53.09**	40.03	-	5.98	-	1.87	-	-	5.21
DMS *Tg(DMS)/a*	**27.52**	-	-	-	-	-	-	27.52	-
NH3 *Tg(NH3)/a*	**62.70**	41.57	-	-	2.41	10.65	-	8.08	-
MEK *Tg(MEK)/a*	**8.44**	3.17	-	-	-	5.27	-	-	-
BC *Tg(C)/a*	**7.55**	4.76	0.01	0.14	-	2.64	-	-	-
OC *Tg(C)/a*	**35.03**	11.62	-	0.15	-	23.26	-	-	-

TABLE B.15: Emission inventory generated with the RCP 8.5 2010 and POET datasets and used as input to MOZART-4.

Species	Total	Anthro.	Aviati.	Shippi.	Soils.	Biomas.	Biogen.	Oceans.	Volcan.
NO_x *Tg(N)/a*	**46.01**	28.31	1.25	5.80	5.27	5.38	-	-	-
CO *Tg(CO)/a*	**1213.17**	583.53	-	1.40	-	448.49	159.84	19.91	-
C_2H_4 *Tg(C)/a*	**8.02**	3.09	-	0.13	-	2.65	2.14	-	-
C_3H_6 *Tg(C)/a*	**2.35**	0.89	-	0.10	-	1.08	0.29	-	-
BIGENE *Tg(C)/a*	**5.63**	4.07	-	0.02	-	1.54	-	-	-
C_2H_6 *Tg(C)/a*	**2.93**	1.23	-	0.07	-	1.23	0.40	-	-
C_3H_8 *Tg(C)/a*	**2.17**	0.98	-	0.13	-	0.51	0.55	-	-
BIGALK *Tg(C)/a*	**37.55**	35.78	-	1.08	-	0.70	-	-	-
TOLUENE *Tg(C)/a*	**29.40**	24.77	-	0.42	-	4.21	-	-	-
CH_2O *Tg(CH2O)/a*	**9.31**	3.58	-	-	-	5.73	-	-	-
CH_3OH *Tg(CH3OH)/a*	**245.19**	4.64	-	-	-	11.18	229.36	-	-
C_2H_5OH *Tg(C2H5OH)/a*	**22.75**	6.68	-	-	-	16.08	-	-	-
CH_3CHO *Tg(CH3CHO)/a*	**5.92**	1.25	-	-	-	4.66	-	-	-
CH_3COCH_3 *Tg(CH3COCH3)/a*	**31.77**	3.06	-	-	-	4.17	24.54	-	-
SO_2 *Tg(S)/a*	**50.73**	40.51	-	3.18	-	1.83	-	-	5.21
DMS *Tg(DMS)/a*	**27.52**	-	-	-	-	-	-	27.52	-
NH3 *Tg(NH3)/a*	**68.64**	47.80	-	-	2.41	10.36	-	8.08	-
MEK *Tg(MEK)/a*	**8.98**	3.80	-	-	-	5.18	-	-	-
BC *Tg(C)/a*	**7.28**	4.51	0.01	0.15	-	2.60	-	-	-
OC *Tg(C)/a*	**34.26**	11.21	-	0.16	-	22.89	-	-	-

TABLE B.16: Emission inventory generated with the RCP 8.5 2020 and POET datasets and used as input to MOZART-4.

Species	Total	Anthro.	Aviati.	Shippi.	Soils.	Biomas.	Biogen.	Oceans.	Volcan.
NO_x *Tg(N)/a*	**37.85**	19.23	1.96	6.39	5.27	5.01	-	-	-
CO *Tg(CO)/a*	**1072.55**	490.14	-	1.54	-	401.12	159.84	19.91	-
C_2H_4 *Tg(C)/a*	**7.16**	2.52	-	0.15	-	2.36	2.14	-	-
C_3H_6 *Tg(C)/a*	**2.06**	0.74	-	0.11	-	0.93	0.29	-	-
BIGENE *Tg(C)/a*	**4.51**	3.09	-	0.03	-	1.39	-	-	-
C_2H_6 *Tg(C)/a*	**2.58**	1.03	-	0.08	-	1.07	0.40	-	-
C_3H_8 *Tg(C)/a*	**1.85**	0.74	-	0.15	-	0.42	0.55	-	-
BIGALK *Tg(C)/a*	**33.58**	31.77	-	1.18	-	0.62	-	-	-
TOLUENE *Tg(C)/a*	**26.62**	22.46	-	0.46	-	3.70	-	-	-
CH_2O *Tg(CH2O)/a*	**7.95**	2.87	-	-	-	5.08	-	-	-
CH_3OH *Tg(CH3OH)/a*	**244.39**	5.21	-	-	-	9.82	229.36	-	-
C_2H_5OH *Tg(C2H5OH)/a*	**21.61**	7.49	-	-	-	14.11	-	-	-
CH_3CHO *Tg(CH3CHO)/a*	**5.13**	1.10	-	-	-	4.04	-	-	-
CH_3COCH_3 *Tg(CH3COCH3)/a*	**32.58**	4.25	-	-	-	3.78	24.54	-	-
SO_2 *Tg(S)/a*	**30.77**	21.64	-	2.31	-	1.61	-	-	5.21
DMS *Tg(DMS)/a*	**27.52**	-	-	-	-	-	-	27.52	-
NH3 *Tg(NH3)/a*	**80.75**	61.28	-	-	2.41	8.99	-	8.08	-
MEK *Tg(MEK)/a*	**9.98**	5.28	-	-	-	4.70	-	-	-
BC *Tg(C)/a*	**5.61**	3.06	0.01	0.17	-	2.37	-	-	-
OC *Tg(C)/a*	**30.28**	9.45	-	0.18	-	20.66	-	-	-

TABLE B.17: Emission inventory generated with the RCP 8.5 2050 and POET datasets and used as input to MOZART-4.

Species	Total	Anthro.	Aviati.	Shippi.	Soils.	Biomas.	Biogen.	Oceans.	Volcan.
NO_x *Tg(N)/a*	**30.80**	12.24	3.58	5.36	5.27	4.36	-	-	-
CO *Tg(CO)/a*	**858.97**	358.36	-	1.69	-	319.16	159.84	19.91	-
C_2H_4 *Tg(C)/a*	**6.05**	1.91	-	0.16	-	1.84	2.14	-	-
C_3H_6 *Tg(C)/a*	**1.65**	0.58	-	0.12	-	0.67	0.29	-	-
BIGENE *Tg(C)/a*	**3.16**	2.01	-	0.03	-	1.12	-	-	-
C_2H_6 *Tg(C)/a*	**2.07**	0.80	-	0.09	-	0.78	0.40	-	-
C_3H_8 *Tg(C)/a*	**1.29**	0.33	-	0.16	-	0.25	0.55	-	-
BIGALK *Tg(C)/a*	**25.99**	24.19	-	1.30	-	0.50	-	-	-
TOLUENE *Tg(C)/a*	**21.51**	18.16	-	0.51	-	2.85	-	-	-
CH_2O *Tg(CH2O)/a*	**5.08**	1.14	-	-	-	3.94	-	-	-
CH_3OH *Tg(CH3OH)/a*	**242.08**	5.23	-	-	-	7.48	229.36	-	-
C_2H_5OH *Tg(C2H5OH)/a*	**18.28**	7.52	-	-	-	10.76	-	-	-
CH_3CHO *Tg(CH3CHO)/a*	**3.75**	0.81	-	-	-	2.94	-	-	-
CH_3COCH_3 *Tg(CH3COCH3)/a*	**32.94**	5.29	-	-	-	3.11	24.54	-	-
SO_2 *Tg(S)/a*	**18.63**	10.30	-	1.87	-	1.24	-	-	5.21
DMS *Tg(DMS)/a*	**27.52**	-	-	-	-	-	-	27.52	-
NH3 *Tg(NH3)/a*	**90.99**	73.87	-	-	2.41	6.64	-	8.08	-
MEK *Tg(MEK)/a*	**10.43**	6.57	-	-	-	3.86	-	-	-
BC *Tg(C)/a*	**4.24**	2.08	0.02	0.19	-	1.96	-	-	-
OC *Tg(C)/a*	**24.04**	7.26	-	0.20	-	16.58	-	-	-

TABLE B.18: Emission inventory generated with the RCP 8.5 2100 and POET datasets and used as input to MOZART-4.

Appendix C

Supporting data to chapter 4

C.1 WDCGG

TABLE C.1: Summary information of WDCGG stationary stations used in this study.

#	Station	Availability	Species	Latitude Degree North	Longitude Degree East	Altitude metre
1	Barrow	2000, 2005	O_3	-156.60	71.32	11.00
2	Alert	2000, 2005	CO	-62.52	82.45	210.00
3	Zeppelinfjellet	2000	O_3	11.88	78.90	475.00
4	Heimaey	2000, 2005	O_3	-20.28	63.40	100.00
5	Saturna	2000	O_3	-123.13	48.78	178.00
6	Trinidad Head	2005	O_3	-124.15	41.05	120.00
7	Sable Island	2005	CO	-60.02	43.93	5.00
8	Tudor Hill	2000, 2005	O_3	-64.87	32.27	30.00
9	Angra do Heroismo	2000	O_3	-27.22	38.67	74.00
10	Funchal	clim.	O_3	-16.88	32.65	58.00
11	Mace Head	2005	O_3	-9.90	53.33	8.00
12	Noia	2000	O_3	-8.92	42.73	685.00
13	Monte Velho	2000	O_3	-8.80	38.08	43.00
14	Mahón	2000	O_3	4.32	39.87	78.00
15	Kloosterburen	clim.	CO	6.42	53.40	0.00
16	Zingst	2000	O_3	12.73	54.43	1.00
17	Giordan Lighthouse	2000, 2005	O_3, CO	14.22	36.07	167.00
18	Rucava	2000, 2005	O_3	21.10	56.10	18.00
19	Utö	2000, 2005	O_3	21.38	59.78	7.00
20	Ryori	2000, 2005	O_3, CO	141.82	39.03	260.00
21	Mauna Loa	2000, 2005	O_3	-155.58	19.54	3397.00
22	Ragged Point	2000, 2005	O_3	-59.43	13.17	45.00
23	Cape Verde Observatory	clim.	O_3, CO	-24.87	16.85	10.00
24	Izaña (Tenerife)	2000, 2005	O_3, CO	-16.50	28.30	2367.00
25	Hok Tsui	clim.	O_3, CO	114.25	22.22	60.00
26	Yonagunijima	2000, 2005	O_3, CO	123.02	24.47	30.00
27	Minamitorishima	2000, 2005	O_3, CO	153.98	24.28	8.00
28	Tutuila (Cape Matatula)	2000, 2005	O_3	-170.57	-14.24	42.00
29	Ushuaia	2000, 2005	O_3, CO	-68.30	-54.83	18.00
30	Cape Point	clim.	O_3, CO	18.48	-34.35	230.00
31	Amsterdam Island	clim.	CO	77.53	-37.80	65.00
32	Cape Grim	2000, 2005	O_3	144.68	-40.68	94.00
33	Baring Head	2000, 2005	O_3	174.87	-41.41	85.00
34	Neumayer	2000, 2005	O_3	-8.25	-70.65	42.00
35	Arrival Heights	2000, 2005	O_3	166.67	-77.80	184.00

C.2 Aircraft data composites

TABLE C.2: Campaigns included in the aircraft composite climatology used in this study (sorted chronologically). Table modified from Emmons et al. [2000].

#	Campaign	Period covered	Platform	Species
1	STRATOZ-3	Jun. 4 to Jun. 26, 1984	Caravelle 116	O_3, CO, NO
2	ABLE-2A	Jul. 12 to Aug. 13, 1985	Electra	O_3, CO, NO
3	CITE-2	Aug. 11 to Sep. 5, 1986	Electra	O_3, CO, NO
4	ABLE-2B	Apr. 1 to May 13, 1987	Electra	O_3, CO, NO
5	TROPOZ-1	Dec. 11 to Dec. 12, 1987	Caravelle 116	O_3, CO, NO
6	ABLE-3A	Jul. 7 to Aug 17, 1988	Electra	O_3, CO, NO
7	INSTAC-1	Mar. 5 to Mar. 10, 1989	Merlin	O_3, NO
8	ELCHEM	Jul. 27 to Aug. 22, 1989	Sabreliner	O_3, NO
9	CITE-3	Aug. 22 to Sep. 29, 1989	Electra	O_3, CO, NO
10	ABLE-3B	Jul. 6 to Aug. 15, 1990	Electra	O_3, CO, NO
11	TROPOZ-2	Jan. 9 to Feb. 1, 1991	Caravelle 116	O_3, CO, NO
12	PEM-West A	Sep. 16 to Oct. 21, 1991	DC-8	O_3, CO, NO
13	TRACE-A	Sep. 21 to Oct. 26, 1992	DC-8	O_3, CO, NO
14	OCTA-1	Mar 23 to May 21, 1993	C-130	O_3, CO, NO
15	OCTA-2	Aug. 19 to Sep. 1, 1993	C-130	O_3, CO, NO
16	OCTA-3	Jan. 12 to Jan. 17, 1994	C-130	O_3, CO, NO
17	OCTA-4	Mar. 1 to Apr. 26, 1994	C-130	O_3, CO, NO
18	PEM-West B	Feb. 7 to Mar. 14, 1994	DC-8	O_3, CO, NO
19	ACE-1	Oct. 31 to Dec. 22, 1995	C-130	O_3, CO, NO
20	TOTE	Dec. 6 to Dec. 22, 1995	DC-8	O_3, CO, NO
21	VOTE	Jan. 20 to Feb. 19, 1996	DC-8	O_3, CO, NO
22	SUCCESS	Apr. 15 to May 15, 1996	DC-8	O_3, CO, NO
23	PEM-Tropics A	Aug. 15 to Oct. 5, 1996	P-3, DC-8	O_3, CO, NO
24	POLINAT-2	Sep. 19 to Oct. 25, 1997	Falcon	O_3, CO, NO
25	SONEX	Oct. 7 to Nov. 12, 1997	DC-8	O_3, CO, NO
26	PEM-Tropics B	Mar. 6 to Apr. 18, 1999	P-3, DC-8	O_3, CO, NO
27	TOPSE-Feb	Feb. 4 to Feb. 27, 2000	C-130	O_3, CO, NO
28	TOPSE-Mar	Mar. 5 to Mar. 26, 2000	C-130	O_3, CO, NO
29	TOPSE-Apr	Apr. 2 to Apr. 30, 2000	C-130	O_3, CO, NO
30	TOPSE-May	May 15 to May 25, 2000	C-130	O_3, CO, NO
31	TRACE-P	Feb. 24 to Apr. 10, 2001	DC-8	O_3, CO, NO

Appendix D

Supporting data to chapter 6

D.1 Surface concentrations of nitrogen oxides

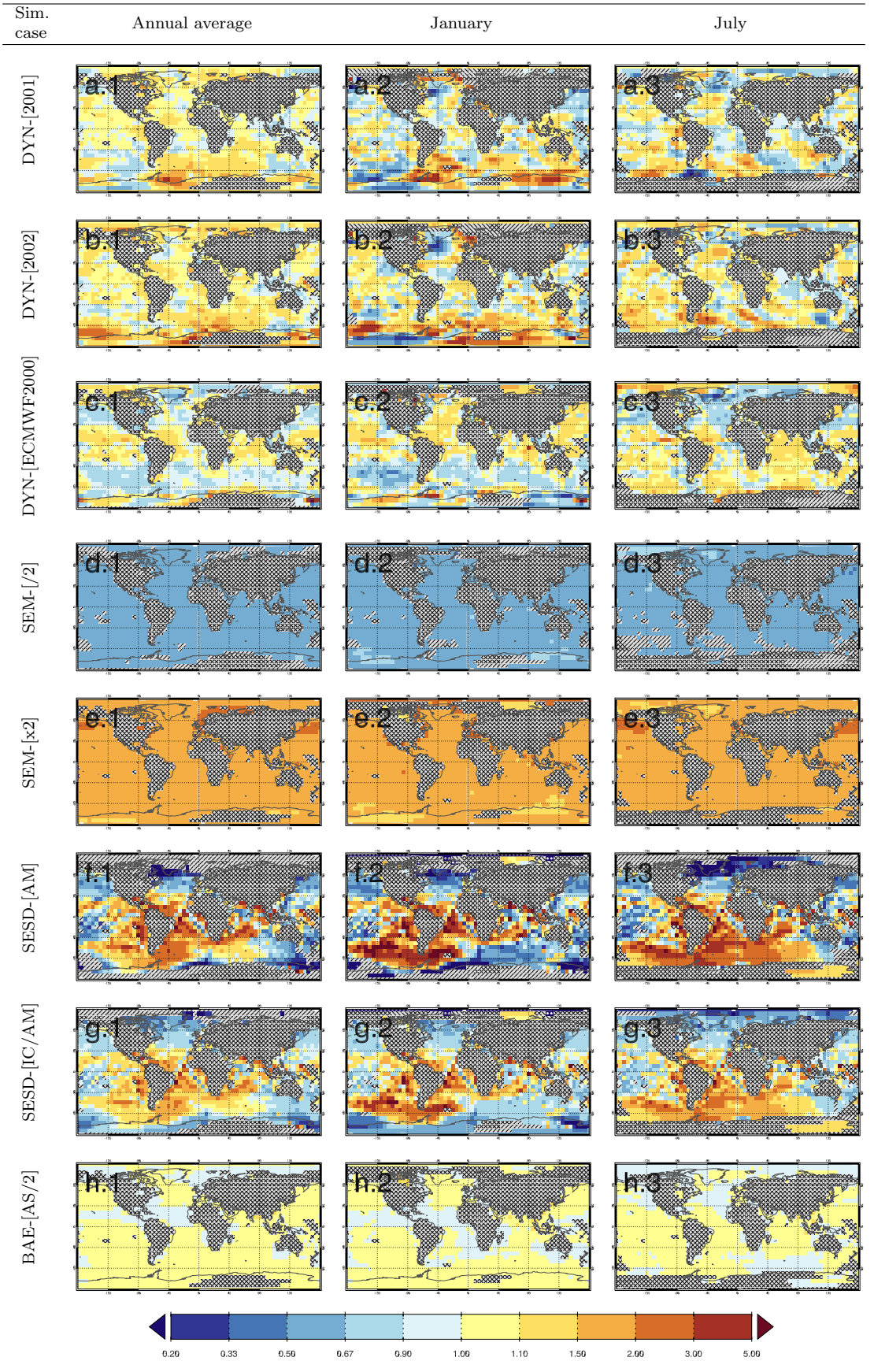
Sim. case
Annual average
January
July
DYN-[2001]
DYN-[2002]
DYN-[ECMWF2000]
SEM-[/2]
SEM-[x2]
SESD-[AM]
SESD-[IC/AM]
BAE-[AS/2]
a.1
a.2
a.3
b.1
b.2
b.3
c.1
c.2
c.3
d.1
d.2
d.3
e.1
e.2
e.3
f.1
f.2
f.3
g.1
g.2
g.3
h.1
h.2
h.3
0.20
0.33
0.50
0.67
0.90
1.00
1.10
1.50
2.00
3.00
5.00

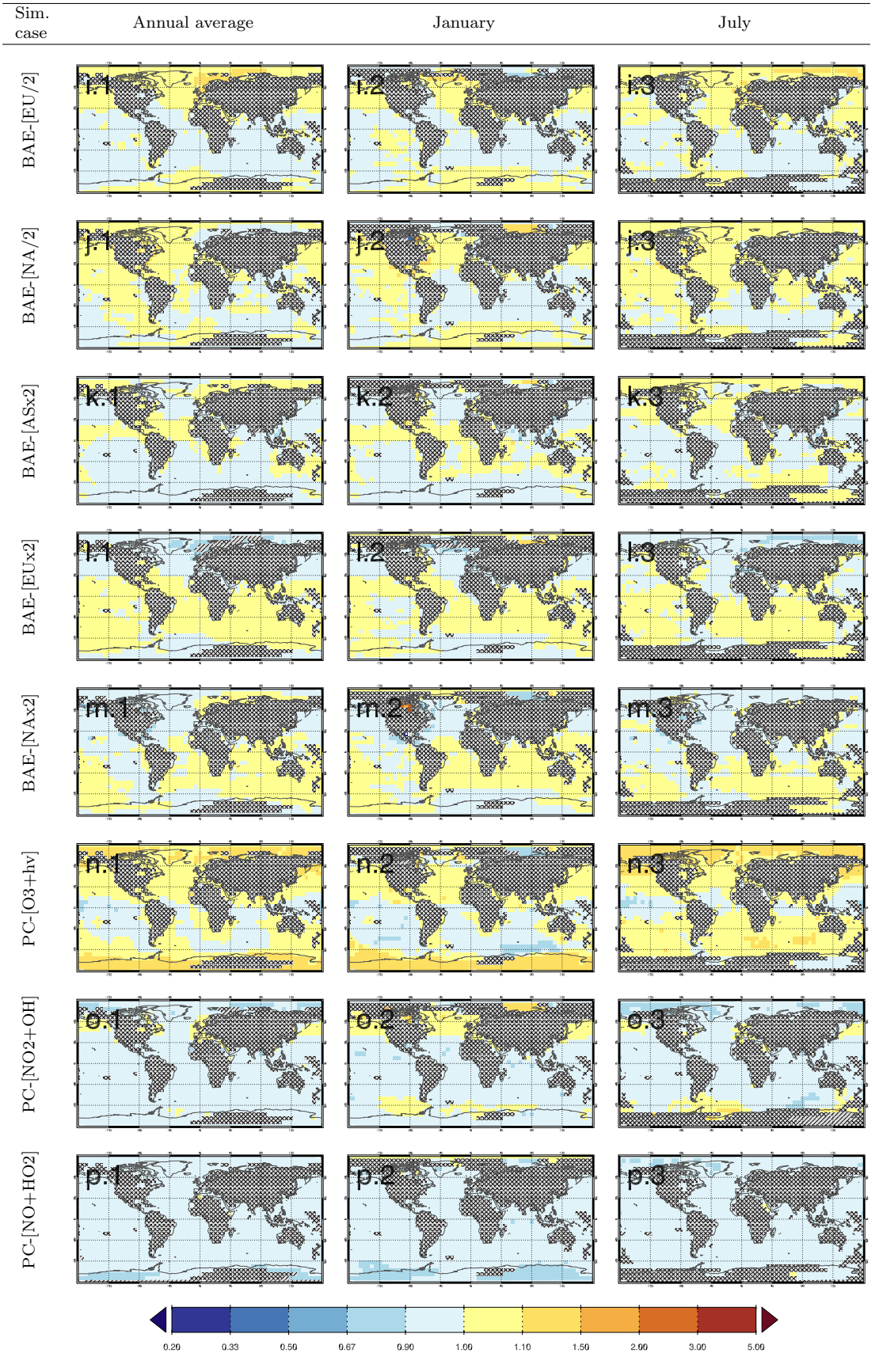
Sim. case
Annual average
January
July
BAE-[EU/2]
BAE-[NA/2]
BAE-[ASx2]
BAE-[EUx2]
BAE-[NAx2]
PC-[O3+hv]
PC-[NO2+OH]
PC-[NO+HO2]
i.1
i.2
i.3
j.1
j.2
j.3
k.1
k.2
k.3
l.1
l.2
l.3
m.1
m.2
m.3
n.1
n.2
n.3
o.1
o.2
o.3
p.1
p.2
p.3
0.20
0.33
0.50
0.67
0.90
1.00
1.10
1.50
2.00
3.00
5.00

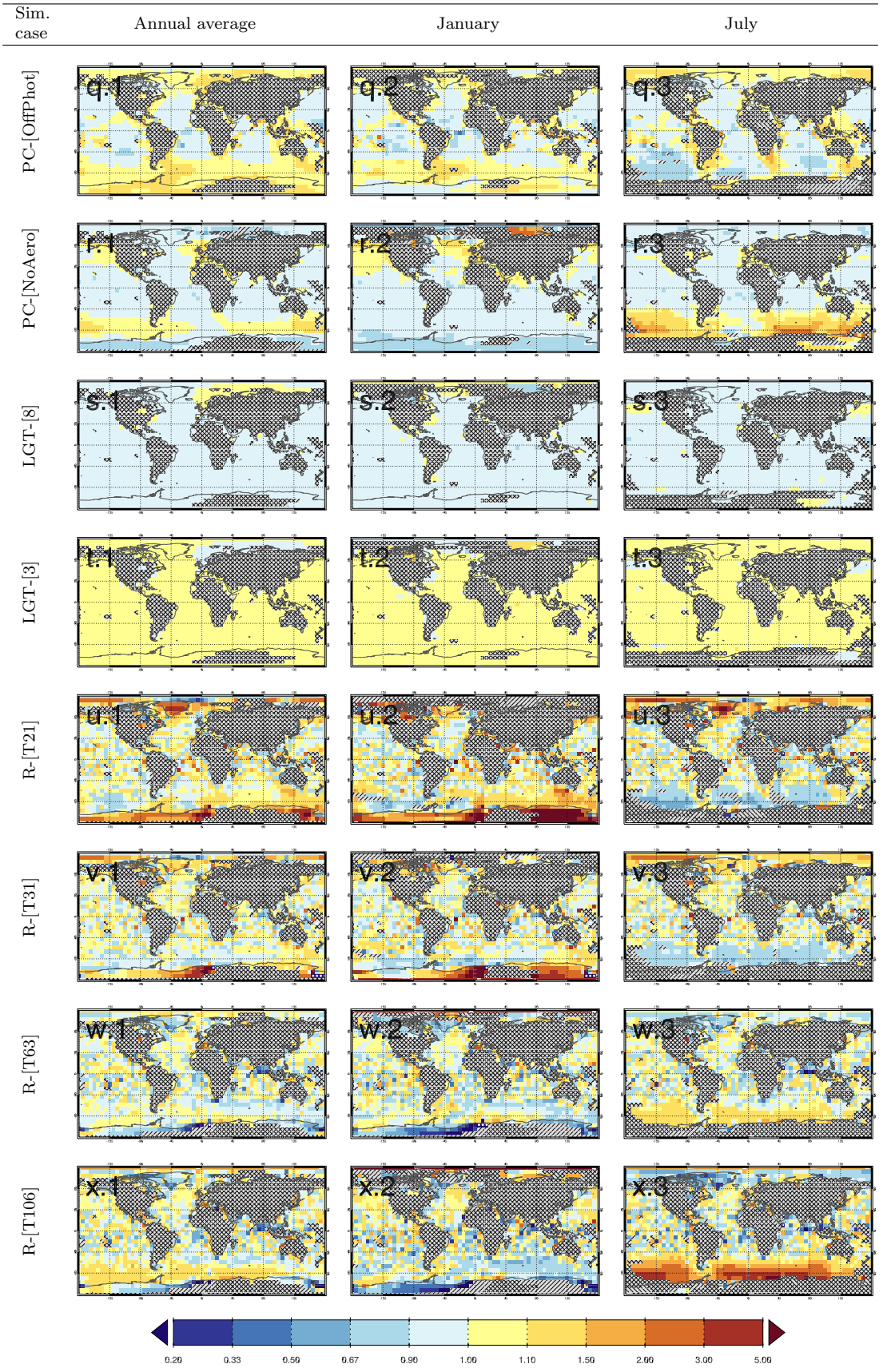

FIGURE D.1: Near-surface maps of NO_x relative differences between the 24 perturbations cases and the reference case. The cutting-value threshold was taken at 10% of relative shipping NO_x perturbations. The corresponding filtered-out regions are displayed with a 135°-angle hatched pattern for the reference case and with a 45°-angle hatched pattern for the perturbation cases.

D.2 Surface concentrations of ozone

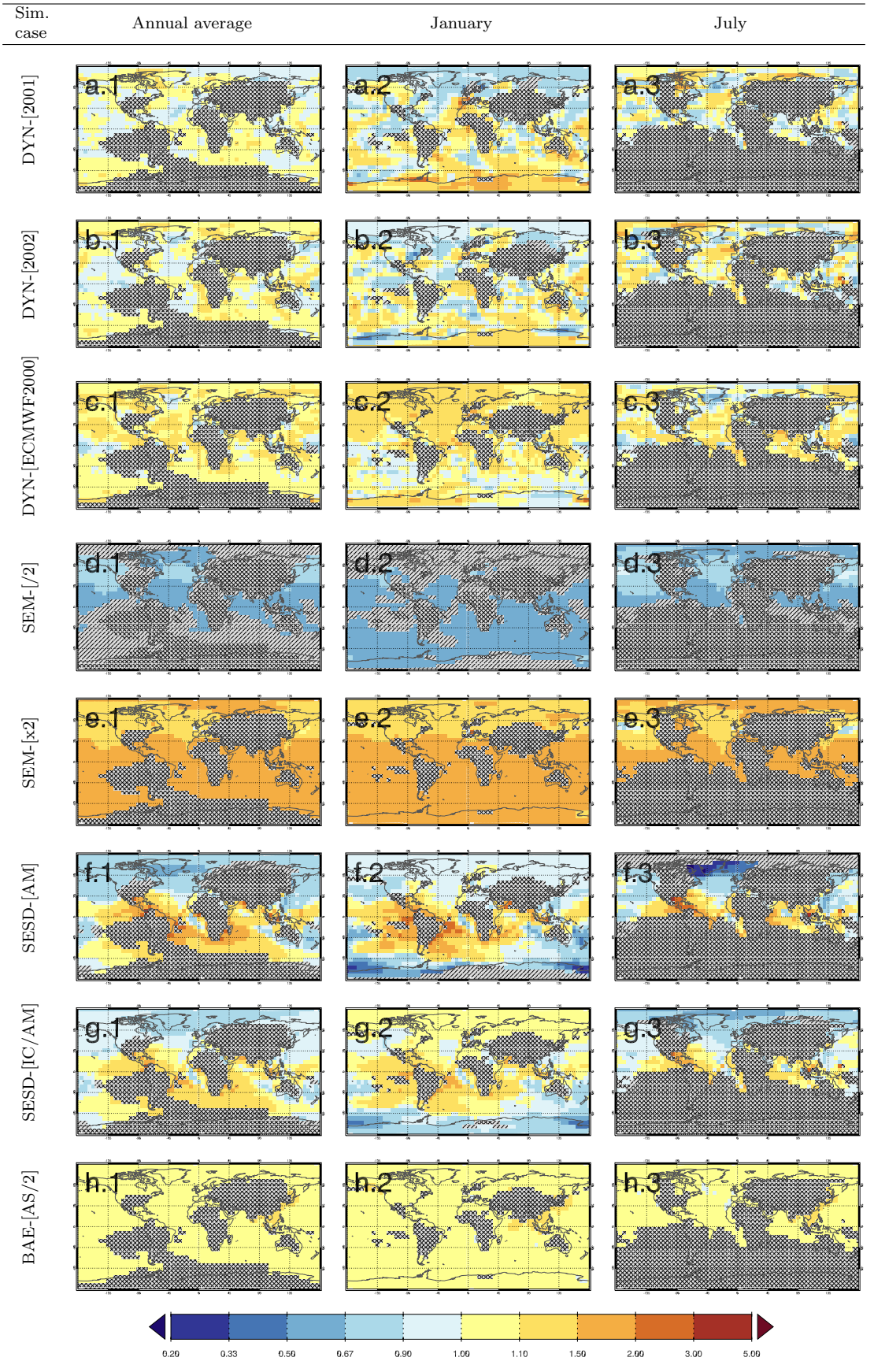
Sim. case
Annual average
January
July
DYN-[2001]
DYN-[2002]
DYN-[ECMWF2000]
SEM-[/2]
SEM-[x2]
SESD-[AM]
SESD-[IC/AM]
BAE-[AS/2]
a.1
a.2
a.3
b.1
b.2
b.3
c.1
c.2
c.3
d.1
d.2
d.3
e.1
e.2
e.3
f.1
f.2
f.3
g.1
g.2
g.3
h.1
h.2
h.3
0.20
0.33
0.50
0.67
0.90
1.00
1.10
1.50
2.00
3.00
5.00

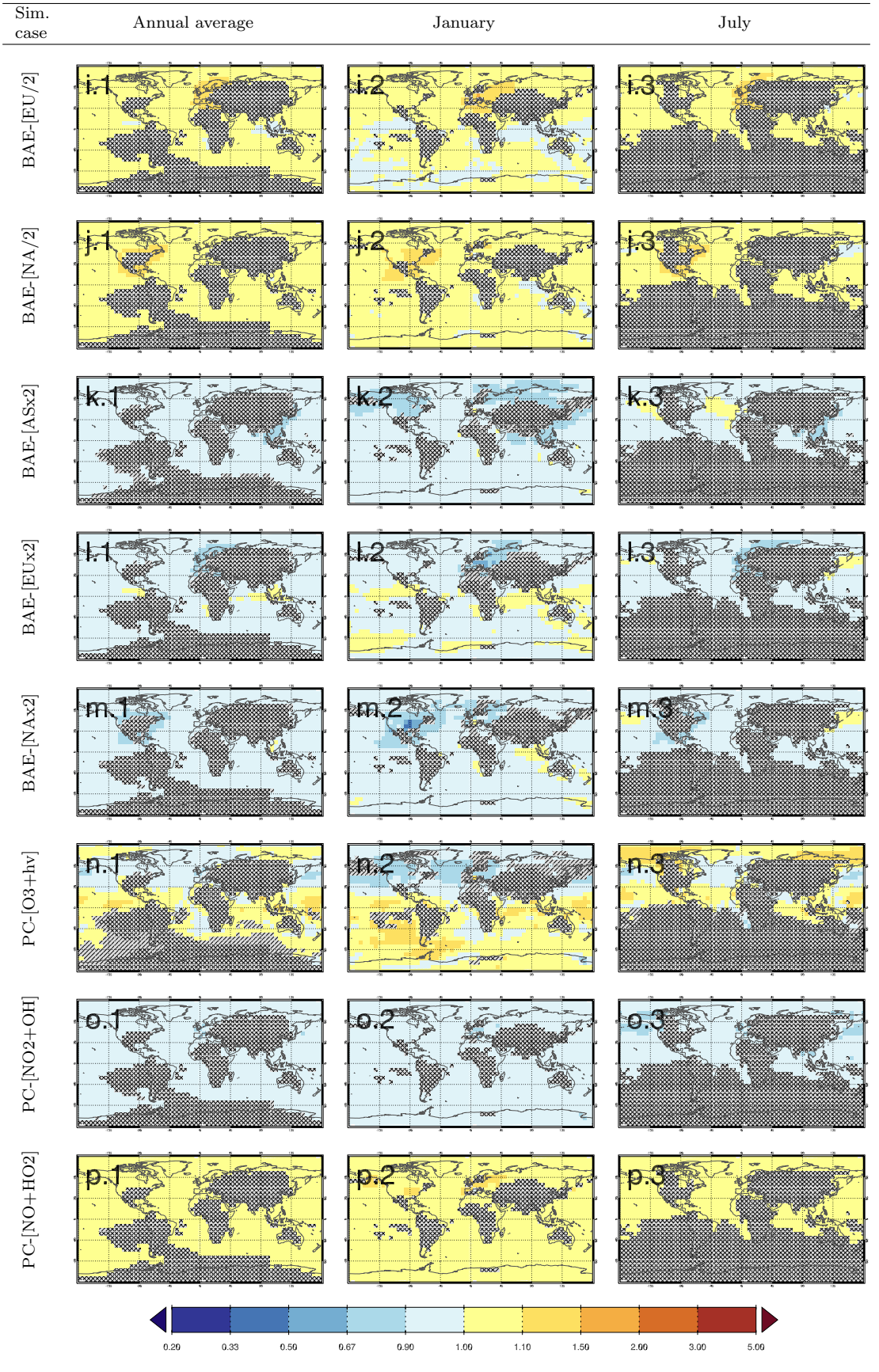
Sim. case
Annual average
January
July
BAE-[EU/2]
i.1
i.2
i.3
BAE-[NA/2]
j.1
j.2
j.3
BAE-[ASx2]
k.1
k.2
k.3
BAE-[EUx2]
l.1
l.2
l.3
BAE-[NAx2]
m.1
m.2
m.3
PC-[O3+hv]
n.1
n.2
n.3
PC-[NO2+OH]
o.1
o.2
o.3
PC-[NO+HO2]
p.1
p.2
p.3
0.20
0.33
0.50
0.67
0.90
1.00
1.10
1.50
2.00
3.00
5.00

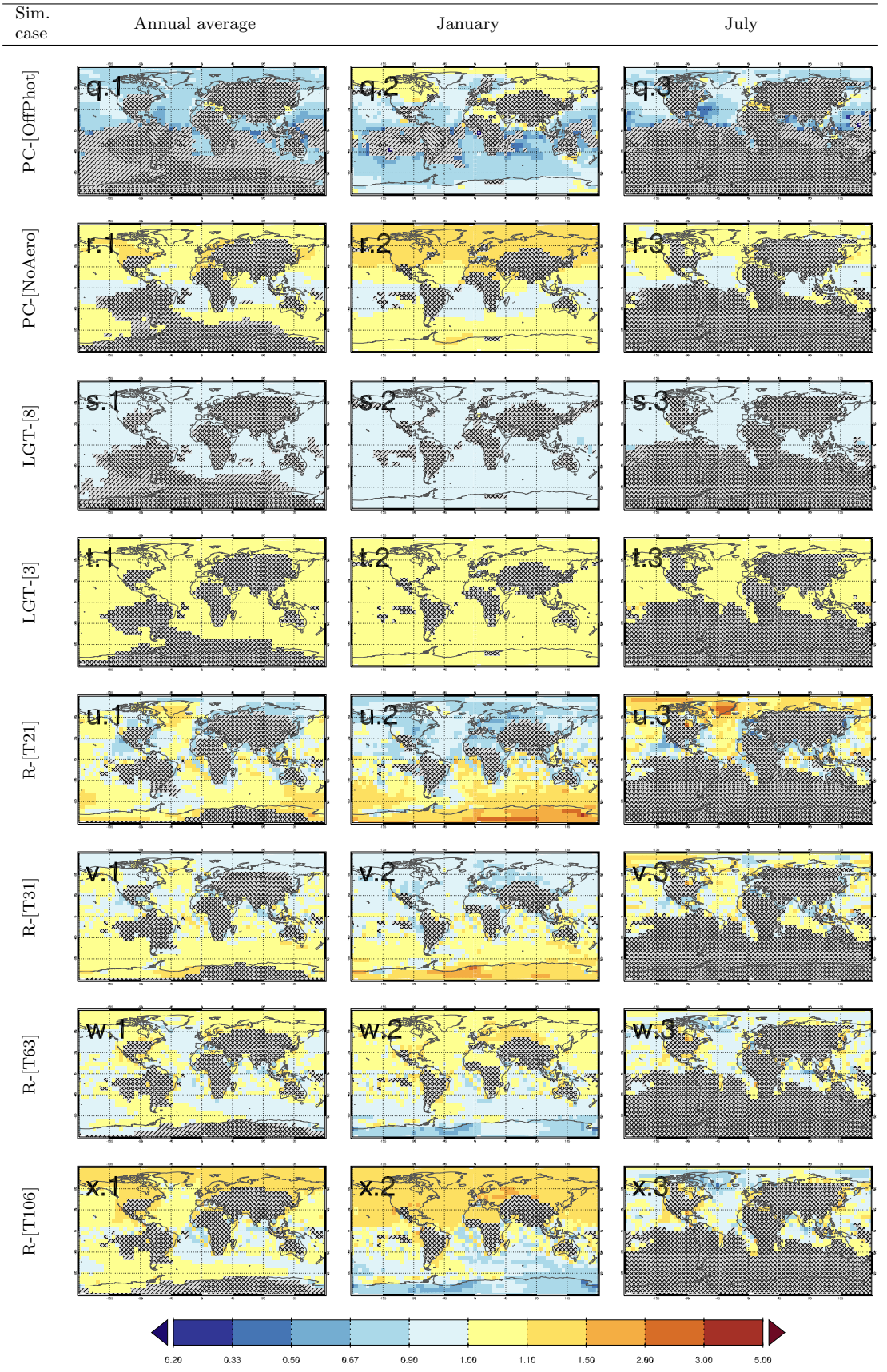

FIGURE D.2: Same as figure D.1 but for O_3. The cutting-value threshold was taken at 5% of relative shipping O_3 perturbations.

D.3 Zonal means of ozone

Sim. case	Annual average	January	July
DYN-[2001]	a.1	a.2	a.3
DYN-[2002]	b.1	b.2	b.3
DYN-[ECMWF2000]	c.1	c.2	c.3
SEM-[/2]	d.1	d.2	d.3
SEM-[x2]	e.1	e.2	e.3
SESD-[AM]	f.1	f.2	f.3
SESD-[IC/AM]	g.1	g.2	g.3
BAE-[AS/2]	h.1	h.2	h.3

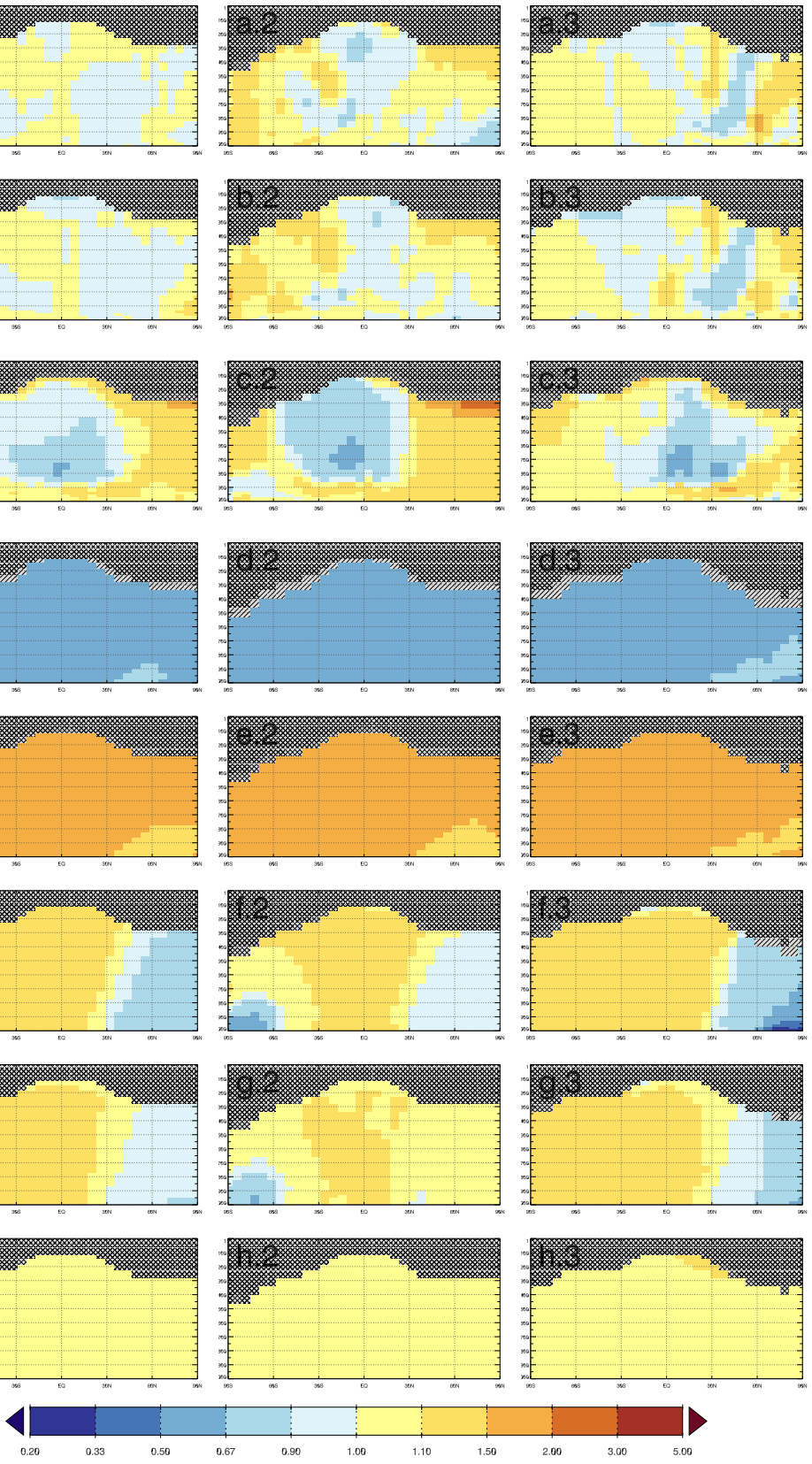

Sim. case	Annual average	January	July
BAE-[EU/2]	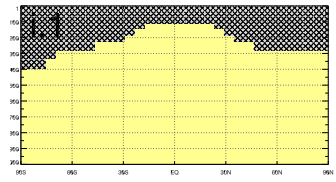	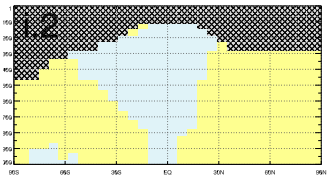	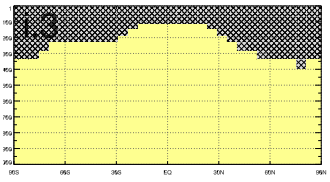
BAE-[NA/2]	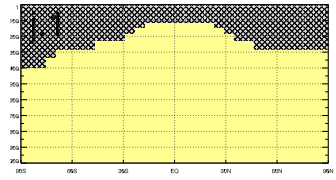	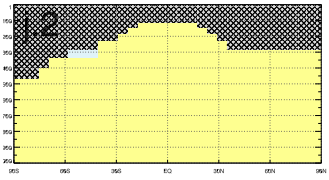	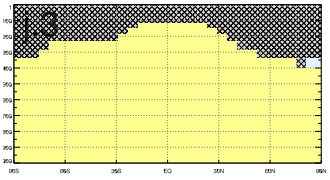
BAE-[ASx2]	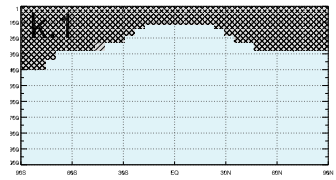	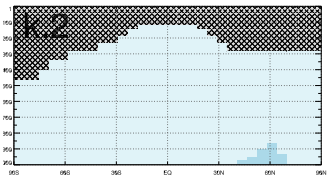	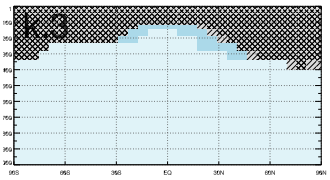
BAE-[EUx2]	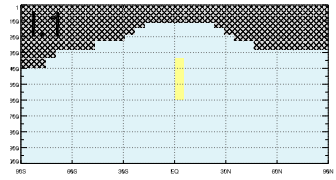	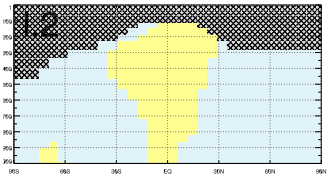	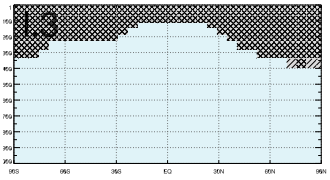
BAE-[NAx2]	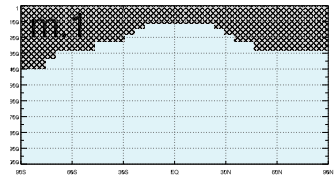	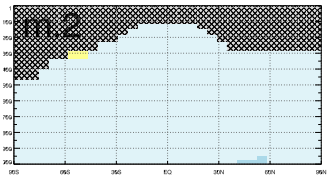	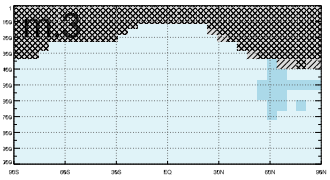
PC-[O3+hv]	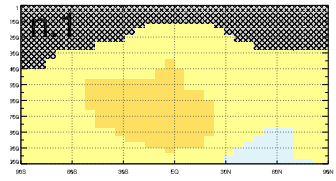	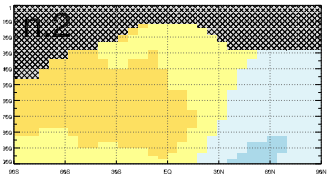	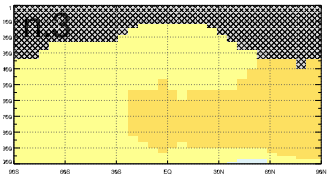
PC-[NO2+OH]	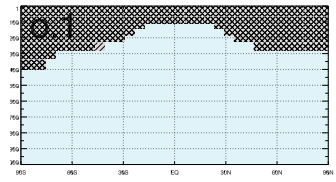	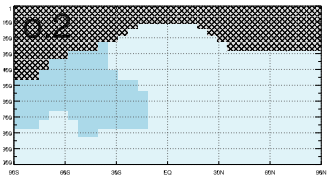	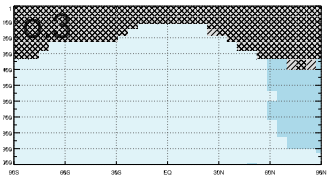
PC-[NO+HO2]	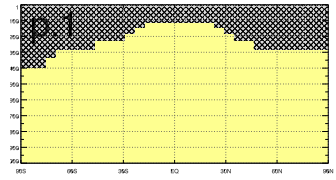	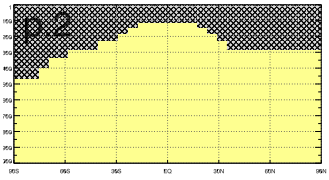	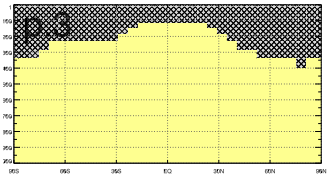

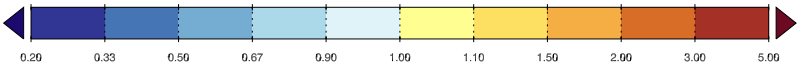

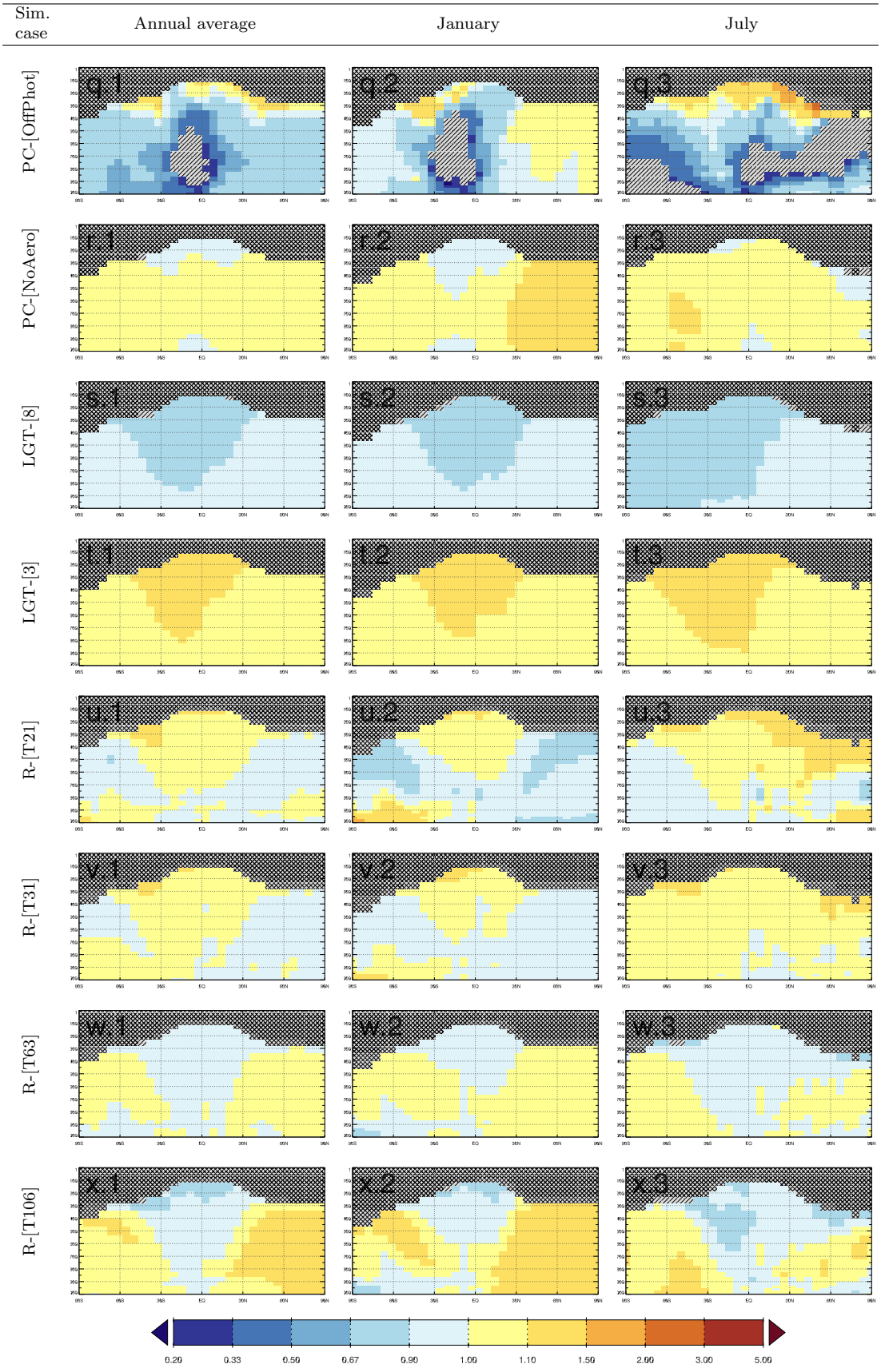

FIGURE D.3: Zonal mean plots of O_3 relative differences between the 24 perturbations cases and the reference case. The cutting-value threshold was taken at 1% of relative shipping O_3 perturbations. The corresponding filtered-out regions are displayed with a 135°-angle hatched pattern for the reference case and with a 45°-angle hatched pattern for the perturbation cases.

D.4 Zonal means of hydroxyl radicals

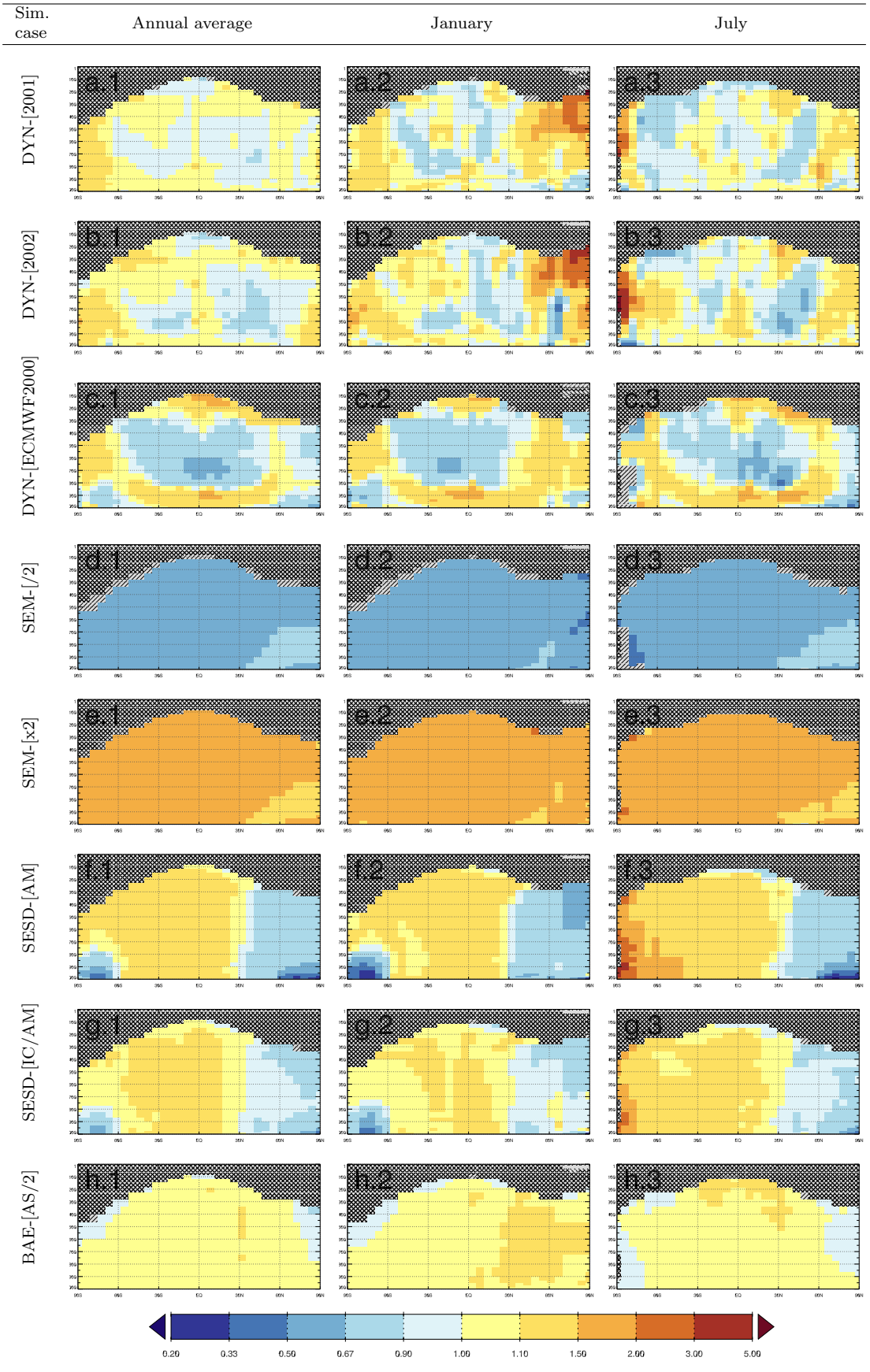
Sim. case
Annual average
January
July
DYN-[2001]
DYN-[2002]
DYN-[ECMWF2000]
SEM-[/2]
SEM-[x2]
SESD-[AM]
SESD-[IC/AM]
BAE-[AS/2]
a.1
a.2
a.3
b.1
b.2
b.3
c.1
c.2
c.3
d.1
d.2
d.3
e.1
e.2
e.3
f.1
f.2
f.3
g.1
g.2
g.3
h.1
h.2
h.3
0.20
0.33
0.50
0.67
0.90
1.00
1.10
1.50
2.00
3.00
5.00

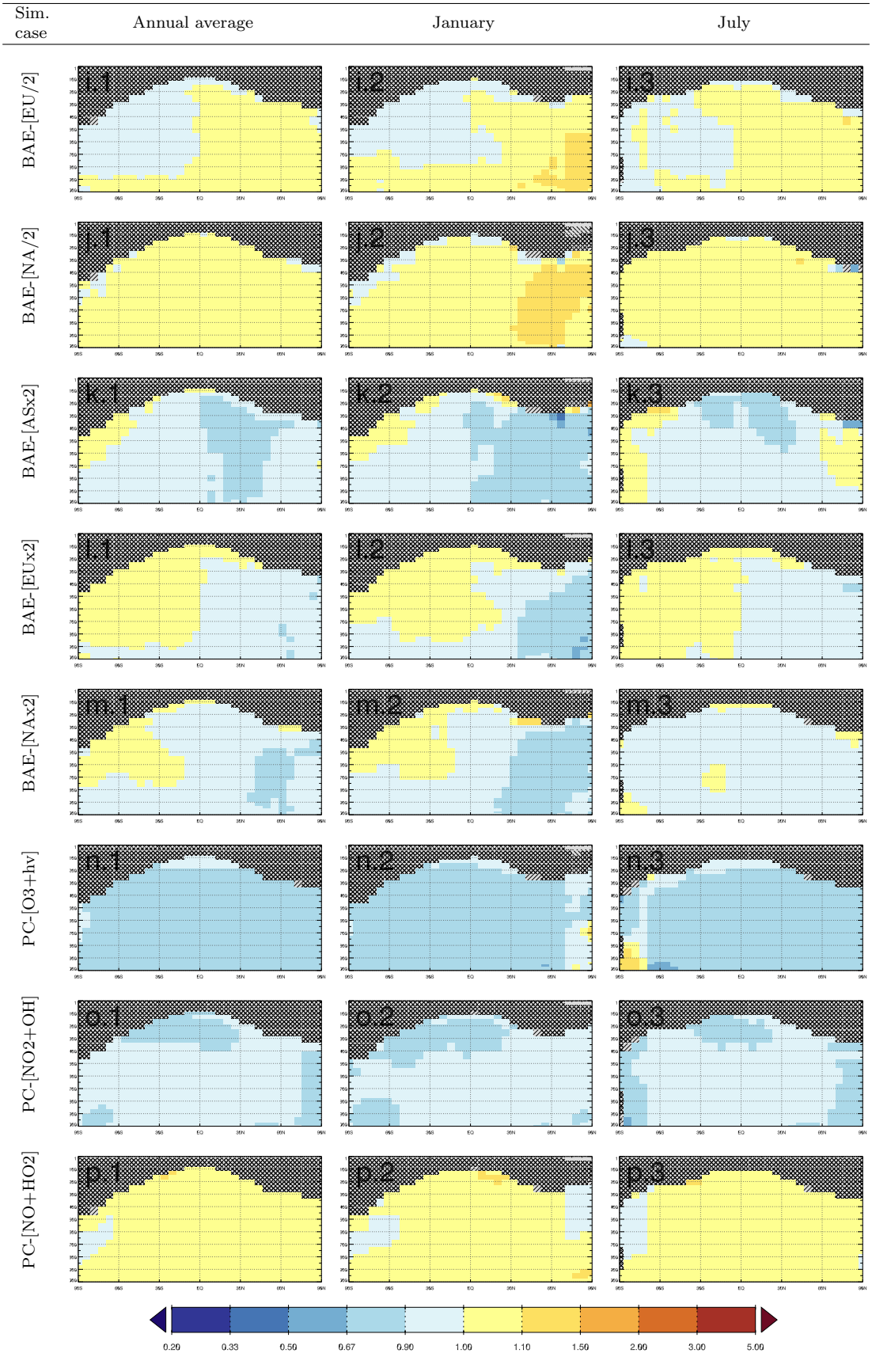
Sim. case
Annual average
January
July
BAE-[EU/2]
BAE-[NA/2]
BAE-[ASx2]
BAE-[EUx2]
BAE-[NAx2]
PC-[O3+hv]
PC-[NO2+OH]
PC-[NO+HO2]
i.1
i.2
i.3
k.1
k.2
k.3
l.1
l.2
l.3
m.1
m.2
m.3
n.1
n.2
n.3
o.1
o.2
o.3
p.1
p.2
p.3
0.20
0.33
0.50
0.67
0.90
1.00
1.10
1.50
2.00
3.00
5.00

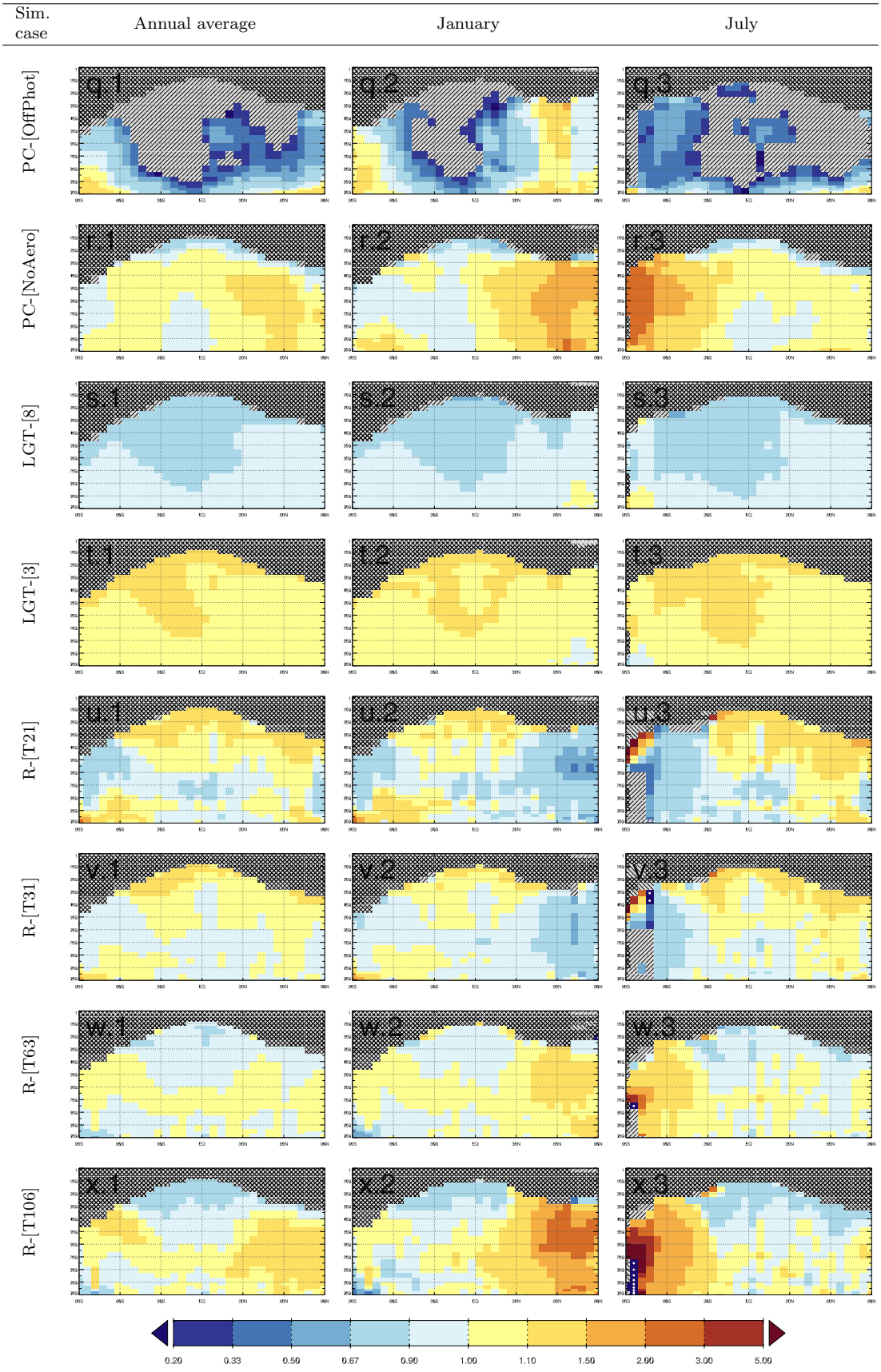

FIGURE D.4: Same as figure D.3 but for OH.

D.5 Tropospheric ozone columns

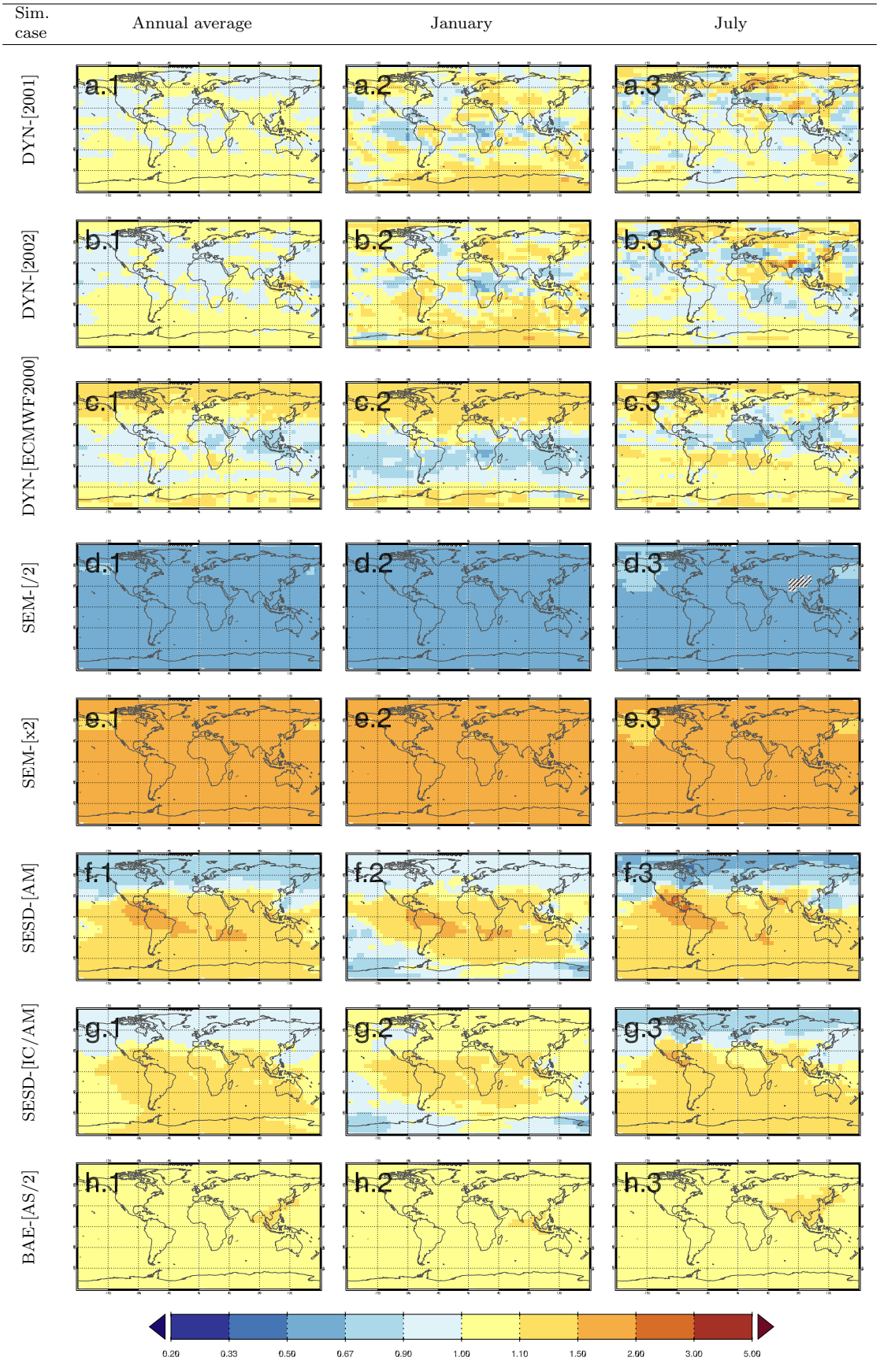
Sim. case
Annual average
January
July
DYN-[2001]
DYN-[2002]
DYN-[ECMWF2000]
SEM-[/2]
SEM-[x2]
SESD-[AM]
SESD-[IC/AM]
BAE-[AS/2]
a.1
a.2
a.3
b.1
b.2
b.3
c.1
c.2
c.3
d.1
d.2
d.3
e.1
e.2
e.3
f.1
f.2
f.3
g.1
g.2
g.3
h.1
h.2
h.3
0.20
0.33
0.50
0.67
0.90
1.00
1.10
1.50
2.00
3.00
5.00

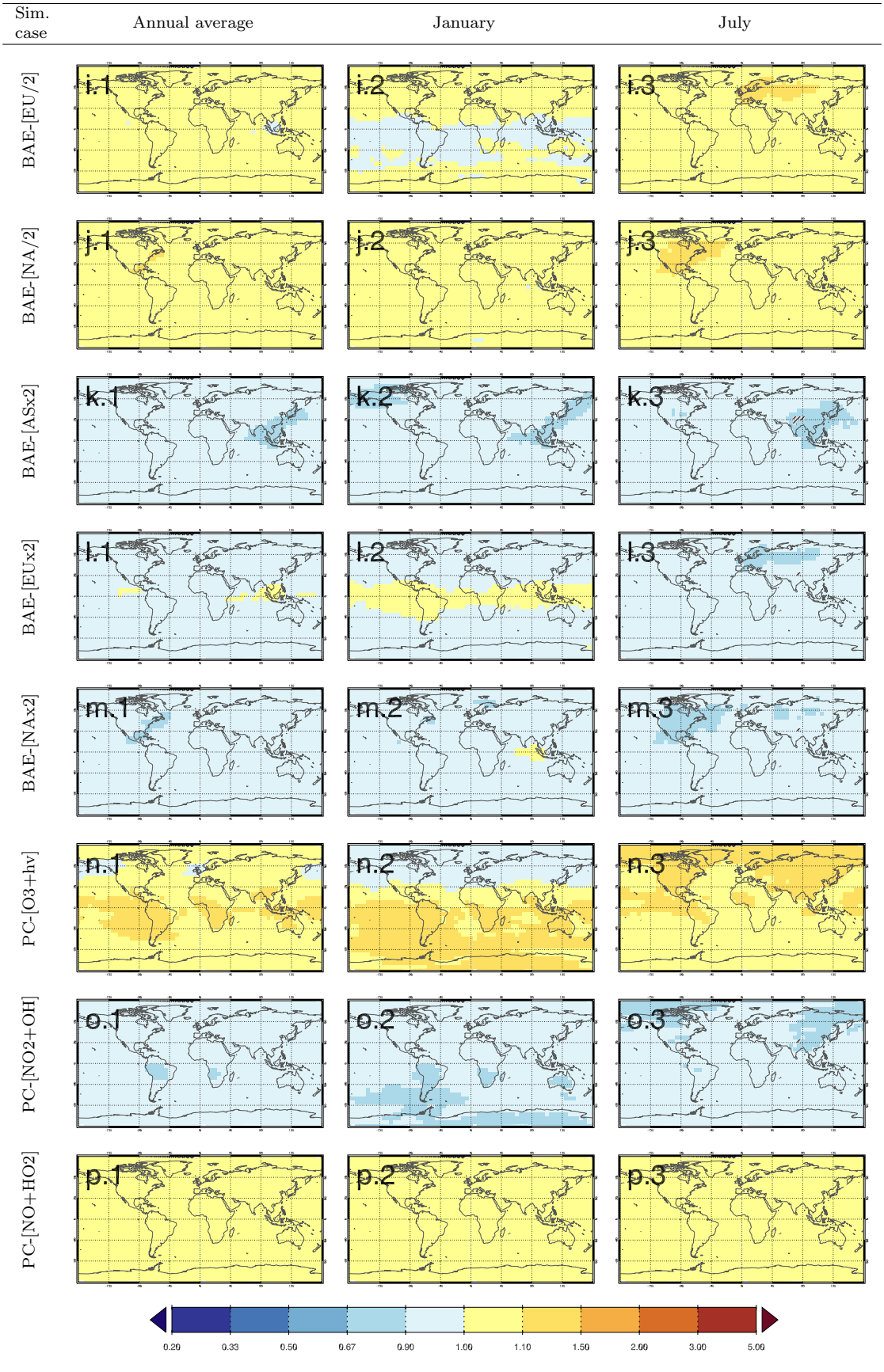
Sim. case
Annual average
January
July
BAE-[EU/2]
BAE-[NA/2]
BAE-[ASx2]
BAE-[EUx2]
BAE-[NAx2]
PC-[O3+hv]
PC-[NO2+OH]
PC-[NO+HO2]
i.1
i.2
i.3
j.1
j.2
j.3
k.1
k.2
k.3
l.1
l.2
l.3
m.1
m.2
m.3
n.1
n.2
n.3
o.1
o.2
o.3
p.1
p.2
p.3
0.20
0.33
0.50
0.67
0.90
1.00
1.10
1.50
2.00
3.00
5.00

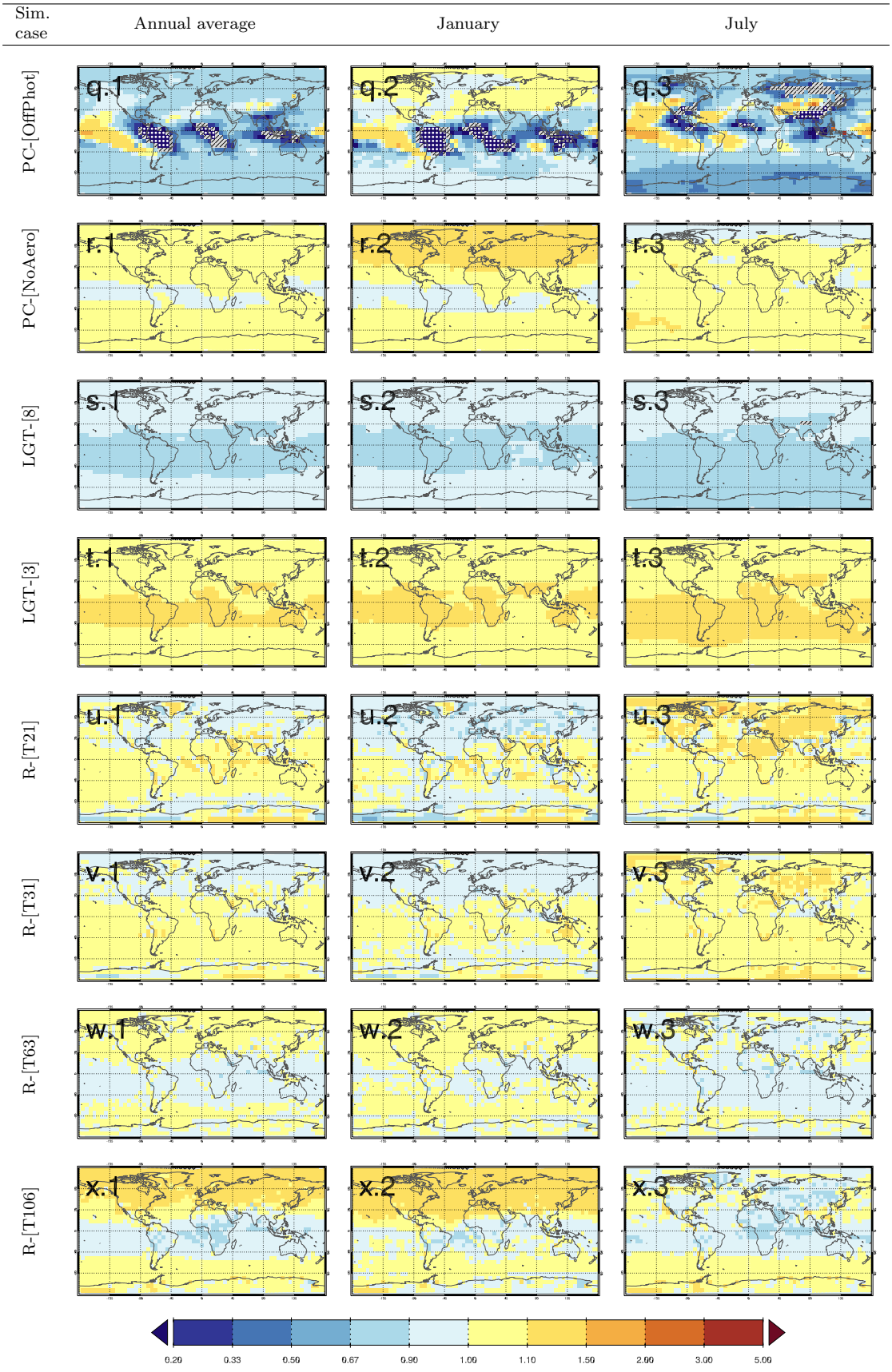

FIGURE D.5: Maps of tropospheric O_3 column relative differences between the 24 perturbations cases and the reference case. The cutting-value threshold was taken at 0.03% of relative shipping O_3 perturbations. The corresponding filtered-out regions are displayed with a 135°-angle hatched pattern for the reference case and with a 45°-angle hatched pattern for the perturbation cases.

Appendix E

Supporting data to chapter 7

This appendix provides the mathematical description of the new approach suggested in this study. The source code of the FORTRAN routines developed for the purpose of this study are available on the thesis' website http://hilaire.jerome.free.fr/PhD_thesis/.

$$\frac{\partial \overline{r_{f1}}}{\partial t} = E - \frac{\overline{r_{f1}}}{\tau} - K_{eff}^{OH} \times \overline{r_{f1}} \times \rho \times \alpha_{NO_x} \times EI_{NO_x} \times \overline{r_{OH}} \times \delta \tag{E.1}$$

$$\frac{\partial \overline{r_{f2}}}{\partial t} = \frac{\overline{r_{f1}}}{\tau} - \frac{\overline{r_{f2}}}{\tau} - K_{eff}^{OH} \times \overline{r_{f2}} \times \rho \times \alpha_{NO_x} \times EI_{NO_x} \times \overline{r_{OH}} \times \delta \tag{E.2}$$

$$\frac{\partial \overline{NO}}{\partial t} = \frac{\overline{r_{f2}}}{\tau} \times \alpha_{NO} \times EI_{NO} \tag{E.3}$$

$$\frac{\partial \overline{NO_2}}{\partial t} = \frac{\overline{r_{f2}}}{\tau} \times \alpha_{NO_2} \times EI_{NO_2} \tag{E.4}$$

$$\frac{\partial \overline{HNO_3}}{\partial t} = K_{eff}^{OH} \times \overline{r_{f1}} \times \rho \times \alpha_{NO_x} \times EI_{NO_x} \times \overline{r_{OH}} \times \delta + K_{eff}^{OH} \times \overline{r_{f2}} \times \rho \times \alpha_{NO_x} \times EI_{NO_x} \times \overline{r_{OH}} \times \delta \tag{E.5}$$

$$\begin{aligned} \frac{\partial \overline{O_3}}{\partial t} = & - \frac{\overline{r_{f1}}}{\tau} \times \alpha_{NO_x} \times EI_{NO_x} \left(\frac{\overline{NO_2}}{\overline{NO_x}} - E_{r_{NO_2}/r_{NO_x}} \right) \times \delta \\ & + K_{eff}^{HO_2} \times \overline{r_{f1}} \times \rho \times \alpha_{NO_x} \times EI_{NO_x} \times \overline{r_{HO_2}} \times \delta \\ & + K_{eff}^{HO_2} \times \overline{r_{f2}} \times \rho \times \alpha_{NO_x} \times EI_{NO_x} \times \overline{r_{HO_2}} \times \delta \\ & + K_{eff}^{CH_3O_2} \times \overline{r_{f1}} \times \rho \times \alpha_{NO_x} \times EI_{NO_x} \times \overline{r_{CH_3O_2}} \times \delta \\ & + K_{eff}^{CH_3O_2} \times \overline{r_{f2}} \times \rho \times \alpha_{NO_x} \times EI_{NO_x} \times \overline{r_{CH_3O_2}} \times \delta \end{aligned} \tag{E.6}$$

Where r_{f1}, r_{f2}, r_{NO}, r_{NO_2}, r_{NO_x}, r_{OH}, r_{O_3}, r_{HO_2} and $r_{CH_3O_2}$ are the volume mixing ratios of the plume tracers, NO, NO_2, OH, HO_2 and CH_3O_2 respectively. E is the shipping emission rate, τ determines the lifetime of the plume tracer, α_{NO} and α_{NO_2} are the ratios of NO and NO_2 to NO_x respectively (hence, $\alpha_{NO_x} = 1$). EI_{NO} and EI_{NO_2} are emission factors of NO and NO_2. $E_{r_{NO_2}/r_{NO_x}}$ is a ratio equal to the proportion of NO_2 in the NO_x emissions. K_{eff} is the pre-calculated effective reaction rate. ρ is the air density. δ equals 1 during daytime and 0 over night. $\langle T \rangle$ represents the contribution of transport processes. All overlined quantities refer to GCTM grid cell averages. Note that in this case, two plume tracers are defined and represent different phases of the ship plume.

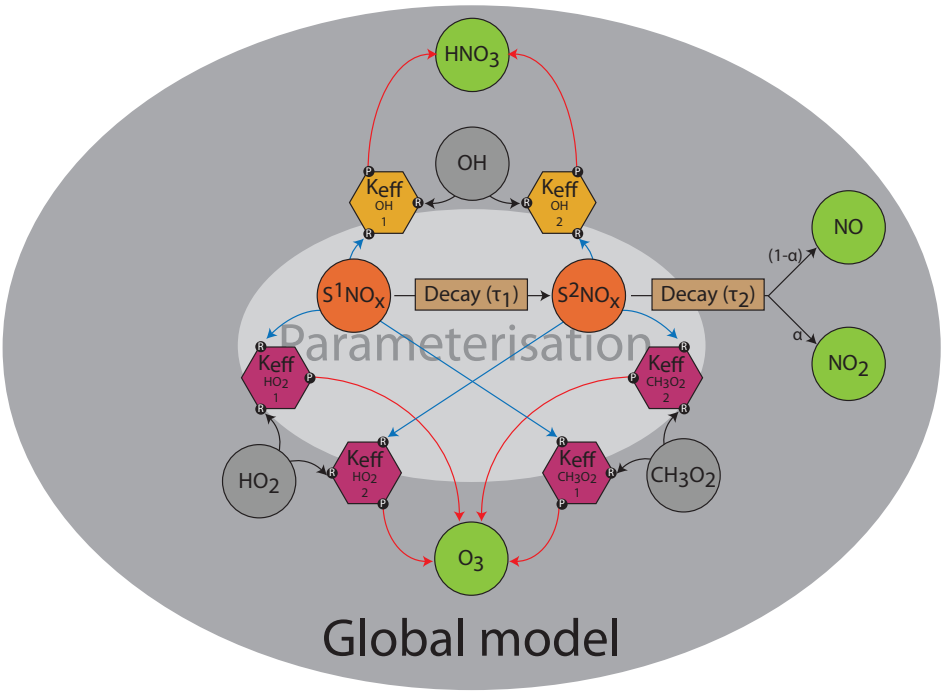

FIGURE E.1: Proposition of parameterisation using various characteristic times (decaying times) and several effective reaction rates to control the production of O_3 and the loss of NO_x.

Appendix F

Publications

In this appendix are provided the two papers published prior to the publication of this thesis and written in the proceedings of the TAC-2 conference and the MMU conference.

Do Radiative forcings of Methane and Ozone cancel out? - A case study from the last IMO Greenhouse gases study

Jérôme Hilaire*, David S. Lee
Dalton Research Institute, Manchester Metropolitan University, UK

Keywords: Shipping, NO_x emissions, Atmospheric composition, Climate impacts, IMO GHG Study 2, MOZART-2, GCTM, Edwards&Slingo, RTM.

ABSTRACT: This modelling work aims at quantifying the perturbation resulting from international maritime transport emissions of nitrogen oxides on the lower atmospheric composition and the climate. We uses the emission dataset created for the new IMO Greenhouse study as input to the tropospheric GCTM MOZART-2. We further run the Edwards&Slingo Radiative Transfer Model to assess impacts on the climate. Due to the large emissions of nitrogen oxides in the atmosphere by shipping, we find significant perturbations in Ozone ($35W.m^{-2}$) and Methane ($-45W.m^{-2}$) leading to a important impact on the climate. However, it is very likely that these impacts are overestimated because the non-linearity introduced by subgrid scale plume processes is not taken into account.

1 INTRODUCTION

International shipping is undeniably a cornerstone of the global economy. However, it is an increasing environmental problem that consumes large quantities of fossil fuel and releases significant amounts of atmospheric pollutants leading to acidification, eutrophication, lung cancer *[Corbett et al, 2007]* and climate change. In addition, it is not covered under the Kyoto Protocol (Article 2.2) for CO_2.

Indeed, by emitting nitrogen oxides (NO_x), carbon monoxide (CO) and volatile organic compounds (VOCs) in the marine boundary layer and through complex chemical processes, these molecules contribute to the formation of ozone (O_3) and the depletion of methane (CH_4) which induce climate change.

Several studies *[Corbett et al, 2001]*, *[Endressen et al, 2003*], *[Eyring et al, 2005]*, *[Eyring et al, 2009]* have presented different values resulting from a large range of shipping emissions. However, all patterns looked similar.

This study focuses on the trade-off between impacts of Ozone and Methane on the climate stemming from a shipping perturbation induced by emissions calculated for IMO in 2007. First, we present the adopted methodology, then we discuss the results from the simulations and finally, we conclude.

2 METHODOLOGY

In order to carry this research, shipping emissions are provided to a Global Chemistry-Transport Model (MOZART-2 *[Horrowitz et al, 2003]*). MOZART-2 is a tropospheric chemical transport model accounting for the most important processes occurring in the lowermost part of the atmosphere. This version of the model calculates the global distribution of 63 gas-phase chemical species over a T63 (roughly equivalent to 1.875◦× 1.875◦) grid and 47 hybrid vertical levels ranging from the surface to about 10 hPa. In addition, the model time step for chemistry and transport is set to 15 minutes. As for the dynamical meteorological data, it is provided by ECMWF Operational data. Chemical species are transported by several physical processes. Advection is performed using a flux-form semi-Lagrangian scheme *[Lin and Rood, 1996]* with a pressure fixer. Vertical diffusion is assured by the Holstag and Boville parametrization *[Holtslag and Boville, 1993]* whereas convec-

* *Corresponding author:* Jérôme Hilaire, PhD Student, Dalton Research Institute, MMU, UK. Email: j.hilaire@mmu.ac.uk

tion is split into two schemes: deep convection *[Hack, 1994]* and shallow convection *[Zhang and McFarlene, 1995]*. Dry and wet depositions are also parameterized in the model. Stratospheric concentrations of 7 long-lived species are constrained by relaxation toward climatological values. Details on the treatment of the gas-phase chemical mechanisms and transport processes are described by *[Horrowitz et al, 2003]*.

The perturbed chemical specie values constitute then an input to a Radiative Transfer Model (Edwards & Slingo *[Edwards and Slingo, 1996]*) that estimates the change in the Earth's radiative balance and thus the impact on climate. Edwards&Slingo has been tested over a significant number of studies. Radiative fluxes are performed using the δ-Eddington form of the two-stream equations in both the short-wave and long-wave regions of the spectrum.

In this study, we use the emission dataset created for the new IMO Greenhouse study *[Ø. Buhaug et al, 2008-2009]*. We then run two 1-year spin-up simulations, one with the IMO emissions and the other one without. After this, we start the same two simulations but this time with initial conditions provided by the spin-up simulations.

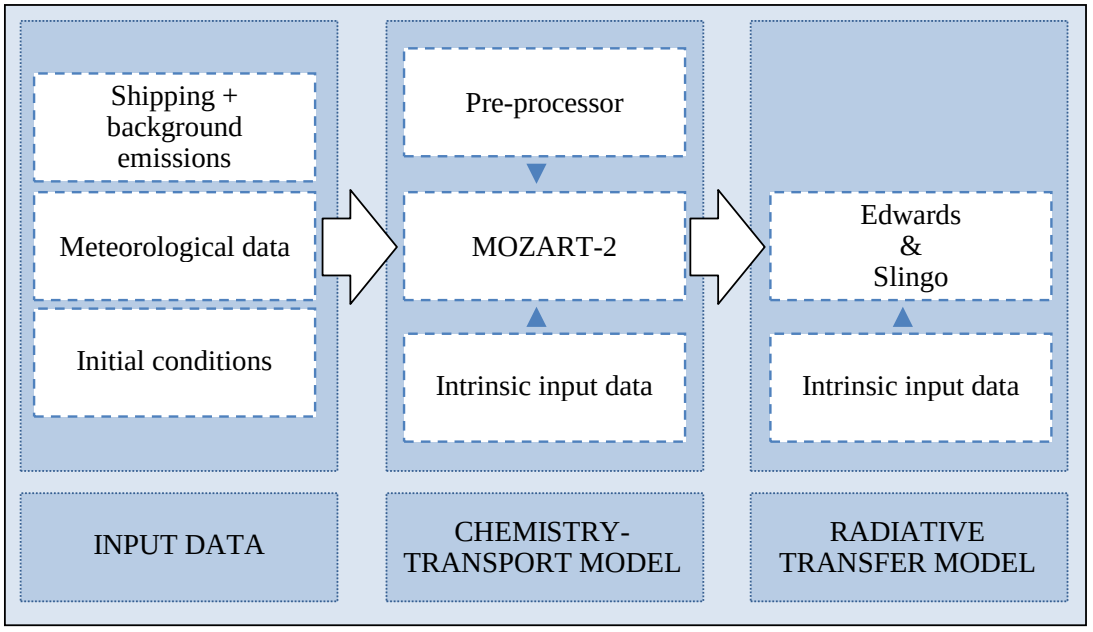

Fig 2.1 – Process flow chart

3 IMPACTS ON ATMOSPHERIC COMPOSITION AND CLIMATE

In this case study, emissions from the recent IMO report on Greenhouse gases are employed. These emissions are very different from previous studies. For instance, NO_x emissions are as high as 7.3 Tg(N)/yr which is almost twice the amount of nitrogen oxides used in the past (*[Eyring et al, 2005]*, *[Eyring et al, 2007]*). Volatile Organic Compounds (VOCs) are also very high (see **Fig 3.1**). Shipping NOx emissions correspond to about 15% of the total input NO_x emissions. Background emissions are from the GEMS study. Emission totals are in good agreement with the Fourth assessment report from the IPCC. Whereas spin-up simulations are run with prescribed methane lower-boundary concentrations, the following simulations account for CH4 emissions (516 Tg(CH_4)/yr).

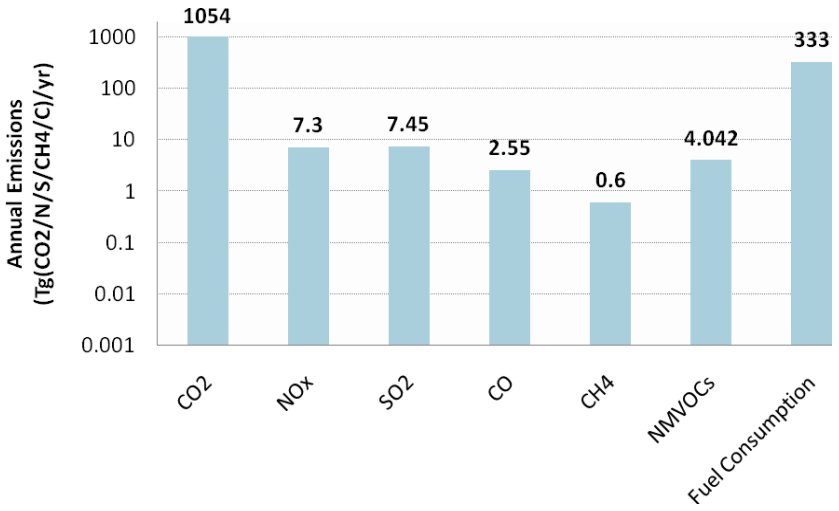

Fig 3.1 – Annual total shipping emissions for different chemical species. *[Source: IMO GHG Study 2009]*

The Ozone shipping perturbation resulting from the difference between the 2 simulations is consistent with previous studies *[Eyring et al, 2007]*. The pattern is also in good agreement (see **Fig 3.2)**. However, the impact on the Methane lifetime is quite significant. Indeed, according to the model, it could be reduced by about 0.9 year. This means that once Methane would reach steady state it could have been globally reduced by more than 250 ppbv. Even though this value is very high compare to the ones presented in Shipping part of the ATTICA report *[Eyring et al, 2009]*, it still belongs to the range of magnitude.

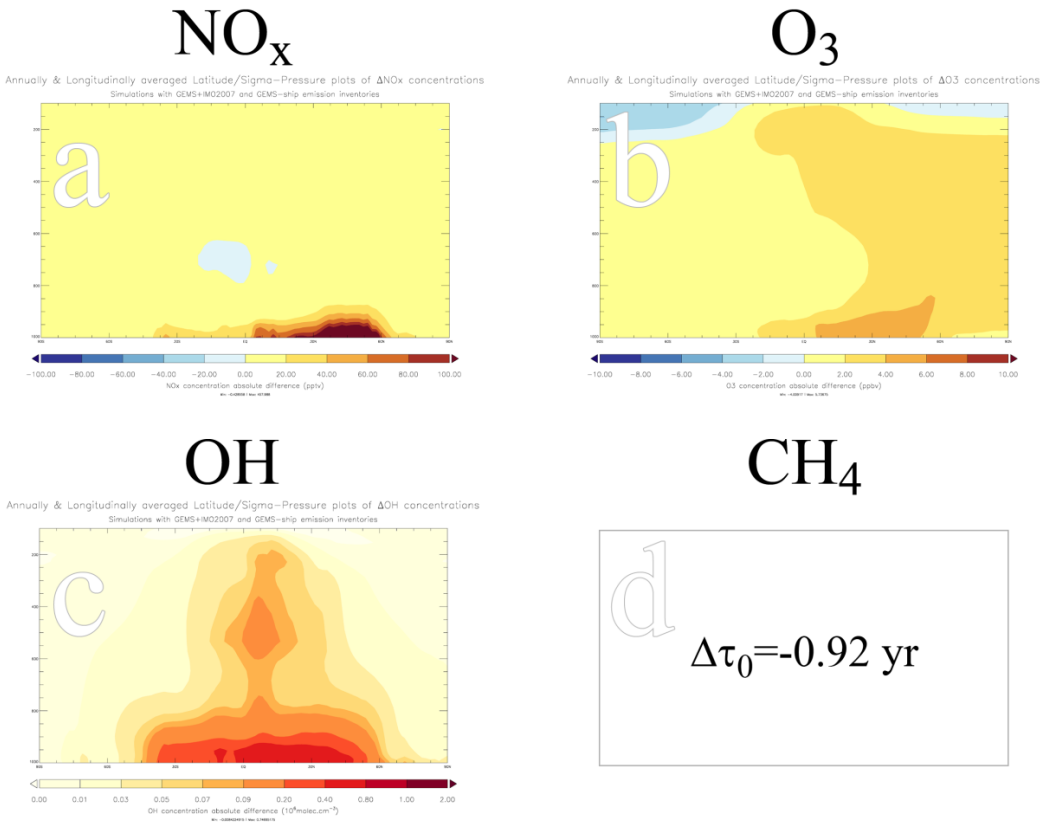

Fig 3.2 – Annual and longitudinal average of atmospheric chemical species. a. Nitrogen Oxides – b. Ozone – c. Hydroxyl radical – d. Methane lifetime

Because of the formation of Ozone and the depletion of Methane due to emissions of Nitrogen Oxides, the radiative forcing from shipping Ozone is positive whereas the radiative forcing of shipping Methane is negative. However, although global values are in the same range of magnitude, they do not cancel out as it can be seen on **Fig 3.3**

The latitudinal distribution clearly shows that the sum of the 2 contributions is mainly negative, But the values are quite different from one latitude to another (there is even some positive area in the North Pole).

Using LinClim *[Lim et al, 2005]* to normalize the results, we find a global radiative forcing from Ozone of 35mW/m2 and radiative forcing from Methane is -45mW/m2 (see **Fig 3.3**).

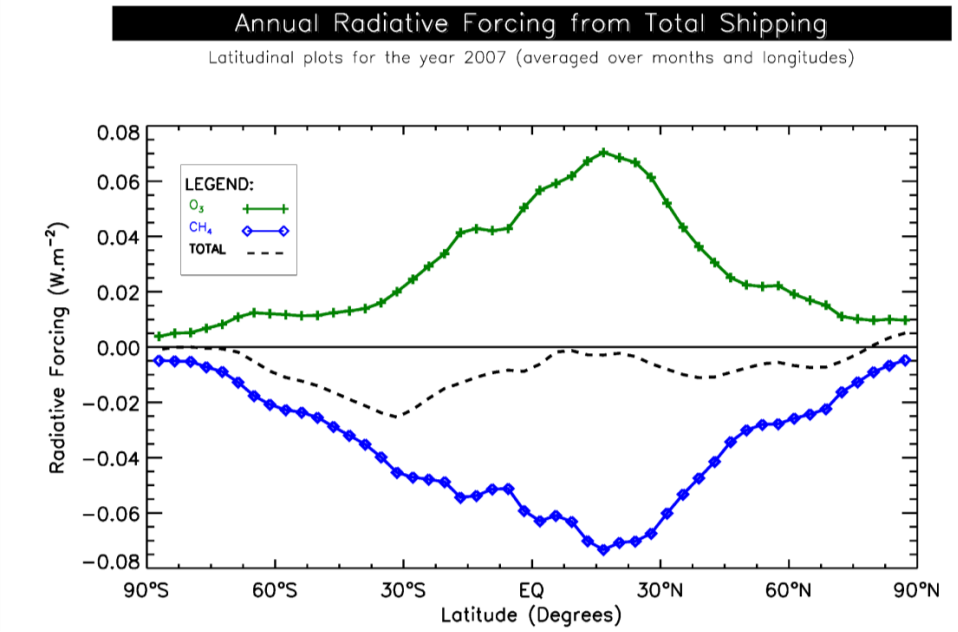

Fig 3.3 – Annual radiative forcing from total shipping in 2007.

4 CONCLUSIONS AND PERSPECTIVES

These results are rather high but they certainly reflect the large amount of emitted NO_x (about 2 times higher) and they are still in good agreement with previous studies, especially for Ozone. However the Methane lifetime perturbation might be overestimated. It would be interesting to look at the whole set of radiatively active components in the future to foresee the impacts of shipping.
A subgrid scale parametrization would probably reduce errors inherent to the use of coarse resolution modelling *[Franke et al, 2007]*, *[Cariolle and Pauli, 2009]*.
Implementing the recent findings on halogen-mediated ozone destruction in the model could also give a different atmospheric composition. And especially, it could lead to another ozone perturbation. *[Read et al, 2008]*

5 REFERENCES

[1] Ø. Buhaug et al, Updated Study on Greenhouse Gas Emissions from Ships: Phase 1 and 2 (2008-2009)

[2] J. J. Corbett et al, Mortality from Ship Emissions: A Global Assessment (2007)

[3] D. Cariolle et al, Parametrization of plume chemistry into large-scale atmospheric models: application to aircraft NO_x emissions (2009)

[4] J. M. Edwards and A. Slingo, Studies with a flexible new radiation code. I: Choosing a configuration for a large-scale model (1996)

[5] V. Eyring et al, Emissions from international shipping 1.Past 50 years (2005)

[6] V. Eyring et al, Multi-model simulations of the impact of international shipping..., (2007)

[7] V. Eyring et al, Transport impacts on atmosphere and climate: Shipping (2009)

[8] K. Franke et al, Towards Effective Emissions of Ships in Global Models (2007)

[9] J. Fuglestvedt et al, Climatic forcing of nitrogen oxides through changes in tropospheric ozone and methane; global 3D model studies (1999)

[10] L. L. Lim et al, Calculating radiative forcing and temperature changes from aviation effects with a climate response model (2005)

[11] K. Read et al, Extensive halogen-mediated ozone destruction over the tropical Atlantic Ocean (2008)

Can recent estimates of shipping NO_x emissions help to reduce current uncertainties in O_3 and CH_4 radiative forcings?

Jérôme D. Hilaire, David S. Lee & Ruben Rodríguez de León
Dalton Research Institute
Manchester Metropolitan University
Manchester, U.K.
Contact: j.hilaire@mmu.ac.uk

***Abstract*—A few studies have looked at the impacts of shipping nitrogen oxides (NO_x) on ozone (O_3) and methane (CH_4) radiative forcings. These studies made use of different methodologies, involving various models, parametrisations and input data, which lead to wide ranges of O_3 and CH_4 radiative forcings. These large uncertainties have been linked to uncertainties in shipping emissions, which magnitudes have spanned over a factor of 3 in the past. However, recent work by the International Maritime Organization (IMO) testifies of the emergence of a consensus value in shipping emissions, and shows also a significant reduction in these uncertainties. In the present study, a Global Transport-Chemistry Model (GCTM) and a Radiative Transfer Model (RTM) are set up to assess the impacts of the current range of shipping emission uncertainties. Shipping and anthropogenic background emissions are taken from recently developed IPCC-AR5 (5^{th} Assessment Report to the International Panel on Climate Change) emission inventory. This inventory combines both global and regional emissions and is therefore likely to be more accurate than previous global inventories. Uncertainty ranges in the magnitude and spatial distribution of shipping emissions are then applied in order to estimate the current range of uncertainty in O_3 and CH_4 radiative forcings. Average values of O_3 and CH_4 radiative forcings equal, respectively, 34.2 mW/m^2 and -56.5 mW/m^2, and are found in agreement with previously reported values. However, the resulting standard deviations $\pm$13.9 and $\pm$21.1 mW/m^2 as well as the range of radiative forcing values [16.8, 53.6] and [-86.3, -30.4] mW/m^2 tend to be larger than those previous studies. This highlights the extreme importance to further reduce uncertainties in shipping emissions with view to decrease uncertainties in shipping-induced radiative forcings.**

***Keywords*-shipping; NO_x emissions; uncertainty; radiative forcing; O_3; CH_4**

I. Introduction

International shipping constitutes a cornerstone of the global economy. Indeed, since the beginning of the industrial revolution, shipping has significantly contributed to the growth in the world trade. Today, about 50,000 ships carry more than 90% of the world trade [1]. Unsurprisingly, the International Maritime Organization claims that "without shipping, half the world would freeze and the other half would starve."

Despite being an efficient mode of transport, especially when compared to aviation and road transport, it consumes large amounts of fossil fuels and releases, as a consequence, significant quantities of greenhouse gases, greenhouse gas precursors and particulate matter into the troposphere.

Among these gases, carbon dioxide (CO_2) is predominantly emitted, but emissions of nitrogen oxides (NO_x) remain of great importance, because they also have an influence on the Earth's climate. Indeed, through complex physical and chemical processes, these emissions will lead to regional enhancements of ozone (O_3) levels and a wide-spread depletion of methane (CH_4) concentrations. O_3 and CH_4 are both greenhouse gases and will therefore perturb the climate. In addition, the magnitude of NO_x emissions are significant. A recent study by the IMO estimated these emissions to reach 5.4 Tg(N)/yr in 2000 [2], corresponding to nearly 15% of all anthropogenic and natural emissions [3]. However, the Kyoto Protocol (KP) from the United Nations Convention on Climate Change (UNFCCC), which is an international binding instrument designed to curb emissions of greenhouse gases and their precursors, does not currently cover emissions from ships [4]. Instead, because of the complexity of the shipping system and the difficulty to create regulations that would suit both the established UNFCCC and the IMO policies, the KP has assigned this task to the IMO. Unfortunately, the international maritime body has not come up with a solution yet.

In order to estimate the impacts from changes in greenhouse gas concentrations, scientists have designed a metric called radiative forcing. Radiative forcing provides a measure of the impact a greenhouse gas has in altering the Earth's radiative budget. Since it is proportional to surface temperature, this metric is very useful for policy makers because it can provide information about climate change. Previous estimates of O_3 and CH_4 radiative forcing from shipping NO_x emissions bear a lot of uncertainties [5], [6], [7], [8]. This uncertainty which is perhaps as high as 67% has been linked to the spread in the magnitude and the spatial distribution of shipping emissions [9].

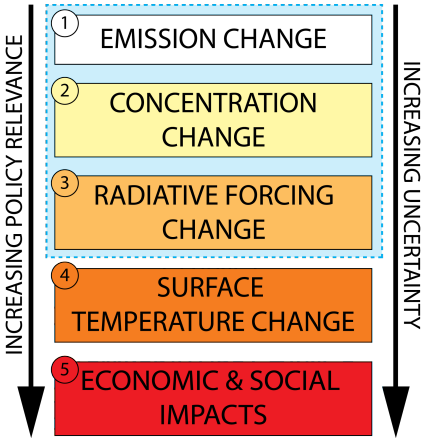

Figure 1. Diagram showing the increase of uncertainty and policy relevance with the advance of a climate impact study. The area highlighted in blue contains the steps treated in this study [10].

Nevertheless, radiative forcing values reported in previous studies were calculated using different methodologies , models and input data. In a effort to better estimate the impacts of shipping NO_x emission uncertainties on O_3 and CH_4 radiative forcings, the current range of shipping emission uncertainty is used as input to a state-of-the-art global chemistry-transport model (GCTM) and a radiative transfer model (RTM). Although the use of a single model could introduce a bias in the results, this modelling approach should allow for a more consistent view of the impacts of this range of uncertainty.

II. Methodology

The methodology employed in this study follows the simple step-by-step approach described in Fig. 1. First, recent estimates of global anthropogenic and natural emissions are used to produce several emission inventories. These inventories are then processed by a GCTM to calculate concentration changes of O_3 and CH_4 in the troposphere. These resulting perturbations are finally computed by using a RTM in order to estimate their corresponding radiative forcings.

A. Emission data

In this study, a total of 6 emission inventories, representative of the year 2000, have been created. Firstly, an emission inventory is generated by merging the recent anthropogenic emissions developed for the fifth IPCC Assessment Report [11] with natural emissions from the POET (Precursors of Ozone and their Effects in the Troposphere) [12], [13] and GEIA (Global Emissions Inventory Activity) [14] datasets. Shipping emissions have been taken from [9]. Shipping NO_x emissions have a magnitude of 5.4 Tg(N)/yr and are spatially distributed using ICOADS (International Comprehensive Ocean-Atmosphere Data Set) data. The five other emission inventories are all derived from the one described above. Two of them are produced by scaling to the extrema of the uncertainty range in magnitude found in Eyring et al. [9]. Two others are created by applying the AMVER (Automated Mutual-Assistance Vessel Rescue System) and the averaged AMVER/ICOADS spatial distributions taken from Wang et al. [15]. Finally, the reference case is built by removing shipping emissions.

B. Global chemistry-transport model

MOZART-4 [16] is a 3D global chemistry-transport model designed for calculating concentrations of gas and particulate matter in the troposphere. The most important processes occurring in that region (e.g. emissions, advection, diffusion, convection, photochemistry and heterogeneous chemistry, dry and wet depositions, cloud processes and lightning) are resolved, providing values which are usually found in good agreement with observations and other GCTM [17], [18], [19]. This version of MOZART-4 runs on a (approximately) 2.8°x2.8° horizontal grid with 28 vertical levels. It accounts for 86 gas-phase species and 12 aerosols. Furthermore, it is driven by offline meteorological fields from the NCEP (National Centers for Environmental Prediction) reanalysis dataset corresponding to the year 2000.

Prior to each simulation, a spin-up run of 1 year is performed so as to set short-and-medium-lived species into equilibrium. In order to calculate gas concentration changes due to shipping emissions, the difference between a simulation with shipping emissions and the reference simulation without shipping emissions was computed. Therefore, a total of 5 cases are considered in this study: *ship* which refers to the case using the default IPCC emission inventory, *ship_hb* that identifies the case with the high bound value of the magnitude range, *ship_lb* that identifies the case with the low bound value of the magnitude range, *ship_amver* which refers to the case using the emission inventory with AMVER spatial distribution and *ship_am-ic* which refers to the case using the emission inventory with the averaged AMVER/ICOADS spatial distribution (see Table I).

C. Radiative transfer model

The Edwards & Slingo RTM [20] computes the changes in the Earth's radiative budget on a 3D grid. The O_3 and CH_4 perturbations from MOZART-4 are prescribed to this model, which calculates the resulting changes in incoming and outgoing shortwave and longwave radiations at the tropopause. Radiative forcings of these species can thus be estimated. This version of the model does not take stratospheric adjustments of temperatures into account. Instead, impacts from these adjustments on the O_3 radiative forcing

Table I
ANNUAL TOTAL SHIPPING NO_X EMISSIONS AND ANNUAL AVERAGES OF O_3 BURDEN CHANGE, CH_4 LIFETIME AND THEIR CORRESPONDING RADIATIVE FORCINGS IN THE DIFFERENT SIMULATION CASES (SEE SECTION II.A). [1]VALUE IS EXTRAPOLATED (SEE SECTION III.B). [2]LIFETIME CHANGE AFTER 1 YEAR. [3]CALCULATION ACCOUNTS FOR CH_4 LIFETIME EQUILIBRIUM STATE (SEE SECTION III.A).

#	Simulation case	NO_x [Tg(N)]	ΔO_3 [Tg]	$\Delta\tau_{CH_4}$[2] [yr]	O_3 RF [mW/m^2]	CH_4 RF[3] [mW/m^2]
1	ship	5.4	10.5	-0.75	28.2	-47.9
2	ship_hb	10.4	17.6	-1.19	48.1	-77.9
3	ship_lb	3.0	6.4	-0.48	16.8	-30.4
4	ship_amver	5.4	11.9	-0.85	33.7	-54.5
5	ship_am-ic	5.4	11.4	-0.81	31.2	-51.8
6	ship_am-hb*[1]	10.4	19.4	-1.32	53.6	-86.3
7	ship_am-lb*[1]	3.0	8.3	-0.62	22.5	-39.4
8	ship_ai-hb*[1]	10.4	18.9	-1.28	52.2	-83.6
9	ship_ai-lb*[1]	3.0	7.8	-0.58	21.1	-36.7
	Mean	-	12.5	-0.88	34.2	-56.5
	Std. dev.	-	5.0	0.31	13.9	21.1

are estimated by reducing its radiative forcing by 22% following the work of Stevenson et al. [21]. This is done to enable comparison of our results to values in previous studies.

III. RESULTS AND DISCUSSION

The results described hereafter present the changes in concentrations and radiative forcings in the different shipping perturbation cases (see Table I).

A. Atmospheric composition

Globally, emissions of 5.4 Tg of nitrogen yields about 10 Tg of O_3 in the troposphere. Although the chemical system involved in O_3 production is non linear, it is worthy to note that globally, this response is almost linear over the studied range of emission values, as shown on Table I. Due to its relatively short lifetime, strongest perturbations are found near the ship lanes exhibiting regional patterns. The magnitude of these perturbations are similar to that reported by other researchers [5], [6]. Nevertheless, maximum concentrations are found in the Northern Pacific Ocean in all cases while they usually found maximum values in the Northern Atlantic Ocean. The production of O_3 is very sensitive to the amount of NO_x and volatile organic compounds (VOC) present in the background atmosphere. This difference in maximum location could be due to the effect of the long-range transport of precursors from Asia and North America. Non negligible amounts of O_3 also reach the top of the troposphere. In particular, in the tropical regions, where transport by convection is significant. Besides, Fig. 2 provides a good example of how the O_3 perturbation in the upper troposphere depends on the spatial distribution of shipping emissions. The zonal average at the top of Fig. 2 (a) shows the strongest perturbation. This is a consequence of the AMVER spatial distribution which has a denser shipping traffic in the tropics than ICOADS (c). The plot in the middle of Fig. 2 (b) is the result of the combined AMVER and ICOADS spatial distributions and presents, therefore, the characteristics of both geospatial proxies. This is of importance since the molecules of O_3 present at the top of the troposphere, near the tropopause, have a greater impact on the Earth's radiative budget than molecules of the same species in the middle or at the bottom of the troposphere.

As for CH_4, this gas species has a long lifetime of about 12 years. The 1-year simulations performed in this study cannot capture the entire response of CH_4. Instead, the lifetime perturbation resulting after a year is used to calculate the equilibrium state following the work of Fuglestvedt et al. [22]. The reduction of CH_4 stems indirectly from the production of O_3, which in turn enhance levels of hydroxyl radicals (OH). These radicals constitute the main removal pathway for CH_4 and hence, a depletion of this gas occurs. The simulation case with 3 Tg of nitrogen emitted in the atmosphere is very similar to the simulations in Eyring et al., 2007 [6]. However, the lifetime perturbation found in the present study is much stronger. This could be due to a number of parametrisations in the GCTM such as, stratospheric-tropospheric ozone fluxes, boundary layer venting out, photochemistry, ... Again, the response of the system remains linear with a correlation factor of over 99%.

B. O_3 and CH_4 radiative forcing

Enhanced O_3 levels in the troposphere lead to a positive O_3 radiative forcing, whereas the reduction in CH_4 lifetime yields a negative CH_4 radiative forcing. These radiative forcings are of similar magnitude. However, they do not necessarily cancel out as shown previously by Hilaire et al. [23]. In the *ship* case, the O_3 radiative forcing is found slightly above the mean value of 21 mW/m^2 reported by Eyring et al. [9]. The range of O_3 radiative forcing values provided by the other cases shows a shift towards higher values. The CH_4 radiative forcing has a smaller value than the mean in Eyring et al. which equals -27 mW/m^2 [9], but again remain within the range of values reported in the literature. The range of CH_4 values is also shifted but towards smaller values. In addition, the difference between the O_3 and CH_4 radiative forcings in this study is nearly three times as high as in [9]. This discrepancy could be explained by differences in photochemical calculations and emissions. However, in absolute values, the negative forcing from CH_4 is larger than the positive radiative forcing from O_3 which is in good agreement with the general tendency [9]. It is also worthy to note that the global annual average of O_3 and CH_4 radiative forcings are both correlated to the global annual average of O_3 burden and CH_4 lifetime

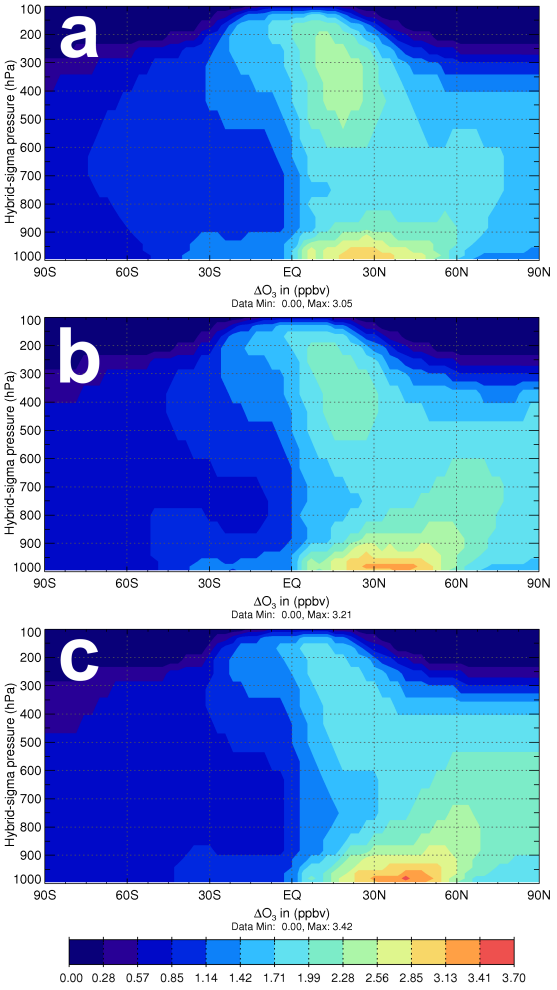

Figure 2. Zonal averages of O_3 volume mixing ratios in parts per billion in volume (ppbv) annually averaged in 3 simulation cases: AMVER (a), AMVER-ICOADS (b) and ICOADS (c)

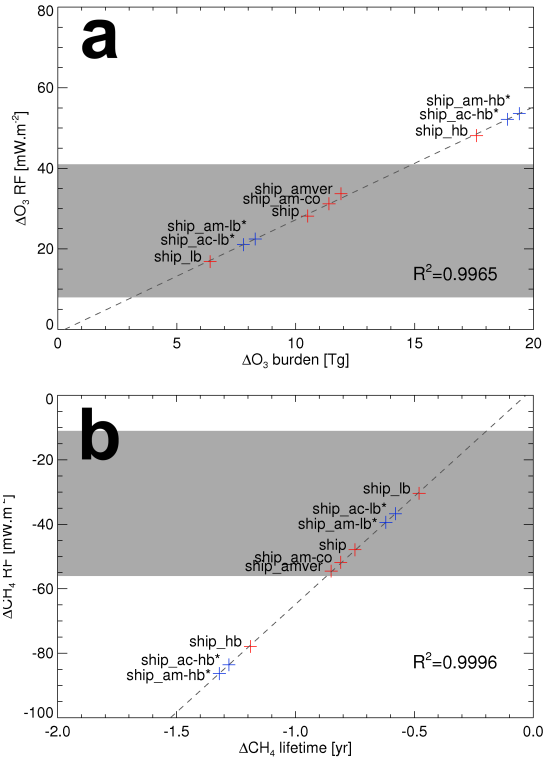

Figure 3. Plots showing the correlation between O_3 radiative forcing and O_3 burden change (a) and CH_4 radiative forcing and CH_4 lifetime change(b). The red crosses correspond to the cases calculated with the GCTM and the RTM. The blue cross corresponds to the cases with interpolation or extrapolation. The grey area shows the range of estimates reported in previous studies [9].

respectively (see Fig. 3).

C. Uncertainty

In order to calculate the maximum impact from ship emissions, a few other cases, in which the magnitudes from the *ship_hb* and *ship_lb* cases would be applied to the spatial distribution from the *ship_amver* and *ship_am-co* cases, would actually be required. However, due to limited amount of time, this value was estimated by interpolation and extrapolation of the other cases values. These cases are defined as *ship_am-hb**, *ship_am-lb**, *ship_ai-hb** and *ship_ai-lb** (see Table I). It is assumed that the GCTM stays in a linear regime of global O_3 production, which seems to be the case for this particular range of emissions. The largest extrapolated value is about 10% higher than the largest value computed with the modelling framework and should therefore be close to the linear tendency.

For instance, the O_3 and CH_4 linear tendencies between the *ship*, *ship_hb* and *ship_lb* cases for O_3 and CH_4 are calculated. By applying them to the *ship_amver* case, this gave a maximum O_3 burden change of 19.4 Tg and a minimum CH_4 lifetime change of -1.32 yr. Similarly, the linear tendencies are calculated for the radiative forcings which yielded estimates of 53.6 mW/m^2 and -86.3 mW/m^2 for O_3 and CH_4, respectively.

Finally, the means and standard deviations are calculated from the range of O_3 and CH_4 radiative forcing values (see Table I). These are found to be 34.2$\pm$13.9 and -56.5$\pm$21.1 mW/m^2, respectively. These results present larger mean values and even larger standard deviations compared to the

work of Fuglesdvedt et al. [7], which reported 32±9 and -43±13. This can be explained by the lower NO_x emission rate of 4.4 Tg(N)/yr and the smaller range of emission uncertainties used in that study. Moreover, the ranges of radiative forcing values calculated in the present study [16.8, 53.6] and [-86.3, -30.4] mW/m^2 for O_3 and CH_4 respectively are much wider than that reported by Eyring et al. [8.0, 41.0] and [-56.0, -11.0] mW/m^2 for O_3 and CH_4 respectively [9]. It is worthy to note that in the case of CH_4, the lifetime and radiative forcing values found in this study display a tendency to higher values, compared to previous studies. This could be due to a number of parametrisations in the GCTM as explained in section III.A.

IV. Conclusion and perspectives

In this study, we used the recently developed anthropogenic emission inventory from Lamarque et al. [11] in conjunction with the POET [12], [13] and GEIA [14] datasets, as well as uncertainty ranges in shipping emissions from [9], [15] in order to create an ensemble of emission inventories. Then, we calculated, via a GCTM, the changes in O_3 concentrations and CH_4 lifetimes due to the shipping emission perturbations. Finally, we computed the radiative forcings of O_3 and CH_4 resulting from these changes. These radiative forcing means 34.2±13.9 and -56.5±21.1 mW/m^2, respectively, are found in good agreement with the work of Fuglestvedt et al. [7], but somewhat exhibit a much widespread range of uncertainty. Consequently, the current range of shipping emission uncertainties cannot help to reduce uncertainties in O_3 and CH_4 radiative forcings. This stresses the great importance of emissions in estimating radiative forcings. The development of AIS (Automated Information System), that includes a Global Positioning System present onboard ships, as well as substantial progress made in satellite data retrieval should help to reduce the uncertainty in spatial distribution in the coming years. However, focus should be put upon uncertainty in the magnitude of emissions. This uncertainty comes from several factors such as emission factors and fuel consumption. While NO_x emission factors are known today with relatively good accuracy, fuel consumption from shipping remains rather uncertain. For instance, fuel consumption for the year 2000 currently ranges roughly between 201 Tg and 289 Tg [9]. AIS could improve to shorten the gap, but better monitoring methodologies would also be required to reduce this range of estimates.

Acknowledgement

The authors would like to thank the Department for Transport for funding this project (PPRO 00/4/054/005) and the reviewers for their useful comments.

References

[1] Shipping Facts website, *Shipping and World Trade*, [online] Available at: http://www.marisec.org/shippingfacts/worldtrade/.

[2] International Maritime Organization (IMO), *Second IMO GHG Study 2009*, Ø. Buhaug, J. J. Corbett, Ø. Endresen, J. Faber, S. Hanayama, D. S. Lee, D. Lee, H. Lindstad, A. Z. Markowska, A. Mjelde, D. Nelissen, J.Nilsen, C. Pålsson, J. J. Winebrake, W.-Q. Wu and K. Yoshida, London, UK, April 2009.

[3] Intergovernmental Panel on Climate Change (IPCC), *Climate Change 2007: The Physical Science Basis. Contribution of Working Group 1 to the Fourth Assessment Report of the Intergovernmental Panel on Climate Change*, S. Solomon, D. Qin, M. Manning, Z. Chen, M. Marquis, K.B. Avery, M. Tignor and H.L. Miller, Eds. Cambridge University Press, Cambridge, United Kingdom & New York, USA, 2007.

[4] United Nations (UN), *Kyoto Protocol to the United Nations Framework Convention on Climate Change*, [online] Available at: http://unfccc.int/resource/docs/convkp/kpeng.pdf, 1998.

[5] Ø. Endresen, E. Sørgard, J. K. Sundet, S. B. Dalsøren, I. S. A. Isaksen, T. F. Berglen and G. Gravir *Emission from international sea transportation and environmental impact*, Journal of Geophysical Research, vol. 108, no. D17, 4560, doi:10.1029/2002JD002898, 2003.

[6] V. Eyring, D. S. Stevenson, A. Lauer, F. J. Dentener, T. Butler, W. J. Collins, K. Ellingsen, M. Gauss, D. A. Hauglustaine, I. S. A. Isaksen, M. G. Lawrence, A. Richter, J. M. Rodriguez, M. Sanderson, S. E. Strahan, K. Sudo, S. Szopa, T. P. C. van Noije and O. Wild *Multi-model simulations of the impact of international shipping on Atmospheric Chemistry and Climate in 2000 and 2030*, Atmos. Chem. Phys., 7, 757-780, 2007.

[7] J. S. Fuglestvedt, T. K. Berntsen, G. Myhre, K. Rypdal and R. Bieltvedt Skeie, *Climate forcing from the transport sectors*, Proceedings of the National Academy of Sciences USA 105, 454-458, 2007.

[8] D. S. Lee, L. Lim, V. Eyring, R. Sausen, Ø. Endresen and H.-L. Behrens *Radiative forcing and temperature response from shipping*, Proceedings of the TAC-Conference, Oxford, UK, 2006.

[9] V. Eyring, I. S. A. Isaksen, T. Berntsen, W. J. Collins, J. J. Corbett, Ø. Endresen, R. G. Grainger, J. Moldanova, H. Schlager and David S. Stevenson *Transport impacts on atmosphere and climate: Shipping*, Atmospheric Environment, 44, 37, 4735-4771, 2009.

[10] J. S. Fuglestvedt, T. K. Berntsen, O. Godal, R. Sausen, K. P. Shine and T. Skodvin, *Metrics of Climate Change: Assessing Radiative Forcing and Emissions Indices*, Climate Change, 58, 267-331, 2003.

[11] J.-F. Lamarque, T. C. Bond, V. Eyring, C. Granier, A. Heil, Z. Klimont, D. Lee, C. Liousse, A. Mieville, B. Owen, M. G. Schultz, D. Shindell, S. J. Smith, E. Stehfest, J. Van Aardenne, O. R. Cooper, M. Kainuma, N. Mahowald, J. R. McConnell, V. Naik, K. Riahi, and D. P. van Vuuren *Historical (1850-2000) gridded anthropogenic and biomass burning emissions of reactive gases and aerosols: methodology and application*, Atmos. Chem. Phys., 10, 7017-7039, 2010.

[12] C. Granier, J.-F. Lamarque, A. Mieville, J. F. Müller, J. Olivier, J. Orlando, J. Peters, G. Petron, G. Tyndall and S. Wallens *POET, a database of surface emissions of ozone precursors*, available on internet at http://www.aero.jussieu.fr/projet/ACCENT/POET.php, 2005.

[13] J. Olivier, J. Peters, C. Granier, G. Pétron, J. F. Müller and S. Wallens *Present and future surface emissions of atmospheric compounds, POET report #2*, EU project EVK2-1999-00011, 2003.

[14] R. J. Andres and A. D. Kasgnoc *A time-averaged inventory of subaerial volcanic sulfur emissions*, Journal of Geophysical Research 103, 25, 251-25, 261, 1998

[15] C. Wang, J. J. Corbett and J. Firestone *Improving Spatial Representation of Global Ship Emissions Inventories*, Environ. Sci. Technol. 2008, 42, 193199, 2008.

[16] L. K. Emmons, S. Walters, P. G. Hess, J.-F. Lamarque, G. G. Pfister, D. Fillmore, C. Granier, A. Guenther, D. Kinnison, T. Laepple, J. Orlando, X. Tie, G. Tyndall, C. Wiedinmyer, S. L. Baughcum, and S. Kloster *Description and evaluation of the Model for Ozone and Related chemical Tracers, version 4 (MOZART-4)*, Geosci. Model Dev., 3, 4367, 2010.

[17] F. Dentener, D. Stevenson, K. Ellingsen, et al. *Global Atmospheric Environment for the next generation*, Environ. Sci. Technol., 40, 35863594, 2006.

[18] D. S. Stevenson, F. Dentener, M. Schultz, et al. *Multimodel ensemble simulations of present-day and near-future tropospheric ozone*, J. Geophys. Res., 111, D08301, doi:10.1029/2005JD006338, 2006.

[19] D. T. Shindell, G. Faluvegi, D. Stevenson, et al. *Multimodel simulations of carbon monoxide: Comparison with observations and projected near-future changes*, J. Geophys. Res., 111, D19306, doi:10.1029/2006JD007100, 2006.

[20] J. M. Edwards and A. Slingo *Studies with a flexible new radiation code. I: Choosing a configuration for a large-scale model*, Q. J. R. Meteorol. Soc., 122, 689-719, 1996.

[21] D. S. Stevenson, C. E. Johnson, W. J. Collins, R. G. Derwent, K. P. Shine, and J. M. Edwards *Evolution of tropospheric ozone radiative forcing*, Geophys. Res. Lett., 25, 38193822, 1998.

[22] J. S. Fuglestvedt, T. K. Berntsen, I. S. A. Isaksen, H. Mao, X.-Z. Liang and W.-C. Wang, *Climatic forcing of nitrogen oxides through changes in tropospheric ozone and methane: global 3D model studies*, Atmospheric Environment, 33, 961-977, 1999.

[23] J. D. Hilaire, D. S. Lee and R. Rodriguez de Leon *Do radiative forcings of methane and ozone cancel out? - A case study from the last IMO Greenhouse gases study*, TAC-2 Proceedings, June 22nd to 25th, Aachen and Maastricht, Germany and The Netherlands, 2009.

[24] S. B. Dalsøren, , Ø. Endresen, I.S.A. Isaksen, G. Gravir, E. Sørgard, *Environmental impacts of the expected increase in sea transportation, with a particular focus on oil and gas scenarios for Norway and northwest Russia*, Journal of Geophysical Research 112, D02310, 2007.

Bibliography

H. Agrawal, Q. G. J. Malloy, W. A. Welch, J. W. Miller, and D. R. Cocker III. In-use gaseous and particulate matter emissions from a modern oceangoing container vessel. *Atmospheric Environment*, 42(21):5504–5510, July 2008a. ISSN 1352-2310. doi: 10.1016/j.atmosenv.2008.02.053.

H. Agrawal, W. A. Welch, J. W. Miller, and D. R. Cocker. Emission measurements from a crude oil tanker at sea. *Environmental Science & Technology*, 42(19): 7098–7103, Oct. 2008b. doi: 10.1021/es703102y.

H. Agrawal, R. Eden, X. Zhang, P. M. Fine, A. Katzenstein, J. W. Miller, J. Ospital, S. Teffera, and D. R. Cocker. Primary particulate matter from ocean-going engines in the southern california air basin. *Environmental Science & Technology*, 43(14):5398–5402, July 2009. doi: 10.1021/es8035016.

R. Andres and A. Kasgnoc. A time-averaged inventory of subaerial volcanic sulfur emissions. *Journal of Geophysical Research*, 103:25251–25261, 1998.

M. Auvray and I. Bey. Long-range transport to europe: Seasonal variations and implications for the european ozone budget. *Journal of Geophysical Research*, 110, June 2005. doi: 10.1029/2004JD005503.

S. Beirle, U. Platt, R. von Glasow, M. Wenig, and T. Wagner. Estimate of nitrogen oxide emissions from shipping by satellite remote sensing. *Geophysical Research Letters*, 31(18), 2004. ISSN 0094-8276. doi: 10.1029/2004GL020312.

G. Bonan, S. Levis, S. Sitch, M. Vertenstein, and K. Oleson. A dynamic global vegetation model for use with climate models: concepts and description of simulated vegetation dynamics. *Global Change Biology*, 9:1543–1566, 2003. doi: 10.1046/j.1529-8817.2003.00681.x.

T. C. Bond, E. Bhardwaj, R. Dong, R. Jogani, S. Jung, C. Roden, D. G. Streets, and N. M. Trautmann. Historical emissions of black and organic carbon aerosol from energy-related combustion. *Global Biogeochemical Cycles*, 21, 2007. doi: doi:10.1029/2006GB002840.

A. F. Bouwman, L. J. M. Boumans, and N. H. Batjes. Modeling global annual N_2O and NO emissions from fertilized fields. *Global Biogeochemical Cycles*, 16, 2002. doi: 10.1029/2001GB001812.

G. Brasseur, J. Orlando, and G. Tyndall. *Atmospheric Chemistry and Global Change*. Oxford University Press, 1999.

G. P. Brasseur, J.-F. Müller, and C. Granier. Atmospheric impact of NO_x emissions by subsonic aircraft: A three-dimensional model study. *Journal of Geophysical Research*, 101(D1):1423–1428, 1996.

G. P. Brasseur, D. A. Hauglustaine, S. Walters, P. J. Rasch, J.-F. Müller, C. Granier, and X. Tie. MOZART: a global chemical transport model for ozone and related chemical tracers 1. model description. *Journal of Geophysical Research*, 103(D21), 1998.

C. A. Briggs. Discussion: Chimney plumes in neutral and strable surroundings. *Atmospheric Environment*, 6:507–510, 1972.

P. N. Brown, G. D. Hyrne, and A. C. Hindmarch. VODE, a variable-coefficient ODE solver. *SIAM journal on Scientific and Statistical Computing*, 1989.

Ø. Buhaug, J. J. Corbett, Ø. Endresen, V. Eyring, J. Faber, S. Hanayama, D. S. Lee, D. Lee, H. Lindstad, A. Z. Markowska, A. Mjelde, D. Nelissen, J. Nilsen, C. Pålsson, J. J. Winebrake, W.-Q. Wu, and K. Yoshida. Second IMO GHG

study 2009. Technical report, International Maritime Organisation (IMO), London (UK), April 2009.

N. Butkovskaya, A. Kukui, N. Pouvesle, and G. L. Bras. Formation of nitric acid in the gas-phase HO_2 + NO reaction: Effects of temperature and water vapor. *Journal of Physical Chemistry*, Jul 2005. doi: 10.1021/jp051534v.

D. Cariolle, M. J. Evans, M. P. Chipperfield, N. Butkovskaya, A. Kukui, and G. L. Bras. Impact of the new HNO_3-forming channel of the HO_2+NO reaction on tropospheric HNO_3, NO_x, HO_x and ozone. *Atmospheric Chemistry and Physics*, page 40614068, 2008.

D. Cariolle, D. Caro, R. Paoli, D. A. Hauglustaine, B. Cuénot, A. Cozic, and R. Paugam. Parameterization of plume chemistry into large scale atmospheric models: Application to aircraft NO emissions. *Journal of Geophysical Research*, 114(D19), 2009. ISSN 0148-0227. doi: 10.1029/2009JD011873.

C. L. Charlton-Perez, M. J. Evans, J. H. Marsham, and J. G. Esler. The impact of resolution on ship plume simulations with NO_x chemistry. *Atmospheric Chemistry and Physics*, 9(19):7505–7518, Oct. 2009. ISSN 1680-7316.

G. Chen, L. G. Huey, M. Trainer, D. Nicks, J. Corbett, T. Ryerson, D. Parrish, J. A. Neuman, J. Nowak, D. Tanner, J. Holloway, C. Brock, J. Crawford, J. R. Olson, A. Sullivan, R. Weber, S. Schauffler, S. Donnelly, E. Atlas, J. Roberts, F. Flocke, G. Hübler, and F. Fehsenfeld. An investigation of the chemistry of ship emission plumes during ITCT 2002. *Journal of Geophysical Research*, 110, May 2005. doi: 10.1029/2004JD005236.

F. Chosson, R. Paoli, and B. Cu'enot. Ship plume dispersion rates in convective boundary layers for chemistry models. *Atmospheric Chemistry and Physics*, 8 (16):4841–4853, 2008. ISSN 1680-7316.

I. Cionni, V. Eyring, J. F. Lamarque, W. J. Randel, D. S. Stevenson, F. Wu, G. E. Bodeker, T. G. Shepherd, D. T. Shindell, and D. W. Waugh. Ozone database in support of cmip5 simulations: results and corresponding radiative forcing.

Atmospheric Chemistry and Physics Discussions, 11(4):10875–10933, 2011. doi: 10.5194/acpd-11-10875-2011.

L. Clarke, J. Edmonds, H. Jacoby, H. Pitcher, J. Reilly, and R. Richels. Scenarios of greenhouse gas emissions and atmospheric concentrations. Technical report, Sub-report 2.1a of Synthesis and Assessment Product 2.1. Climate Change Science Program and the Subcommittee on Global Change Research, Washington D.C., 2007.

J. Cofala, M. Amann, Z. Klimont, K. Kupiainen, and L. Höglund-Isaksson. Scenarios of global anthropogenic emissions of air pollutants and methane until 2030. *Atmospheric Environment*, 41:84868499, 2007. doi: doi:10.1016/j.atmosenv.2007.07.010.

B. Collins, M. Sanderson, and C. Johnson. Impact of increasing ship emissions on air quality and deposition over europe by 2030. *Meteorologische Zeitschrift*, 18 (1):025–039, 2008.

J. J. Corbett. New directions: Designing ship emissions and impacts research to inform both science and policy. *Atmospheric Environment*, 37(33):4719–4721, 2003.

J. J. Corbett and H. W. Köhler. Updated emissions from ocean shipping. *Journal of Geophysical Research*, 108(D20), 2003. ISSN 0148-0227. doi: 10.1029/2003JD003751.

J. J. Corbett, J. J. Winebrake, E. H. Green, P. Kasibhatla, V. Eyring, and A. Lauer. Mortality from ship emissions: A global assessment. *Environmental Science & Technology*, 41(24):8512–8518, Dec. 2007. doi: 10.1021/es071686z.

J. J. Corbett, D. A. Lack, J. J. Winebrake, S. Harder, J. A. Silberman, and M. Gold. Arctic shipping emissions inventories and future scenarios. *Atmospheric Chemistry and Physics*, page 96899704, 2010. doi: 10.5194/acp-10-9689-2010.

P. J. Crutzen. The influence of nitrogen oxides on the atmospheric ozone content. *Quarterly Journal of the Royal Meteorological Society*, 96:320–325, 1970.

S. B. Dalsøren, Ø. Endresen, I. S. A. Isaksen, G. Gravir, and E. Sørgård. Environmental impacts of the expected increase in sea transportation, with a particular focus on oil and gas scenarios for norway and northwest russia. *Journal of Geophysical Research*, 112(D2), 2007. ISSN 0148-0227. doi: 10.1029/2005JD006927.

S. B. Dalsøren, M. S. Eide, Ø. Endresen, A. Mjelde, G. Gravir, and I. S. A. Isaksen. Update on emissions and environmental impacts from the international fleet of ships: the contribution from major ship types and ports. *Atmospheric Chemistry and Physics*, 9(6):2171–2194, Mar. 2009. ISSN 1680-7316.

S. B. Dalsøren, M. S. Eide, G. Myhre, Ø. Endresen, I. S. A. Isaksen, and J. S. Fuglestvedt. Impacts of the large increase in international ship traffic 2000-2007 on tropospheric ozone and methane. *Environmental Science & Technology*, 44 (7):2482–2489, 2010. doi: 10.1021/es902628e. PMID: 20210355.

D. D. Davis, G. Grodzinsky, P. Kasibhatla, J. Crawford, G. Chen, S. Liu, A. Bandy, D. Thornton, H. Guan, and S. Sandholm. Impact of ship emissions on marine boundary layer NO_x and SO_2 distributions over the pacific basin. *Geophysical Research Letters*, 28(02):235–238, 2001. doi: 10.1029/.

A. J. DeCaria, K. E. Pickering, G. L. Stenchikov, and L. E. Ott. Lightning-generated NO_x and its impact on tropospheric ozone production: A three-dimensional modeling study of a stratosphere-troposphere experiment: Radiation, aerosols and ozone (STERAO-A) thunderstorm. *Journal of Geophysical Research*, July 2005.

R. Derwent. Trace gases and their relative contribution to the greenhouse effect. Technical report, Atomic Energy Research Establishment, Harwell, Oxon, UK, 1990.

B. N. Duncan, J. J. West, Y. Yoshida, A. M. Fiore, and J. R. Ziemke. The influence of European pollution on ozone in the Near East and northern Africa. *Atmospheric Chemistry and Physics*, 8:2267–2283, Apr. 2008.

J. M. Edwards and A. Slingo. Studies with a flexible new radiation code I: choosing a configuration for a large-scale model. *Q. J. R. Meteorol. Soc.*, 122:689–719, 1996.

L. K. Emmons, D. A. Hauglustaine, J.-F. Müller, M. A. Carroll, G. P. Brasseur, D. Brunner, J. Staehelin, V. Thouret, and A. Marenco. Data composites of airborne observations of tropospheric ozone and its precursors. *Journal of Geophysical Research*, 105:20497–20538, 2000.

L. K. Emmons, E. C. Apel, J.-F. Lamarque, P. G. Hess, M. Avery, D. Blake, W. Brune, T. Campos, J. Crawford, P. F. DeCarlo, S. Hall, B. Heikes, J. Holloway, J. L. Jimenez, D. J. Knapp, G. Kok, M. Mena-Carrasco, J. Olson, D. OSullivan, G. Sachse, J. Walega, P. Weibring, A. Weinheimer, and C. Wiedinmyer. Impact of mexico city emissions on regional air quality from MOZART-4 simulations. *Atmospheric Chemistry and Physics*, 2010a.

L. K. Emmons, S. Walters, P. G. Hess, J.-F. Lamarque, G. G. Pfister, D. Fillmore, C. Granier, A. Guenther, D. Kinnison, T. Laepple, J. Orlando, X. Tie, G. Tyndall, C. Wiedinmyer, S. L. Baughcum, and S. Kloster. Description and evaluation of the model for ozone and related chemical tracers, version 4 (MOZART-4). *Geoscience Model Development*, 3:43–67, 2010b.

Ø. Endresen, E. Sørgård, J. K. Sundet, S. B. Dalsøren, I. S. A. Isaksen, T. F. Berglen, and G. Gravir. Emission from international sea transportation and environmental impact. *Journal of Geophysical Research*, 108(D17), 2003. ISSN 0148-0227. doi: 10.1029/2002JD002898.

Ø. Endresen, E. Sørgård, H. L. Behrens, P. O. Brett, and I. S. A. Isaksen. A historical reconstruction of ships' fuel consumption and emissions. *Journal of Geophysical Research*, 112(D12), 2007. ISSN 0148-0227. doi: 10.1029/2006JD007630.

EPA. Analysis of commercial marine vessels emissions and fuel consumption data. Technical report, EPA, 2000.

J. G. Esler. An integrated approach to mixing sensitivities in tropospheric chemistry: A basis for the parameterization of subgrid-scale emissions for chemistry

transport models. *Journal of Geophysical Research*, 108(D20), 2003. ISSN 0148-0227. doi: 10.1029/2003JD003627.

M. J. Evans and D. J. Jacob. Impact of new laboratory studies of N_2O_5 hydrolysis on global model budgets of tropospheric nitrogen oxides, ozone, and OH. *Geophysical Research Letters*, 32, 2005. doi: 10.1029/2005GL022469.

V. Eyring, H. W. Köhler, A. Lauer, and B. Lemper. Emissions from international shipping: 2. impact of future technologies on scenarios until 2050. *Journal of Geophysical Research*, 110(D17), 2005a. ISSN 0148-0227. doi: 10.1029/2004JD005620.

V. Eyring, H. W. Kohler, J. van Aardenne, and A. Lauer. Emissions from international shipping: 1. the last 50 years. *Journal of Geophysical Research*, 110 (D17), 2005b. ISSN 0148-0227. doi: 10.1029/2004JD005619.

V. Eyring, D. S. Stevenson, A. Lauer, F. J. Dentener, T. Butler, W. J. Collins, K. Ellingsen, M. Gauss, D. A. Hauglustaine, I. S. A. Isaksen, M. G. Lawrence, A. Richter, J. M. Rodriguez, M. Sanderson, S. E. Strahan, K. Sudo, S. Szopa, T. P. C. van Noije, and O. Wild. Multi-model simulations of the impact of international shipping on atmospheric chemistry and climate in 2000 and 2030. *Atmospheric Chemistry and Physics*, 7(3):757–780, Feb. 2007. ISSN 1680-7316.

V. Eyring, I. S. Isaksen, T. Berntsen, W. J. Collins, J. J. Corbett, Ø. Endresen, R. G. Grainger, J. Moldanov'a, H. Schlager, and D. S. Stevenson. Transport impacts on atmosphere and climate: Shipping. *Atmospheric Environment*, In Press, Corrected Proof, 2009. ISSN 1352-2310. doi: 10.1016/j.atmosenv.2009.04.059.

P. Forster, V. Ramaswamy, P. Artaxo, T. Bernsten, and T. Betts. Changes in atmospheric constituents and in radiative forcing. in: Solomon, S., Qin, D., Manning, M., Chen, Z., Marquis, M., et al. (Eds.), climate change 2007: The physical science basis. contribution of working group I to the fourth assessment report of the intergovernmental panel on climate change. Technical report,

IPCC, Cambridge University Press, United Kingdom and New York, NY, USA., 2007.

K. Franke, V. Eyring, R. Sander, J. Hendricks, A. Lauer, and R. Sausen. Toward effective emissions of ships in global models. *Meteorologische Zeitschrift*, 17(2): 117–129, 2008. doi: 10.1127/0941-2948/2008/0277.

J. Freiberg. The iron catalyzed oxidation of SO_2 to acid sulphate mist in dispersing plumes. *Atmospheric Environment*, 10:121–130, 1976.

J. S. Fuglestvedt, T. K. Berntsen, O. Godal, R. Sausen, K. P. Shine, and T. Skodvin. Metrics of climate change: Assessing radiative forcing and emissions indices. *Climate Change*, pages 267–331, 2003.

J. S. Fuglestvedt, T. K. Berntsen, G. Myhre, K. Rypdal, and R. B. Skeie. Climate forcing from the transport sectors. *Proceedings of the National Academy of Sciences*, 105(2):454–458, Jan. 2008. doi: 10.1073/pnas.0702958104.

J. S. Fuglestvedt, K. P. Shine, T. Berntsen, J. Cook, D. S. Lee, A. Stenke, R. B. Skeie, G. J. M. Velders, and I. A. Waitz. Transport impacts on atmosphere and climate: Metrics. *Atmospheric Environment*, 2009. doi: 10.1016/j.atmosenv.2009.04.044.

J. N. Galloway, F. J. Dentener, D. G. Capone, E. W. Boyer, R. W. Howarth, S. P. Seitzinger, G. P. Asner, C. C. Cleveland, P. A. Green, and E. A. Holland. Nitrogen cycles: Past, present, and future. *Biogeochemistry*, 70:153–226, 2004. doi: 10.1007/s10533-004-0370-0.

L. Ganzeveld, D. Helmig, C. W. Fairall, J. Hare, and A. Pozzer. Atmosphere-ocean ozone exchange: A global modeling study of biogeochemical, atmospheric, and waterside turbulence dependencies. *Global Biogeochemical Cycles*, 23, 2009. doi: 10.1029/2008GB003301.

M. Gauss, I. S. A. Isaksen, D. S. Lee, and O. A. Sovde. Impact of aircraft NO_x emissions on the atmosphere tradeoffs to reduce the impact. *Atmospheric Chemistry and Physics*, 6:1529–1548, 2006.

C. W. Gear. *Numerical Initial Value Problem in Ordinary Differential Equations*. Prentice Hall PTR, Upper Saddle River, NJ, USA, 1971.

F. Giorgi and W. L. Chameides. The rainout parameterization in a photochemical model. *Journal of Geophysical Research*, 90:7872–7880, 1985.

L. Goldsworthy. Design of ship engines for reduced emissions of oxides of nitrogen. Technical report, Flame Marine Diagnostic, 2002.

C. Granier, J.-F. Lamarque, A. Mieville, J.-F. Müller, J. Olivier, J. Orlando, J. Peters, G. Petron, G. Tyndall, and S. Wallens. Poet, a database of surface emissions of ozone precursors. available on internet at http://www.aero.jussieu.fr/projet/ACCENT/POET.php, 2005.

C. Granier, U. Niemeier, J. H. Jungclaus, L. Emmons, P. Hess, J.-F. Lamarque, S. Walters, and G. P. Brasseur. Ozone pollution from future ship traffic in the arctic northern passages. *Geophysical Research Letters*, 33(13), 2006. ISSN 0094-8276. doi: 10.1029/2006GL026180.

A. Grant, C. S. Witham, P. G. Simmonds, A. J. Manning, and S. O'Doherty. A 15 year record of high-frequency, in-situ measurements of hydrogen at mace head. *Atmospheric Chemistry and Physics*, 10:1203–1214, 2010.

V. Grewe and A. Stenke. Airclim: an efficient tool for climate evaluation of aircraft technology. *Atmospheric Chemistry and Physics*, pages 4621–4639, 2008.

V. Grewe, M. Dameris, C. Fichter, and D. Lee. Impact of aircraft NO_x emissions. part 2: Effects of lowering the flight altitude. *Meteorologische Zeitschrift*, 11: 197–205, 2002a.

V. Grewe, M. Dameris, C. Fichter, and R. Sausen. Impact of aircraft NO_x emissions. part 1: Interactively coupled climate-chemistry simulations and sensitivities to climate-chemistry feedback, lightning and model resolution. *Meteorologische Zeitschrift*, 11:177–186, 2002b.

A. Guenther, T. Karl, P. Harley, C. Wiedinmyer, P. Palmer, and C. Geron. Estimates of global terrestrial isoprene emissions using megan (model of emissions of gases and aerosols from nature). *Atmospheric Chemistry and Physics*, 2006.

J. J. Hack. Parameterization of moist convection in the national center for atmospheric research community climate model (CCM2). *Journal of Geophysical Research*, 99(D3):5541–5568, 1994.

S. R. Hanna, G. A. Briggs, and R. P. Hosker Jr. Handbook on atmospheric diffusion. Technical report, Department of Energy, 1982.

S. R. Hanna, L. L. Schulman, R. J. Paine, J. Pleim, and M. Baer. Development and evaluation of the offshore and coastal dispersion model. *J. Air Pollut. Control Assoc.*, page 10391047, 1985.

J. Hansen, M. Sato, and R. Ruedy. Radiative forcing and climate response. *Journal of Geophysical Reseach*, 102:6831–6861, 1997.

P. Hess and J. Lamarque. Ozone source attribution and its modulation by the arctic oscillation during the spring months. *Journal of Geophysical Research*, 112, 2007. doi: 10.1029/2006JD007557.

H. Hidalgo and P. Crutzen. The tropospheric and stratospheric composition perturbed by NO_x emissions of high-altitude aircraft. *Journal of Geophysical Research*, 82:5833–5866, 1977.

J. Hilaire, D. S. Lee, and R. Rodriguez-de-Leon. Do radiative forcings of methane and ozone cancel out? - a case study from the last IMO greenhouse gas study. In *Proceedings of the TAC-2 conference*, 2009.

P. V. Hobbs, T. J. Garrett, R. J. Ferek, S. R. Strader, D. A. Hegg, G. M. Frick, W. A. Hoppel, R. F. Gasparovic, L. M. Russell, D. W. Johnson, C. O'Dowd, P. A. Durkee, K. E. Nielsen, and G. Innis. Emissions from ships with respect to their effects on clouds. *Journal of the Atmospheric Sciences*, 57(16):2570–2590, aug 2000.

Ø. Hodnebrog, T. K. Berntsen, O. Dessens, M. Gauss, V. Grewe, I. S. A. Isaksen, B. Koffi, G. Myhre, D. Olivi'e, M. J. Prather, J. A. Pyle, F. Stordal, S. Szopa, Q. Tang, P. van Velthoven, J. E. Williams, , and K. Ødemark1. Future impact of non-land based traffic emissions on atmospheric ozone and OH an optimistic scenario and a possible mitigation strategy. *Atmospheric Chemistry and Physics Discussions*, 11:16801–16859, 2011a. doi: 10.5194/acpd-11-16801-2011.

Ø. Hodnebrog, F. Stordal, and T. K. Berntsen. Does the resolution of megacity emissions impact large scale ozone? *Atmospheric Environment*, 45:6852–6862, Dec 2011b. doi: 10.1016/j.atmosenv.2011.01.012.

M. Höök, A. Sivertsson, and K. Aleklett. Validity of the fossil fuel production outlooks in the ipcc emission scenarios. *Natural Resources Research*, 19, 2010.

P. Hoor, J. Borken-Kleefeld, D. Caro, O. Dessens, O. Endresen, M. Gauss, V. Grewe, D. Hauglustaine, I. S. A. Isaksen, P. Jöckel, J. Lelieveld, G. Myhre, E. Meijer, D. Olivie, M. Prather, C. S. Poberaj, K. P. Shine, J. Staehelin, Q. Tang, J. van Aardenne, P. van Velthoven, and R. Sausen. The impact of traffic emissions on atmospheric ozone and OH: results from QUANTIFY. *Atmospheric Chemistry and Physics*, 9(9):3113–3136, May 2009. ISSN 1680-7316.

L. W. Horowitz, S. Walters, D. L. Mauzerall, L. K. Emmons, P. J. Rasch, C. Granier, X. Tie, J.-F. Lamarque, M. G. Schultz, and G. S. Tyndall. A global simulation of tropospheric ozone and related tracers: Description and evaluation of MOZART version 2. *Journal of Geophysical Research*, 108(D24): 4784, 2003.

A. A. M. Hosltag and B. A. Boville. Local versus nonlocal boundary-layer diffusion in a global climate model. *Journal of Climate*, 6:1825–1842, Oct. 1993.

J. T. Houghton, Y. Ding, D. J.Griggs, M. Noguer, P. J. van der Linden, and D. Xiaoxu. Intergovernmental panel on climate change (IPCC): 2001, climate change 2001 - the scientific basis. Technical report, Intergovernmental Panel on Climate Change (IPCC), Cambridge University Press, UK, 2001.

P. Huszár, D. Cariolle, R. Paoli, T. Halenka, M. Belda, H. Schlager, J. Miksovsky, and P. Pisoft. Modeling the regional impact of ship emissions on NO_x and ozone levels over the eastern atlantic and western europe using ship plume parameterization. *Atmospheric Chemistry and Physics*, 10:6645–6660, July 2010. doi: 10.5194/acp-10-6645-2010.

ICS. International shipping: Life blood of world trade. CD-ROM, 2009.

IMO. Amendments to the technical code on control of emission of nitrogen oxides from marine diesel engines (NO_x technical code 2008). Resolution, 2008. Adopted on 10 October 2008.

IMO. Marine environment protection committee (MEPC) 62nd session: 11 to 15 july 2011. Technical report, International Maritime Organisation, 2011.

I. S. A. Isaksen, Ø. Hov, and E. Hesstvedt. Ozone generation over rural areas. *Environmental Science and Technology*, 12:1279–1284, 1978.

D. J. Jacob. Heterogeneous chemistry and tropospheric ozone. *Atmospheric Environment*, 34:2131–2159, 2000.

C. Junker and C. Liousse. A global emission inventory of carbonaceous aerosol from historic records of fossil fuel and biofuel consumption for the period. *Atmospheric Chemistry and Physics*, 8:11951207, 2008. doi: doi:10.5194/acp-8-1195-2008.

E. Kalnay, M. Kanamitsu, R. Kistler, W. Collins, D. Deaven, L. Gandin, M. Iredell, S. Saha, G. White, J. Woollen, Y. Zhu, M. Chelliah, W. Ebisuzaki, W. Higgins, J. Janowiak, K. C. Mo, C. Ropelewski, J. Wang, A. Leetmaa, R. Reynolds, R. Jenne, and D. Joseph. The NCEP/NCAR 40-year reanalysis project. *Bulletin of American Meteorological Society*, 77:437–471, 1996.

P. Kasibhatla, H. Levy, W. J. Moxim, S. N. Pandis, J. J. Corbett, M. C. Peterson, R. E. Honrath, G. J. Frost, K. Knapp, D. D. Parrish, and T. B. Ryerson. Do emissions from ships have a significant impact on concentrations of nitrogen

oxides in the marine boundary layer? *Geophysical Research Letters*, 27(15), 2000.

H. S. Kim, C. H. Song, R. S. Park, G. Huey, and J. Y. Ryu. Investigation of ship-plume chemistry using a newly-developed photochemical/dynamic ship-plume model. *Atmospheric Chemistry and Physics*, 9(19):7531–7550, Oct. 2009. ISSN 1680-7316.

D. E. Kinnison, G. P. Brasseur, S. Walters, R. R. Garcia, D. R. Marsh, F. Sassi, V. L. Harvey, C. E. Randall, L. Emmons, and J.-F. Lamarque. Sensitivity of chemical tracers to meteorological parameters in the MOZART-3 chemical transport model. *Journal of Geophysical Research*, 112, 2007.

R. Kistler, E. Kalny, and W. Collins. The NCEP-NCAR 50-year reanalysis: Monthly means CD-ROM and documentation. *Bulletin of American Meteorological Society*, 82:247–267, 2001.

B. Koffi, S. Szopa, A. Cozic, D. Hauglustaine, and P. van Velthoven. Present and future impact of aircraft, road traffic and shipping emissions on global tropospheric ozone. *Atmospheric Chemistry and Physics*, 10:11681–11705, Dec. 2010. doi: 10.5194/acp-10-11681-2010.

J. Kowalski and W. Tarelko. NO_x emission from a two-stroke ship engine: Part 1 - modeling aspect. *Applied Thermal Engineering*, 29, 2009. doi: 10.1016/j.applthermaleng.2008.06.032.

A. Lacis, D. Wuebbles, and J. A. Logan. Radiative forcing of climate by changes in the vertical distribution of ozone. *Journal of Geophysical Research*, 95:9971–9981, 1990.

J.-F. Lamarque, P. Hess, L. Emmons, L. Buja, W. Washington, and C. Granier. Tropospheric ozone evolution between 1890 and 1990. *Journal of Geophysical Research*, 110, 2005.

J.-F. Lamarque, T. C. Bond, C. G. V. Eyring and, A. Heil, Z. Klimont, D. Lee, C. Liousse, A. Mieville, B. Owen, M. G. Schultz, D. Shindell, S. J. Smith,

E. Stehfest, J. Van Aardenne, O. R. Cooper, M. Kainuma, N. Mahowald, J. R. McConnell, V. Naik, K. Riahi, and D. P. van Vuuren. Historical (18502000) gridded anthropogenic and biomass burning emissions of reactive gases and aerosols: methodology and application. *Atmospheric Chemistry and Physics*, 10, 2010. doi: doi:10.5194/acp-10-7017-2010.

M. G. Lawrence and P. J. Crutzen. Influence of NO_x emissions from ships on tropospheric photochemistry and climate. *Nature*, 402(6758):167–170, Nov. 1999. ISSN 0028-0836. doi: 10.1038/46013.

M. G. Lawrence, P. Jöckel, and R. von Kuhlmann. What does global mean OH concentration tell us? *Atmospheric Chemistry and Physics*, pages 37–49, 2001.

D. S. Lee, L. Lim, V. Eyring, R. Sausen, Ø. Endresen, and H. Behrens. Radiative forcing and temperature response from shipping. In *Aviation, Atmosphere and Climate (TAC-1) Proceedings*, 2006.

S. J. Lin and R. B. Rood. Multidimensional flux-form semi-lagrangian transport schemes. *Monthly Weather Review*, 124(9):2046–2070, 1996.

X. Lin, M. Trainer, and S. Liu. On the nonlinearity of the tropospheric ozone production. *Journal of Geophysical Research*, 93:1587915888, 1988.

S. Liu, M. Trainer, F. Fehsenfeld, D. Parrish, E. Williams, D. Fahey, G. Hübler, and P. Murphy. Ozone production in the rural troposphere and the implications for regional and global ozone distributions. *Journal of Geophysical Research*, 92:4191–4207, 1987.

J. A. Logan, M. J. Prather, S. C. Wofsy, and M. B. McElroy. Tropospheric chemistry: A global perspective. *Journal of Geophysical research*, 86:7210–7254, 1981.

H. M. Markowitz. The elimination form of the inverse and its application to linear programming. *Management Science*, 3, Apr 1957.

T. Masui, K. M. K, Y. Hijioka, T. Kinoshita, T. Nozawa, S. Ishiwatari, E. Kato, P. Shukla, Y. Yamagata, and M. Kainuma. A emission pathway to stabilize at 6 W/m^2 of radiative forcing. *Climatic Change*, 2010.

Y. Matsumi, F. Comes, G. Hancock, A. Hofzumahaus, A. Hynes, M. Kawasaki, and A. Ravishankara. Quantum yields for production of $O(^1D)$ in the ultraviolet photolysis of ozone: Recommendation based on evaluation of laboratory data. *Journal of Geophysical Research*, 107(D3), 2002. doi: 10.1029/2001JD000510.

O. T. Melo, M. Lusis, and R. Stevens. Mathematical modelling of dispersion and chemical reactions in a plume - oxidation of no to NO_2 in the plume of a power plant. *Atmospheric Environment*, 12:1231–1234, 1978.

A. Miola and B. Ciuffo. Estimating air emissions from ships: Meta-analysis of modelling approaches and available data sources. *Atmospheric Environment*, 45:2242–2251, 2011.

K. Miyashita, M. Kawano, M. Motomura, Y. Nojiri, K. Ota, M. Shinohara, T. Takagi, Y. Yamada, and H. Yamato. Research study: The world's changing maritime industry and a vision for japan. Technical report, Ocean Policy Research Foundation, 2008. A pdf file for this report is available in English at http://www.sof.or.jp/en/topics/08_04.php.

J. Moldanová. Report on ship plume simulations and analysis - deliverable d2.1.3.5 to project quantify. Technical report, IVL, April 2010.

J. Moldanová, E. Fridell, O. Popovicheva, B. Demirdjian, V. Tishkova, A. Faccinetto, and C. Focsa. Characterisation of particulate matter and gaseous emissions from a large ship diesel engine. *Atmospheric Environment*, 43(16):2632–2641, May 2009. ISSN 1352-2310. doi: 10.1016/j.atmosenv.2009.02.008.

R. H. Moss, J. A. Edmonds, K. A. Hibbard, M. R.Manning, S. K. Rose, D. P. van Vuuren, imothy R. Carter, S. Emori, M. Kainuma, T. Kram, G. A. Meehl, J. F. B. Mitchell, N. Nakicenovic, K. Riahi, S. J. Smith, R. J. Stouffer, A. M. Thomson, J. P. Weyant, and T. J. Wilbanks. The next generation of scenarios

for climate change research and assessment. *Nature*, 463:747–756, 2010. doi: 10.1038/nature08823.

G. Myhre, M. Kvalevåg, G. Rädel, J. Cook, K. Shine, H. Clark, F. Karcher, K. Markowicz, A. Kardas, P. Wolkenberg, Y. Balkanski, M. Ponater, P. Forster, A. Rap, and R. Rodriguez De Leon. Intercomparison of radiative forcing calculations of stratospheric water vapour and contrails. *Meteorologische Zeitschrift*, 18:585–596, 2009.

G. Myhre, K. Shine, G. Rädel, M. Gauss, I. Isaksen, Q. Tang, M. Prather, J. Williams, P. van Velthoven, O. Dessens, B.Koffi, S. Szopa, P. Hoor, V. Grewe, J. Borken-Kleefeld, T. Berntsen, and J. Fuglestvedt. Radiative forcing due to changes in ozone and methane caused by the transport sector. *Atmospheric Environment*, 45:387–394, 2011.

N. Nakicenovic, O. Davidson, G. Davis, A. Grbler, T. Kram, E. L. L. Rovere, B. Metz, T. Morita, W. Pepper, H. Pitcher, A. Sankovski, P. Shukla, R. Swart, R. Watson, and Z. Dadi. Special report on emission scenarios. Technical report, Intergovernmental Panel on Climate Change (IPCC), Cambridge University Press, UK, 2000.

R. Nassar, J. A. Logan, H. M. Worden, I. A. Megretskaia, K. W. Bowman, G. B. Osterman, A. M. Thompson, D. W. Tarasick, S. Austin, H. Claude, M. K. Dubey, W. K. Hocking, B. J. Johnson, E. Joseph, J. Merrill, G. Morris, M. Newchurch, S. J. Oltmans, F. Posny, F. J. Schmidlin, H. Vömel, D. N. Whiteman, and J. C. Witte. Validation of tropospheric emission spectrometer (TES) nadir ozone profiles using ozonesonde measurements. *Journal of Geophysical Research*, 113, May 2008. doi: 10.1029/2007JD008819.

J. Neu and M. Prather. Toward a more physical representation of precipitation scavenging in global chemistry models: cloud overlap and ice physics and their impact on tropospheric ozone. *Atmospheric Chemistry and Physics Discussions*, 2011. doi: 10.5194/acpd-11-24413-2011.

K. Ødemark, S. B. Dalsøren, B. H. Samset, T. K. Berntsen, J. S. Fuglestvedt, and G. Myhre. Short lived climate forcers from current shipping and petroleum activities in the arctic. *Atmospheric Chemistry and Physics Discussions*, pages 21569–21599, 2011. doi: 10.5194/acpd-11-21569-2011.

J. Olivier. Description of edgar version 2.0. a set of global emission inventories of greenhouse gases and ozone-depleting substances for all anthropogenic and most natural sources on a per country bases and on 1°x1° grid. Technical report, RIVM (National Institute of Public Health and the Environment, Bilthoven, 1996.

J. Olivier and J. Berdowski. *Global emissions sources and sinks, in: The climate system*. Swets & Zeitlinger Publishers, Lisse, The Netherlands, 2001.

G. Osterman, S. Kulawik, H. Worden, N. Richards, B. Fisher, A. Eldering, M. Shephard, L. Froidevaux, G. Labow, M. Luo, R. Herman, K. Bowman, and A. M. Thompson. Validation of tropospheric emission spectrometer (TES) measurements of the total, stratospheric and tropospheric column abundance of ozone. *Journal of Geophysical Research*, 113, May 2008. doi: 10.1029/2007JD008801.

M. Park, W. J. Randel, D. E. Kinnison, R. R. Garcia, and W. Choi. Seasonal variation of methane, water vapor and nitrogen oxides near the tropopause: Satellite observations and model simulations. *Journal of Geophysical Research*, 109, 2004.

M. Park, W. J. Randel, L. K. Emmons, and N. J. Livesey. Transport pathways of carbon monoxide in the asian summer monsoon diagnosed from model of ozone and related tracers (MOZART). *Journal of Geophysical Research*, 2009.

T. W. Patzek and G. D. Croft. A global coal production forecast with multi-Hubbert cycle analysis. *Energy*, 35:3109–3122, 2010.

A. Paxian, V. Eyring, W. Beer, R. Sausen, and C. Wright. Present-day and future global bottom-up ship emission inventories including polar routes. *Environmental Science & Technology*, 44(4):1333–1339, 2010. doi: 10.1021/es9022859. PMID: 20088494.

G. P. Peters, T. B. Nilssen, L. Lindholt, M. S. Eide, S. Glomsrød, L. I. Eide, and J. S. Fuglestvedt. Future emissions from shipping and petroleum activities in the arctic. *Atmospheric Chemistry and Physics*, 11:53055320, 2011. doi: 10.5194/acp-11-5305-2011.

H. Petry, J. Hendricks, M. Mollhoff, E. Lippert, A. Meier, A. Ebel, and R. Sausen. Chemical conversion of subsonic aircraft emissions in the dispersing plume: Calculation of effective emission indices. *Journal of Geophysical Research*, 103: 5759–5772, 1998.

G. G. Pfister, L. K. Emmons, P. G. Hess, R. Honrath, J.-F. Lamarque, M. Val Martin, R. C. Owen, M. A. Avery, E. V. Browell, J. S. Holloway, P. Nedelec, R. Purvis, T. B. Ryerson, G. W. Sachse, and H. Schlager. Ozone production from the 2004 north american boreal fires. *Journal of Geophysical Research*, 111, 2006.

G. G. Pfister, L. K. Emmons, P. G. Hess, J.-F. Lamarque, J. J. Orlando, S. Walters, A. Guenther, P. I. Palmer, and P. J. Lawrence. Contribution of isoprene to chemical budgets: A model tracer study with the NCAR CTM MOZART-4. *Journal of Geophysical Research, in press*, 2008a.

G. G. Pfister, L. K. Emmons, P. G. Hess, J.-F. Lamarque, A. M. Thompson, and J. E. Yorks. Analysis of the summer 2004 ozone budget over the united states using intercontinental transport experiment ozonesonde network study (IONS) observations and model of ozone and related tracers (MOZART-4) simulations. *Journal of Geophysical Research*, 2008b.

K. Pickering, Y. Wang, W.-K. Tao, C. Price, and J.-F. Müller. Vertical distributions of lightning NO_x for use in regional and global transport models. *Journal of Geophysical research*, 103:31203–21216, 1998.

C. Price, J. Penner, and M. Prather. NO_x from lightning 1. global distribution based on lightning physics. *Journal of Geophysical Research*, 102:5929–5941, 1997.

V. Ramanathan, L. Callis, R. Cess, J. Hansen, I. Isaksen, W. Kuhn, A. Lacis, F. Luther, J. Mahlman, R. Reck, and M. Schlesinger. Climate-chemical interactions and effects of changing atmospheric trace gases. *Reviews of Geophysics*, 25(7):1441–1482, 1987.

P. Rasch and J. Kristjansson. A comparison of the CCM3 model climate using diagnosed and predicted condensate parameterizations. *Journal of Climate*, pages 1587–1614, 1998.

P. J. Rasch, N. M. Mahowald, and B. E. Eaton. Representations of transport, convection, and the hydrologic cycle in chemical transport models: Implications for the modeling of short-lived and soluble species. *Journal of Geophysical Research*, 102:28217–28138, 1997.

K. A. Read, A. S. Mahajan, L. J. Carpenter, M. J. Evans, B. V. E. Faria, D. E. Heard, J. R. Hopkins, J. D. Lee, S. J. Moller, A. C. Lewis, L. Mendes, J. B. McQuaid, H. Oetjen, A. Saiz-Lopez, M. J. Pilling, and J. M. C. Plane. Extensive halogen-mediated ozone destruction over the tropical atlantic ocean. *NATURE*, 453:1232–1235, 2008. doi: 10.1038/nature07035.

K. Riahi, A. Grübler, and N. Nakicenovic. Scenarios of long-term socio-economic and environmental development under climate stabilization. *Technological Forecasting and Social Change*, pages 887–935, 2007.

K. Riahi, V. Krey, S. Rao, V. Chirkov, G. Fischer, P. Kolp, G. Kindermann, N. Nakicenovic, and P. Rafai. RCP-8.5: Exploring the consequence of high emission trajectories. *Climatic Change*, 2010.

N. A. D. Richards, G. B. Osterman, E. V. Browell, J. W. Hair, M. Avery, and Q. Li. Validation of tropospheric emission spectrometer ozone profiles with aircraft observations during the intercontinental chemical transport experimentb. *Journal of Geophysical Research*, 113, May 2008. doi: 10.1029/2007JD008815.

A. Richter, V. Eyring, J. P. Burrows, H. Bovensmann, A. Lauer, B. Sierk, and P. J. Crutzen. Satellite measurements of NO_2 from international shipping emissions. *Geophysical Research Letters*, 31(23), 2004. ISSN 0094-8276. doi: 10.1029/2004GL020822.

B. Ridley, K. Pickering, and J. Dye. Comments on the parameterization of lightning-produced NO in global chemistry-transport models. *Atmospheric Environment*, 39:6184–6187, 2005.

S. Sander, R. Friedl, A. Ravishankara, D. Golden, C. Kolb, M. Kurylo, M. Molina, G. Moortgat, B. Finlayson-Pitts, P. Wine, R. Huie, and V. Orkin. Chemical kinetics and photochemical data for use in atmospheric studies - evaluation number 15. Technical report, Jet Propulsion Laboratory (JPL) of the National Aeronautics and Space Administration (NASA), 2006.

S. Sander, R. Friedl, J. Abbatt, J. Barker, J. Burhholder, D. Golden, C. Kolb, M. Kurylo, G. Moortgat, P. Wine, R. Huie, and V. Orkin. Chemical kinetics and photochemical data for use in atmospheric studies - evaluation number 16. Technical report, Jet Propulsion Laboratory (JPL) of the National Aeronautics and Space Administration (NASA), 2009.

R. Sausen and U. Schumann. Estimates of the climate response to aircraft CO2 and NOx emissions scenarios. *Climate Change*, 44:27–58, 2000.

H. Schlager, R. Baumann, M. Lichtenstern, A. Petzold, F. Arnold, M. Speidel, C. Gurk, and H. Fischer. Aircraft-based trace gas measurements in a primary european ship corridor. In *Proceedings of the TAC-Conference*, Oxford, 2006.

U. Schumann and H. Huntrieser. The global lightning-induced nitrogen oxides source. *Atmospheric Chemistry and Physics*, 7:3823–3907, 2007. doi: 10.5194/acp-7-3823-2007.

J. H. Seinfeld and S. N. Pandis. *Atmospheric Chemistry and Physics From Air Pollution to Climate Change*, volume 1. John Wiley & Sons, Inc., second edition, 2006.

D. T. Shindell, G. Faluvegi, D. S. Stevenson, M. C. Krol, L. K. Emmons, J.-F. Lamarque, G. Pétron, F. J. Dentener, K. Ellingsen, M. G. Schultz, O. Wild, M. Amann, C. S. Atherton, D. J. Bergmann, I. Bey, T. Butler, J. Cofala, W. J. Collins, R. G. Derwent, R. M. Doherty, J. Drevet, H. J. Eskes, A. M. Fiore, M. Gauss, D. A. Hauglustaine, L. W. Horowitz, I. S. A. Isaksen, M. G. Lawrence, V. Montanaro, J.-F. Müller, G. Pitari, M. J. Prather, J. A. Pyle, S. Rast, J. M. Rodriguez, M. G. Sanderson, N. H. Savage, S. E. Strahan, K. Sudo, S. Szopa, N. Unger, T. P. C. van Noije, and G. Zeng. Multimodel simulations of carbon monoxide: Comparison with observations and projected near-future changes. *Journal of Geophysical Research*, 111, Oct. 2006. doi: 10.1029/2006JD007100.

D. T. Shindell, G. Faluvegi, D. M. Koch, G. A. Schmidt, N. Unger, and S. E. Bauer. Improved attribution of climate forcing to emissions. *Science*, 326:716–718, 2009. doi: 10.1126/science.1174760.

A. Simmons and R. Strüfing. An energy and angular-momentum conserving finite-difference scheme, hybrid coordinates and medium-range weather prediction. Technical report, ECMWF, European Centre for Medium-Range Weather Forecasts, Reading, U.K., 1981.

S. J. Smith, J. van Aardenne, Z. Klimont, R. Andres, A. Volke, and S. Delgado Arias. Anthropogenic sulfur dioxide emissions : 1850-2005. *Atmospheric Chemistry and Physics*, 11:1101–1116, 2011. doi: doi:10.5194/acp-11-1101-2011.

S. Solomon, D. Qin, M. Manning, Z. Chen, M. Marquis, K. Averyt, M. Tignor, and H. Miller. Contribution of working group I to the Fourth Assessment Report of the Intergovernmental Panel on Climate Change. Technical report, International Panel on Climate Change, Cambridge University Press, UK, April 2007.

C. H. Song, G. Chen, and D. D. Davis. Chemical evolution and dispersion of ship plumes in the remote marine boundary layer: investigation of sulfur chemistry. *Atmospheric Environment*, 37(19):2663–2679, June 2003a. doi: 10.1016/S1352-2310(03)00198-5.

C. H. Song, G. Chen, S. R. Hanna, J. Crawford, and D. D. Davis. Dispersion and chemical evolution of ship plumes in the marine boundary layer: Investigation of $O_3/NO_y/HO_x$ chemistry. *Journal of Geophysical Research*, 108(D4):41–43, Feb. 2003b. doi: 10.1029/2002JD002216.

G. Sousa Santos. *The effects of halogens on global tropospheric ozone*. PhD thesis, International Max Planck Research School on Earth System Modelling, 2008.

C. M. Spivakovsky, J. A. Logan, S. A. Montzka, Y. J. Balkanski, M. Foreman-Fowler, D. B. A. Jones, L. W. Horowitz, A. C. Fusco, C. Brenninkmeijer, M. J. Prather, S. Wofsy, and M. B. McElroy. Three-dimensional climatological distribution of tropospheric OH: Update and evaluation. *Journal of Geophysical Research*, pages 8931–8980, 2000.

D. S. Stevenson, C. E. Johnson, W. J. Collins, R. G. Derwent, K. P. Shine, and J. M. Edwards. Evolution of tropospheric ozone radiative forcing. *Geophysical Research Letters*, 25:38193822, 1998.

D. S. Stevenson, F. J. Dentener, M. G. Schultz, K. Ellingsen, T. P. C. van Noije, O. Wild, G. Zeng, M. Amann, C. S. Atherton, N. Bell, D. J. Bergmann, I. Bey, T. Butler, J. Cofala, W. J. Collins, R. G. Derwent, R. M. Doherty, J. Drevet, H. J. Eskes, A. M. Fiore, M. Gauss, D. A. Hauglustaine, L. W. Horowitz, I. S. A. Isaksen, M. C. Krol, J.-F. Lamarque, M. G. Lawrence, V. Montanaro, J.-F. Müller, G. Pitari, M. J. Prather, J. A. Pyle, S. Rast, J. M. Rodriguez, M. G. Sanderson, N. H. Savage, D. T. Shindell, S. E. Strahan, K. Sudo, and S. Szopa. Multimodel ensemble simulations of present-day and near-future tropospheric ozone. *Journal of Geophysical Research*, 111, Apr. 2006. doi: 10.1029/2005JD006338.

S. Stich, P. M. Cox, W. J. Collins, and C. Huntingford. Indirect radiative forcing of climate change through ozone effects on the land-carbon sink. *Nature*, 2007. doi: 10.1038/nature06059.

K. Sudo and H. Akimoto. Global source attribution of tropospheric ozone: Long-range transport from various source regions. *Journal of Geophysical Research*, 102, June 2007. doi: 10.1029/2006JD007992.

O. A. Svøde, C. R. Hoyle, G. Myhre, and I. S. A. Isaksen. The HNO_3 forming branch of the HO_2 + NO reaction: pre-industrial-to-present trends in atmospheric species and radiative forcings. *Atmospheric Chemistry and Physics*, 2011.

C. Ordóñez, J.-F. Lamarque, S. Tilmes, D. E. Kinnison, E. L. Atlas, D. R. Blake, G. Sousa Santos, G. Brasseur, and A. Saiz-Lopez. Bromine and iodine chemistry in a global chemistry-climate model: description and evaluation of very short-lived oceanic sources. *Atmospheric Chemistry and Physics Discussions*, 11: 27421–27474, 2011. doi: 10.5194/acpd-11-27421-2011.

A. Thomson, K. Calvin, S. Smith, G. Kyle, A. Volke, P. Patel, S. Delgado-Arias, B. Bond-Lamberty, M. Wise, L. Clarke, and J. Edmonds. RCP4.5: A pathway for stabilization of radiative forcing by 2100. *Climatic Change*, 2010.

X. Tie, S. Madronich, S. Walters, R. Zhang, P. Rasch, and W. Collins. Effect of clouds on photolysis and oxidants in the troposphere. *Journal of Geophysical Research*, 108:4642, 2003.

K. E. Trenberth, J. Fasullo, and J. Kiehl. Earth's global energy budget. *Bulletin of the American Meteorological Society*, 90:311–324, 2009. doi: 10.1175/2008BAMS2634.1.

UNCTAD. Review of maritime transport. Technical report, United Nations Conference on Trade and Development, 2008.

UNFCCC. Kyoto protocol. http://unfccc.int/essential_background/kyoto_protocol/items/1678.php Retrieved 11 November 2010, 2011.

N. Unger, D. T. Shindell, D. M. Koch, M. Amann, J. Cofala, and D. G. Streets. Influences of man-made emissions and climate changes on tropospheric ozone,

methane, and sulfate at 2030 from a broad range of possible futures. *Journal of Geophysical Research*, 111, 2006. doi: 10.1029/2005JD006518.

N. Unger, T. Bond, J. S. Wang, D. M. Koch, S. Menon, D. T. Shindell, and S. Bauer. Attribution of climate forcing to economic sectors. *Proceedings of the National Academy of Science of the United States of America*, 107:3382–3387, Feb 2010.

T. P. C. van Noije, H. J. Eskes, F. J. Dentener, D. S. Stevenson, K. Ellingsen, M. G. Schultz, O. Wild, M. Amann, C. S. Atherton, D. J. Bergmann, I. Bey, K. F. Boersma, T. Butler, J. Cofala, J. Drevet, A. M. Fiore, M. Gauss, D. A. Hauglustaine, L. W. Horowitz, I. S. A. Isaksen, M. C. Krol, J.-F. Lamarque, M. G. Lawrence, R. V. Martin, V. Montanaro, J.-F. Müller, G. Pitari, M. J. Prather, J. A. Pyle, A. Richter, J. M. Rodriguez, N. H. Savage, S. E. Strahan, K. Sudo, S. Szopa, and M. van Roozendael. Multi-model ensemble simulations of tropospheric NO_2 compared with gome retrievals for the year 2000. *Atmospheric Chemistry and Physics*, 6(10):2943–2979, July 2006. ISSN 1680-7316.

D. Van Vuuren, M. Den Elzen, P. Lucas, B. Eickhout, B. Strengers, B. Van Ruijven, S. Wonink, and R. Van Houdt. Stabilizing greenhouse gas concentrations at low levels: An assessment of reduction strategies and costs. *Climatic Change*, pages 119–159, 2007.

D. van Vuuren, K. Riahi, R. Moss, J. Edmonds, A. Thomson, N. Nakicenovic, T. Kram, F. Berkhout, R. Swart, A. Janetos, S. Rose, and N. Arnell. Developing new scenarios as a common thread for future climate research, 2010.

D. Van Vuuren, E. Stehfest, M. Den Elzen, S. Deetman, A. Hof, M. Isaac, K. Klein Goldewijk, T. Kram, A. Mendoza Beltran, R. Oostenrijk, J. van Vliet, and B. Van Ruijven. RCP3PD: Exploring the possibilities to limit global mean temperature change to less than 2°C. *Climatic Change*, 2010.

G. C. M. Vinken, K. F. Boersma, D. J. Jacob, and E. W. Meijer. Accounting for non-linear chemistry of ship plumes in the geos-chem global chemistry transport

model. *Atmospheric Chemistry and Physics Discussion*, 11:1778917823, 2011. doi: 10.5194/acpd-11-17789-2011.

R. von Glasow, M. G. Lawrence, R. Sander, and P. J. Crutzen. Modeling the chemical effects of ship exhaust in the cloud-free marine boundary layer. *Atmospheric Chemistry and Physics*, 3(1):233–250, Feb. 2003. ISSN 1680-7316.

C. Wang, J. J. Corbett, and J. Firestone. Improving spatial representation of global ship emissions inventories. *Environmental Science & Technology*, 42(1): 193–199, Jan. 2008. doi: 10.1021/es0700799.

W.-C. Wang and N. D. Sze. Coupled effects of atmospheric N_2O and O_3 on the Earth's climate. *Nature*, 286:589–590, 1980. doi: 10.1038/286589a0.

P. Wennberg. Atmospheric chemistry: Bromine explosion. *NATURE*, 397:299–301, 1999. doi: 10.1038/16805.

M. Wesely. Parameterization of surface resistances to gaseous dry deposition in regional-scale numerical models. *Atmospheric Environment*, 23:1293–1304, 1989.

T. Wigley, S. Smith, and M. Prather. Radiative forcing due to reactive gas emissions. *Journal of Climate*, 15:2690–2696, 2002.

O. Wild and M. J. Prather. Global tropospheric ozone modeling: Quantifying errors due to grid resolution. *Journal of Geophysical Research*, 111(D11305), 2006. doi: 10.1029/2005JD006605.

O. Wild, M. Prather, and H. Akimoto. Indirect long-term global radiative cooling from NO_x emissions. *Geophysical Research Letters*, 28:1719–1722, 2001.

J. Yienger and H. Levy. Empirical model of global soil biogenic NO_x emissions. *Journal of Geophysical Research*, 100:11447–11464, 1995.

G. J. Zhang and N. A. McFarlane. Sensitivity of climate simulations to the parameterization of cumulus convection in the canadian climate centre general circulation model. *ATMOSPHERE OCEAN*, 33:407–407, 1995.